CRANFIELD UNIVERSITY

Fibre optic sensing for measuring rotor blade structural dynamics

SIMONE WEBER

School of Aerospace, Transport and Manufacturing
Dynamics, Simulation & Control Group
Department of Aerospace Engineering

PhD THESIS

This page is intentionally left blank.

CRANFIELD UNIVERSITY

SCHOOL OF AEROSPACE, TRANSPORT AND MANUFACTURING

PhD THESIS

ACADEMIC YEAR 2018-19

SIMONE WEBER

FIBRE OPTIC SENSING FOR MEASURING ROTOR BLADE STRUCTURAL DYNAMICS

SUPERVISOR :
DR MUDASSIR LONE & DR ALASTAIR COOKE

APRIL 2019

This page is intentionally left blank.

Abstract

Researchers and practitioners spend much effort in developing theoretical methods to design and predict the performance of helicopter rotor blades. These blades have evolved to become complex structures designed to operate in extreme conditions and over the exceptionally broad flight envelopes of helicopters. As a result, these vehicles are subject to strict maintenance regimes that increase the overall operational costs. The need to reduce such costs and improve aircraft performance together with the emergence of novel fibre optic-based sensor technologies form the context of the research presented in this thesis. Opportunities for blade health and usage monitoring created by sensor technologies such as fibre Bragg gratings (FBG) for measuring strain and direct fibre optic shape sensing (DFOSS) present today's industry with a critical question: Does the designer follow contemporary technological trends and adopt a preventative approach where he/she invests in such instrumentation systems or is a reactive approach more appropriate where he/she awaits to have sufficient evidence of operational need? A survey was carried out as part of this research to understand this dichotomy faced by rotorcraft engineers and systems architects. Adhering to the safety orientated culture within the aerospace community, the aim of this research work is the numerical and experimental exploration of challenges associated with the deployment of fibre optic instrumentation systems for future health and usage monitoring. This was achieved through three objectives: (1) development of a computational framework allowing the simulation of rotor blade dynamics at an appropriate fidelity, (2) exploration of blade health monitoring capabilities using fibre optic instrumentation systems and, (3) laboratory-based structural testing. Health and usage monitoring capabilities were explored theoretically through a parametric damage study using the computational framework. The experimental testing highlighted the need for a sensor placement methodology for distributing FBG-based strain sensors over the blade (both in terms of spanwise and chordwise locations) for accurately recovering mode shapes. This was followed by investigating the accuracy of the novel DFOSS system by deploying it on a bearingless main rotor blade along with other commercially available instrumentation systems. Test results were used to (1) perform multi-step indirect finite element modelling to increase the accuracy of the developed structural model and, (2) to explore the suitability of FBG and DFOSS measurements for damage detection. The main finding of this work is that future rotor health and usage monitoring systems based on fibre optic sensing technologies require the development of a hybrid FBG and DFOSS instrumentation system. Although numerous areas of further work have been identified, it is hoped that the adoption of such an instrumentation system will not only help reduce operational costs but also provide much needed operational data on helicopter blade dynamics to validate methods and improve designs.

Keywords: bearingless main rotor, health monitoring, fibre optic sensors, shape sensing, helicopter dynamics, damage detection

This page is intentionally left blank.

Acknowledgements

"*All I know is that I know nothing [Socrates]*", but what I know for sure is that the past years have taken me on an incredible journey full of learning, steep climbs and falls, patience, growth, fun, and experiencing wonderful friendship. Now as I reach the end of this journey I finally can express my gratitude to all these truly incredible people who made this possible, although knowing that these words will not give any justice.

First I want to thank my family for their unconditional love, their immense support and understanding for anything I have pursued in life so far, for being here for me whenever I needed it. Mum, I just have no words for you, feelings would be the only way how to truly express my gratefulness. Dad, thank you for spoiling me whenever I was home and for always giving me those useful advices. My incredible sisters, Daniela and Anja, who are my inspiration and to whom I always look up to. Leonardo for bringing so much joy to our family and without knowing, his cuteness was sometimes the only thing that could cheer me up. Granddad for his wisdom, advices and brilliant mind (*nein, es gibt keine Gewinnbeteiligung!*), cheekiness, and teaching me how to enjoy life to the fullest. Finally, I am deeply thankful to my partner for continuously believing in me and always encouraging me to dream a little bit bigger.

I would like to acknowledge and thank Airbus Helicopters UK, especially the inspirational managing director Colin James, for supporting and funding my PhD and allowing me to grow professionally, as well as personally. I have found myself to be extremely lucky to pursue my PhD in combination with the project BladeSense.

I must express my profound gratitude to my supervisors, Mudassir Lone and Alastair Cooke. Mudassir has been one of my most important mentors and by pushing me to look beyond the horizon, getting me out of my comfort zone, and making me jump over my shadow I would not be where I am today. It still amazes me how he manages to inspire with his enthusiasm and charisma. I am also very grateful to Alastair for his constructive feedback and corrections, especially towards the end of my PhD. I would also like to thank James Whidborne for his invaluable advice and support and time throughout my studies.

I was very lucky to be part of such a wonderful, inspiring and diverse research group. Sezsy, who is the strongest, funniest and most caring person I have ever met. You have no idea what an inspiration you are to this group! I am deeply thankful for all the conversations we had; from random midnight talks in the office all the way to whether *something* makes sense. Raheeg for always being so cheerful, for the laughs and fun photo sessions we had! Gaétan, I am immensely thankful for your help and showing me how to master Matlab plots. With your incredible humbleness, creativeness, and random facts you gave something very special to the group. Martin, thank you so much for all your help in the lab - the person I could always rely on for immediate help. And not to forget the provision of breakfast after long nights! Alessandro, I have always been impressed by how you stand for what you believe in. Thank you for all your knowledge and our little climbing sessions! Dave, I miss the lunch breaks with you, it has been so much

fun and refreshing. Vilius, thanks for all the chocolates and thoughtful little gifts from Lithuania. Thanks Estela for being a breath of fresh air to the group, Shun for your structural feedback and Matt for always trying so hard to drag me out for a little break! And last but not least: Octavio, thank you so much for your helicopter support and good times we had :-). And of course, I am deeply thankful for all the students who helped me and from whom I learnt a lot: Laura, Xavier, Cerys, Anaïs and Marie-Emmanuelle.

The Aerospace Research Integration Centre (AIRC) has been a wonderful place to work! Thank you Mudassir for rescuing us from the "fish tank" and many thanks to Tim Mackley for giving us the opportunity to work in such an inspiring environment. Furthermore, I am very grateful to Iain Gray and Tim for all the networking opportunities. Many thanks to Lisa Rice for organising events, meetings and for the office supplies!

BladeSense has been an incredible opportunity to develop myself. I want to thank all project partners for what I have learnt and Alan Levenston for his kindness and incredible support on the project. I am extremely grateful to Stefan Emmerling and Raphael Rammer from Airbus Helicopters Deutschland for their support, trust and time for giving invaluable answers to my questions. I am also deeply thankful to Dan Williams for his continuous support and help. In particular, I feel very grateful towards Cranfield's academics and staff members who have supported and helped me throughout the project and my PhD. I first want to acknowledge Cranfield's Engineering Photonics team, which under the leadership of Ralph Tatam, is exceptional. Helpfulness, cheerfulness, kindness are one of the key attributes I appreciated so much about this team. Ralph, thank you so much for the caring conversations and for constant indications on figure and label sizes! Steve James for always being available when needed and your thorough English and comma corrections. Thomas Kissinger, thank you for your constructive feedback and fun lab work. Kevin Mullaney, for your industrial strategic advices and humour.
Furthermore, I would like to thank Luca Zanotti Fragonara and Ivan Petrunin for introducing me to the world of experimental testing, and Ivan for his kind advices and help to set up the shaker. Thank you to Nick Lawson for his aerodynamic expertise, Irene Moulitsas for her advice with regards to computational modelling and Graham Hartwell for the help of manufacturing some important lab equipment. I would also like to acknowledge all survey participants for their invaluable comments and feedback.

Mark Young, I am so incredibly thankful for your help and encouragements for applying to Cranfield, for your friendship and invaluable practical advices. Special thanks to Rémi Boucher, Sebastian Pupek and Gavin Wingate-Pearse who always stood behind me. Tanja and Anita, thank you so much for your wonderful friendship and support. To all my London friends, alias *"Bordeaux Group"* who ensured there is some life outside of work, especially many thanks to Julien who took the burden to read my *Denglisch*!

I also want to express a special thank you to CFTS (Central Federation of Traditional Shotokan) for the warm welcome and giving me the feeling to belong to a little family. The stress relief after each training was always invaluable and worthwhile. Renshi, thank you so much for the fun training sessions, for believing in me and encouragements for achieving the seemingly impossible of Nidan!

And finally, I am deeply grateful to Anita Pollinger for the guidance and encouragements, ensuring that I walk in the right direction.

Contents

This page is intentionally left blank.

List of Figures

This page is intentionally left blank.

List of Tables

Nomenclature

A	Cross section, (m^2)
A	Rotor disc area, (m^2)
CN	Condition number
C_T	Rotor thrust coefficient
C_d	Section drag coefficient
C_f	Skin-friction coefficient
C_l	Section lift coefficient
C_m	Aerofoil pitching moment coefficient
C_{L_H}, C_{M_H}	Roll and pitching moment coefficient
C_{d_0}	Section zero-lift drag coefficient
C_{l_α}	Section lift-curve slope
D	Direction cosine matrix
D	Drag force, (N)
E	Young's modulus, (N/m^2)
EA	Longitudinal stiffness, (N)
EI	Bending stiffness, (Nm^2)
F	Prandtl's tip-loss function
F_C	Centrifugal force acting on blade element, (N)
G	Shear modulus, (N/m^2)
GJ	Torsional stiffness, (Nm^2/rad)
I	Cross-sectional area moment of inertia, (m^4)
J	Cost function
L	Lagrange, (kgm^2/s^2)
L	Lift force, (N)
M	Mach number

M	Pitching moment, (Nm)
NSI	Non-structural mass moment of inertia, (kgm)
N_b	Number of rotor blades
O	Origin of reference frame
Q	Generalised force, (N)
R	Rotor radius, (m)
Re	Reynolds number
T	Kinetic energy, (kgm^2/s^2)
T	Rotor thrust, (N)
T	Tension in beam, (N)
U	Strain energy, (Nm)
U	Velocity in potential flow, (m/s)
U_e	Velocity at the edge of the boundary layer, (m/s)
U_∞	Fluid velocity, (m/s)
V	Total blade velocity, (m/s)
V_M	Mass flow parameter
V_P	Out-of-plane velocity component, (m/s)
V_R	Resultant flow, (m/s)
V_T	In-plane velocity component, (m/s)
V_{X1}, V_{X2}, V_{X3}	Orientation vector in x,y and z-direction
W	Gravitational force acting on blade element, (N)
W_o	Observability Gramian
Δt	Sampling time, s
$\bar{\mathbf{S}}_{\Delta M}$	Scaled MAC sensitivity matrix
$\bar{\mathbf{S}}_{\lambda}$	Scaled eigenvalue sensitivity matrix
$\breve{u}$	Lower uncertainty bound, (m)
$\delta \bar{A}$	Virtual action, (Nm)
$\delta \bar{W}$	Virtual work, (Nm)
$\hat{\mathbf{L}}$	Inflow gain matrix

$\hat{\mathbf{d}}$	Estimated displacement vector
$\hat{u}$	Upper uncertainty bound, (m)
$\mathbf{A}$	System matrix
$\mathbf{B}$	Input matrix
$\mathbf{C}$	Damping matrix, (kg/s)
$\mathbf{C}$	Output matrix
$\mathbf{D}$	Feedthrough matrix
$\mathbf{E}$	Orthogonal projection matrix
$\mathbf{F}$	Fisher information matrix
$\mathbf{F}$	Force vector, (N)
$\mathbf{K}$	Stiffness matrix, (N/m)
$\mathbf{M}$	Mass matrix, (kg)
$\mathbf{M}$	Matrix of the apparent mass terms
$\mathbf{Q}, \dot{\mathbf{Q}}, \ddot{\mathbf{Q}}$	Nodal displacement, velocity and acceleration state vectors
$\mathbf{S}_{\Delta M}$	MAC sensitivity matrix
$\mathbf{S}_{\lambda}$	Eigenvalue sensitivity matrix
$\mathbf{V}_{\mathbf{M}}$	Mass flow parameter matrix
$\mathbf{W}$	Weighting matrix
$\mathbf{d}$	Displacement vector, (m)
$\mathbf{e}$	Normalised estimation error vector
$\mathbf{q}, \dot{\mathbf{q}}, \ddot{\mathbf{q}}$	Generalised displacement, velocity and acceleration state vectors
$\mathbf{u}$	Input vector
$\mathbf{v}$	Measurement noise vector
$\mathbf{w}$	Process vector
$\mathbf{x}$	State vector
$\mathcal{F}$	Reference frame
$\mathbf{T}$	Displacement-strain transformation matrix
$\widetilde{\mathbf{C}}$	Generalised damping matrix, (kg/s)
$\widetilde{\mathbf{F}}$	Generalised force vector, (N)

$\widetilde{\mathbf{K}}$	Generalised stiffness matrix, (N/m)
$\widetilde{\mathbf{M}}$	Generalised mass matrix, (kg)
a	Speed of sound, (m/s)
a_0, a_1	Damping coefficients
b	Semi-chord, (m)
c	Blade chord, (m)
c_f, c_l	Linear spring rate in flapping and lagging direction, (N/m)
c_t	Rotational spring rate, (Nm/rad)
c_x, c_z	Distance between strain reading and neutral axis in x- and z-direction, (m)
cg	Distance of centre of mass, (m)
e	Error, (%)
e	Mass centroid offset from elastic axis, positive when in front of the elastic axis, (m)
e_A	Tensile axis (area centroid) offset from elastic axis, positive when in front of the elastic axis, (m)
f	FBG wavelength strain coefficient, usually given as 1.2 $\mu\epsilon$ pm^{-1}
g	Acceleration due to gravity, (m/s^2)
h	Thickness of blade profile, (m)
k	Reduced frequency
l	Fibre optic path length, (m)
m	Mass, (kg)
m_t	Total mass of blade, (kg)
na	Distance of neutral axis, (m)
p	Updating parameter
p, q, r	Roll, pitch, and yaw rate
r	Radial position of blade element, (m)
r_e, r_s	Residual for eigenvector and mode shape
s	Frequency sweep input
t	Time, (s)

t_f	Protrusion thickness due to fibre optic cable
u, v, w	Elastic displacements in the x,y,z directions, (m)
v_i	Induced velocity, (m/s)
w	Normal component of induced flow, positive downward, dimensionless on ΩR
w_α	Weighting factor for c_z
w_β	Weighting factor for c_x
x, y, z	Mutually orthogonal directions of axes system
FDI	Frequency damage index
MAC	Modal assurance criterion
MDI	Mode shape damage index
VDI	Variance damage index

Greek Alphabet

α	Angle of attack, (rad)
α	Natural frequency weighting factor
α_n^m, β_n^m	Induced-flow coefficients
β	Mode shape weighting factor
χ	Wake angle, (rad)
Δf	Frequency sensitivity
Δl	Distance between strain stations, (m)
ΔM	Change in MAC
δz_{tip}	Difference in tip deviation, (m)
Δ	Wind angle, (rad)
δ	Boundary layer thickness
δ	Distance between fibre optic cores, (m)
$\Delta \lambda_i f$	Wavelength change, (nm)
δ^*	Displacement thickness
ϵ_f	Surface strain due to flap displacement
ϵ_l	Surface strain due to lag displacement

ϵ_T	Total axial surface strain
η	Refractive index
η	Sectional coordinate corresponding to major principal axis for a given point on the elastic axis, (m)
$\eta_0, \eta_{1s}, \eta_{1c}$	Pilot's collective lever, cyclic longitudinal, and cyclic lateral stick positions
γ	Tilt angle, (rad)
$\hat{\phi}$	Sensor mode shape
κ	Curvature
κ	Shear correction factor (most authors use $\kappa = 5/6$)
Λ	Grating period (distance between the gratings), (m)
λ	Eigenvalue, $\lambda = \omega^2$
$\lambda_0, \lambda_s, \lambda_c$	Uniform, lateral, and longitudinal inflow
λ_i	Induced inflow
λ_m	Normal induced inflow
λ_b	Bragg wavelength, (m)
$\mathbf{\Phi}$	Mode shape matrix
$\mathbf{\Psi}$	Strain mode shape matrix
μ	Dynamic viscosity, (kg/ms)
μ	Non-dimensional velocity component parallel to rotor disc
μ_1, μ_2, μ_3	Non-dimensional velocity components in $x-$,$y-$,z-direction
ν_0, ν_s, ν_v	Uniform, lateral, and longitudinal variations in rotor inflow
Ω	Rotor rotational speed, (rad/s)
ω	Circular frequency, (rad/s)
ϕ	Blade cross-sectional elastic rotation, (rad)
ϕ	Inflow angle, (rad)
ϕ_e, θ_e, ψ_e	Euler angles, (rad)
ϕ_t	Total rotation around feathering axis, (rad)
Ψ	Azimuth angle, (rad)
ψ	Arc angle of the bent fibre, (rad)

ψ	Rotation of beam cross section, (rad)
ψ	Strain mode shape
ψ_T	Surface strain mode shape
ρ	Density, (kg/m^3)
σ	Blade solidity
τ_w	Shear stress on wall
θ	Deflection angle at each sensor location, (rad)
θ	Momentum thickness
θ_{0_T}	Tail rotor collective pitch angle, (rad)
$\theta_0, \theta_{1s}, \theta_{1c}$	Collective, longitudinal cyclic, and lateral cyclic pitch angle, (rad)
θ_p	Main rotor pitch angle, (rad)
θ_{tw}	Blade pre-twist angle, (rad)
ϑ	Built-in twist angle, (rad)
ξ	Coordinates along the elastic axis, (m)
ζ	Damping ratio
ζ	Sectional coordinate normal to η axis at elastic axis, (m)
f	Natural frequency
f_s,f_r	Static and rotating natural frequency, (rad/s)

Subscript

A	Analytical
AD	Aerodynamic
B	Body system
el	Rotor blade structural deformation
F	Force
H	Hub system
I	Inertial system
M	Moment
N	Rotor blade nodal system
r	Rotating

RB	Rotor blade system
s	Non-rotating
t	Total
W	Wind system
X	Experimental

Superscript

$(\,)'$	$\frac{\partial}{\partial x}$, $(1/m)$
$(\,)''$	$\frac{\partial^2}{\partial x^2}$, $(1/m^2)$
$(\dot{})$	$\frac{\partial}{\partial t}$, $(1/s)$
$(\bar{})$	Normalised
$*$	Damage case

List of Acronyms

ACC (1D)	Uniaxial accelerometers
ACC (3D)	Triaxial accelerometers
AHD	Airbus Helicopters Deutschland (Germany)
AHUK	Airbus Helicopters UK (United Kingdom)
AVT	Ambient Vibration Test
BC	Boundary Condition
BEMT	Blade Element Momentum Theory
BET	Blade Element Theory
BMR	Bearingless Main Rotor
CAA	Civil Aviation Authority
CAD	Computer Aided Design
CAMRAD	Comprehensive Analytical Model of Rotorcraft Aerodynamics and Dynamics
CBEAM	Beam element connection (NASTRAN command)
CDF	Central Difference Formulation
CELAS	Scalar spring property and connection (NASTRAN command)
CFD	Computational Fluid Dynamics
CONM2	Concentrated mass element (NASTRAN command)
DFOSS	Direct Fibre Optic Shape Sensing
DLR	Deutsches Zentrum für Luft- und Raumfahrt (German Research Centre)
DOF	Degree Of Freedom
DRT	Decomposition of the Rotation Tensor
DST	Displacement-Strain-Transformation
EASA	European Aviation Safety Agency
EFI	Effective Independence
EMA	Experimental Modal Analysis
FAA	Federal Aviation Administration
FBG	Fibre Bragg Grating
FE	Finite Element
FEMU	Finite Element Model Updating
FFT	Fast Fourier Transform
FIM	Fisher Information Matrix
FOD	Foreign Object Debris
GA	Genetic Algorithm
GRID	Grid point (NASTRAN command)
GVT	Ground Vibration Test
HUMS	Health and Usage Monitoring System
IHT	Impact Hammer Test
IPCT	Image Pattern Correlation Technique
KIAS	Knots-Indicated Air Speed
LR	Low-Reflectivity

MTOW	Maximum Takeoff Weight
NASA	National Aeronautics and Space Administration
NASTRAN	**NA**SA STRucture ANalysis
NSI	Nonstructural mass moment of inertia (NASTRAN command)
OMA	Operational Modal Analysis
OSP	Optimal Sensor Placement
OSS	Optimal Strain Sensor
PS	Pattern Search
PSD	Power Spectral Density
PBEAM	Beam property (NASTRAN command)
RMS	Root Mean Square
RPM	Rounds Per Minute
RoR	Random-on-Random vibration control
RSS	Random Strain Sensor
SPC1	Single-point constraint (NASTRAN command)
SSI	Stochastic Subspace Identification
SVD	Singular Value Decomposition
TDD	Time-Domain Decomposition
VABS	Variational Asymptotic Beam Sectional analysis
VAM	Variational Asymptotic Method

`

CHAPTER 1

Introduction

Health monitoring and usage systems (HUMS) were introduced in the early 1990s on the North Sea helicopter fleet as a consequence of a series of accidents. Data analysis by the Civil Aviation Authority (CAA) estimated that a total of 6 out of 63 airworthiness related issues were classified as potentially catastrophic and hazardous, while 2 cases could have led to accidents if they had not been identified in time [1]. However, an investigation of HUMS towards rotor health monitoring suggested that there is limited benefit from rotor monitoring due to a decline in the accident rate [2]. Figure 1.1 shows the estimated trend of the main rotor benefit rating over the years, with the peak being reflected through the high accident rates in the 1980s.

Although little statistical accident evidence points towards the need for a health monitoring system for rotor blades [2], today there is a growing interest in the rotorcraft community [3–6] to expand the HUMS portfolio with operational in-flight blade measurements. Especially as technological advancements start to become mature, such data collection for the in-flight operation could be just a step away from being implemented. The intense research in this area proves that designers and practitioners have a great interest in such information. This effort started as early as 1940 when Carl Bode successfully filmed a rotating rotor blade of a Fa 223 by mounting a camera at the rotor hub. At a frame rate of 16 Hz some low-frequency blade dynamics could be observed [7]. Bode discovered that blade dynamics were not calculated correctly and proved that the Coriolis acceleration term could not be neglected. This first experiment made a significant contribution to the improvement of the theoretical modelling methods and demonstrated the importance of integrating practice with theory. Although modelling techniques for main rotor dynamics are now very advanced, a lack of knowledge of in-flight behaviour for validation purposes still remains.

This background has motivated the rotorcraft community to expand effort towards advanced mathematical modelling and instrumentation techniques. Recent work with fibre optic strain gauges utilising fibre Bragg gratings (FBG) on a main rotor blade has shown their potential for in-flight measurement [8]. However, there are advantages and disadvantages of sensing strain. Although highly sensitive measurements can be obtained, a detailed structural model is required to determine structural loading [9] and to relate

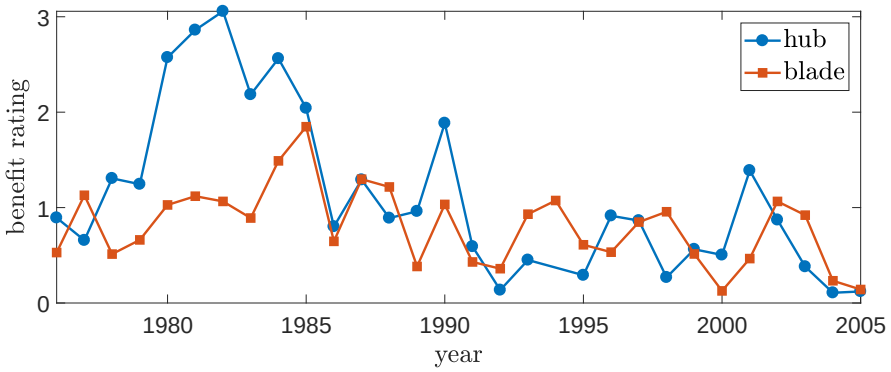

Figure 1.1: Benefit rating for monitoring rotor health (reproduced from Reference [2])

the measured strain mode shapes to deformation, using measurements with low spatial resolution. Since the shape of a structure is the most fundamental characteristic that can be analysed and deviations from the expected shape can be easily visualised and interpreted, much effort was put into converting strain into displacement [10–15]. Although several shape sensing approaches have been reported [16–18], the majority relies on the measurement of the differential strain experienced by several laterally offset optical fibres mounted on opposing surfaces of the structure to determine local curvature, from which the shape of the structure can be determined. This highlights the need for a fibre optic instrumentation system, such as direct fibre optic shape sensing (DFOSS) [19]. DFOSS allows changes in the sensor path and thus changes in the structural shape in three dimensions. A key advantage of DFOSS is that the shape is determined directly within the sensing cable, removing the dependency on efficient strain transfer from the structure to the sensor, where simple surface mounting, for example using adhesive tape, is sufficient for it to follow the shape of the structure.

Until now rotor health monitoring capabilities are limited to model-based exploration due to lack of experimental evidence [4]. The inability to explicitly monitor the operational loading environment and resulting blade deformations have led to pragmatic solutions that rely on human qualitative judgement. Maintenance organisations still rely on traditional servicing methodologies, such as the tap test that requires practice and experience to detect damage efficiently. Furthermore, operating hour-based methods rely on conservative guidelines that have been extrapolated using loading tests from whirl rigs. These have been the main subject for performance testing of rotor blades that started to find its application in the pioneering years of helicopter development. Figure 1.2 shows that this technology is still commonly used. It is believed that rotor health monitoring systems are promising tools for supporting the maintenance actions, and further contribute to condition-based maintenance for reducing operating costs and improving aircraft availability.

Data collection during operation should benefit the research community and designers by validating mathematical models within design tools. Yet, the question of whether the operator would benefit from such systems remains unanswered. Industrial competition often forces designers to follow technological trends, but are such data collection efforts beneficial from an operator's perspective and do these systems contribute towards safety?

Although the rotorcraft engineering community is striving to continuously increase operational and economical efficiency, sometimes the needs of the end-users are overlooked.

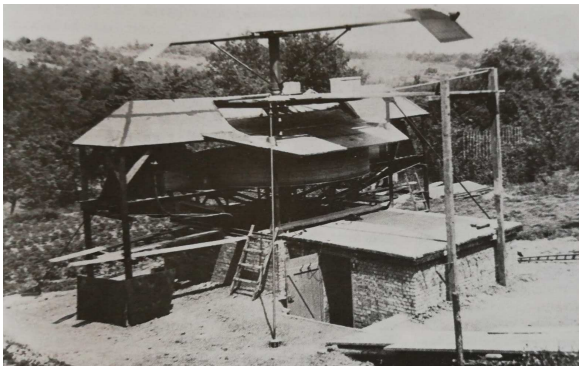

(a) Early test rig developed by Albert Hirth in 1914 (reproduced from Gersdorff and Knobling [7])

(b) Modern test rig at AHD [20]

Figure 1.2: Evolvement of test rig

Consequently, this research work first focuses on a survey that was conducted to provide a user-orientated context that could inform the decision-making process for integrating state-of-the-art rotor blade health monitoring systems onboard operational helicopters. This is then followed by a description of the deployment of novel fibre optic sensors (FBG and DFOSS) to a bearingless main rotor blade (BMR) to prove their suitability for characterising blade dynamics. Possible damage indicators are explored using theoretical simulation results in the rotating frame. This work is concluded by pinpointing benefits of each instrumentation systems.

1.1 Aims and objectives

The aim of this research work is the numerical and experimental exploration of challenges associated with the deployment of fibre optic instrumentation systems for future health and usage monitoring. This was achieved through the following objectives:

1. Development of the computational framework:
    - Development of structural H135 bearingless main rotor blade model.
    - Development of coupled aeroelastic main rotor model.
    - Definition of optimal mapping path using fibre optic-based strain sensors.
2. Exploration of blade health monitoring capabilities through fibre optic instrumentation systems:
    - Parametric study to investigate the impact of damage (lumped mass) on the structural response of a rotating rotor blade.
    - Development of a damage metric to distinguish between a damaged and a healthy blade.

3. Experimental testing:

   - Perform structural loading and ground vibration test in a static environment to assess the predictive capabilities of the structural model.
   - Assessment of the accuracy of each instrumentation system: (1) multiplexed arrays of FBGs that act as strain gauges, and (2) a novel method that allows the direct measurement of shape.
   - Demonstration of damage index on the experimental test case and pinpoint the benefits of each instrumentation system for capturing blade dynamics.

1.2 Thesis outline

This thesis explores health and monitoring capabilities through theoretical studies and demonstration in a non-rotating test environment. The thesis structure is illustrated in Figure 1.3.

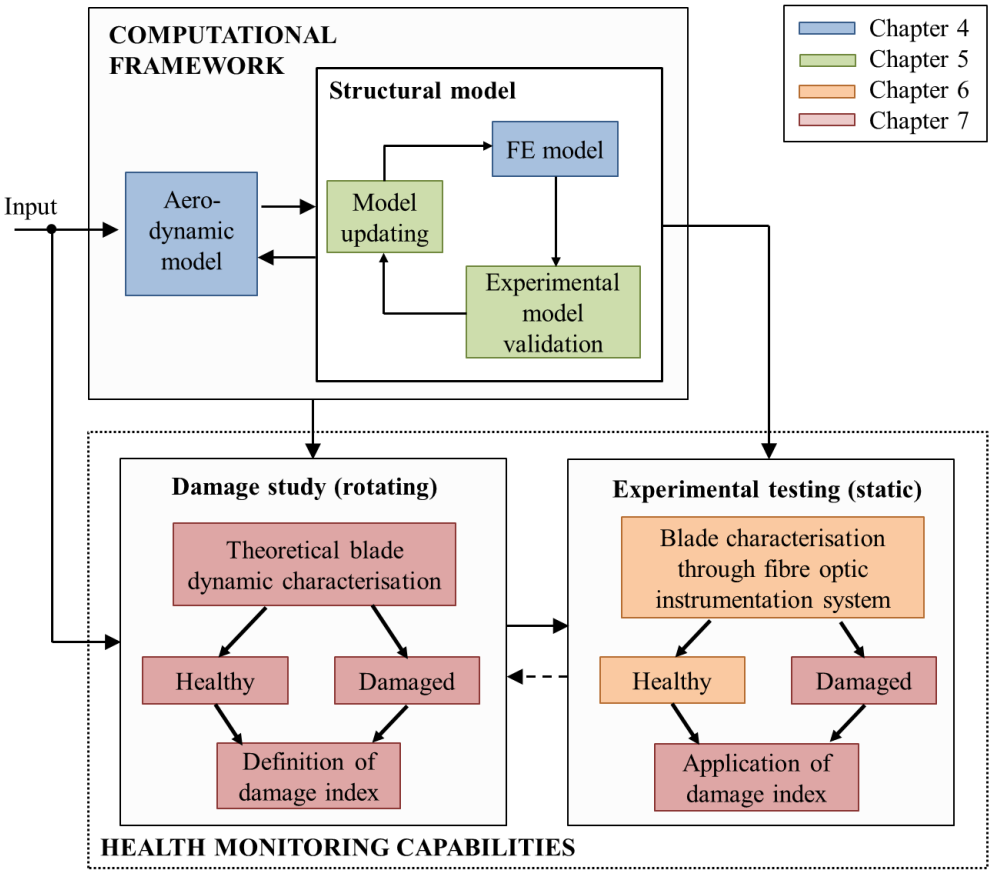

Figure 1.3: Thesis structure

Chapter 2 provides a user-orientated context that can inform the decision making process for integrating state-of-the-art instrumentation systems for rotor blade health monitoring onboard operational helicopters. Chapter 3 presents a literature review covering aeroelastic modelling techniques of main rotors, that is followed by a summary of rotor

blade health monitoring aspects including historic and state-of-the-art instrumentation systems. This provides the reader with an understanding of the benefits of deploying highly advanced fibre optic sensing technologies for in-flight operations over current measurement techniques. This chapter concludes by addressing existing sensor placement methodologies. The core of the computational framework is outlined in Chapter 4 that describes the structural model development of a bearingless main rotor blade that is coupled with a quasi-steady dynamic inflow model. Chapter 5 discusses the validation and refinement of the structural model in virtue of experimental evidence. Then Chapter 6 moves away from model development and explores the capabilities of highly advanced fibre optic sensors: (1) multiplexed arrays of FBG acting as strain gauges and (2) the novel method DFOSS that allows the direct measurement of shape for a healthy blade. While the first part of Chapter 7 explores the theoretical instrumentation capabilities in the rotating frame, this research work concludes by developing damage indicators for health monitoring purposes through a parametric damage study and uses experimental test data from a damage case for validation purposes. Finally, the key conclusions, contributions to knowledge, areas of future work and the various ways in which the findings of this research have been disseminated are presented in Chapter 8.

This page is intentionally left blank.

CHAPTER 2

Monitoring systems - a user perspective

It is well understood in the rotorcraft community that metallic blades in comparison to composite blades are more prone to damage. At the same time, the engineering community is putting significant effort towards developing health monitoring systems [3–6]. The objective of this chapter was to provide a user-orientated context that can inform the decision making process for integrating state-of-the-art instrumentation systems for rotor blade health monitoring [19] onboard operational helicopters. This was done by conducting a survey with over 100 participants worldwide consisting of pilots, flight test engineers, and licensed engineers. Usually major accidents are recorded and analysed by the aviation authorities and in some cases lead to changes in regulations to increase safety. As an accumulation of small damages can lead to a catastrophic event it is important to be aware of the nature and frequency of such. Apart from a detailed aircraft accident and incident analysis given by CAA between 1976 - 2005 [2] there are, to the authors' knowledge, no publicly available collections of statistical data summarising the type and number of minor rotor blade damage incidents. Over the past 10 years fibre optic instrumentation systems have matured significantly, and hence a reinvestigation of rotor blade accident or incidents is timely.

A short summary of statistical data collection reported in the past is presented before providing details of the subjects who participated in this activity. The subsequent section discusses damage occurrence rates and types. This is followed by two sections that focus on the key damage types associated with operational experience and the overall impact.

2.1 Review of previous statistics

Over the past 40 years statistics collected show that the rotorcraft accident rate has decreased drastically. In the USA alone, the rate reduced from 30.5% per 100,000 flight hours in 1970 [21] to 11.3% in 1979 [21] and decreased further to 3.19% in 2016 [22]. This reflects significant technological advances in helicopter design and operations, such as the availability of improved materials, more reliable power plants, advanced avionics and flight control systems. Yet, many factors can lead to an accident and these are not

only dependent on factors such as pilot experience, operational environment, or weather conditions [21], but also on the helicopter as an engineered system. Out of all components the main rotor system is the most flight critical. Several fatalities are reported in the literature involving rotor blades that utilise a combination of metallic and composite materials. These were mainly due to fatigue fracture [23–29] or corrosion [30] of the metallic part. No fatal accident has been reported that involved fatigue damage of composite materials. It should be noted that composite blades are qualified to EASA/FAA regulations that require the demonstration of robust manufacturing and inspection processes [31]. In addition, both fatigue safe life, damage tolerance and in-service damage limits have to be demonstrated [31]. The high fatal accident rate of metallic blades compared to composite blades suggests the need for an instrumentation systems that can detect internal damage at an early stage, highly relevant to an accident involving an S-76A operating in the North Sea [29] which suffered catastrophic failure caused by fatigue crack in the spar. The affected blade was previously struck by lighting resulting in microstructural damage that was not detectable when the blade was returned for assessment.

Incidents involving main rotor blades are not always reported and consequently it is not known what damage commonly occurs in flight. Such information is difficult to gather due to the increasing number of helicopters entering service. Minor incidents, such as trim tab or blade protection tape damage are usually recorded internally by the maintenance organisation and tend to be treated as proprietary information. However, an interesting summary of trends and categorisation of main rotor faults extracted from an available data base to the CAA is given in [2]. Out of a total number of 2,685 entries, 510 cases were related to the rotor faults from which 143 cases concerns rotor blades, 225 rotor hub and 142 tail rotor. This database also revealed that hub defects resulted in 16 accidents and serious incidents, while 9 cases were related to the blade. Figure 2.1 shows a trend of main rotor faults by year, highlighting a significant peak in the 1980s hub faults that have a rapid decrease, while blade faults decrease more steadily. Figure 2.2 presents a detailed breakdown, showing that hub faults were dominated by damper issues, pitch control or pitch link, while most blade faults were related to cracks or delamination, pocket or tip cap defects. Note that no differentiation was made between blades constructed of metal or composite material.

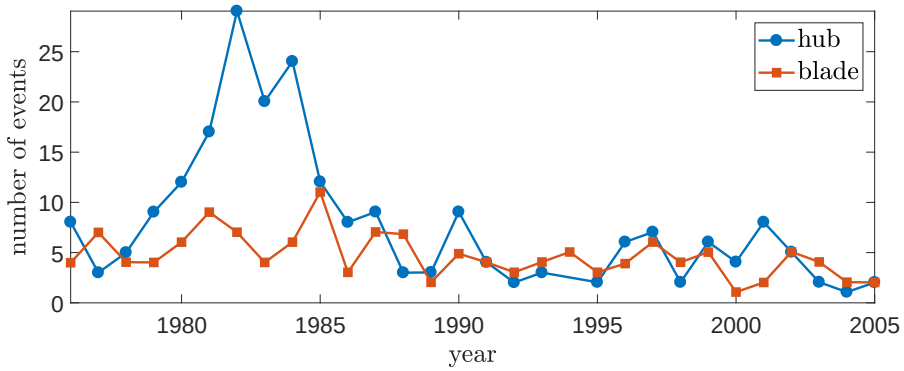

Figure 2.1: Trends in main rotor damage (reproduced from Reference [2])

In 2015 it was reported that approximately 34,000 helicopters operated worldwide [32]. Only a few reports list events involving blade damage, resulting from bird strike [33], wire strike [34], or lightning strike [35]. These reports show that only 3 out of 628 bird strike cases between 1990 and 2015 had a direct impact on the main rotor blade causing a

landing (emergency or precautionary). Two out of 13 lightning strikes between 1999 and 2009 involving transport helicopters used in the petrochemical sector resulted in damage to the rotor blade [35]. The study also forecasted a 0.5% increase in accidents due to expected changes in weather conditions for the period between 2010 and 2019.

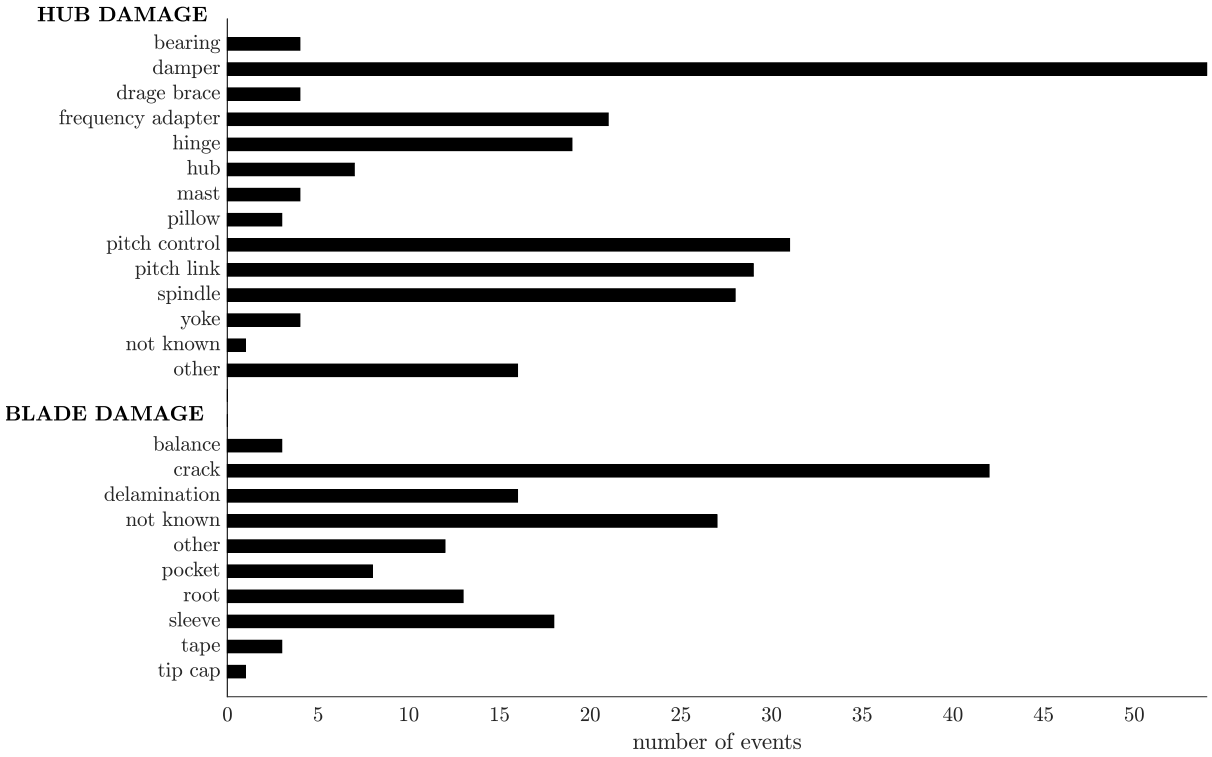

Figure 2.2: Type of main rotor damage occurred between 1976 - 2005 (modified from Reference [2])

2.2 Recent experience of main rotor blade damage

The author carried out a survey to obtain a view of main rotor blade damage occurring in service and their impact on today's helicopter operations. In total 115 participants worldwide consisting of test pilots (30%), flight test engineers (14%), military pilots (5%), commercial pilots (36%), private pilots (4%) and licensed engineers (11%) answered the survey. Figure 2.3 shows the distribution of the participants and their respective experience in terms of flight hours. Each target group provided valuable input based on their extensive flying experience, different operational tasks, maintenance expertise, and their ability to evaluate the helicopter's performance and behaviour in a practical way. The participants operational experience cover a large variety of helicopters, ranging from a maximum takeoff weight (MTOW) of 600 kg up to 18,000 kg. Some of the pilots had flown over 100 different types.

2.2.1 Frequency of occurrence

Estimating how often rotor blade damage occurs is very difficult, because it depends heavily on the helicopter type, its operational environment, mission, and its handling by the pilot or maintenance engineers. For example, certain helicopters are known to be prone to water ingress through the pitch control cuff requiring rebalancing before flight. One pilot stated that on some occasions the lateral oscillations caused by water ingress were so high that the mission had to be aborted. Problems associated with water ingress or moisture absorption are strongly related to the operating environment and often occur in tropical and humid regions. Foreign object debris (FOD) or other erosion damage is also dependent on the flying environment, such as regions of high levels of airborne particles (sand and salt) or flying in the low-level environment (below 500 above ground level).

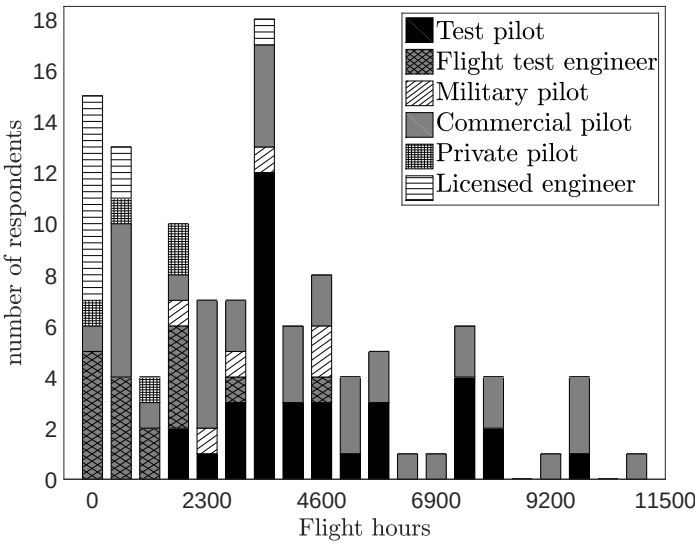

Figure 2.3: Respondents flying experience.

One pilot mentioned that when operating in the desert, erosion would happen on a daily basis but it was difficult to estimate how long it would take before the blade became unserviceable. Frequency of damage also depends on the type of mission flown. It was suggested by one respondent that damage occurs once in 500 operating hours for inland operations and once in 1000 operating hours for offshore operations and confirmed by another who stated that offshore operations are low risk missions, whereas Helicopter Emergency Medical Service are medium risk. High risk missions were found to be logging or agriculture (dusting/spraying) operations, or missions in a forest or jungle. It was also mentioned that in the cattle mustering industry in Australia typically a couple of FOD incidents occur within a month. Operating out of unprepared airfields is also more likely to cause blade damage than maritime operations. Apart from these factors, rotor blade damage also depends on the pilots and maintenance engineers skills and the degree of care taken when performing ground handling tasks or using blade folding equipment. The thoroughness of periodic inspections such as the commonly used tap test[1] is also

[1]Some other early blade internal inspection (BIM) methods have been implemented in some Sikorsky helicopters blades. This method involved pressurizing the rotor blade during the manufacturing process which was connected to an indicator at the blade root changing colour if pressure was lost due to internal damage [36]. Later this indication was linked to the cockpit display.

critical. Tap tests require practice and experience to be effective for identifying damage such as delamination and bond separation. Depending on the maintenance environment, damage can be easily overlooked. It was mentioned that it is very difficult to detect minor/superficial main rotor damage (especially on the upper surface) in a military environment because pilots and maintainers do not have access to work stands to inspect the full length of the blade.

Rotor blade damage is normally found during periodic inspections or during pre/post-flight checks. Results from the survey show that 71% of the respondents believe that damage occurs approximately once in every 500 operating hours, 14% think the damage rate is twice as probable and 15% believe it will be more common still. Some pilots reported that in their more than 8000 hours flying experience they have never experienced any blade damage.

2.2.2 Experience of main rotor blade damage

Before questioning the participants on common rotor blade damage scenarios they had experienced, they were asked to state whether they have ever flown a helicopter with a damaged rotor blade and whether they were aware of the damage in flight. Out of all respondents, 65% had flown a helicopter with a damaged blade. In total 105 damage situations were reported and these were classified into five categories: structural damage (39%), auxiliary components (10%), object strike (24%), environment (22%), and maintenance/ground handling (6%). A detailed breakdown of these damage types is presented in Figure 2.4. It should be noted that not all damage events were noticed by the pilot or crew. Altogether 33% of the participants were not aware of the damage during flight. This feedback confirms that minor defects do not change the blade rotational frequencies significantly due to the high centrifugal loading [4] and hence, is not noticeable by the pilot or crew. Interestingly all leading edge damage or droop shroud damage went unnoticed in flight. It can be seen that the most common damage events (14 out of 105) are caused by debonding or complete loss of the blade protection tape. FOD was reported 13 times, internal damage 12 times and water ingress 10 times, followed by bird strikes and erosion which both occurred 7 times. The survey results showed that 9 out of the 12 reported internal damage occurred on composite rotor blades and in only one case the pilot was aware of damage. It is interesting to note that external causes are considerably greater than damage associated with the blade design, which account for only 13% of all listed damage events.

2.2.3 Influence of damage on helicopter behaviour and pilot workload

This survey has found that the most common damage type is loss or damage to the blade protection tape. Three examples have been given where the blade protection tape was damaged or even separated due to heavy rain. Depending on the severity of the damage, it can cause issues such as increased or excessive vibrations which can be accompanied by noise ("distracting *whooshing* sound"). One pilot described that while flying through a storm cloud he/she was more concerned about the consequences of the severe weather.

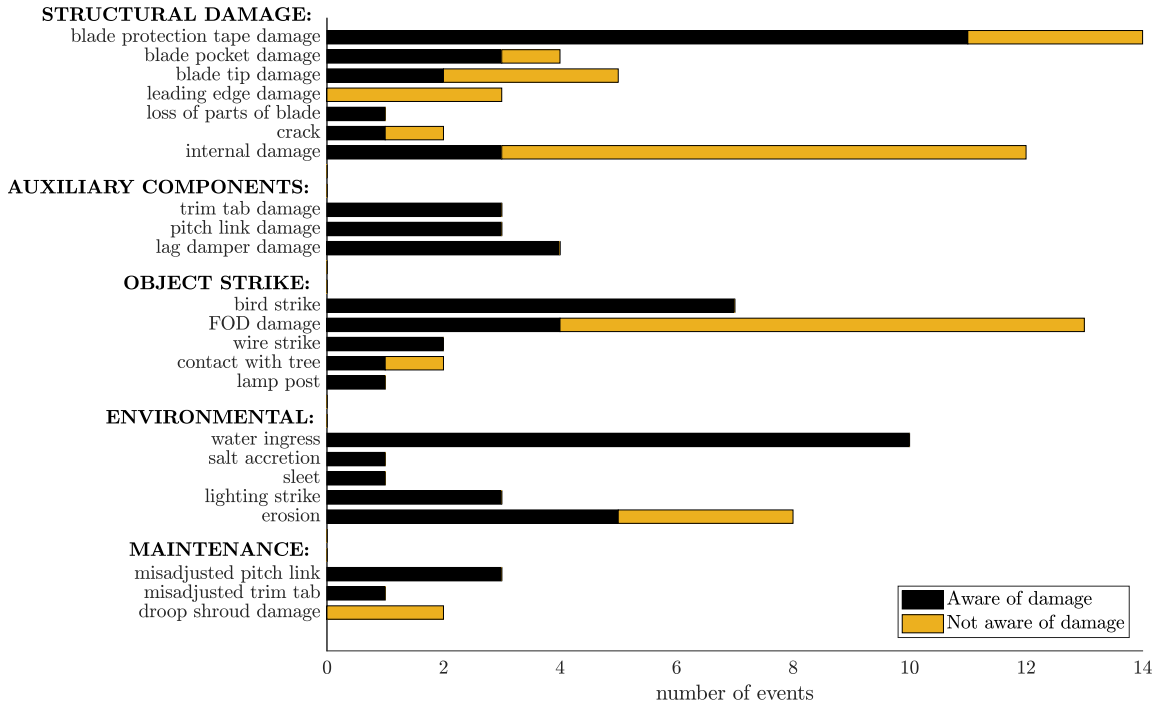

Figure 2.4: Awareness of damage during flight for all occurrences.

Only after leaving the storm the effect of the loss of the protection tape became noticeable. Two more cases of blade tape separation resulted in excessive vibrations. In one case the pilots were not able to read the instrument panel gauges and therefore made an immediate landing. Other scenarios where parts separated from the actual structure are related to blade pocket damage. Here pilots noticed that the blade pockets which delaminated or "flew off in flight" resulted in increased vibration and increase in the flapping noise level. A precautionary landing was carried out to prevent further damage. In another case, the blade upper pocket peeled back causing very strong 1R[2] vibrations which in turn resulted in a very high workload and an emergency landing.

The diverse range of helicopter missions and the vehicle's ability to land in very tight spaces also subject the blade tips to harsh environments. However, in most blade tip damage events, no change in behaviour was observed although some severe cases increased vibrations or increased pilot workload. One pilot reported that after a tip strike, increased vibrations were present yet there was no noticeable effect on the rotorcraft's performance, although "one does take things easy after". In another case, although most of the blade tips were ripped off, the "symptoms in the cockpit were minimal and the helicopter landed normally". All reported leading edge damage cases were only detected after a post-flight check. One pilot commented that "leading edge damage funnily enough had little affect [*sic*] on flight or flying characteristics (effect)". A pilot stated that the loss of 1/3 of the blade of a mid-sized helicopter resulted in ditching.

The effect of cracks is again dependent on size: a small chordwise crack on a composite blade does not change the behaviour at all, whereas some other cracks on composite blades have a good vibration signature leading to early detection. The most difficult structural damage to detect is internal damage. Only two internal damage cases involving blades

[2]Frequency that is an integer multiple of the rotational frequency, such as 1R, 2R, 3R, etc.

with metallic components resulted in increased and severe vibration, and in one case vertical vibration was reported due to damage on a composite blade. All other damage cases involving composite rotor blades were not noticeable in flight and is often only found during a maintenance check. In some cases only a slight discolouration of the surface of the composite rotor blade was noticed after impact during chaff and flare trials, and significant debonding was discovered only through tapping tests. Small internal damage on composite blades does not necessarily mean that the blade requires immediate repair. One pilot reported that damage due to delamination was "acceptable for one more flight to repair station". With the use of a continuous health and monitoring system that allows for condition based maintenance internal damage can be monitored over time ensuring enhanced maintenance.

Damage to auxiliary components that are part of the main rotor system (such as trim tabs, pitch links or lead lag dampers) often cause increased vibration and control activity that has a significant impact on workload. For example a broken trim tab led to an aborted take-off after a marked vertical bounce (3R) was noticed during transition to forward flight at approx 40 KIAS. A heavily worn bolt fitting the blade pitch link horn and the pitch rod caused high levels of 1R and 4R vibration in translational flight. This led to a high level of stress and discomfort for pilot and crew as it was not possible to read the instrument panel adequately. A lead-lag damper failure or damage also causes noticeable vibrations and/or movements in the controls. It was reported that the vibration levels were sufficient to cause the "pilot to abort a sortie with a noticeable vertical thump felt if the cyclic was moved in a circular fashion (e.g. hover spot turn through 360 deg)". One pilot commented that during flight it is difficult, especially without specific training, to definitively diagnose what level and type of damage has occurred. For example, one participant described that a "5R on the main blades can feel much like a 1T on the tail". However, the type of damage does not really matter as the resulting operating procedure is normally very similar.

Wire strike can cause serious impact damage to the rotor blade or pitch control rods and in some situations resulted in such severe vibrations that the instruments could not be read, or the pilot was forced to carry out an emergency landing. The effect of a bird strike is dependent on the size of the bird and where the blade is damaged. Some reported increased vibration and loud noises resulting in a precautionary landing or control activity. In some cases however, it leaves "no damage to the blade other than a blood stain". FOD damage can happen quite commonly but the participants reported that in most cases it had no effect on the behaviour of the rotorcraft at all. However, in some more severe cases "the workload was increased due the to additional care required in handling the aircraft" as the helicopter was controlled more gently to avoid getting close to the prescribed limits. One pilot describes that after a FOD incident the blade tip was damaged and caused very high 1R vibrations and undesired stick movements. The workload was very high when maintaining control. In another situation FOD impact created loss of power (torque) and dynamic instability with vibration.

The majority of events related to environmental damage were recognised by aircrew, except some erosion damage. Water ingress often resulted in lateral vibrations. One participant mentioned that when water ingress is "very bad, it is very rough" and it can lead to stress, discomfort, distraction and such severe vibrations that the instruments could not be read. Although salt accretion resulted in the same perception and workload, no effect on handling was reported by the pilot. After flying into sleet a pilot reported

that the subsequent landing was necessary due to uneven and erratic main rotor balance track. It increased power requirements and fuselage vibrations including the antenna. Erosion related damage was often reported to cause no effects. However, in one severe situation it was described that more torque was required to remain in the hover than was predicted by the flight manual charts.

Maintenance related issues which are reported include misadjusted pitch link, misadjusted trim tab, or droop shroud damage. One pilot reported that a flattened trim tab during flight resulted in a "rough ride". Misadjustment of pitch link or trim tab was reported to cause no significant increase in control and workload but decrease comfort or degrade the performance of sensitive on-board equipment. If care is not taken during maintenance significant stress related factors including distraction, fatigue and decrease in comfort can occur in flight.

The results of the survey have been arranged into different groups relating to pilot perception and workload (Figure 2.5). It can be seen that most of the damage is immediately felt by the pilot either through increased vibration or noise. The relationship of how damage affects pilot workload highlights that most internal damage and all erosion type damage resulted in no additional workload even though vibration was evident.

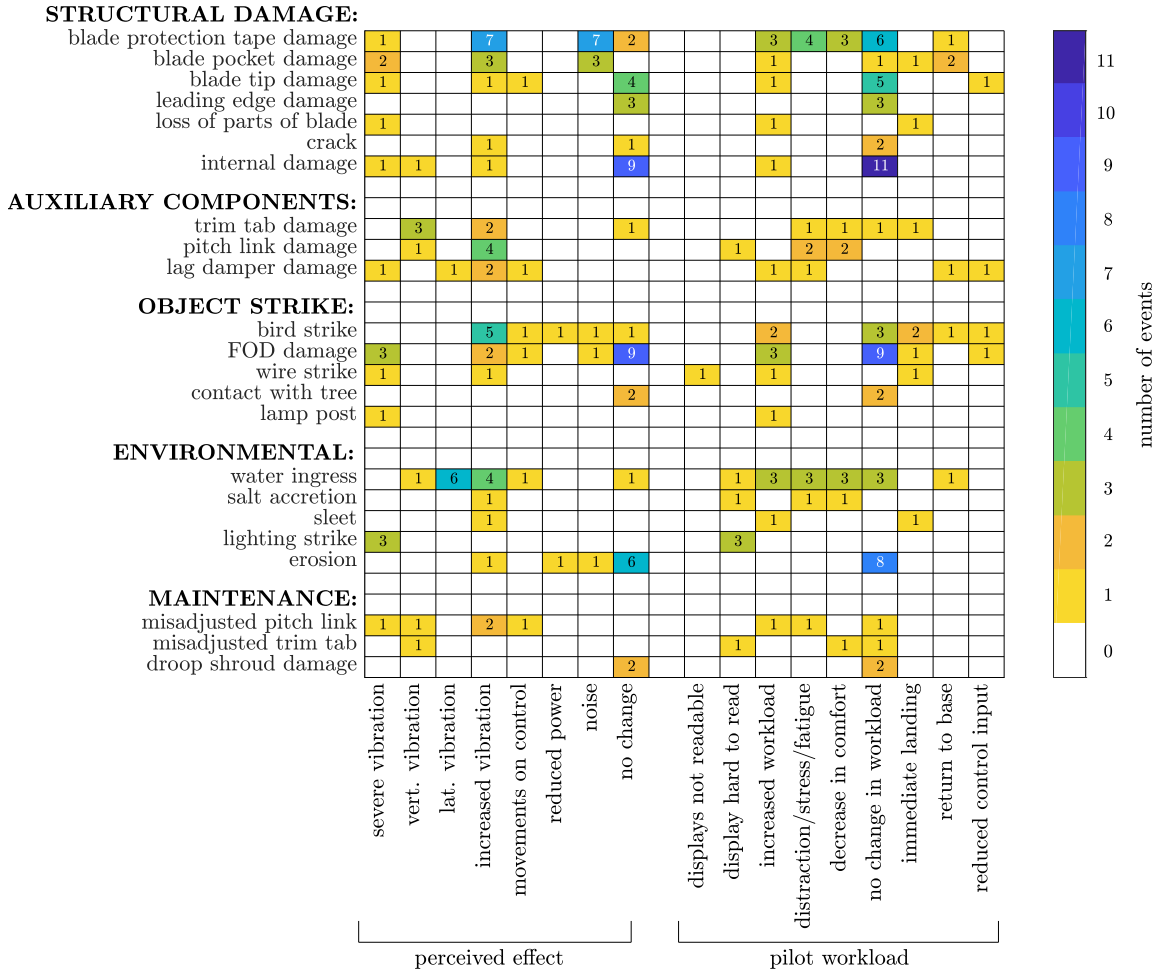

Figure 2.5: Damage linked to perceived effects and pilot workload.

2.3 Summary

This chapter summarises the results of a survey carried out to obtain a view of main rotor blade damage occurring in service and their impact on today's helicopter operations. Only minor incidents were reported by the survey participants highlighting the reliability of rotor blades for the harsh operating environment, even with damage. Although this study covers feedback from subjects with a very broad range of experience, the limited number of participants has meant that it only provides a glimpse into the operational challenges faced by pilots and engineers. The survey has presented feedback that confirms widely accepted beliefs, such as the fact that visually identifiable rotor blade damage is often directly sensed by the pilot through increased vibration or noise, while internal damage often goes unnoticed in flight and can be hard to detect, even during maintenance.

However, more importantly the survey has highlighted the dichotomy faced by today's rotorcraft engineers and systems architects. Does the designer follow today's technological trends and adopt a preventative approach where he/she invests in such instrumentation systems or is a reactive approach more appropriate where he/she awaits to have sufficient evidence of operational need? There is little operational evidence that points towards the need for complex sensors on rotor blades for health monitoring due to the conservative design practices and the consequent robustness of modern composite blades. Yet, technological advancements in sensor technology are now presenting an opportunity to monitor blade dynamics in operational environments and in doing so, potentially furthering understanding of blade dynamics with/without damage and improving design methods. The subsequent chapter provides historic and current research efforts towards blade health monitoring, while highlighting the great interest in operational in-flight data collection by the rotorcraft community.

This page is intentionally left blank.

CHAPTER 3

Literature review

Current rotor health monitoring capabilities rely on model-based approaches due to a lack of experimental evidence. This chapter discusses existing numerical modelling methods for structural dynamics and aerodynamics that focus on aeroelastic analysis. A brief review of rotor health monitoring aspects together with historic and state-of-the-art instrumentation systems provide the reader with an understanding of the benefits of deploying highly advanced fibre optic sensing technologies for in-flight operations over current measurement techniques. The chapter is concluded by addressing existing sensor placement methodologies for direct and indirect measurement systems that are combined with shape reconstruction algorithms.

3.1 Main rotor models

The main rotor remains the most challenging component of a helicopter due to its complex dynamic behaviour and its requirement to perform over a broad flight envelope. As it has considerable influence on helicopter performance and dynamic behaviour [37] much attention is given to accurately model the systems aeroelastic behaviour. The long and slender rotor blades are highly flexible structures and in operational conditions, aerodynamic forces will be influenced by the deforming rotor blade. Aeroelastic phenomena can be conveniently described using the so-called "Collar's triangle" (Figure 3.1) that shows the interaction between inertial forces, elastic forces and dynamic forces.

The structural model has to be coupled with an aerodynamic inflow model to predict the dynamic characteristics of rotating rotor blades. This has been a challenge for many decades. Peters [39] mentions that one *"aspect of rotary-wing aeroelasticity that makes aerodynamic modelling so difficult is the close coupling between structure and flow field"*. A critical aspect is that the inflow model must be in the time domain to allow its integration with unsteady aerodynamics. The aeroelastic modelling principle is described as a feedback loop to precisely manage the interactions between the blade aerodynamics and its structural mechanics. This aeroelastic problem is outlined in Figure 3.2. The rotor blades bend and twist under the influence of unsteady and non-linear aerodynamic loads,

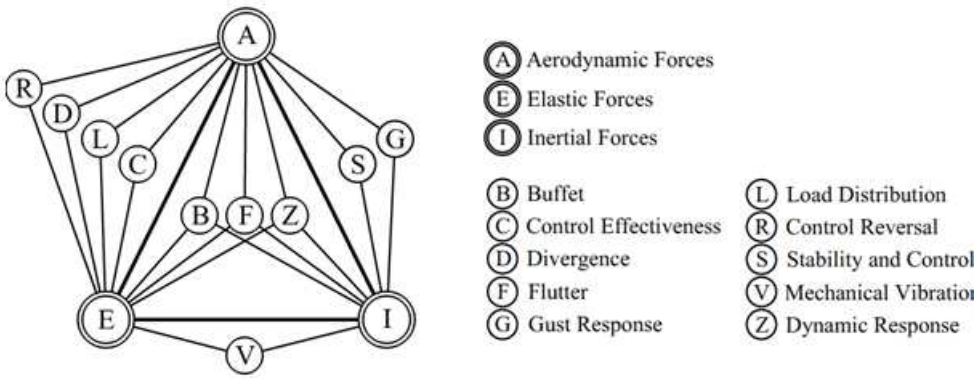

Figure 3.1: Collar's triangle (reproduced from Collar [38])

which are functions of the rotor blade dynamic states [40]. The flow-chart shows that any change of collective or cyclic blade pitch control from the pilot, blade motion, or flow field due to gust or flight condition alters the angle of attack of the blade. This results in changes in aerodynamic loads and consequently dynamic behaviour. Furthermore, the blade's structural dynamics influence the dynamics of other aircraft components, such as the fuselage, and vice versa. The choice of the aeroelastic modelling approach is dependent on the helicopter's rotor configuration, as well as the flight conditions that are the focus of analysis. The following subsections concentrate on existing structural and aerodynamic modelling approaches for main rotor blades.

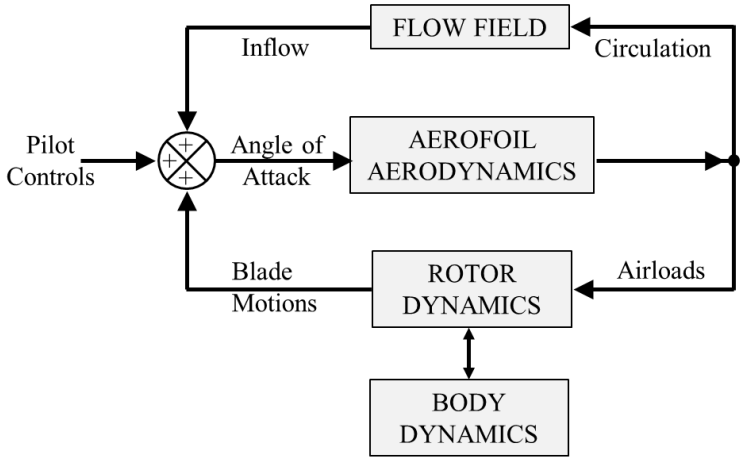

Figure 3.2: Aeroelastic interaction (reproduced from Peters et al [41])

3.1.1 Structural dynamics

Previously much effort was put on the development of mathematical models for rotor blade design. To account for structural mechanics of the blades, linear and non-linear beam theories were used [42–47]. The geometry of the blade is often modelled as a one-dimensional problem [45] as rotor blades are slender, beam-like structures. Modern studies extend small angle and small displacement approximations to model beams un-

dergoing moderate[1] and large deflections [48, 49]. This was achieved through variational formulation based on intrinsic equations, exact geometrical formulation, and multi-body formulation [47, 50]. Hodges's and Johnson's textbooks [45, 51] provide an excellent overview of the history of beam theory as well as the application of these methodologies.

The earliest work pioneering modern beam theory was carried out by Kirchhoff and Clebsch as described by Love [42], followed by the classical linear Euler-Bernoulli theory which governs the extension and bending of isotropic beams. Here, it is assumed that the cross-section remains undeformed in its plane and stays normal to the deformed axis of the beam [52]:

$$\frac{\partial^2}{\partial x^2}\left(EI\frac{\partial^2 w}{\partial x^2}\right) + \rho A\frac{\partial^2 w}{\partial t^2} = f(x,t) \tag{3.1.1}$$

where x is the coordinate in spanwise direction, w is the transverse displacement, ρ is the material density, EI is the bending stiffness, and $f(x,t)$ is the transverse loading. The Timoshenko beam theory is an extension of the Euler-Bernoulli theory that incorporates the transverse shear deformation and rotational inertia and allows the cross section of the beam to deform with respect to the neutral axis of the beam. The governing equations of motion are defined as [52]:

$$\rho A\frac{\partial^2 w}{\partial t^2} - f(x,t) = \frac{\partial}{\partial x}\left[\kappa AG\left(\frac{\partial w}{\partial x} - \psi\right)\right] \tag{3.1.2}$$

$$\rho I\frac{\partial^2 \psi}{\partial t^2} = \frac{\partial}{\partial x}\left(EI\frac{\partial \psi}{\partial x}\right) + \kappa AG\left(\frac{\partial w}{\partial x} - \psi\right) \tag{3.1.3}$$

where A is the cross-sectional area, κ is the shear correction coefficient, G is the shear modulus, and ψ is the total section rotation of the beam cross section. With the introduction of the Timoshenko beam theory, accuracy can be improved. In fact, a study [53] was carried out to compare the Timoshenko theory with the Euler-Bernoulli theory. Nowadays, significant interest is still shown into the use of Timoshenko model, especially for modelling initially curved and twisted composite beams [54]. Euler-Bernoulli and Timoshenko beam theory were also applied to rotating beams by extending the equations of motion to include the centrifugal term [55–57], and is used in industrial software (such as NASTRAN) for beam modelling applications [58].

In the past, rotor blades have been designed with their elastic axis, aerodynamic centre, and centre of mass coincident at the quarter chord. This is the reason why classical flutter and divergence of a rotor blade involving the coupling of flap bending and torsion have not caused any significant aeroelastic issues [59]. As explained by Curtiss and Peters [59], a favourable effect on overall stability can be achieved for hingeless and bearingless rotor blades if the blade sectional centre of gravity and elastic axis position are moved away from the quarter chord line. However, this had to be compromised with coupling effects that can lead to unwanted structural behaviour, such as flutter. As described

[1]Here, the term moderate refers to displacements up to 10-15% of the blade length [48].

by Bielawa [37] the main sources for coupling effects in rotor blades mainly stem from (1) general misalignment of the blade section principal axes, (2) non-coincidence of the various elastomechanical centres within the blade sections, or (3) non-linear effects of combined flapping and lag bending. Figure 3.3 shows the position of the structural axes and illustrates the forces and moments acting on the axes that are mainly responsible for coupling effects.

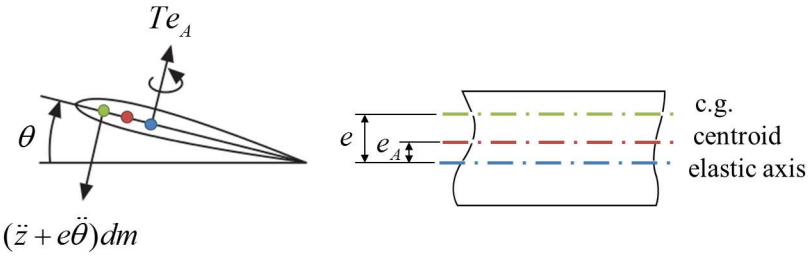

Figure 3.3: Blade section geometry (modified from Bramwell [60])

Based on the position of the structural axes the coupled flap-bending equation [60] can be written as:

$$\frac{\partial^2}{\partial x^2}\left(EI\frac{\partial^2 z}{\partial x^2} - Te_A\theta\right) - \frac{\partial}{\partial x}\left(T\frac{\partial z}{\partial x}\right) - \frac{\partial}{\partial x}(\Omega^2\, x\, m\, e\, \theta) + m\left(\frac{\partial^2 z}{\partial t^2} + e\frac{\partial^2 \theta}{\partial t^2}\right) = \frac{\partial F_z}{\partial x} \tag{3.1.4}$$

where T is the centrifugal tension of the blade, e_A is the tensile axis (area centroid) offset from elastic axis, θ is the pre-twist angle, m is mass per unit length, x is the radial distance, e is the mass centroid offset from elastic axis, and F_z is the force in z-direction (out-of plane). For the special case of zero built-in twist, this equation reduces to the equation for flapwise bending [60] given by Houbolt and Brooks [43] in 1957, where they derived linear differential equations of motion for combined bending and torsional deflection of twisted non-uniform rotor blades using the Newtonian and Lagrangian methods. Importantly, Houbolt and Brooks included the neutral, elastic, and mass axes into the formulation. From this work, it was concluded that centrifugal-force coupling should be included in the mathematical formulation of rotating rotor blades [43]. In 1974, Hodges and Dowell [44] derived the non-linear equations of motion for the elastic bending and torsion of twisted non-uniform rotor blades using the Hamiltonian and Newtonian approaches and it was explained that *"the two methods are complementary in that the Newtonian method provides clearer physical understanding of the force components and reactions, while the variational method is more precise mathematically"* [44]. The Lagrangian methods derive the equation of motion from energy considerations instead of equilibrium of forces:

$$\frac{d}{dt}\left(\frac{\partial L}{\partial \dot{q}_i}\right) - \frac{\partial L}{\partial q_i} = Q_i \tag{3.1.5}$$

where q is the generalised coordinate for $i = 1, ..., n$, and n is the number of generalised coordinates. The Lagrangian L is defined as:

$$L = T - V \tag{3.1.6}$$

where T is the kinetic energy and V is the potential energy of the system. If the Lagrangian L is the difference between kinetic and potential energies of a system, action $A = A(q)$ is defined from time t_1 to t_2 where the generalised coordinates $\mathbf{q} = (q_1, ..., q_n)^T$ are a functional of action [61]:

$$A(\mathbf{q}) = \int_{t_1}^{t_2} L(\mathbf{q}, \dot{\mathbf{q}}, t)dt \tag{3.1.7}$$

Hamilton realised in 1834 that the Lagrange's equation of motion is equivalent to a variational principle [62]. As explained by Malham [61] *"the correct path of motion of a mechanical system with holonomic constraints and conservative external forces, from time t_1 to t_2, is a stationary solution of the action. Indeed, the correct path of motion $\mathbf{q} = \mathbf{q}(t)$, with $\mathbf{q} = (q_1, ..., q_n)^T$, necessarily and sufficiently satisfies Lagrange's equations of motion for $j = 1, ..., n$"*. Hodges [50] made use of Hamilton's principle to derive intrinsic equations for the dynamics of initially curved and twisted beams in a moving frame. Hamilton's principle can be written as:

$$\int_{t_1}^{t_2} \int_0^l [\delta(T - U) + \delta\bar{W}]dx\, dt = \delta\bar{A} \tag{3.1.8}$$

where t_1 and t_2 are arbitrary fixed times, T and U are kinetic and strain energy densities per unit length l, $\delta\bar{A}$ is the virtual action at the ends of the beam and at the ends of the time interval, and $\delta\bar{W}$ is the virtual work of applied loads per unit length [50].

With the work of Hodges and his co-workers, a method was developed to create a workable, practical and yet, rigorous analysis. These models are based on the concept of decomposition of the rotating tensor (DRT) [63] and the variational-asymptotic method (VAM) based on Berdichevsky [64]. DRT is a kinematic description which was developed by Danielson and Hodges [63] that allows the three-dimensional strain field to be expressed in terms of the intrinsic one-dimensional measures for initially twisted and curved beams [45]. This concept of decomposition of the rotation tensor is a very powerful kinematic concept for systematically capturing all geometric non-linearities [65]. VAM is a powerful mathematical tool that can be used to find the one-dimensional energy that approximates the three-dimensional (3D) energy as closely as possible [45]. Herein the 3D problem is split into two complementary reduced-dimensional problems, which are [66]:

1. a two-dimensional (2D) cross-sectional analysis which outputs cross-sectional properties and recovers the three-dimensional stresses, and
2. a compact set of geometrically exact one-dimensional beam equations that treats geometric non-linearities exactly.

The 2D cross-sectional analysis provides necessary constitutive models for a variety of beam analyses, such as the classical beam models and the refined models, such as the Vlasov beam model or the Timoshenko model [65, 66].

For thin-walled beams with open sections, it is known that classical beam theory does not suffice [66]. The Saint-Venant-principle implies that typical torsion stresses only occur if warping[2] can take place freely. However, in engineering practice, this is rarely the case. Vlasov [68] takes into account the effects of torsional warping restraint which are particularly important for beams with thin-walled open cross sections [66]. Examples of these are typically used for modelling BMRs. As the resulting governing equation for torsion in the Vlasov theory is of fourth order, rather than second order as in the Saint-Venant treatment of torsion, an additional boundary condition is required at each end of the beam. Vlasov theory applies to thin-walled beams with open cross-sections, adding strain measures to account for the constraint of warping at the end of the beam, which produces a significant increase in local torsional stiffness [51].

In the studies of Yu et al [69] a meaningful Vlasov model was developed by first constructing a Timoshenko model from which the shear centre location is deduced. After this step, the origin was moved to the shear centre and a generalized Vlasov theory was developed using appropriate terms from the second-order approximation [69]. With this construction, this theory considers all possible 3D deformation but still creates a seamless connection to traditional beam theories so that the 1D beam analysis remains essentially the same [69]. As explained in Reference [69], the Vlasov correction is relatively unimportant for slender beams with closed cross-sections; in fact, Timoshenko theory should be used instead. Additionally, for rotating structures such as helicopter rotor blades, the trapeze effect has to be included [45]. This is a coupling in beams between tension and torsion that accounts for the increase in effective torsional rigidity due to axial force [66].

Based on the principle of DRT and VAM a finite element code was developed by Cesnik, Yu, Hodges and his co-workers [46, 54] that is called Variational Asymptotic Beam Sectional analysis (VABS). This development is a unified approach that achieves the accuracy comparable to that of three-dimensional finite element analysis and it proves to be far more computationally efficient [70]. VABS is a powerful tool, not only because of its fast computing time but through its process of dimensional reduction that takes the original 3D body and represents it as a 1D body and yet, considers all possible deformation in 3D representation [46]. The resulting equations govern both sectional and global deformation and also provide the 3D displacement and strain fields in terms of beam deformation quantities [46].

This computer-based programme also includes the classical beam model as well as the two refined models: the Timoshenko and Vlasov theory. Hodges [45] suggests that the Timoshenko theory should be used for analysing composite rotor blades for applications that require accurate prediction of second and higher bending modes as it includes transverse shear deformation at the kinematic level [46]. Apart from using VABS for detailed rotor blade design or design optimisation procedures [46], it can also be used to study matrix cracking, delamination or fibre breakage [71]. The geometrically exact beam equations obtained from VABS are now widely accepted[3] as the governing equations for beams used in three comprehensive rotorcraft codes [66]: DYMORE [72], the Comprehensive Analytical Model of Rotorcraft Aerodynamics and Dynamics (CAMRAD II) [73, 74], and Rotorcraft Comprehensive Analysis System (RCAS) [75]. The University of Mary-

[2]Warping is often referred to as a three-dimensional cross-sectional deformation [67].

[3]The reason behind this is that VABS has been shown to have accuracy comparable to that of standard 3D finite element codes, but at a far smaller computational cost.

land Advanced Rotorcraft Code (UMARC) also adopted a geometrically nonlinear beam formulation to analyse BMRs [76]. A summary of available computational tools can be found in Appendix B.

3.1.2 Aerodynamics

The complex aerodynamic flow field around a helicopter has been the subject of extensive research. Figure 3.4 illustrates the general complexity which stems from the interactions between the rotor blade tip vortices, the resulting wake and interaction with the following blades and airframe. As explained by Leishman [77] these vortices *"produce a complicated three-dimensional induced flow field that affects its aerodynamic loads, performance, vibration levels, aeroelasticity, and acoustics"*. In forward flight the rotor blades experience an asymmetric velocity field in which case the aeroloads become more unsteady and the patch of trailing wake vortices become significantly more complicated to predict. Furthermore, in high forward airspeed the advancing side of the rotor disc experiences transonic flow that leads to an increase of rotor drag and consequently to the requirement of more power to drive the rotor [77]. However, on the retreating side, the relative flow velocities are lower and the blades must operate at increasingly higher angles of attack to maintain rotor thrust which eventually leads to flow separation. This can lead to dynamic stall on the rotor blades which can cause structural damage to the rotor by overloading the pitch links due to the rapid change in lift and pitching moment [78]. It should be noted, that due to the scope of this research work this literature review focuses on suitable rotor inflow models for hovering applications.

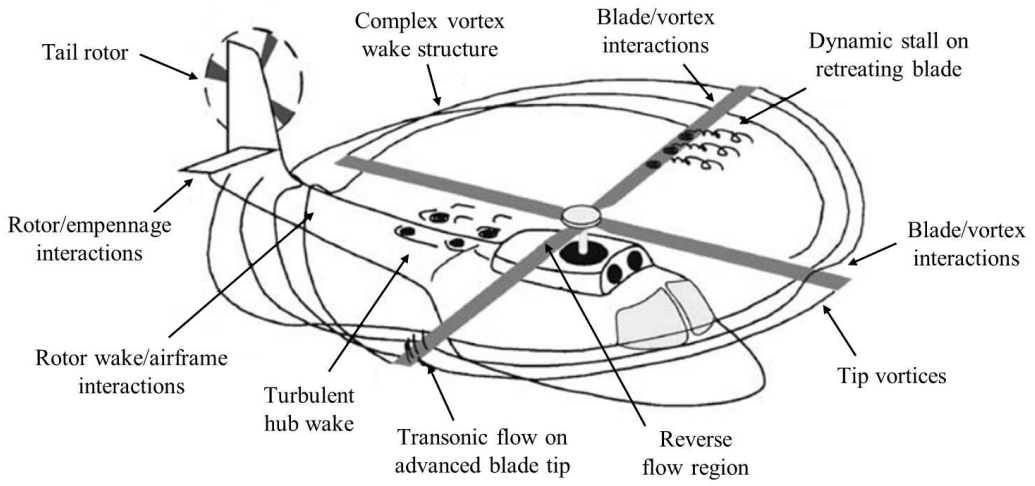

Figure 3.4: Forward flight helicopter dynamics (reproduced from Leishman [77])

Blade element momentum theory (BEMT) for hovering helicopters allows the estimation of the inflow distribution along the blade. It is a combination of the basic principles of the blade element theory and momentum theory. The blade element theory (BET) calculates the distribution of aerodynamic forces over the rotor blades and it assumes that each blade section acts as a two-dimensional aerofoil to produce aerodynamic forces and moments [79]. The momentum theory uses the conservation laws of mass, momentum and energy, and derives the relationship between rotor thrust, torque and the rotor inflow [40]. The experimental flow visualisation in Figure 3.5 shows that the rotor aerodynamics are

even complicated in hover, resulting in intertwining helicoidal trailing blade tip vortices and inboard turbulent vortical wake sheets [77]. This can be idealised by a surrounding control volume and the occurring vortices or wake effects can be simplified by accounting for correction factors, such as the tip-loss factor [79]. The fluid velocity is smooth as it goes through the rotor disc plane while a pressure jump is experienced over the rotor disc plane that can be determined by the application of Bernoulli's equation to above and below the rotor disc; the jump in pressure Δp over the disc is equal to the ratio T/A which is called disc loading. The induced velocity v_i at the plane of the rotor disc in hover is defined as:

$$v_i = \sqrt{\frac{T}{2\rho A}} \tag{3.1.9}$$

where T is the rotor thrust, ρ is the air density, while A represents the rotor disc area.

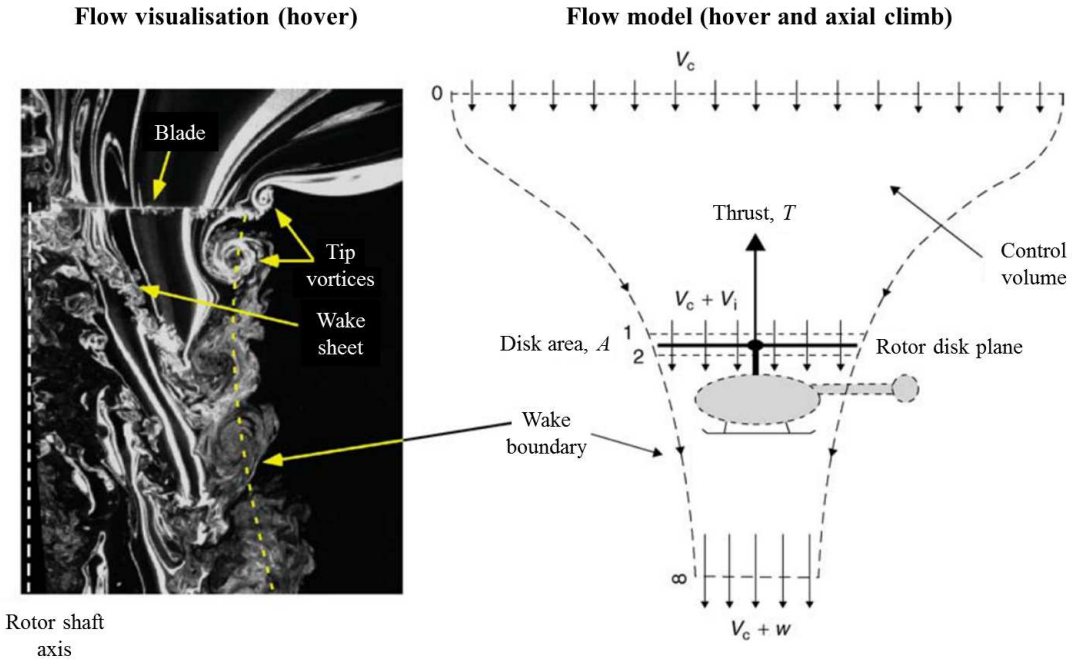

Figure 3.5: Flow visualisation of a rotor in hover and an idealised control volume surrounding its flow field (reproduced from Leishman [77])

With momentum theory as its basis, the thrust T on the annulus of the rotor disc can now be calculated. Assuming that rotor thrust is equal the weight of the helicopter in hover, $T = W$, the idealised rotor thrust coefficient C_T is given by [79]:

$$C_T = \frac{T}{\rho A(\Omega R)^2} \tag{3.1.10}$$

where A is the rotor disc area. Blade element momentum theory is applied to estimate the inflow distribution along the blade [79]. With the assumption that the climb velocity

$V_c = 0$ the incremental thrust dT is defined as:

$$dT = 4\pi\rho v_i^2 y \, dy \tag{3.1.11}$$

Substituting Eq. 3.1.11 into Eq. 3.1.10 and after rearrangement the incremental thrust coefficient dC_T can be written as [79]:

$$dC_T = 4F\lambda^2 r \, dr \tag{3.1.12}$$

for which F is Prandtl's tip-loss factor that approximates the loss of rotor thrust at the tip of the blade:

$$F = \left(\frac{2}{\pi}\right)\cos^{-1}(\exp(-f)) \tag{3.1.13}$$

where f is defined such that:

$$f = \frac{N_b}{2}\left(\frac{1-r}{r\phi}\right) \tag{3.1.14}$$

where N_b is the number of rotor blades and ϕ is the local induced inflow angle given by:

$$\phi = \tan^{-1}\left(\frac{v_i}{\Omega r}\right) \tag{3.1.15}$$

and the inflow ratio λ is given by:

$$\lambda = \frac{v_i}{\Omega R} \tag{3.1.16}$$

A relationship is formed between lift per unit length of span dy and the distribution of circulation Γ on the blade that is given by the Kutta-Joukowski theorem [79]:

$$dL = \rho(\Omega y)\Gamma dy = \frac{1}{2}\rho(\Omega y)^2 c C_l dy$$

Now the lift coefficient C_l can be written as a combination of momentum and vortex theory:

$$C_l = \frac{4R}{y}\left(\frac{C_T}{\sigma}\right) \tag{3.1.17}$$

Example 3.1.1 ***Comparison of rotor thrust gradient for the idealised case and Prandtl's tip loss factor included***

Figure 3.6 shows the spanwise variation of the rotor thrust gradient along the radial position of the rotor blade in an idealised case with and without Prandtl's tip loss factor.

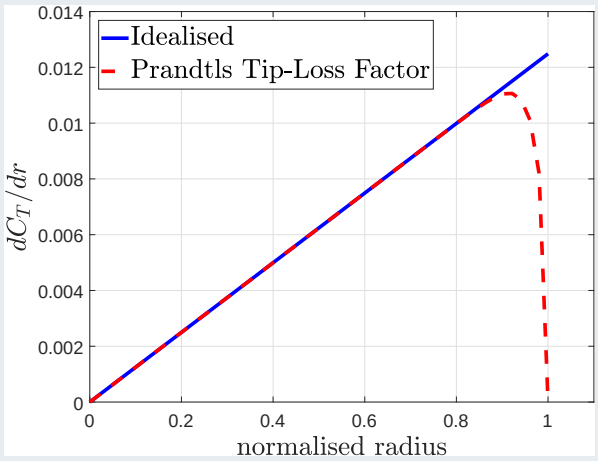

Figure 3.6: Spanwise variation of blade thrust coefficient

For this calculation it was assumed that the helicopter is in hover, the blades ($N_b = 4$) are straight, untwisted with a rectangular geometry. Further assumptions are steady and uniform incompressible inviscid flow conditions, the disc has negligible thickness in the axial direction. As expected the inclusion of the Prandtl's tip loss factor results in a significant reduction of the rotor thrust gradient at 90 % rotor radius due to the effect of blade tip vortices.

For a realistic prediction of the aerodynamic behaviour of a rotor system unsteady aerodynamic effects have to be taken into account [79]. The sources of unsteady effects stem from the variations in angle of attack caused by the time-varying flow velocities along the blade, blade flapping motion, blade pitch control inputs, and elastic blade responses that can have considerable influence upon the resulting forces and moments [79, 80]. As explained by Leishman [79] unsteady aerodynamic effects are relatively local and are a consequence of the time history of the vorticity contained in the shed wake immediately behind each blade. This often permits simplified forms of the mathematical analysis without substantial loss of accuracy in predicting the unsteady aeroloads on the rotor [79].

In 1988, Peters [39] listed important regimes for rotor aeroelasticity that is dependent on the desired area of interest of the aeroelastic phenomenon, summarised in Figure 3.7. It should be noted that the categories are not rigidly defined, yet they do represent the qualitative aspect of most helicopter aeroelasticity problems [39].

The reduced frequency k is plotted against the non-dimensionalised circular frequency $\bar{\omega} = \omega/\Omega$ (per/rev). Reduced frequency is used in the description of unsteady aerodynamics and unsteady aerofoil behaviour and is used to characterise the degree of unsteadiness

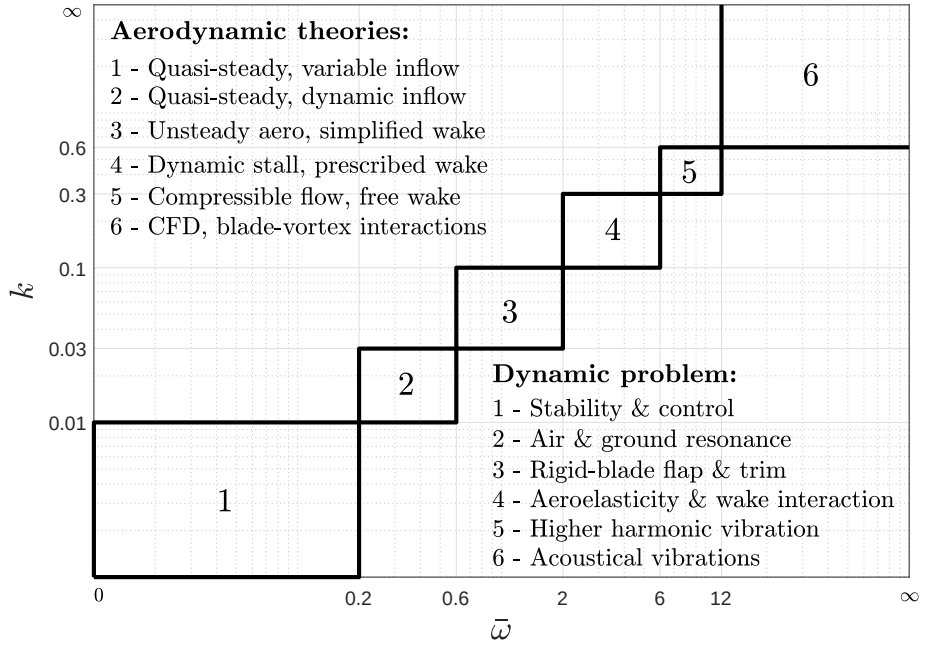

Figure 3.7: Aerodynamic regimes

of the problem [79]. It is defined in terms of circular frequency ω, tangential velocity V and aerofoil semi-chord $b = c/2$ so that [79]:

$$k = \frac{\omega b}{V} = \frac{\omega c}{2V} \tag{3.1.18}$$

For $k = 0$ the flow is steady, and for $0 \leq k \leq 0.03$ the flow can be considered quasi-steady[4]. For $k = 0.2$ or above highly unsteady terms will dominate the aeroload behaviour, such as those associated with acceleration effects [79]. It should be noted that k changes as a function of rotor radius because the local sectional velocity is changing [79]. The consideration of aerodynamic damping is very important for aeroelastic stability analyses. Figure 3.8 illustrates the variation of damping with incidence angle and reduced frequency [60]. The unstable region indicates that negative damping occurs [60].

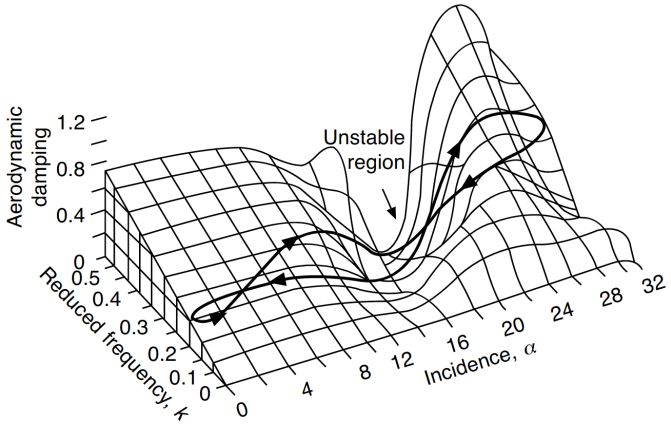

Figure 3.8: Blade torsional damping contours (reproduced from Bramwell [60])

[4]Leishman [79] states that for $0 \leq k \leq 0.05$ the flow can be considered quasi-steady.

Example 3.1.2 ***Reduced frequency as a function of rotor radius for the hover case***

A first-order approximation for the reduced frequency k can give some insight about the degree of unsteadiness found on a rotor and the importance of including unsteady aerodynamic effects in the analysis. It should be noted that this is an approximation and only illustrates the potential significance of unsteady effects. A study was performed using the H135 rotor blade (rotor radius $R = 5.1m$, chord length $c = 0.3m$) to estimate the unsteady effects induced by its blade frequency. The first flapping frequency is about 0.9Ω, then the reduced frequency k_{75} at the 75 % radius location ($r = 0.75$) is:

$$k_{75} = \frac{0.9\Omega c}{2 \times 0.75\Omega R} = 0.6\frac{c}{R} \tag{3.1.19}$$

Assuming ideal hover condition (no wind) the local velocity at the blade element is the rotational velocity $r\Omega R$. With a blade aspect ratio $R/c = 17$ the resulting reduced frequency $k_{75} = 0.035$, which is just inside the unsteady range. Figure 3.9 plots the spanwise variation of k, calculated for each of the first eight modes. At the tip the reduced frequency associated with aeroloads generated by the fourth mode is in excess of 0.4, and as explained by Leishman [79] "at these reduced frequencies, there is a significant amplitude and phasing introduced into the airloads by the effects of the unsteady aerodynamics, and the modeling of unsteady aerodynamics is critical if erroneous predictions of the airloads are to be avoided". The results also show that k increases further inboard to the decreasing local sectional velocity.

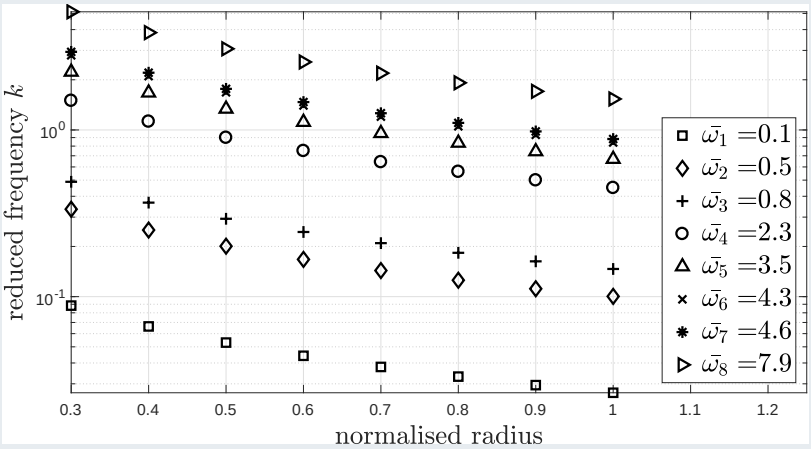

Figure 3.9: Spanwise variation of reduced frequency

Depending on the dynamic problem of interest, such as stability and control analysis, quasi-steady aerodynamic models are sufficient as the frequency range of interest is very low [39] (refer to Figure 3.7).

A detailed discussion of the various aerodynamic regimes, as well as appropriate modelling required in each area, can be found in [39]. Depending on the dynamic problem a variety

of wake and inflow models have been developed. The simplest are either variable or dynamic inflow [39]. The induced flow for the variable inflow model is obtained through elementary actuator-disc theory and is applicable for stability and control problems, while the induced flow for the dynamic inflow model must be described by an unsteady theory [39]. Until 1988 the most popular model of dynamic inflow was that of Pitt and Peters [81]: the only viable model for both hover and forward flight [82, 83].

As the complexity of the dynamic inflow models increase they need to be replaced by prescribed-wake or free-wake models [39, 84, 85]. Here, the induced-flow field stems from a coupled wake-lift model, and consequently cannot perturb the aerodynamic state variables, and thus is not suitable for aeroelasticity [39]. Furthermore, some of the most fundamental and well known classical quasi-steady aerodynamic theories of Theodorsen, Greenberg and Loewy are in the frequency domain which makes it inappropriate for rotorcraft nonlinear aeroelasticity [39, 41, 86]. The periodic coefficients and the large aerodynamic damping of rotor make the frequency domain impractical, whereas fixed-wing aeroelasticity can often be done in the frequency domain [39].

The first step towards time-domain models was done by Friedmann and Venkatesan [87] in 1985 that approximated the lift-deficiency functions by finite-states. However, due to the strong coupling between radial blade position in forward flight this was found to be unsuitable [39]. An alternative was provided by Peters and He [88] that used the higher-harmonic actuator-disc theory for finite-state models. The induced flow w is expressed in terms of harmonics and arbitrary radial functions, $\psi_s^m(v)$ [41, 89]:

$$w(r,\psi) = \sum_{n,m} \psi_s^m(v)\left[\alpha_n^m \cos(m\psi) + \beta_n^m(t)\sin(m\psi)\right] \tag{3.1.20}$$

where the unknown coefficients α_n^m and β_n^m of the shape functions become the state variables [39]. This is expressed similarly for the pressure distribution, that allows the formulation of rotor lift through the pressure difference between upper and lower surfaces [39, 90]. Over the years this theory was refined and expanded by Peters and his co-workers [41, 89–91], which was later used by Yu and Peters [92] to extend the theory to include dynamic ground effect. Even now the improved Peters and He model is commonly used by the research community [76, 93–97]. Goulos et al [96, 97] used Peters-He finite-state induced flow model [41, 89] in combination with the Leishman-Beddoes unsteady nonlinear blade element aerodynamics model [98], and the Zhao-Prasad dynamic wake distortion model [99] for real-time simulation. An excellent overview of aerodynamic modelling techniques can be found in References [40, 100–102].

3.1.3 Aeroelastics

Aeroelastic models often rely on the combination of methods discussed in the last two sections. Depending on the rotor configuration and flight envelope point of interest, the chosen structural model has to be coupled with an aerodynamic inflow model for analysis. In the 1970's Friedmann [103] analysed the aeroelastic stability of a hingeless rotor blade with the use of two-dimensional quasi-steady aerodynamic loads and nonlinearly

coupled flap-lag-pitch equations of motion [104]. Later in 1976, Hodges and Ormiston [105] performed a stability analysis using the equations of motion derived by Hodges and Dowell [44] in combination with a steady induced inflow that was calculated from classical blade element-momentum theory implementing Theodorsen's theory that was judged to be adequate for low frequency stability analyses of a hovering rotor [105]. With the development of the nonlinear intrinsic structural model formulation for the dynamics of initially curved and twisted beams [50], it has now become the most popular method for aeroelastic stability analyses [93, 106] and for structural load predictions [49, 76, 94, 95]. In 1999, this method was combined by Shang, Hodges and Peters [93] with VABS [46] and lifting models with the finite-state inflow formulation developed by Peters and He [88] which proved to be of high computational efficiency. Friedmann [48] used VABS in combination with a simple quasi-steady, incompressible aerodynamic model [107] for examining displacements and stresses under static loads, as well as aeroelastic stability of a composite rotor blade in hover and forward flight of a four-bladed composite rotor.

A multicomponent analysis was developed [76, 94, 95] using the structural model based on Hodges [50] in combination with kinematic constraints between the structural components and pitch link coupled with Peters and He's [90] finite-state three-dimensional induced flow model. Once the dynamic inflow analysis reached convergence, the aeroloads acting along each aerofoil were estimated to predict the sectional forces and moments [76]. To obtain a convergent solution, interpolation and transformation were done between structural and aerodynamic models [76]. These research efforts allowed the prediction of deformation and internal loading on various structural components.

With the work of Goulos et al [96, 97, 108, 109] a Lagrangian approach along with Euler-Bernoulli theory was used for aeroelastic analyses. This work intended to investigate natural vibration characteristics, trim performance, oscillatory loads and transient control response. Guruswamy [110] used Euler/Navier-Stokes flow equations and finite element structural equations to compute the dynamic aeroelastic characteristics of a rotor blade. The approach was based on a time-accurate analysis procedure that is suitable for nonlinear fluid-structure interaction problems. The results compare well both in magnitude and phase angles of displacement responses with experimental results from wind-tunnel tests, showing that the present time-accurate coupling procedure is valid.

Recently, Fleischmann et al [111] coupled an unsteady vortex lattice method with the numerical solution of the inhomogeneous Euler-Bernoulli partial differential equation to predict the aeroelastic behaviour of the H135 rotor blade. The algorithm used a free wake model to estimate the downwash and flow interaction of the preceding blade. Figure 3.10 presents an example of the predicted wake geometry that also illustrates the calculated lift for each blade. This simulation framework is particularly well suited for early design stages due to simple input and fast execution time [111].

3.2 Blade health monitoring

Health monitoring aims to inform the pilot and maintenance engineer about the abnormal change of a component. Traditionally, accelerometers are used for monitoring drive train components, engines, or gearbox, from which the health is extrapolated [112]. Since the introduction of HUMS, the engineering community has been interested in monitoring the

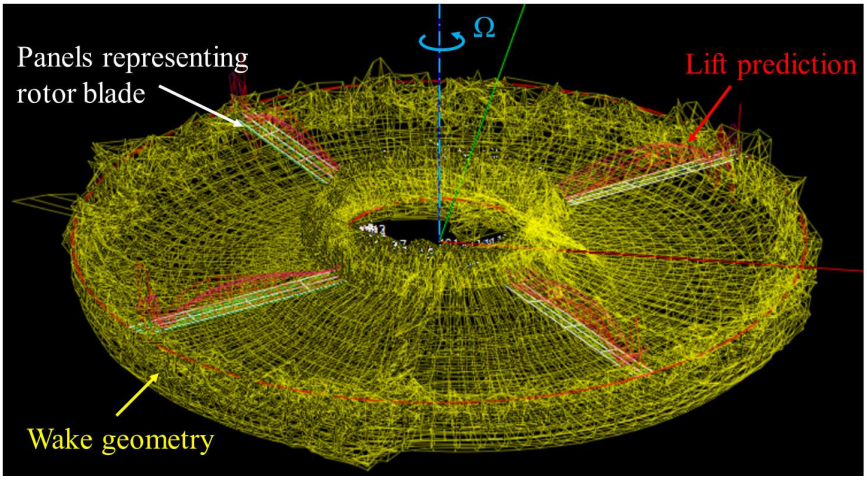

Figure 3.10: Wake geometry prediction on an H135 rotor blade (modified from Fleischmann et al [111])

health of the rotor blades in flight. However, so far only a small extent of measurements could be taken due to limited technological advancements in instrumentation systems. This has led to the utilisation of measured data from track and balancing systems. As explained by Pawar and Ganguli [4] most HUMS use rotor track and balance methods for damage prediction, that would log mistracking as fault since it cannot be corrected through balancing. Recent research [113] focused on investigating methods that allow rotor blade kinematics estimation in real-time. In most cases, however, theoretical model-based methods are deployed for damage isolation and prognostics [4], such as through neural networks trained using real vibration data. As a consequence model-based methods have been widely used to study the effects of damage in rotor blades. Nonetheless, due to the complicated nature of rotor flow real-time modelling is impracticable, and moreover, such off-line modelling is limited to simple flight manoeuvres, hover and steady speed forward flight [113]. For more information on rotor health monitoring systems, the reader is referred to the work of Pawar and Ganguli [4] that provides a detailed review of rotor health monitoring, modelling of typical rotor system faults and the use of damage detection algorithms. Guidance on HUMS and necessary capabilities is given by the CAA in References [114], while another CAA report [2] provides a review of mathematical models, along with pre-processing approaches and machine learning techniques for the evaluation of diagnostic strategies using in-service data.

3.2.1 Damage effect models

Main rotor blades are designed to withstand the heavy loading environment in flight and due to the large centrifugal forces, the blade dynamics are less sensitive to minor damage [4]. Nevertheless, the field of rotor blade damage and its effect on the dynamic behaviour of a helicopter has attracted much attention in the past 25 years. Ganguli et al [115] investigated the impact of moisture absorption, loss of trim mass, misadjusted pitch-link, damaged flap, and damaged pitch control. This work was expanded by Yang et al [116] who analysed how rotor blade faults impact fuselage vibrations. Ganguli and Chopra [117] predicted the change in rotor hub loads and blade tip response based on structural damage, blade mistracking, friction, and freeplay. The impact of ballistic

damage was studied by Tawk et al [118], and Kim [119] and Fries [120] investigated how such damage affects helicopter vibrations. Fries [121] calculated the vibration level in the cockpit as a result of the loss of outboard rotor blade sections. Leishman [79] analysed the impact on blade aerodynamics caused by bullet damage at the blade leading and trailing edges. Some work has been done to examine environmental influences, such as the impact of blade erosion coatings to aerodynamic efficiency [122] or consequences of icing conditions [123]. Recent work by Eren et al [124] or Chandra Naik et al [125] focused on modelling bird strike on a composite rotor blade. With the growing use of non-metallic composite materials for rotor blades, much effort has also been directed towards analysing the effects of internal damage, such as damage growth through matrix cracking, debonding/delamination and fibre breakage [71, 126, 127].

Safety factors are used in the design and development process to account for possible damage to the internal or outer structure of the rotor blade. However, other damage impacting system dynamics must be thoroughly evaluated. These include adjacent rotor blade components, such as damage to kinematic links, lead-lag damper, trim tab, or alteration of rotor blade inertia properties as a result of water absorption or loss of trim mass. Mathematical damage modelling work has a valuable contribution, yet human factors play a significant role in how a pilot reacts to certain damage scenarios. These factors are difficult to include in a mathematical model and consequently, it is difficult to relate theory and practice in virtue of lack of experimental and operational evidence.

3.2.2 Damage identification

The basis of most structural health monitoring (SHM) approaches is the identification of vibrational change due to damage [128]. Structural damage will result in changes in mass, stiffness, or damping that will be reflected in either a change of natural frequency, mode shapes, damping ratios, or a combination of these. Vibration-based damage identification methods can be categorised into four groups [5, 129, 130]:

- natural frequency-based methods,
- mode shape-based methods,
- curvature/strain mode shape-based methods,
- modal parameter-based methods.

However, as explained by Worden and Inman [128] damage is a local event while modal information is a reflection of the global system properties. Hence, no indication of damage location is given. Considering a simple example of a single mass-spring model (neglecting damping), the frequency can be related to its physical stiffness k and mass m by $\omega^2 = k/m$ [128]. With the use of a simple derivative, the change in frequency with respect to stiffness is [128]:

$$\frac{d\omega}{dk} = \frac{1}{2\sqrt{km}} = \frac{\omega}{2k} \tag{3.2.1}$$

and the change in frequency with respect to mass is:

$$\frac{d\omega}{dm} = -\frac{1}{2}\sqrt{\frac{k}{m^3}} = -\frac{\omega}{2m} \tag{3.2.2}$$

These derivatives represent the sensitivity of the natural frequency to changes in stiffness and mass, respectively [128]. For example, as shown by Worden and Inman [128] a 1% change in mass of a 10 Hz system will produce a 0.05 Hz change in frequency. It is hard to detect such a small change confidently with the use of transfer functions or other curve fitting methods, as well as due to other factors such as measurement errors, temperature and humidity [128]. For this reason, most damage identification methods based on frequency change are only applicable in a controlled laboratory environment [5].

In 1991, Pandey et al [130] argued that changes in curvature mode shapes (obtained from strain measurements) can be used for locating damage within a structure because the absolute change in a curvature mode shape is localised in the region of the damage. However, to obtain a reliable curvature for higher modes in practical applications, a large number of sensors are needed [129]. On the other hand, displacement mode shapes are not localised and give no indication about the damage location [130]. Pandey et al [130] also showed that the modal assurance criterion or the coordinate modal assurance criterion are not sensitive enough to detect damage. Messina et al [131] introduced a correlation coefficient that is called multiple damage location assurance criterion by combining two methods of estimating the size of defects in a structure. Much later in 2013, Peeters et al [132] showed that coordinate modal assurance criterion indeed could be used for locating damage on a helicopter blade if a correct choice of sensitive mode shapes were considered. Fan and Qiao [129] concluded from their review of vibration-based damage identification methods that optimisation algorithms and signal processing techniques have to be applied to localise damage using mode shapes. Furthermore, it was concluded that the damage detection methods based on curvature mode shape are very effective for damage localisation [129].

The strain energy index is another type of damage detection method, that uses the assumption that there is only a change in the energy quantity at the damaged location, whereas the overall energy remains the same. Detection methods based on strain energy methods have been applied extensively in the literature [133–137]. Peeters et al [136, 137] showed that modal strain energy is more sensitive than coordinate modal assurance criterion (see Figure 3.11), yet many approximations were made, such as for the derivation of the strain mode shape and simplification of the structure.

Cheraghi and Taheri [138] derived two damage indices based on empirical mode decomposition and fast Fourier integration for the identification of structural damage that was caused by a change in structural stiffness. The damage indices could be used to locate defects and the energy indices could be applied to distinguish the size of the defect. Fan and Qiao [129] carried out a comparative study in which five commonly used damage detection algorithms were compared which included a frequency-based method, mode shape-based method, curvature-based method and strain energy-based method. These were analysed in terms of single and multiple damage detection, large-area damage detection, noise immunity and sensor spacing tolerance. From this study, it was concluded that frequency change-based damage identification methods could localise and quantify damage in simple structures in a controlled laboratory environment, yet it was suggested that it is not reliable for damage detection for complex structures. Furthermore, it was found that curvature mode shapes are more effective in damage localisation than mode shape-based methods. Moreover, the curvature mode shape-based method and strain energy-based methods were able to detect multiple and large-area damage, while also being robust to high measurement noise and large sensor spacing condition. For more

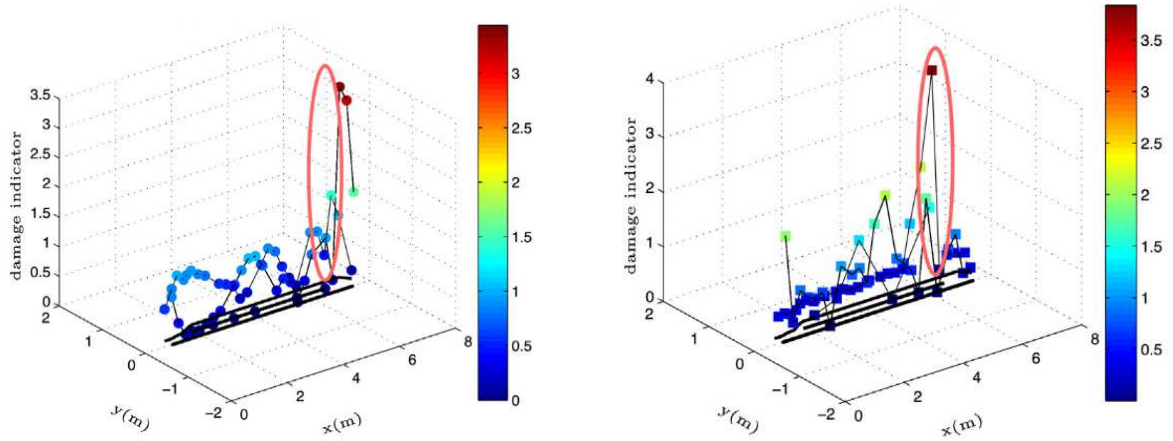

(a) Coordinate modal assurance criterion damage index

(b) Strain energy damage index

Figure 3.11: Experimental damage detection (reproduced from Peters et al [137])

detail, the reader is referred to Reference [129]. Kiddy et al [134] used eigenstructure assignment techniques to detect damage of a Hughes TH-55A helicopter main rotor blade, highlighting that the centrifugal force enhances the sensitivity of this method to mass changes. As already explained by Pawar et al [4] the blade dynamics are less sensitive to minor damage due to the large centrifugal forces, which can be confirmed through the work of Kiddy et al [134]. This work was experimentally validated by Kiddy and Pines [135] showing that damage can be only detected on systems with high energy. Ganguli et al [115] used helicopter track and balancing guidelines for defining quantitative measures of the rotor system response to damage. Changes in blade tip response, vibratory hub forces and moments were investigated due to a variety of rotor faults, such as moisture absorption, or misadjusted pitch-link [115]. These quantitative measures were defined in a range of moderate to significant levels that were used for analysis and diagnostic purposes. A structural damage detection algorithm was developed by Reddy and Ganguli [139] that used radial basis function neural networks by implementing the first ten flap, lag, torsional and axial modes for training purposes. Based on this analysis, it could be identified which modes give the most information for damage detection purposes. As an outcome of this study three modal rotating frequency sets were identified for the detection of structural damage of rotor blades [139].

3.2.3 Health and damage indicators

Traditional health indicators implemented into HUMS are based on acceleration data from which, for instance, the overall root mean square (RMS) energy of the signal is taken. This allows the categorisation of potential damage [1]. Examples of current HUMS rotor fault detection capabilities are given in a CAA report [2]. For the identification of a damaged blade relevant literature suggests the following technical approaches [4][140]:

- Comparison of the healthy and damaged blade to formulate damage indicator.
- High-frequency phenomena allow the indication of damage location more accurately.
- Monitoring the effect of damage on hub loads and fuselage.

Roy et al [127] proposed a damage indicator that is subject to frequency shifts referred to as "health residual". Because small damage results in a very small frequency change, it was argued that this damage indicator acts like a filter avoiding false alarms. Furthermore, Roy et al suggested that a limited number of higher modes were sufficient for damage detection, such as third lag, flap and torsion modes. Bernardini et al [140] proposed two blade damage criteria that were based on strain measurements taken at different positions on the blade. The first criterion observed a natural frequency shift that was obtained through Welch's power spectral density (PSD) that converted the collected time-signals to the frequency domain. The second criteria made use of the amplitudes of these PSD peaks. The idea behind monitoring a frequency shift is to avoid that blade natural frequencies coincide with the rotor harmonics. Another damage indicator for health monitoring purposes of wind turbines was introduced by Tcherniak [141] based on mode shape asymmetry caused through rotor anisotropy due to damage. Much higher sensitivity for damage was obtained than indicators related to a natural frequency shift. Although the algorithm was useful for identifying the damaged blade, no suggestion was given that would indicate the extent of damage and whether the blade has to be replaced.

3.3 Measurement techniques

Due to the increasing interest in operational in-flight monitoring, much effort was put towards developing instrumentation systems to allow the characterisation of blade dynamics in the rotating frame. While most instrumentation methodologies are applicable in a controlled laboratory environment, only a few have been proven suitable for flight. Existing techniques usually determine the structural behaviour via (1) surface strain measurements or (2) by directly measuring the shape. The following sections summarise the technological advancements towards instrumentation systems that are applicable for the aerospace sector.

3.3.1 Strain

3.3.1.1 Electrical strain gauges

In the late 1970s, electrical strain gauges and pressure sensors were deployed to measure in-flight rotor blade loading in hover and forward flight conditions of a Boeing CH-47A [142, 143]. Work conducted in the 1990s also used a combination of strain gauges and pressure sensors to predict the aerodynamic loading and rotor blade structural deformation for the hover case and for a variety of forward speeds on a Puma helicopter [144]. Work done by Wilkie et al [145] applied strain gauges on a whirl rig to correlate the rotating natural frequencies with a blade analytical model. However, methods using electrical strain gauges have numerous disadvantages. These range from operational limitations, such as high sensitivity to temperature and precipitation, to long installation times because the strain gauges have to be bonded to the surface for correct strain transfer. Moreover, the large amount of wiring interferes with the aerodynamic and dynamic behaviour of the blade performance. The measurements at discrete spanwise and chordwise locations result in a low spatial resolution, leading to the use of interpolated data for

the validation of aerodynamic analyses [146, 147]. Also, it is not uncommon that strain gauges fail during the testing and often exhibit poor signal-to-noise ratio when transferring data from the rotating to the fixed frame with an electric slip ring [148]. Robust and reliable measurement of rotating blade deformation is challenging [148] and the search for new non-intrusive measurement techniques have been the subject of numerous studies.

3.3.1.2 Fibre Bragg gratings

The potential of the use of optical fibres for monitoring aircraft structures has been well-documented [149]. They offer several key benefits, including their flexibility, low weight, electromagnetic immunity, small dimensions (diameter: ∼0.2 mm) and no requirement for electrical connection to the sensing elements. In addition, optical fibres can be embedded within fibre reinforced composites during fabrication [150], or, alternatively, can be surface-mounted to facilitate retrofitting [151–153]. Most fibre optic strain sensing techniques use FBGs, which are in-fibre strain sensors of typically $0.5 - 5$ mm gauge length [154]. FBGs represent a mature technology that is commercially available, where tens of sensors per fibre can be typically multiplexed in a single optical fibre at data rates on the order of 1 kHz and with strain resolutions of 1 $\mu m/m$. Figure 3.12 illustrates the principle of fibre optic sensors using FBGs.

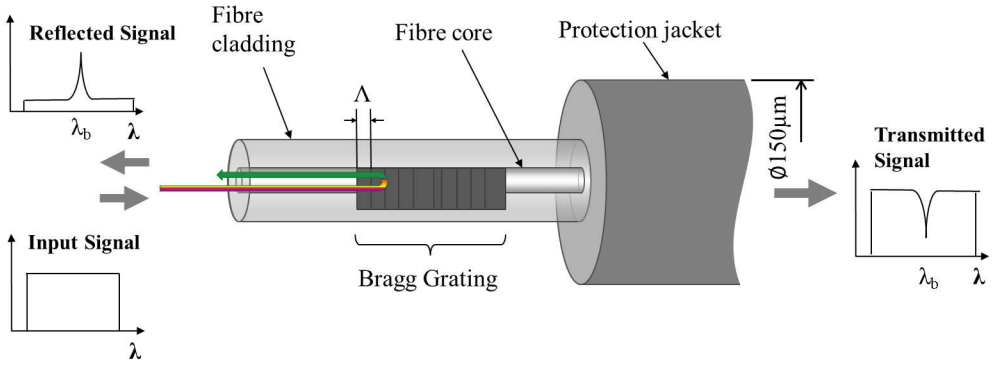

Figure 3.12: Principle of FBG

Fibre optic sensors use a thin glass cable that transmits light within its core, where the light is reflected from the cladding back into the core which assures minimum transmission loss. This is achieved with a higher refractive index η in the core compared to the cladding which leads to complete reflection. The outer coating protects the fibre from external conditions and physical damage. The main principle of an optical glass fibre sensor is the modulation of characteristics of a propagating light source [155]. The FBG only reflects one special light frequency whereas all other wavelengths of the light are transmitted unaffected [155]. The grating acts as a wavelength selective mirror, reflecting a single wavelength of light back along the optical fibre. Perturbation of the grating by strain or temperature results in a change in the reflected wavelength, the measurement that is the basis of the sensing approach.

The reflected wavelength and period of grating have the following relationship [156]:

$$\lambda_b = 2\eta\Lambda \tag{3.3.1}$$

where λ_b is the Bragg wavelength, η is the fibre core refractive index and Λ is the distance between the gratings, also called the grating period. The in-flight use of FBG sensors on fixed-wing aircraft has been investigated for some time [17, 151, 157]. More recently, their use on rotorcraft has been explored [158], with FBG strain sensors deployed on a scaled helicopter rotor operated in a wind tunnel to estimate its tip displacement by using a shape reconstruction algorithm. They have also been integrated into the root of a BMR blade [159], where the measured strain was used in the calculation of the useful remaining life of the blade. Suesse et al [9, 160] adopted these sensors to identify structural loading and elastic blade movements based on surface strain measurements. Fibre optic systems have a wide range of applications outside the aerospace sector, such as for wind turbines [161, 162].

Recently, Serafini et al [8] applied FBG strain gauges to a T-22 helicopter blade (Figure 3.13(a)) in operation, which was the first time that the reliability and performance of such a system was assessed in-flight. For the flight test, six FBG arrays (Figure 3.13(b)) were multiplexed in a single length of optical fibre and were connected to a battery-powered interrogator located at the top of the rotor mast. The rotor blade non-rotating dynamic characteristics in the flap, lead-lag and torsional directions were identified successfully up to 250 Hz. Furthermore, the collected data allowed the distinction between signals associated to the helicopter rigid body motion and to blade aeroelastic behaviour. Figure 3.13(c) shows an example of the collected flap signal during the flight, in which the frequencies at Ω and 2Ω, as well as the first elastic flap and its rigid flap motion are identified resulting from collective pitch actuation [8]. During the flight testing, the pilot did not report any problems with regards to the additionally mounted instrumentation system. This was the first step towards structural health monitoring capabilities.

3.3.2 Shape

3.3.2.1 Optical systems

Optical imaging metrology techniques are attractive as these are non-intrusive (non-contact) and provide full-field displacement measurements [148]. The use of optical imaging methods to determine blade dynamics has a rich history, with measurements on rotor blades dating back to as early as 1940, when a rotor hub-mounted camera was used to capture low-frequency dynamics on a rotating rotor [7]. Since then a variety of non-contact optical imaging metrology approaches have been shown to be effective in providing a clear visualisation of the structural dynamics of rotor blades in controlled environments such as wind tunnels.

In 1997 a blade deformation system was developed by Bosnyakov et al [163] to measure the displacement of a Ka-25 helicopter rotor blade in a wind tunnel environment with the use of two charge coupled device cameras. These were mounted on the rotor hub and retroreflectors were adopted as measurement points. Fleming and Althoff Gorton [164] utilised a projection Moiré interferometry method on a scaled helicopter in a subsonic wind tunnel to obtain full field rotor blade deformation data, sampled as a function of rotor azimuth. As part of the HART II (Higher Harmonic Control Aeroacoustic Rotor Test) programme, the stereo pattern recognition method [165] deployed stereo camera images to reconstruct the rotor blade deformation in a three-dimensional way using visible

(a) FBGs mounted on rotor blade (reproduced from Serafini et al [8])

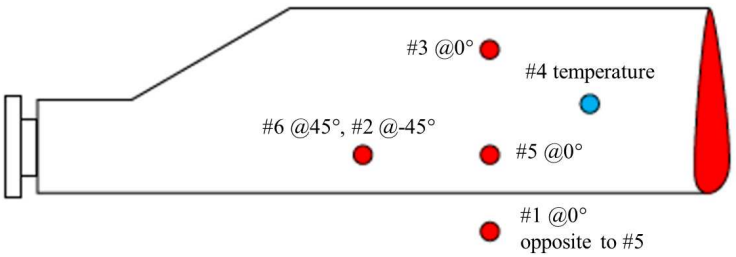

(b) Sensor location (modified from Serafini et al [8])

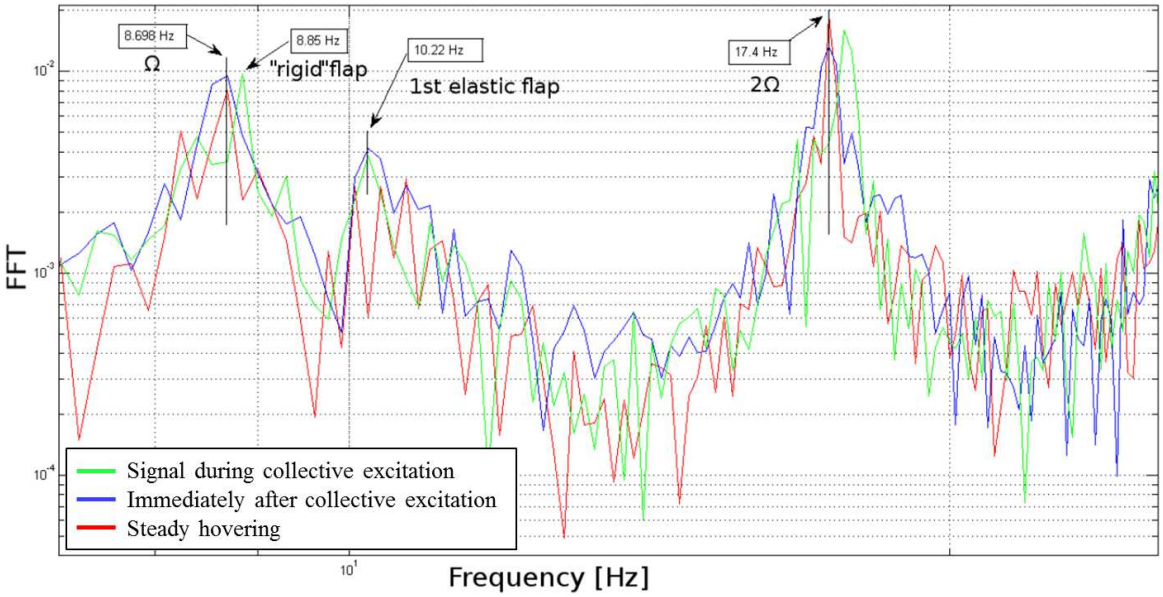

(c) Test results (modified from Serafini et al [8])

Figure 3.13: Suitability of FBGs during flight test on a T-22 helicopter

marker locations. Later, Kim et al [166] applied the stereo pattern recognition technique with twelve infrared cameras to measure blade behaviour of a scaled helicopter in hover and forward flight conditions in a low-speed wind tunnel.

Sirohi and Lawson [148, 167] demonstrated on scaled rotor blades that the digital image correlation technique can be adopted to measure rotor blade structural dynamics using speckle patterns that are painted onto the rotor surface. The aim of their work was to provide a full-field alternative for discrete strain measurements for wind tunnel or flight testing. Later, the digital image correlation method was applied for operational modal analysis of a rotating cantilever beam [168]. Barrows and Abrego et al [169, 170] utilised multi-camera photogrammetry to acquire blade displacement measurements of a full-scale UH-60A rotor in a wind tunnel (see Figure 3.14(a)) under a variety of simulated flight condition. Figure 3.14(b) shows the rotor blade that was instrumented with retro-reflective targets at discrete measurement locations in the chord and spanwise direction.

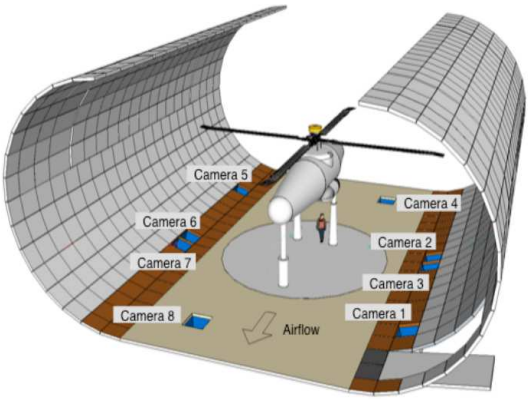

(a) Test section showing multi-camera port locations (reproduced from Abrego et al [169])

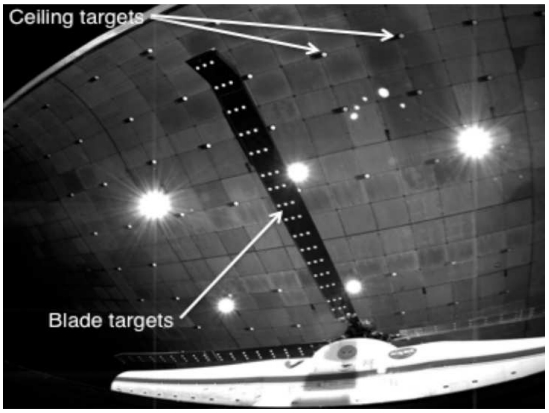

(b) Retro-reflective targets at blade and test section ceiling (reproduced from Abrego et al [169])

Figure 3.14: Multi-camera photogrammetry on a full-scale UH-60A rotor

Ozbek et al [171] made use of laser doppler vibrometer in combination with electrical strain gauges to identify structural modal properties of a full-scale wind turbine in rotation, and later photogrammetry was deployed on the same test item [172]. The proposed instrumentation set-ups showed great potential for the identification of structural dynamics in a controlled environment. However, their use is impractical for in-flight deformation measurements due to the required number of cameras and the large observation angles needed for the camera systems.

However, as part of the AIM (Advanced In-Flight Measurement Techniques) project, DLR (German Aerospace Centre) and Eurocopter (now Airbus Helicopters) have developed an optical measurement technique that was applied to measure the H135 rotor blade deformation during a ground run [173–175]. A special multi-camera video system, High-Speed Video Stroboscope, has been developed at DLR for visualisation, making use of the quantitative video technique in combination with image pattern correlation technique (IPCT). IPCT is a type of digital image correlation that is based on photogrammetry in combination with cross-correlation algorithms developed for particle image velocimetry [174]. The experimental test set-up (see Figure 3.15(a)) has been installed underneath the transmission deck outside the airframe pointing towards a speckle-pattern-instrumented blade. Test results were verified with strain gauge measurements, which were within the correct order of magnitude and, despite the large vibrations, good pictures were obtained with the High-Speed Video Stroboscope [174]. However, the error for shape prediction increases towards the blade tip, as shown in Reference [174, 175]. Wolf and Boden [176] validated IPCT measurements against accelerometers on a small wing test item during a ground vibration test, exploring a variety of instrument parameters, such as camera observation angles. IPCT has also been applied to aircraft propellers [173], and in both systems, measuring helicopter rotor blade deformation or aircraft propeller deformation, the instrumentation system was mounted statically and only took measurements of the passing blade. Due to this limitation efforts were made to develop a rotating camera that is able to co-rotate with the measurement object. This camera system that is also able to withstand the extreme vibrations and centrifugal forces of aircraft propellers was further developed [177] and adapted for helicopter applications [178].

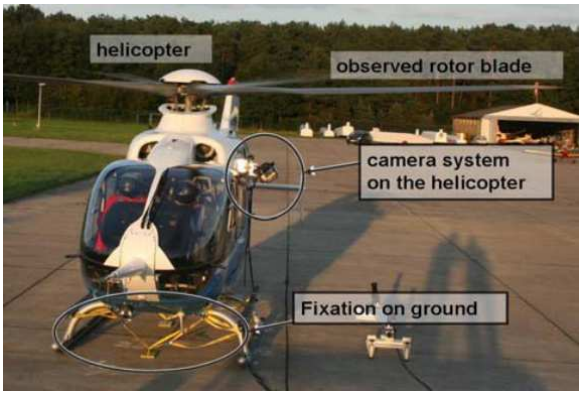

(a) Tied-down test using static camera (reproduced from Boden et al [174])

(b) Rotating camera system (reproduced from Boden et al [178])

Figure 3.15: Camera systems developed by DLR

The rotating camera system as shown in Figure 3.15(b) was mounted on top of the rotor shaft. As the system is co-rotating with the rotor blade the camera exposure time is much longer. It was found that no stroboscope was required, as the ambient light was sufficient for image recording. Yet reflection of the sunlight should be avoided as this could result in faulty measurements [178]. The developed non-intrusive optical measurement system showed great potential for flight test, especially as the washable speckle pattern or pattern sticker does not alter the production blade [178]. Despite this promising outlook, this system might not be suitable for continuous in-flight health monitoring, as the speckle pattern might not be weather robust and the surfaces of the camera or blade can wear and get dirty over time.

3.3.2.2 Indirect fibre optic shape sensing

A number of indirect fibre optic-based shape sensing approaches have been reported [16–18]. The majority of these techniques rely on the measurement of the differential strain experienced by several laterally offset optical fibres mounted on opposing surfaces of the structure under test (see Figure 3.16). The local curvature is determined, from which the shape of the structure can be obtained.

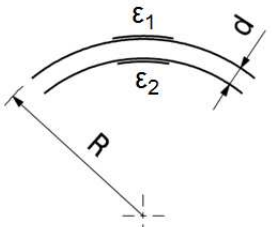

Figure 3.16: Shape sensing configuration (modified from Reference [179])

The curvature ($\kappa = 1/R$) of a beam can be determined by measurement of the strain profile of the upper and lower surfaces. The radius R of the curvature can be written as:

$$R = \frac{d}{\epsilon_1 - \epsilon_2} \tag{3.3.2}$$

where ϵ_1 and ϵ_2 are the strains measured by two FBGs located on either side of the neutral axis. Such indirect FBG-based shape measurements require a detailed model of the structure, and the determination of shape could fail through inappropriate strain transfer, inaccurate positioning of sensors, the presence of thermal gradients [180], or inaccuracies of the structural model, which would be exacerbated where the structure suffers damage [181]. A similar approach was adopted by NASA to measure wing-shape but required the use of arrays consisting of thousands of FBGs to achieve an acceptable measurement resolution [182]. The measurements were coupled with a shape reconstruction algorithm, the so-called "Ko-displacement theory" [157, 182–184]. This methodology was found to be highly accurate for weakly non-linear, non-uniform cantilever beams [184]. The vertical displacement $\hat{d}_i$ and deflection angle θ at each sensor location ($i = 1, 2, 3..., n$) [157] is calculated as follows:

$$\hat{d}_i = \frac{(\Delta l)^2}{6c_{i-1}} \left(\left(3 - \frac{c_i}{c_{i-1}} \right) \epsilon_{i-1} + \epsilon_i \right) + \hat{d}_{i-1} + \Delta l \tan \theta_{i-1} \tag{3.3.3}$$

where

$$\tan \theta_i = \frac{(\Delta l)}{2c_{i-1}} \left(\left(2 - \frac{c_i}{c_{i-1}} \right) \epsilon_{i-1} + \epsilon_i \right) + \tan \theta_{i-1} \tag{3.3.4}$$

where Δl is the distance between the ith strain stations, c is the distance between the wing's neutral axis and the location on the wing where strain reading ϵ_i is taken [157]. Variation of the distance c is considered through the following equation [11]:

$$c_i = \frac{\epsilon_{it}}{\epsilon_{it} - \epsilon_{ib}} h_i \tag{3.3.5}$$

where ϵ_{it} is the ith measured strain at the top surface, ϵ_{ib} is the ith measured strain at the bottom surface and h_i is the thickness of the profile and the distance between the top and bottom strain sensors. By installing FBG sensors on either side of the surfaces, the Ko-displacement theory circumvents the issue of knowing the exact position of the neutral axis. While a high number of strain measurements are required to achieve accurate results with the Ko-displacement theory [182], a few strain readings are sufficient to obtain the structural shape from the "modal approach" [10]. Although the modal approach relies on a detailed FE model for a successful outcome, it is one of the most commonly adopted strain-displacement algorithms [11, 12, 14, 15, 158, 161, 162, 185–188]. Its computational efficiency suggests applicability for real-time monitoring purposes [12, 158]. However, in operations, structural properties can change due to damage or variability of mass, which might affect the recorded strain data and lead to inaccuracy of estimations when compared with the undamaged mode shape [12].

With the use of a finite number of displacement and strain mode shapes, the displacement of a linear system can be approximated. This is achieved by the summation of their mode

shapes weighed by their corresponding generalised coordinates $\mathbf{q} \in \mathbb{R}^{m\times 1}$, where m is the number of modes considered:

$$\mathbf{d} = \mathbf{\Phi q} \tag{3.3.6}$$

$$\epsilon = \mathbf{\Psi q} \tag{3.3.7}$$

where $\mathbf{d} \in \mathbb{R}^{N\times 1}$ is the displacement vector, $\epsilon \in \mathbb{R}^{M\times 1}$ is the measured strain vector, $\mathbf{\Phi} \in \mathbb{R}^{N\times m}$ is the displacement mode shape matrix and, $\mathbf{\Psi} \in \mathbb{R}^{M\times m}$ is the strain mode shape matrix. M is the number of measurements taken, while N represents the number of nodal locations. The generalised coordinates can be approximated via least squares algorithm as proposed by Foss and Haugse [10]:

$$\mathbf{q} = \left[\mathbf{\Psi}^T\mathbf{\Psi}\right]^{-1}\mathbf{\Psi}^T\epsilon \tag{3.3.8}$$

and substituted in Eq. 3.3.6 to estimate displacements $\hat{\mathbf{d}} \in \mathbb{R}^{N\times 1}$ from strain:

$$\hat{\mathbf{d}} = \mathbf{T}\epsilon \tag{3.3.9}$$

where the displacement-strain transformation (DST) matrix $\mathbf{T} \in \mathbb{R}^{N\times M}$ is given by:

$$\mathbf{T} = \mathbf{\Phi}\left(\mathbf{\Psi}^T\mathbf{\Psi}\right)^{-1}\mathbf{\Psi}^T \tag{3.3.10}$$

where $\mathbf{T}$ is the displacement-strain-transformation (DST) matrix. The accuracy of the results are dependent on the number of modes; the higher the number of modes, the higher the accuracy. Example 3.3.1 demonstrates that even with a small number of strain measurements the displacement of the structure can be predicted. The rank of $\left(\mathbf{\Psi}^T\mathbf{\Psi}\right)^{-1}\mathbf{\Psi}^T$ cannot exceed the number of strain sensors, which means that only as many mode shapes as the number of sensors can be identified [15].

Example 3.3.1 ***Effect of number of sensors on the estimation of displacement shape using modal approach***

The modal approach is demonstrated using a cantilever aluminium beam with a constant rectangular cross section. Geometrical and material properties are listed in Table 3.1. The strain values are obtained from a finite element (FE) model, that are used as sensor strain reading. Figure 3.17 shows the first three mode shapes ϕ in out-of-plane direction and the second spatial derivatives of the mode shapes also called the strain mode shape ψ.

Table 3.1: Properties of cantilever aluminium beam

Properties	Values
Length	5.2 m
Width	0.3 m
Thickness	0.035 m
Young's Modulus	69 $\times 10^9$ N/m^2
Density	2700 kg/m^3
Poisson's ratio	0.334

The aim of this example is to show the impact of the number of sensors and their location on the prediction of displacement. Four different cases are explored, in which two (2x), three, and four strain sensors are distributed along the length of the beam (see Figure 3.18). The estimated displacement $\hat{d}$ is calculated for the four cases. In all cases, the number of modes n is equal to the number of sensors M ($M = n$). Case I and II demonstrate the importance of the sensor location, while case III and IV prove that the use of an increasing number of modes will also increase the accuracy. Figure 3.19 shows the results of the calculated displacement d due to gravity loading based on simple beam theory, and the estimated displacement $\hat{d}$ using an increasing number of sensors. The bottom diagram depicts the normalised error (Eq. 3.4.2) between the calculated and estimated displacement.

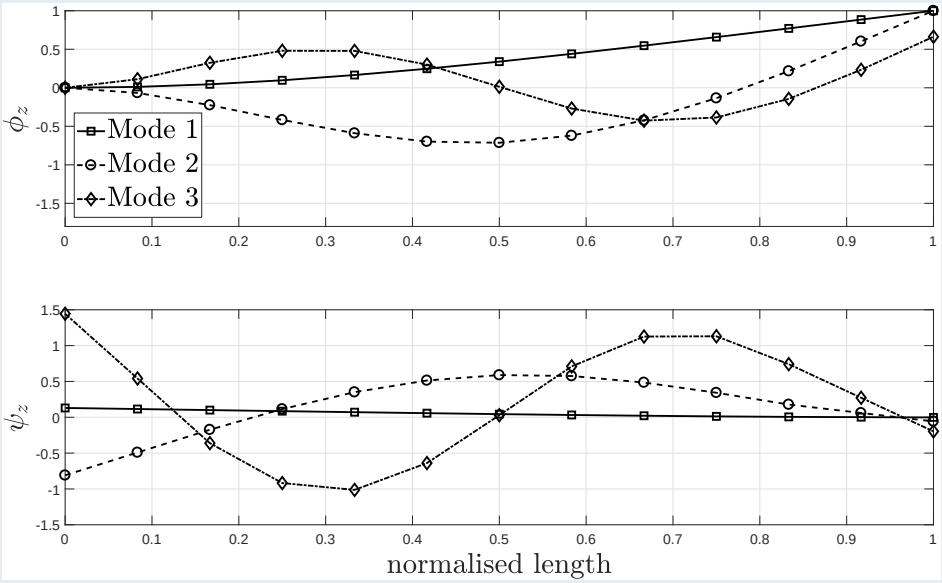

Figure 3.17: Displacement and strain mode shapes of aluminium beam

As expected, case I yield higher accuracy than case II as the highest strain reading is measured at the clamped end. Furthermore, results show that increasing the number of sensors and modes used for the algorithm improves the accuracy of the estimation significantly. The estimation displacement for case I have an average error of about 0.54%, that increases to 6.61% if the sensors are shifted towards the tip (case II). For the use of 3 sensors (case III) the average estimation error is reduced to 0.51% and

decreases even more to 0.10% for the use of 4 sensors (case IV). This example demonstrates that the location of the sensor, as well as the number of modes is important for the reduction of estimation error.

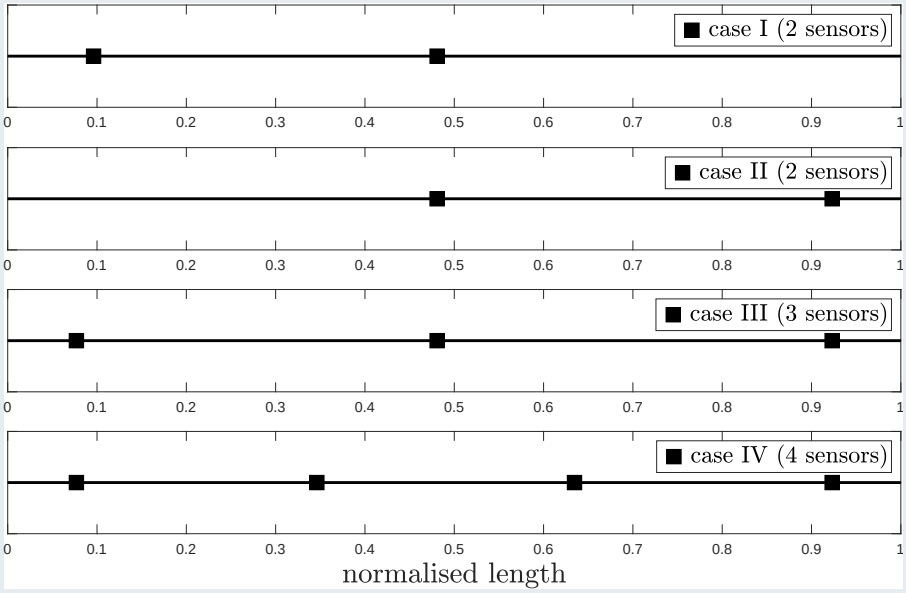

Figure 3.18: Chosen sensor position

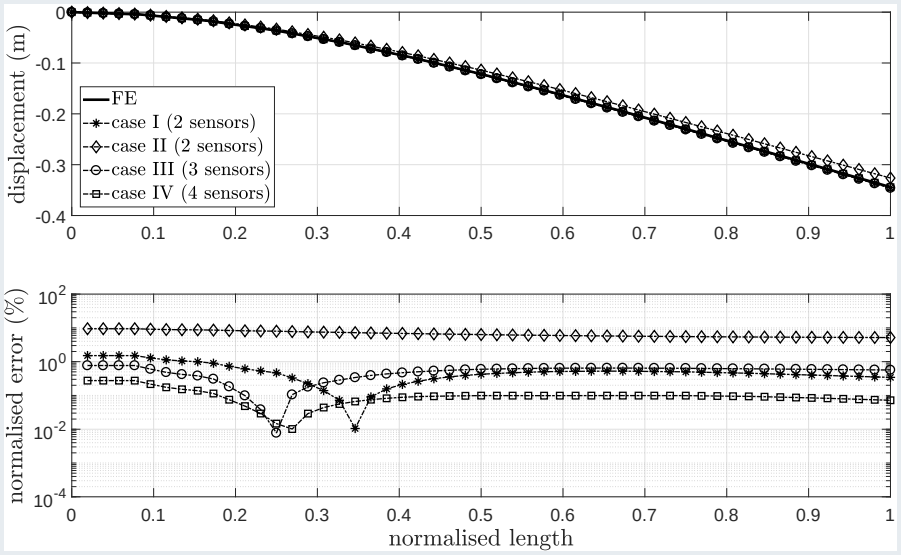

Figure 3.19: Effect of number of sensors on the estimation of displacement shape

Derkevorkian et al [11] carried out a comparative performance study between the Ko-displacement theory and the modal approach. Three lines of fibre optic cables were mounted on a flat swept plate, while 100 strain measurements were recorded from each optical fibre. Derkevorkian et al [11] argue that a dense FBG-based strain sensor distribution gives advantages in terms of detection, quantification and localisation of small damages at an early stage. Furthermore, it increases the reliability of the measure-

ments, especially if the FBG sensors are mounted on the surface and malfunctions occur due to harsh operational environment [11]. From the study, it was found that the Ko-displacement theory resulted in shape estimation errors of below 2%, while 3.7% was achieved by applying the modal approach. Different types of loading conditions, in particular, that of torsional loading, showed a normalised error of around 30% using the modal approach. It was suggested that this error could be reduced with off-axis strain data which is referred to as chordwise strain sensor distribution. The same issue was also highlighted in the work of Jutte et al [157] where results for wing twist was found to be sensitive to errors in bending.

Example 3.3.2 ***Accuracy comparison of modal approach and Ko- displacement theory***

In this study, strain measurements are converted to displacement by applying the Ko-displacement theory and the modal approach. The accuracy of both is compared to the displacement that is calculated from an FE model. Here, the same cantilever beam as in Example 3.3.1 is used. For both cases, the same number of strain measurements are assumed, while for the modal approach the first six out-of-plane modes are included. The top diagram in Figure 3.20 shows the comparison between the Ko-displacement theory and modal approach.

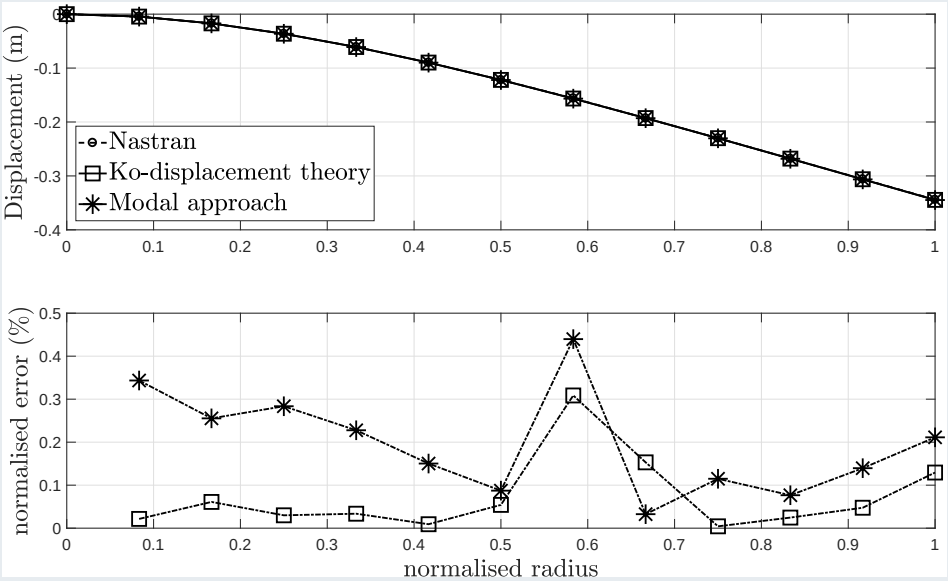

Figure 3.20: Comparison of modal approach with Ko-displacement theory

Both methods yield a close match with the FE calculation. However, when comparing their respective normalised errors (Eq. 3.4.2) a smaller average error is achieved through the Ko-displacement theory. An increased error is obtained from the modal approach, that could have resulted from the inclusion of only six modes. The outcome of this study confirms a similar trend of accuracy as discussed by Derkevorkian et al [11].

Recently, Bernardini et al [140, 189] showed that the modal approach is only valid for small-deflection type beams, and instead proposed an algorithm able to reconstruct the shape of a nonlinear, moderate lag, flap and torsional deflections, that are typical for helicopter structural dynamics. The equations are based on the non-linear approach for the elastic bending and torsion of twisted nonuniform rotor blades originally developed by Hodges [44]. Although the sensor positions were not optimised, a small number of deployed strain sensors resulted in a reconstruction error of only a few percents. The strain-displacement relationship can be written as follows:

$$\epsilon_{\xi\xi} = u' + \frac{1}{2}(v'^2 + w'^2) - \lambda\phi'' + (\eta^2 + \zeta^2)\left(\vartheta'\varphi' + \frac{\varphi'^2}{2}\right) \tag{3.3.11}$$

$$- v''[\eta\cos(\vartheta + \varphi) - \zeta\sin(\vartheta + \varphi)] \tag{3.3.12}$$

$$- w''[\eta\sin(\vartheta + \varphi) - \zeta\cos(\vartheta + \varphi)] \tag{3.3.13}$$

$$\epsilon_{\xi\eta} = -\frac{1}{2}\left(\zeta + \frac{\partial\lambda}{\partial\eta}\right)\varphi' \tag{3.3.14}$$

$$\epsilon_{\xi\zeta} = \frac{1}{2}\left(\eta - \frac{\partial\lambda}{\partial\zeta}\right)\varphi' \tag{3.3.15}$$

where η and ζ are the coordinates along the cross-section principal axes, ξ is the coordinate along the elastic axis, u, v, w are the axial, lagging and flapping displacements of the elastic axis. The angles ϑ and ϕ are the built-in twist angle and the blade cross-sectional elastic rotation (torsion).

3.3.2.3 Direct fibre optic shape sensing

Unlike NASA's fibre optic shape sensing system [17], the novel DFOSS [19] approach can determine shape directly within the sensing fibre, removing the dependence on strain transfer from the structure and thus the requirement for an analytical model of the structure. This approach is deployed and tested within this research work and was developed as part of the BladeSense project [190]. The DFOSS system is based on fibre segment interferometry, an approach pioneered at Cranfield University [191, 192], that was described in detail by Kissinger et al in Reference [19]. The approach relies on differential measurements of strain that are determined within each of the optical fibre's broadband low-reflectivity FBGs that act as in-fibre reflectors. These define the boundaries of fibre segments that form long gauge-length interferometric strain sensors. Simple surface mounting, for example using adhesive tape, is sufficient for it to follow the shape of the structure and significantly simplifying sensor installation. While for this research project the DFOSS prototype uses three single-core fibres that are hold by a custom designed 3D printed support structure (more details are given in Section 6.3.1), ultimately, the DFOSS system has the potential to be implemented completely within a single multi-core optical fibre (diameter: ∼0.2 mm), illustrated in Figure 3.21(a).

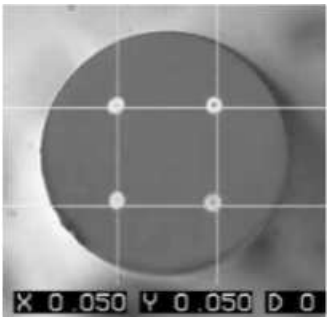

(a) Multi-core optical fibre (reproduced from Reference [179])

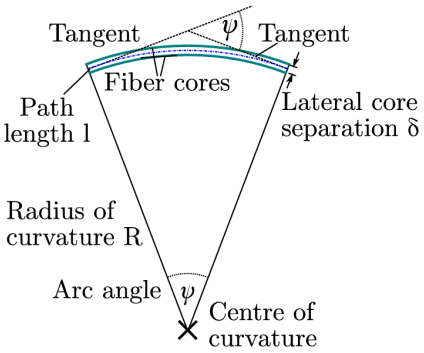

(b) The change in core length can be related to the arc angle ψ (reproduced from Reference [19])

Figure 3.21: Principle of shape sensing system

Appropriate processing of the differential strains experienced by the corresponding fibre segments allows the direct independent measurement of the slope angle in the out-of-plane and in-plane directions [19]. The relationship between differential strain ϵ_{diff} and the two fibre cores over path length l is given by [19]:

$$\epsilon_{diff} = \frac{\psi\delta}{l} \tag{3.3.16}$$

where ψ is the arc angle, δ is the distance between the cores (see Figure 3.21(b)). The slope angles are determined relative to the angle of the measurement origin of the system [19]. The only assumption required to obtain the desired shape deformation data from the measured slope angle data is the use of an interpolation (using a cubic spline) between the sample points to permit spatial integration of the slope angle. Note that this interpolation method does not require knowledge of the underlying structure.

3.3.2.4 Accelerometers

While accelerometers are widely used for ground vibration test environments or to measure the fuselage vibration level during track and balancing tasks, their use for in-flight blade measurement is impractical. This stems from the aerodynamic impact of their housing and electrical wiring, and the superposition of the desired vibration measurements with the signals corresponding to the centrifugal acceleration of the blade and overall helicopter movement. However, accelerometers are simple to deploy and are useful for determining the structural characteristics in a static environment. For example, Mironov et al [193] deployed several triaxial transducers measuring electric signals that are proportional to accelerations at the measurement point and also a set of dynamic deformation transducers acting as strain gauges. Due to aerodynamic interference, the triaxial transducers are only applicable in controlled laboratory environments.

3.4 Optimal sensor placement

Optimal sensor placement (OSP) methodologies are considered as one of the most important pretest steps in experimental and operational modal analysis (OMA) [194–196] because of its significance for accurate target frequency estimation and structural mode shape identification [195]. While careful sensor positioning is particularly important for discrete measurement techniques, such as accelerometers or strain gauges, this task is redundant for optical imaging metrology methods or NASA's fibre optic shape sensing system [16, 17, 182, 183] that requires a high density of FBGs. Although accuracy can be improved by increasing the number of sensors [13], it is desirable to instrument the structure with a minimum amount of sensors due to high costs of the acquisition systems, large data sets and often due to accessibility limitations on structures [195]. This is especially important when using electrical strain gauges on lightweight structures due to the very strict weight requirements [11], while with the use of FBGs a dense distribution has insignificant weight penalties. The determined sensor positions are dependent on the applied OSP algorithm, sensor type, and chosen criteria, as demonstrated by Papadopoulos et al [195]. For this study 21 sensor placement methodologies were compared and it was found that no approach produced exactly the same set of sensor locations. In this subsection, some of the most commonly applied sensor placement techniques are summarised.

3.4.1 Modal approach

Several methodologies were suggested to define optimal strain sensor positions in combination with the modal approach (refer to Subsection 3.3.2.2). These are based on qualitative measures[5], while the aim is to reduce the measurement error between analytical and experimental results in a controlled way. One of the most effective approaches is to determine the strain sensor positions so that it corresponds to the lowest condition number N of the DST matrix $\mathbf{T}$ [11–15, 185] (see Eq. 3.3.9):

$$CN = \|\mathbf{T}\| \cdot \left\|\mathbf{T}^{-1}\right\| \tag{3.4.1}$$

where $\|\cdot\|$ denotes the Euclidean matrix norm [14]. The condition number is a measure of stability or sensitivity of a matrix to numerical operations [185]. In general CN is greater than or equal to 1 (i.e. $CN \geq 1$). Matrices with condition numbers near 1 are well-conditioned and most of the information is preserved [11], whereas condition numbers which go to infinity yield an ill-conditioned matrix and will give large measurement errors [14]. A high number of sensors increases the accuracy of the prediction and avoids spatial aliasing of the modes [13]. To assess the effects of the number of sensors on the modal approach, the normalised estimation error $\mathbf{e}$ is calculated based on the real displacement $\mathbf{d}$ and the predicted displacement $\hat{\mathbf{d}}$:

$$\mathbf{e} = \frac{|\mathbf{d} - \hat{\mathbf{d}}|}{|\mathbf{d}|} \tag{3.4.2}$$

[5] In the literature it is often referred to quality criterion [195] or sensitivity analysis [12, 161].

Kim et al [161] introduced a modal assurance criterion (MAC) to calculate the shape estimation error for quantifying the similarity of two mode shapes. This provides a measure of statistical correlation between model predictions and experimental observations [197]. If the scalar quantity for MAC is close to 1.0 then the experimental and theoretical mode shapes are from the same mode. Lu [188] proposed an OSP method that combined the modal approach with an improved genetic algorithm to predict optimal sensor positions on a flexible plate. The optimal sensor layout resulted in a reconstruction accuracy of 96%, compared to that of 83% using evenly distributed sensors. Li et al [198] extended this work by proposing a modal superposition principle taking into account strain measurements in an arbitrary direction to increase the accuracy of the shape reconstruction of complex structures.

Kang et al [15] utilised the modal approach to study dynamic structural displacements of aluminium and acryl beams. Sensor locations were optimised such that the DST matrix has a minimum condition number. Four years later this work was extended by Kim and Kang et al [161] who demonstrated the applicability of the modal approach to rotating structures. Again, optimal sensor placement was determined by minimising the condition number of the DST matrix. The outcome was evaluated using the MAC criterion, resulting in values of MAC>0.98 and hence, small shape estimation errors. Finally, Kim and Kang et al [162] succeeded to integrate FBG sensors in the structure of a wind turbine blade to estimate tip displacement with the modal approach. Here, the sensors were arranged in a U-shape along the leading and trailing edge of the blade. For the formulation of the DST, displacement and strain mode shapes were obtained from a detailed FE model and OMA. It was found that the best results were achieved with the DST calculated from the FE model.

3.4.2 Effective independence method

One of the most popular iterative techniques is the effective independence method (EFI) method developed by Kammer [199]. The aim herein is to place sensors such that their locations maintain the linear independence of the modal partitions. The sensor placement algorithm uses the determinant of the Fisher information matrix (FIM) $\mathbf{F}$ as its metric [200]:

$$\mathbf{F} = \mathbf{\Phi}^T \mathbf{W} \mathbf{\Phi} \tag{3.4.3}$$

where $\mathbf{\Phi}$ is the mode shape matrix and $\mathbf{W}$ is a weighting matrix [200]. Maximisation of $\mathbf{F}$ results in minimising the corresponding covariance matrix which results in the optimal estimate. Therefore, Kammer [200] suggests maximising the determinant of $\mathbf{F}$ to find optimal sensor locations. The FIM is symmetric and positive semi-definite and cases with linearly independent mode shape vectors (system eigenvectors) result in a full rank FIM [194]. An FE model must exist to apply the EFI. This is an iterative process and it deletes degrees-of-freedom (DOF) that do not contribute to the matrix $\mathbf{E}$ (the orthogonal projection matrix) defined as:

$$\mathbf{E} = \mathbf{\Phi}\mathbf{F}^{-1}\mathbf{\Phi}^T \tag{3.4.4}$$

The ith diagonal element of matrix $\mathbf{E}$ denoted by E_{ii} represents the fractional contribution of the ith DOF to the rank of $\mathbf{E}$ [194]. The DOF with the lowest value of E_{ii} is deleted as a candidate sensor location, and the corresponding row is deleted from the modal matrix [194]. The determinant of the FIM is given by:

$$\det(\mathbf{F}) = \det(\mathbf{F}_0)(1 - E_{ii}) \tag{3.4.5}$$

where $\mathbf{F}_0$ is the original FIM and $\mathbf{F}$ is the FIM after the removal of the ith sensor. This determinant increases in magnitude every time one row is deleted from the mode shape matrix $\mathbf{\Phi}$. During the early development of the EFI method the following limitations were identified [201]:

- The sensor location is dependent on the mesh size of the FE model.
- The geometry of the structure is not taken into account and hence, yields sensor locations that contribute redundant information.
- There is no indication of the number of sensors which can be removed at each iteration.
- There is no indication of the final number of sensors that should be retained.

Nevertheless, this method has become one of the most popular sensor placement approaches for structural dynamics [194, 200, 202–205] and was embedded into the commercial software MSC/NASTRAN [206]. To address some of the aforementioned limitations, Poston [201] extended the EFI to a time-dependent effective independence distribution optimisation algorithm considering natural frequencies, modal damping, types of sensor measurements and sampling rates. Kammer [199] has shown that with the use of an eigensystem realisation algorithm the modal identification process can be improved. By maximising the determinant of the FIM, the EFI method maximises the observability of the system [199]. Recent studies by Rama Mohan Rao et al [204] showed that combining the EFI with principal component analysis a sensor placement technique can be obtained in the frequency domain.

Friswell and Castro-Triguero [194] investigated the EFI method and the linear independence of the modes which was found to be better quantified by the minimal condition number (also known as SVD ratio [203]) of the mode shape matrix, rather than the maximum determinant of the FIM. An exhaustive search was deployed to find the minimum condition number and consequently better sensor locations than with the EFI method were determined. Their work was commented on by Li and Fritzen [203] who showed that *"the condition number criterion is approximately equivalent to that of the FIM criterion"*. Li and Fritzen also explain why the two criterion yielded different results in the work of Friswell and Castro-Triguero: the condition number was implemented in the global optimal sense (e.g. to exhaustively search all possible sensor combinations), whereas the EFI was implemented in a suboptimal sense (e.g. to seek the minimum perturbation of the condition number in each of its iteration) [194]. Li and Fritzen suggested using a subspace approximation to develop an efficient way to search for the global optimal row combination instead of the *"prohibitive exhaustive search"* [203]. The mentioned OSP methods can be applied for identifying the spatial distribution of accelerometers, that

was further extended to determine strain sensor locations [181]. Loutas and Bourikas [181] used the FIM to optimise strain sensor locations by combining mode shapes in two in-plane directions. Furthermore, the effect of damage on the initially optimal configuration was investigated showing that the OSP task is dependent on the damage size, location and frequency of interest [181]. For example damage in areas of high modal strain has a small impact on the initial position.

3.4.3 Observability Gramian

Reynier and Abou-Kandil [207] proposed an OPS method from control theory based on Observability Gramian W_o, where the optimal sensor locations have to ensure observability requirements. The state-space system matrix $\mathbf{A}$ and output matrix $\mathbf{C}$ define an observable system if the matrix of the Observability Gramian W_o is non-singular:

$$W_o = \int_0^\infty e^{\mathbf{A}^T t} \mathbf{C}^T \mathbf{C} e^{\mathbf{A}t} dt \tag{3.4.6}$$

The idea is to maximise a measure associated to the Observability Gramian [207], such as the maximisation of the eigenvalue of the Observability Gramian [207], or by maximising the trace of W_o as proposed in Reference [208]. In the latter case, it was shown that the observability of the dynamic system increased and improved the output signal of the sensor. As this methodology is general it can be also used for optimising strain sensor locations. This is especially useful if a large number of sensor combinations would be possible [209]. Geeraert et al [209] linked electrical strain gauge outputs with modal responses via an observation equation. The benefit of this approach over the classical modal approach is that sensor locations are identified that have the largest dynamic contribution of a structure, whereas the modal approach is only dependent on the mode shapes. To overcome this issue, Samad et al [210] extended the work of maximising the trace of the Observability Gramian to observe certain modes or eigenvalues instead of all eigenvalues of the system. This is done by either using (1) the trace analysis multiplied by the associated eigenvalues, or (2) by the orthogonal projections of the mode shapes onto the observable subspace [210].

3.4.4 Structurally independent algorithms

While most sensor placement algorithms are dependent on detailed structural models, some structurally independent OSP methods are suggested in the literature. In the early work of strain sensor placement methodologies, basis functions as a linear combination of sines and polynomials were developed by Kirby et al [13] and in later work, Kirby et al [211] applied a method using linear and quadratic local basis functions. A modal estimation method was presented by Dyllong and Kreuder [212] and a cubic spline-interpolation procedure together with a suitable choice of interpolation points was used to obtain the optimal placement for non-uniform strain sensor spacing. To reconstruct the deflection curve it was shown that five sensors were sufficient to predict three mode shapes. Jung et al [213] applied the Gaussian quadrature formula to determine optimal sensor positions.

3.5 Summary

This chapter has presented a brief review of the aspects thought to be necessary to develop the required baseline models for this research and identify relevant knowledge gaps. Literature covering aeroelastic modelling, damage modelling and identification methods, and optimal sensor placement methodologies in combination with existing shape reconstruction algorithms were studied. Considering the aim of this research, the following key points can be made:

- Sophisticated FE formulations are used for designing rotor blades, structural dynamics optimisation procedures and aeroelastic tailoring, such as the VABS tool developed by Cesnik and Hodges [46]. Yet, often it is sufficient to approximate the structure of a rotor blade with multiple one-dimensional beam elements utilising industry-accepted FE software, such as NASTRAN. Limitations of such models are that detailed damage modelling, such as matrix cracking within composite blades, cannot be performed. Here, a compromise has to be made between the versatility of structural modelling capabilities and the computational efficiency of coupling the FE model with aerodynamics to study its aeroelastic behaviour.

- It is assumed that the quasi-steady dynamic inflow model developed by Pitt and Peters [81] is sufficient for aeroelastic analysis examining the main rotor blade under the hover (and forward flight) loading environment, as no aeroelastic stability analysis is performed and only the first few modes are considered for analyses. Assuming that the reduced frequency associated with aeroloads generated by the first mode at 70% rotor radius results in $k = 0.03$, the aerodynamic damping extracted using Figure 3.8 is approximately $\zeta_a = 0.07$ valid for incidence angles $\alpha = 0 - 10°$.

- Current rotor health monitoring capabilities adopted theoretical model-based methods that are linked to measured data from track and balancing systems. Such model-based methods are limited to simple flight manoeuvres while lacking experimental evidence for validation purposes.

- Natural frequency-based damage detection only provides a global understanding of whether a structure is damaged, but is not suitable for localising the damage. Curvature mode shapes, as well as strain energy techniques, could be used. The main challenge is to obtain a curvature mode shape with either a high number of sensors for a sufficient resolution or an optimal spatial distribution of the sensors.

- Most measurement systems are only applicable in controlled laboratory environments or useable for limited number of flight tests. The recent advances in fibre optic instrumentation show potential for in in-service operation applications.

- The successful application of the modal approach for reconstructing the shape of a complex structure is dependent on the number of deployed strain sensors, used strain mode shape matrix and detailed structural knowledge such as the location of the neutral axis. Although this methodology is computationally efficient, it is not considered suitable for robust damage detection. The modal approach is only valid for small deflections. The Ko-displacement theory allows accurate shape

reconstruction, yet it relies on a large number of sensors that have to be taken on either side of the structural surface to circumvent the issue related to the neutral axis location. To avoid the problem of inaccurately estimating the shape due to torsional load a two-dimensional sensor distribution is necessary.

From the literature review, it was found that a lot of work was done in each area of research. However, the following gaps in knowledge were identified that are addressed in the research work presented in this thesis:

1. Data collection during operation brings benefits for the research community and designers for validating aeroelastic tools and optimising the blade. However, what is the need for a continuous blade health monitoring system from a user-oriented context and what is the link between the designer, maintainer and operator?

2. Since the approach of DFOSS is novel and unique no literature exists that discusses the benefits of displacement and strain measurements in the static and rotating frame. These technological advancements in fibre optic instrumentation systems open up new pathways for rotor health monitoring capabilities, especially for the determination of rotor blade damage indicators. Therefore, this leads to the research question what the benefit of shape measurements over strain measurements is for a healthy and damaged blade?

3. Current optimal sensor placement algorithms for aerospace structures consider one-dimensional distribution (straight line) of strain sensors. Is there an effect of measurement noise on chordwise strain sensor positions?

Shape reconstruction algorithms are needed to obtain meaningful displacement information from strain readings. This post-processing step can result in errors induced by measurement noise, number and location of strain measurements or through structural model inaccuracies. In this research work, the novel direct fibre optic shape sensing system DFOSS has been deployed and tested on the H135 BMR and its sensor performance assessed against the developed FE model.

This page is intentionally left blank.

CHAPTER 4

The main rotor model

Current rotor health monitoring capabilities rely on model-based methods that are used for damage isolation and prognostics. Due to a lack of experimental evidence the use of these methods for estimating a healthy baseline case are widely accepted practices in the industry. Although such theoretical predictions rely on simple flight manoeuvres, such as hover and forward flight, they are commonly used for studying the effect of damage in rotor blades. Sophisticated FE formulations have to be used for detailed damage modelling, such as matrix cracking within composite blades. Although many accurate aeroelastic frameworks have been proposed in the literature, often a compromise has to be made between the versatility of modelling approach with the computational cost. The described computational framework forms the baseline for exploring theoretical instrumentation capabilities in the rotating frame for a healthy and damaged case (Chapter 7).

This chapter presents a coupled aeroelastic simulation framework (see Figure 4.1) of the Airbus Helicopters H135 BMR that links a reduced-order blade FE model with a quasi-steady dynamic inflow model coupled with blade element analysis to calculate the local angles of attack at each time step. The adopted aerodynamic modelling approach was believed to be sufficient for aeroelastic analysis examining the first few aeroelastic modes under the hover loading environment (see Chapter 3). Only structural and aerodynamic interactions are considered, while all other helicopter parts are neglected, such as fuselage, tail rotor, fin and tail plane.

This chapter begins by defining the adopted axes reference frames, which is followed by a description of the pilot control map. Particular focus is put on the structural model development of the complex BMR blade to predict structural dynamics as well as surface strain for the static and rotating environment. After a description of the aerodynamic model, this chapter concludes by discussing the aeroelastic coupling approach. General properties of the H135 T2 and details about the blade design can be found in Appendix A. For this analysis, a total aircraft weight of 2950 kg was used.

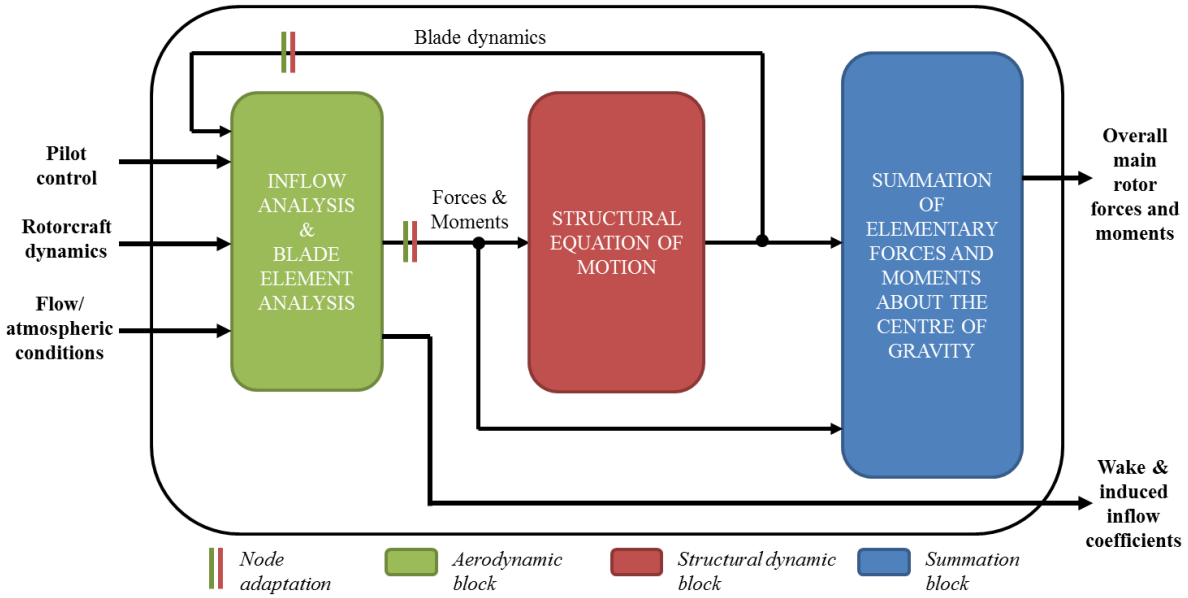

Figure 4.1: Flow chart for the aeroelastic coupling of the main rotor

4.1 Rigid body equation of motion

For the derivation of equations of motion of the helicopter, two reference systems are needed. These are the inertial frame $\mathcal{F}_I$ (earth-fixed frame) and a body-fixed reference frame $\mathcal{F}_B$. The earth-fixed frame has the typical convention of North-East-Down, where the x-axis is in the north direction, the y-axis is in the east direction and the z-axis points to the centre of the earth [214]. The motion of a rigid body using Newton's second law, valid in an inertial reference frame, defined as follows [214]:

$$\vec{f} = m \left. \frac{d\vec{v}}{dt} \right|_I \tag{4.1.1}$$

where m is the total mass of the helicopter and $\frac{d\vec{v}}{dt}|_I$ is the time derivative of the linear velocity vector in the inertial reference frame [214]. The time derivative of $\vec{v}$ in the inertial reference frame is given by:

$$\left. \frac{d\vec{v}}{dt} \right|_I = \left. \frac{d\vec{v}}{dt} \right|_B + \vec{\omega} \times \vec{v} \tag{4.1.2}$$

where $\frac{d\vec{v}}{dt}|_B$ denotes the time derivative of the velocity vector $\vec{v}$ and $\vec{\omega}$ is the angular velocity in the body-fixed reference frame. The following direction cosine matrix is used to transform motion variables from the inertial frame to the body-fixed reference frame:

$$D_I^B = \begin{bmatrix} \cos\theta_e \cos\psi_e & \cos\theta_e \sin\psi_e & -\sin\theta_e \\ \sin\phi_e \sin\theta_e \cos\psi_e - \cos\phi_e \sin\psi_e & \sin\phi_e \sin\theta_e \sin\psi_e + \cos\phi_e \cos\psi_e & \sin\phi_e \cos\theta_e \\ \cos\phi_e \sin\theta_e \cos\psi_e + \sin\phi_e \sin\psi_e & \cos\psi_e \sin\theta_e \sin\psi_e - \sin\phi_e \cos\psi_e & \cos\phi_e \cos\theta_e \end{bmatrix} \tag{4.1.3}$$

where the attitude of the helicopter is defined using Euler angles: these are yaw (ψ), pitch (θ), and roll (ϕ).

4.2 Frames of reference and coordinate transformation

Several axes systems are introduced to simplify the equations of motion within each main rotor component as shown in Figure 4.2. The origin O_{F_B} of the body-fixed reference frame $\mathcal{F}_B$ is located at the centre of gravity of the helicopter. This co-location significantly simplifies the derivation of the equations of motion.

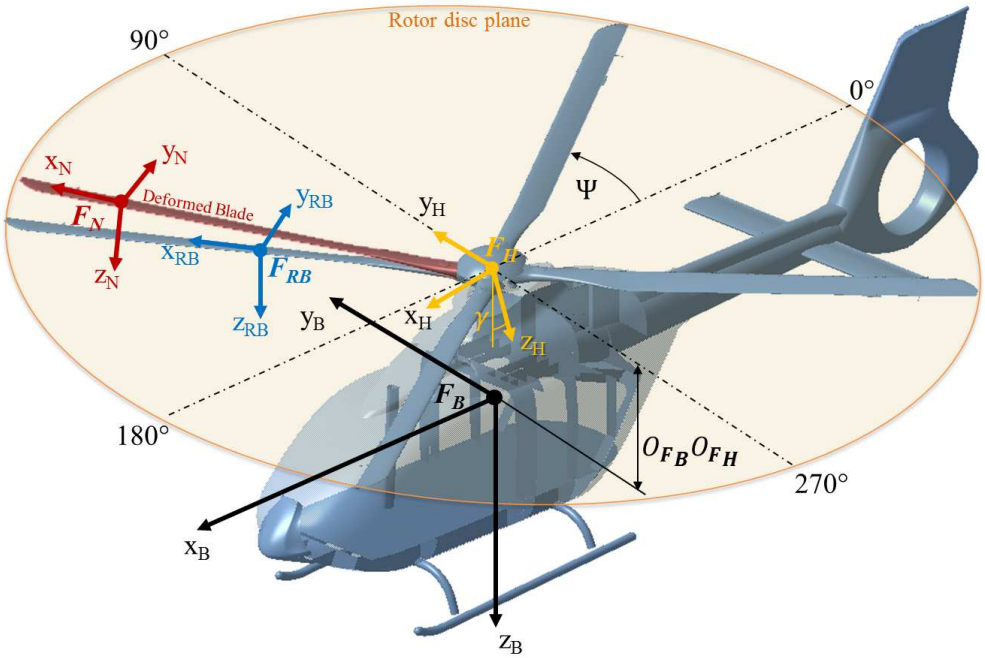

Figure 4.2: Definition of axes systems

It is more convenient to refer to a non-rotating hub axes system for the derivation of rotor kinematics and loads [40]. The origin O_{F_H} of the hub axes reference frame $\mathcal{F}_H$ is at the centre of the rotor hub with the xy-plane parallel to the rotor disc plane. The z_H axis is in line with the rotor shaft axis. The transformation from the body to the hub axes system is defined as follows:

$$D_B^H = \begin{bmatrix} \cos\gamma & 0 & \sin\gamma \\ 0 & 1 & 0 \\ -\sin\gamma & 0 & \cos\gamma \end{bmatrix} \tag{4.2.1}$$

where γ is the angle of the forward tilt of the rotor shaft. To convert the non-rotating axes system to a rotating axes system a blade reference system $\mathcal{F}_{RB}$ is introduced. The z_{RB} axis is aligned with the feather or pitch axis of the blade that points along the span of the rigid rotor blade with an in-built coning angle of 2.5 °. A rotation around the z_H axis is considered using:

$$D_H^{RB} = \begin{bmatrix} -\cos\Psi & -\sin\Psi & 0 \\ \sin\Psi & -\cos\Psi & 0 \\ 0 & 0 & 1 \end{bmatrix} \tag{4.2.2}$$

where Ψ is the azimuth angle of the rotating system where 0° describes the position at the rear of the rotor disc plane. The aerodynamic parameters for a deformed blade section are calculated in the node reference system $\mathcal{F}_N$. $\mathcal{F}_{RB}$ is transformed to $\mathcal{F}_N$ adopting the following transformation matrix:

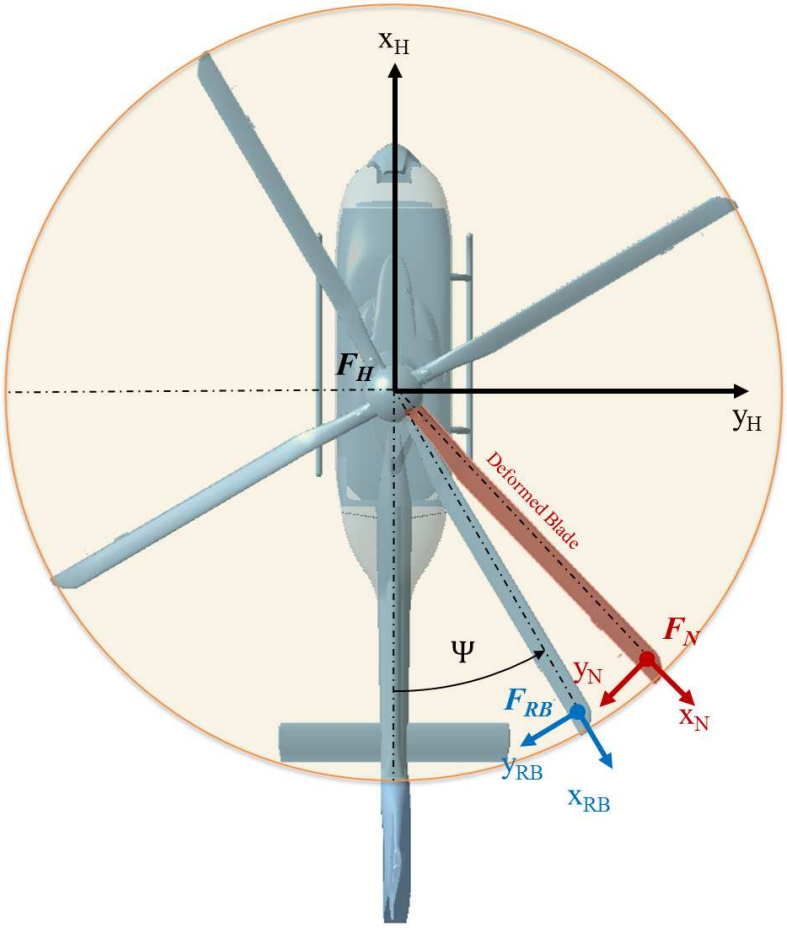

Figure 4.3: Definition of blade to node axis system

$$D_{RB}^{N} = \tag{4.2.3}$$

$$\begin{bmatrix} \cos\theta_{el}\cos\psi_{el} & \cos\theta_{el}\sin\psi_{el} & -\sin\theta_{el} \\ \sin\phi_t\sin\theta_{el}\cos\psi_{el} - \cos\phi_t\sin\psi_{el} & \sin\phi_t\sin\theta_{el}\sin\psi_{el} + \cos\phi_t\cos\psi_{el} & \sin\phi_t\cos\theta_{el} \\ \cos\phi_t\sin\theta_{el}\cos\psi_{el} + \sin\phi_t\sin\psi_{el} & \cos\phi_t\sin\theta_{el}\sin\psi_{el} - \sin\phi_t\cos\psi_{el} & \cos\phi_t\cos\theta_{el} \end{bmatrix} \tag{4.2.4}$$

where the subscript el denotes structural deformation, so that θ_{el} is defined as the flapping angle, ψ_{el} is the lagging angle, and ϕ_{el} is the rotation around the z-axis (feathering axis) that coincides with the aerodynamic centre of the blade profile. The total rotation ϕ_t around the feathering axis is given by:

$$\phi_t = \phi_{el} + \theta_{tw} + \theta_p \tag{4.2.5}$$

where θ_{tw} is the blade pre-twist angle and θ_p is the main rotor pitch angle written as:

$$\theta_p = \theta_0 + \theta_{1s}\sin\Psi + \theta_{1c}\cos\Psi \tag{4.2.6}$$

where θ_0 is the collective pitch angle, θ_{1s} is the longitudinal cyclic pitch angle, and θ_{1c} is the lateral cyclic pitch angle.

4.3 Control mapping

The connection between the movement of the pilot control and blade pitch angles is mapped via lookup tables that were generated using relationships between pilot input and the corresponding kinematic relationships of the so-called "upper control system" as shown in Figure 4.4. A collective lever input η_0 is used to change the blade pitch collectively by the same amount θ_0. If the cyclic longitudinal input η_{1s} is used by the pilot, then the blades at azimuth positions 90° and 270° will undergo the blade pitch change θ_{1s}. As explained by Padfield [40] *"the flap response to cyclic pitch is close to phase resonance, and hence is about* 90° *out of phase with the pitch control input"*. Due to this phase lag, the blade response becomes effective 90° later, which is at 180° and 0° azimuth position respectively. Each rotor experiences a different phase lag as it is dependent on the rotor stiffness; the stiffer the rotor the smaller the phase lag [40]. For example, the Lynx has a phase lag of 80°. Assuming a linear link between pilot stick/lever position and feathering angle, a relationship for longitudinal and lateral rotor disc as a function of stick position is formed. The adopted methodology is based on the work of Price [215] and modelled by Payo [216] in a Simulink environment using data from the Lynx helicopter. It is assumed that this is sufficient for this work, yet for accurate representation, the control map has to be adjusted to represent the H135.

The different pitch angles as a function of the pilot stick position are shown in Figure 4.5. The top left diagram depicts the longitudinal cyclic pitch θ_{1s} as a function of the cyclic stick position (η_{1s} and η_{1c}). A forward-left positioning of the cyclic stick corresponds to

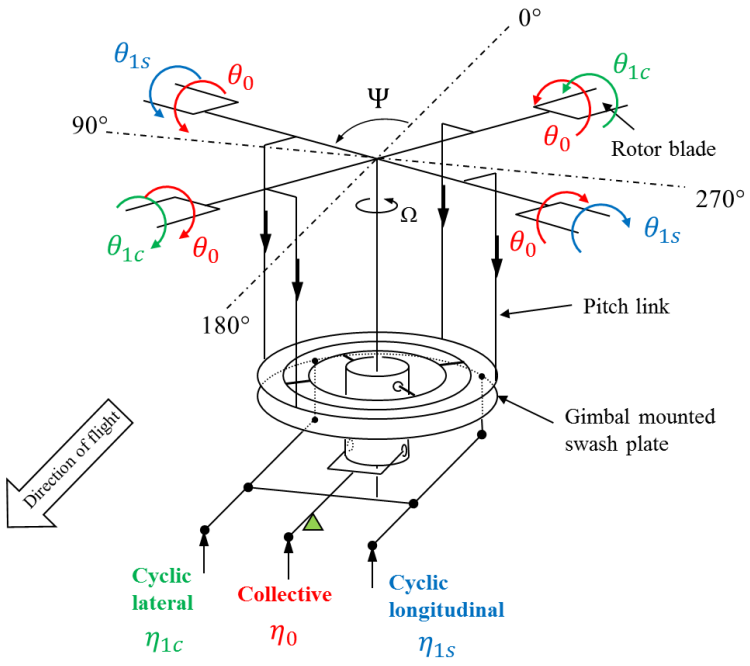

Figure 4.4: H135 upper control system (reproduced from Reference [217])

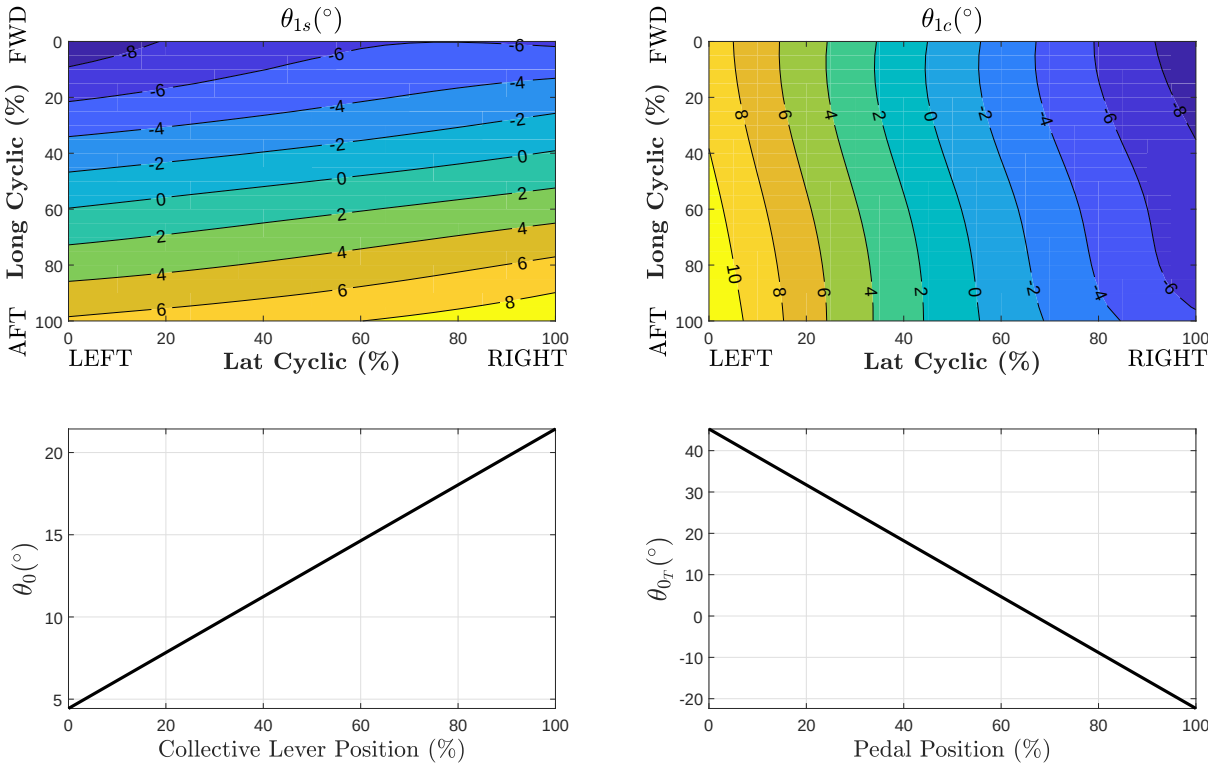

Figure 4.5: Pilot map used for main rotor model

[0,0] and produces a pitch down and left roll response of the helicopter. Moving the stick backwards a pitch up attitude response is expected due to the change of longitudinal cyclic pitch angle θ_{1s}. This pitch angle input is applied approximately at the blade azimuth position 90° and 270° (refer to Figure 4.4). Due to the phase lag, the flap movement acts approximately 90° later, consequently causing a pitch up attitude. The top right diagram

represents the lateral cyclic pitch θ_{1c} as a function of the cyclic stick position. In this case, a backward movement of the stick does not change the lateral cyclic pitch angle θ_{1c} significantly. The bottom left figure shows the collective pitch angle θ_0 as a function of collective lever input η_0. For completeness, the tail rotor collective pitch angle θ_{0_T} is shown as a function of pedal position in the bottom right figure. Payo [216] explains that this data was produced based on the best match for flight test data. For the expansion of the BMR framework to a fully coupled 6 DOF model, the suitability of the tail rotor collective pitch angles has to be reinvestigated.

4.4 Structural model development

The FE beam model was constructed adopting standard finite-element-modelling techniques in MSC/NASTRAN (version 2014.0). The analysis of transient and steady-state structural behaviour is carried out through a state-space formulation that utilises structural modal properties. Two-dimensional profiles are coupled with the FE beam model to obtain displacement information at a chosen surface position. An overview of the modelling approach is given in Figure 4.6.

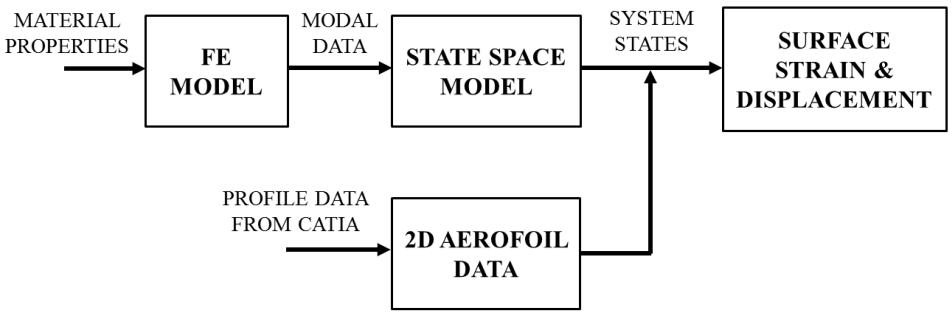

Figure 4.6: Flow chart of structural modelling approach

Material and cross sectional properties for the blade were obtained from data provided by Airbus Helicopters Germany (AHD) for a certain number of radial distances representing the structural nodes. This data was given as a product of material properties and second moment of area, such as EI_x, EI_z, or torsional stiffness GJ. Although the material properties vary with rotor radius, it is assumed that these stay constant between the structural nodes. Due to the nature of the data format, NASTRAN seemed to be especially suited. A schematic of the one-dimensional modelling principle is shown in Figure 4.7(a). The complex structure of the rotor blade is modelled through multiple beams consisting of a primary one-dimensional stick for the flexbeam and the blade aerofoil section, and a secondary stick parallel to the flexbeam representing the pitch control cuff.

The blade root boundary condition was selected so that the first node is constrained in all six degrees of freedom, using the NASTRAN entry SPC1. Each nodal position is defined with geometric GRID points. The entire blade structure is modelled utilising CBEAM one-dimensional beam elements. Material and cross-sectional properties of the beam elements are defined through the PBEAM entry that also allows the use of shear stiffness factors to adjust the effective transverse shear cross section area according to the Timoshenko beam theory [218]. The tapered beam option is chosen for the PBEAM

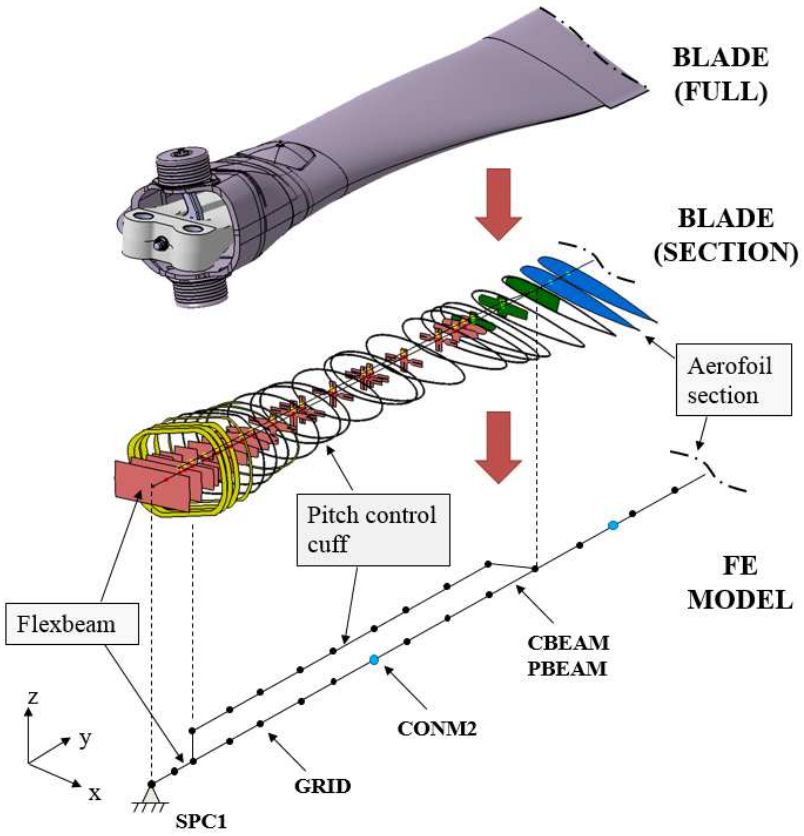

(a) Beam model development

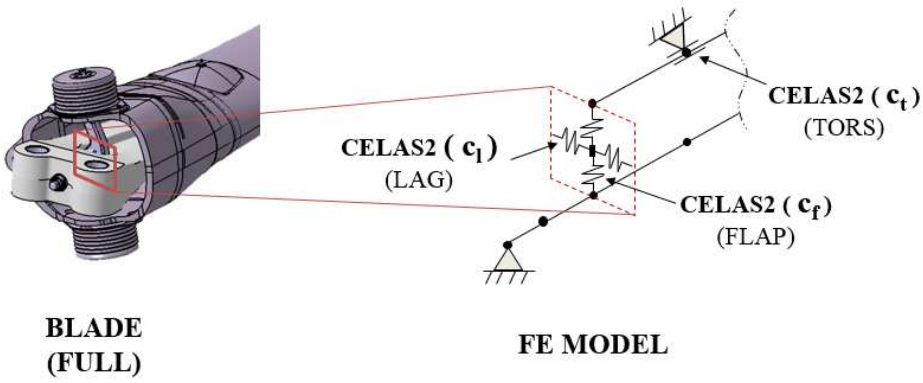

(b) Boundary condition

Figure 4.7: Structural modelling principle

entry. To model the correct torsional behaviour the non-structural mass moment of inertia[1] NSI must be included in the PBEAM command. As the PBEAM entry only allows a neutral axis entry, the given values of the elastic centre are used. Point masses, which are CONM2 zero-dimensional elements, are added to include the weight of the damper, balancing weights and tuning masses. To connect the pitch control cuff and blade aerofoil section one common GRID point is used, while flexible joints are chosen

[1]Without the torsional moment of inertia the torsional mode could not be predicted. The required values were obtained from AHD.

to model the interconnection between pitch link, pitch control cuff and lead-lag damper. This was done by introducing two CELAS2 scalar spring elements with a linear spring rate in the flapping (c_f) and the lagging (c_l) directions. To take into account the rotational stiffness of the pitch control cuff an additional CELAS2 element is introduced using a rotational spring rate (c_t) acting around the feathering axis. This was modelled by adding another GRID point to represent the connection point between pitch link and pitch horn. The pitch horn was connected to the pitch control cuff via the rotational spring element c_t that acts around the feathering axis. The correct value for c_t, that represents the so-called clamping stiffness, is important for correct dynamic structural analysis both in the static and the rotating environment. The pre-twist of the rotor blade is taken into account by measuring (in CATIA V5) the pre-twist angle θ_{tw} between the blade profiles' chord and a plane that is parallel to the tip-path plane (see Figure 4.8). With this angle, the x- and z-components (V_{X2},V_{X3}) of the orientation vector V can be calculated and applied to the CBEAM entry.

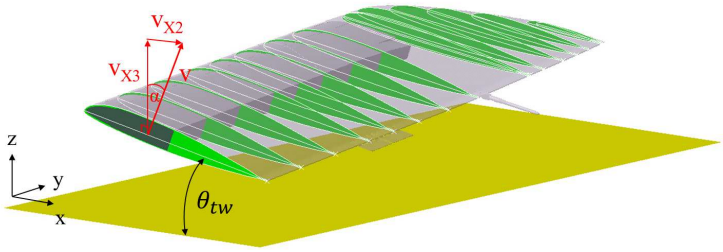

Figure 4.8: Definition of orientation vector

Figure 4.9 shows the distribution of flap bending stiffness EI_x, lag bending stiffness EI_z, torsional stiffness GJ and longitudinal stiffness EA for the first 30% of rotor radius. From the drop in flap stiffness distribution, it can be seen that the flapping hinge is located at around 9%. The low lag stiffness indicates that the lagging hinge is located in between 9-20%. As expected the torsional stiffness is high for the pitch control cuff as the blade must be torsionally stiff so that coupling between elastic flap bending and torsion is minimised and flutter problems reduced [59]. Simultaneously low torsional stiffness is required for the flexbeam to give adequate blade pitch change. Finally, the high longitudinal stiffness of the flexbeam indicates that this is the main component for centrifugal load transfer. The variation of twist over the full length of the rotor blade is depicted in Figure 4.10. As explained by Kampa [219] blade twist is often a compromise between the requirements of hover (high twist angle) and forward flight (low twist angle). In forward flight the optimum twist increases with rotor disc inclination, that is with the aerodynamic drag of the aircraft. Furthermore, through flapping and lag deflections an elastic coupling arises from the built-in blade twist [37]. The H135 blade has 10° twist [219]. The blade tip is designed to be of thin profile to avoid too negative angle of attack in high-speed flight.

NASTRAN has a restriction on the choice of axes in that it only allows the entry of a neutral axis, the centre of mass, and shear centre. The neutral axis and centre of mass are defined in the PBEAM entry, and the shear centre is defined in the CBEAM entry. To ensure similar characteristics to the actual blade, the definition and understanding of these axes are important and a compromise was required as it was not possible to enter the elastic axis values. As explained by Stodieck [220] "*there is still a great deal of confusion as to the actual definition of the axis about which there is no bending/torsion coupling*"

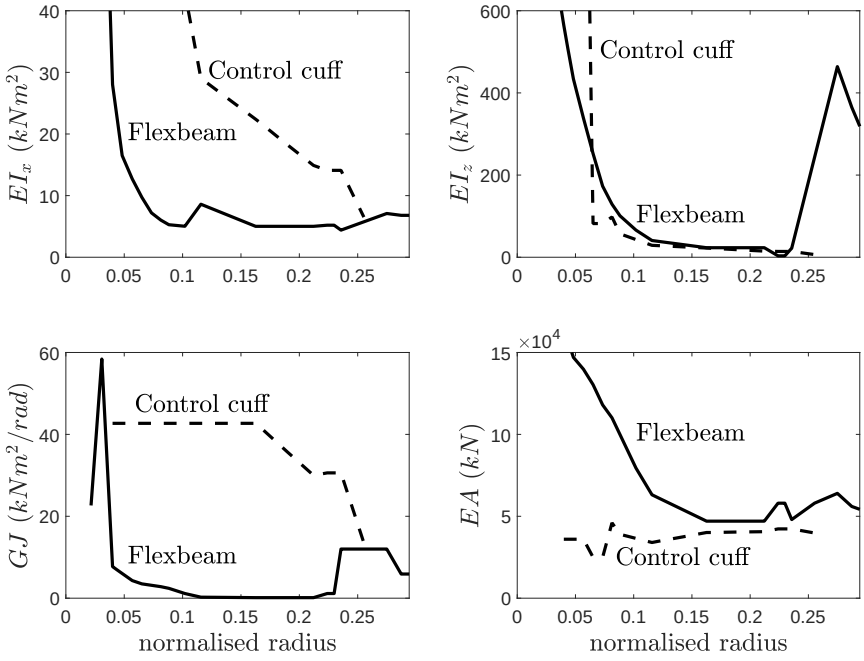

Figure 4.9: Distribution of material properties

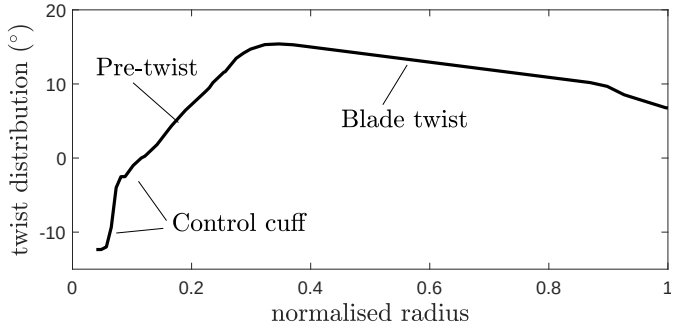

Figure 4.10: Twist distribution along blade span

and an attempt was made to unify some of the conflicting definitions. Stodieck defines the shear centre as "*the position on a two-dimensional (2D) cross-section where there is zero rate of change of the twist along the beam for a shear load applied to that cross-section and does not include bend/twist coupling (i.e. the shear centre is characteristic of a particular section)*". The locus of shear centres along a wing is defined as the elastic axis. The neutral axis is the axis in a cross section of a profile where there are no longitudinal stresses or strains. Furthermore, throughout this work, the neutral axis is defined as the intersection between the neutral plane and spanwise cross-section. For simplicity, it was decided to keep the shear centre coincidence with the GRID point and the elastic axis values were entered in the NASTRAN neutral axis section. This is justified as the neutral axis values were not known, but still expected to be around the quarter chord line (also aerodynamic centre). Figure 4.11 shows the distribution of the centres for the blade, where the *struct* centres are the GRID points.

Coupling the FE structural dynamics model to surface points representing the blades geometric surface is necessary as the sensors are placed on the surface during structural testing. A Matlab code to visualise the geometrical profiles that are linked to the beam

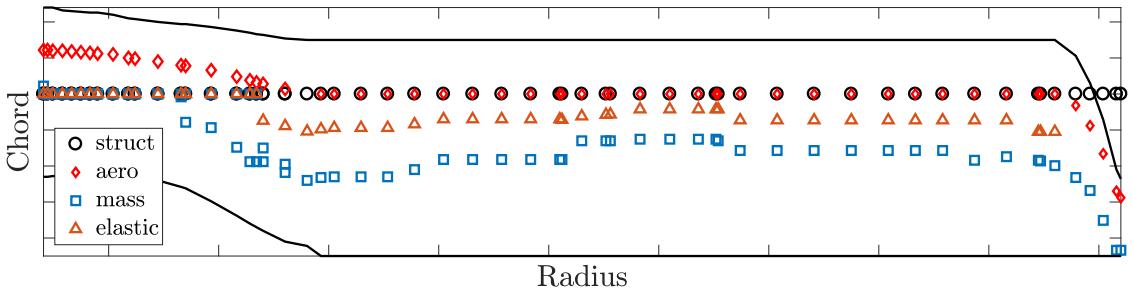

Figure 4.11: Schematic representation of centres for the H135 rotor blade

model was developed in-house by Gaétan Dussart[2]. Profiles of arbitrary shapes can be used in the form of normalised coordinates, which are positioned to the defined leading edge coordinates. This task is simplified by using only two geometrical profiles for the cuff and blade profiles, which are then scaled according to the spanwise thickness to chord ratio for each nodal point. However, as the geometry of the cuff profile changes as a function of rotor radius, the data profile points were adjusted with correction factors according to the available CAD model. The profiles are rotated around the structural centre with the use of transformation matrices. It is assumed that the shape of the cross-section remains unaltered during deformation, regardless of the loading conditions. Also, warping and shear deformations are neglected.

4.4.1 Modal analysis

Modal properties, such as natural frequencies and mode shapes, provide important structural information. These are computed through the NASTRAN modal solver SOL 103 for the non-rotating rotor blade, while the non-linear solver SOL 106 is applied to determine the modal properties under the centrifugal stiffening effect. Mathematical background theory is presented in Appendix D.1.1 and D.1.2, while the input data deck can be found in Appendix D.3. To ensure that a coupled mass matrix is generated by NASTRAN the bulk data card needs to state "PARAM COUPMASS 2"[3]. The blade feather angle was set to 4° collective defined at 70% rotor radius. Results of non-rotating natural frequencies are listed in Table 4.1 in comparison to data extracted from Rammer et al [221]. It was found that the computed FE natural frequencies are in agreement with an average error of 4.2%. The mode shapes can be visually represented through geometrical blade profiles. Figure 4.12 shows the first eight structural mode shapes. Each plot is labelled, such that 1F stands for first flapping mode, 1L is the first lagging mode and, 1T is the first torsional mode, etc. While the first four mode shapes have a dominant flapping or lagging component, Mode 2L exhibits coupled flapping/lagging, and Mode 1T has a coupled torsion/flapping component. This coupling occurs mainly due to the chord-wise locations of the centre of mass and shear centre [37].

In the rotating environment centripetal force produces a stiffness-like term [58] that arises due to spanwise stretching [222, 223] leading to a higher natural frequency. This effect can be easily modelled through the NASTRAN non-linear solver SOL 106 that treats the

[2]PhD candidate at Dynamic Simulation and Control Group at Cranfield University.
[3]AHD experienced problems with lumped mass methods resulting in wrong outcomes.

Table 4.1: Comparison of non-rotating natural frequencies

Mode number	Mode type	Natural frequencies AHD (Hz)	Natural frequencies FE (Hz)	Error (%)
1	1st flapping	0.9	0.9	0.0
2	1st lagging	3.5	3.4	2.9
3	2nd flapping	4.8	5.0	-4.2
4	3rd flapping	14.4	15.3	-6.3
5	2nd lagging	24.1	22.7	5.8
6	1st torsion	27.3	28.6	-4.8
7	4th flapping	28.4	30.0	-5.6
			average	|4.2|

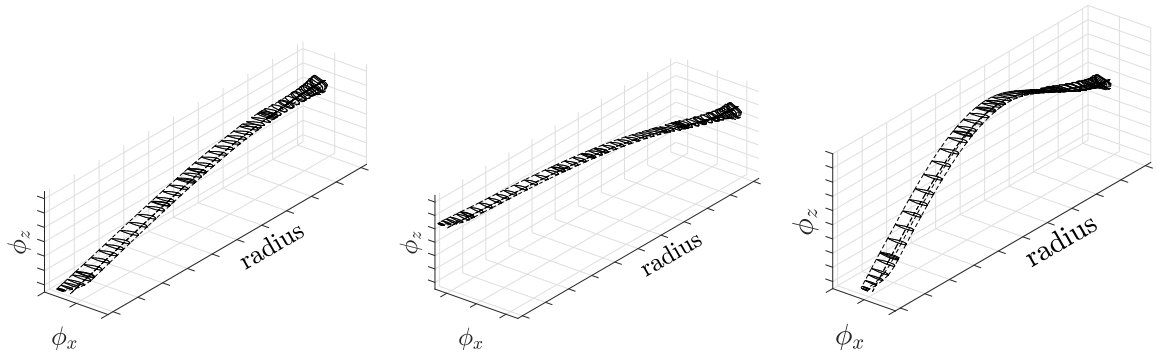

(a) 1st flapping mode (1F) (b) 1st lagging mode (1L) (c) 2nd flapping mode (2F)

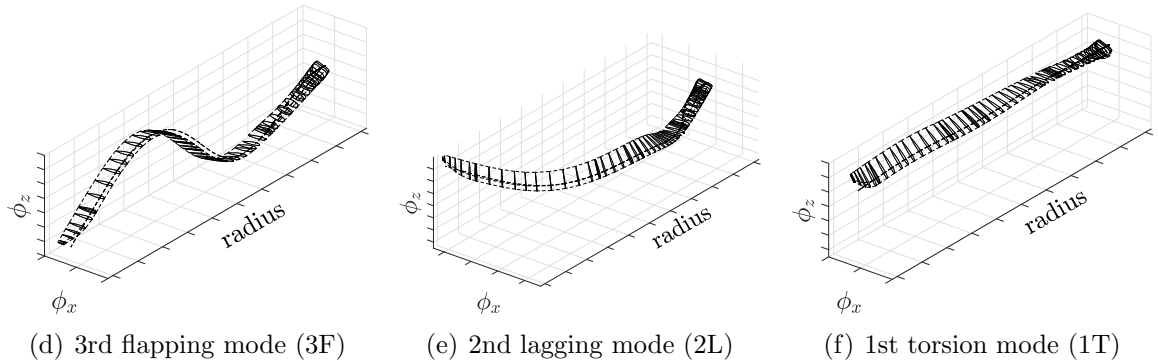

(d) 3rd flapping mode (3F) (e) 2nd lagging mode (2L) (f) 1st torsion mode (1T)

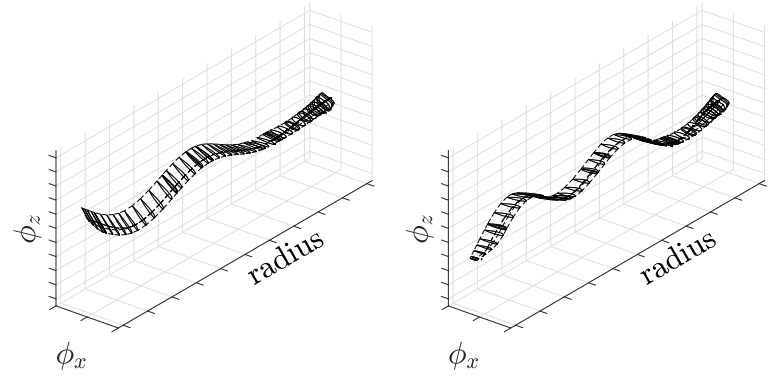

(g) 4th flapping mode (4F) (h) 5th flapping mode (5F)

Figure 4.12: Displacement mode shapes of the H135 rotor blade

centrifugal force as a follower force [222]. Within SOL 106 the geometric non-linear effects are treated by updating element coordinates, rotation vectors and the differential stiffness matrix (effects of stress stiffening) in an iterative method. NASTRAN uses a modified Newton's method to update the stiffness matrix at every iteration. Therefore, command NLPARAM is used to control the incremental and iterative solution process. In addition to NLPARAM, the entry PARAM,LGDISP,1 has to be used in the NASTRAN's bulk entry card to account for geometric non-linear effects and to make sure that the stiffness due to follower forces are included; these stress stiffening effects are ignored in SOL 101. Due to the influence of centrifugal stiffening, the natural frequencies are defined as follows [37]:

$$\omega_{r_j}^2 = \omega_{s_j}^2 + \Omega^2 K_{w_j} = \frac{K_{s_j}}{M_j} + \Omega^2 \frac{K_{CF_j}}{M_j} \tag{4.4.1}$$

where ω_{s_j} is the jth mode non-rotating blade natural frequency, K_{CF_j} is the generalised centrifugal stiffness, K_{w_j} is an additional term to account for centrifugal stiffening, and M_j and K_j are the generalised mass and stiffness, respectively. The inclusion of these stiffness terms is of importance if a pre-stressed modal analysis is to be performed. To achieve this, eigenvalue analysis entry EIGRL has to be included in the non-linear solver SOL 106 as METHOD in the specified sub-case section. By adopting this approach a so-called "Campbell diagram" (also known as "Southwell diagram" or "fan plot") was generated that is presented in Figure 4.13. This diagram is commonly used at the design stage of rotor blades and the natural frequencies of the modes must not be in the frequency range of excitation. The excitation frequencies are plotted as thin dot-dashed lines originating from zero and fanning out as the rotational speed increases. At the operational speed, no resonances are excited as coincidence between excitation and response was avoided in the blade design stage. As explained by Watkinson [224] "*the only coincidence between excitation and response is the close correspondence between the fundamental flapping resonant frequency and the rotor fundamental frequency*". The first flapping mode is higher than 1/rev[4], that is $\nu = \omega_1/\Omega$. This also results in a higher mast-moment-capacity[5].

The Campbell diagram shown in Figure 4.13 presents the rotating natural frequencies for the first seven modes calculated with SOL 106 compared with CAMRAD II, MOSES[6], and with data obtained from a whirl tower test, which were extracted from [221]. All calculations were performed for a collective setting of $\theta_{0.7} = 4°$. At this setting, no large aerodynamic loads are produced by the rotor blade and so the MOSES calculations could be performed in a linear manner using SOL 103 in combination with a loads subcase. Within CAMRAD II an option is available to select "wind tunnel calculations" which corresponds with the whirl tower test. Two data points were extracted from a whirl tower test for two different RPM-settings (90% RPM and 100% RPM). From the CAMRAD II calculation, a coupling between first torsion[7] and second lagging mode is present [221]. MOSES, however, is not able to predict such couplings [221]. The first three modes

[4]For a teetering or so-called seesaw rotor the flapping hinge is at the rotor shaft, which means that the first flapping mode is at 1/rev.

[5]The term "mast-moment-capacity" is used at AHD and is defined as $M_R = \frac{N}{2} M_B$, where M_B is the root bending moment and N specifies the number of blades (see also Reference [217]).

[6]MOSES is an AHD in-house tool that incorporates NASTRAN.

[7]Typically the torsional frequency of a modern blade is expected to be around 5-8 per revolution [59].

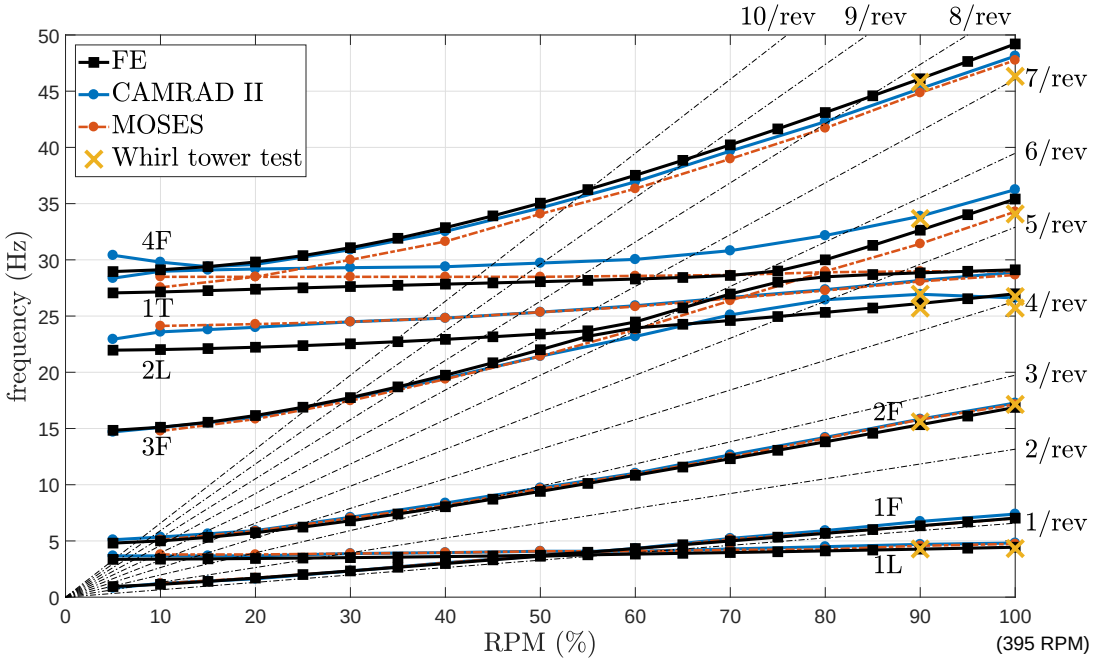

Figure 4.13: Campbell diagram, collective setting: 4°(data was reproduced from Rammer et al [221])

have a close correlation with the data calculated by AHD. For the higher modes, a coupling between torsion and flapping or lagging is found. Despite the limitations within NASTRAN initial results show an agreement with CAMRAD II.

4.4.2 Transient and steady-state analysis

Throughout this work a variety of analyses were performed, such as studying the transient response of the rotor blade in a static environment, determining the steady-state response for several loading conditions, or analysing the aeroelastic behaviour of a rotating rotor blade. This was achieved by coupling the structural modal properties from the FE model, that are imported from the NASTRAN *.f06* file to Matlab, and linked with a state-space representation of the system. The following standard equation of motion was used to determine the structural response:

$$\mathbf{M}\ddot{\mathbf{Q}} + \mathbf{C}\dot{\mathbf{Q}} + \mathbf{K}\mathbf{Q} = \mathbf{F}(t) \tag{4.4.2}$$

where $\mathbf{Q}$, $\dot{\mathbf{Q}}$, and $\ddot{\mathbf{Q}}$ ($[\mathbf{Q}, \dot{\mathbf{Q}}, \ddot{\mathbf{Q}}] \in \mathbb{R}^{n\times 1}$), are the nodal displacement, velocity and acceleration state vectors, $\mathbf{M}$ is the mass matrix, $\mathbf{C}$ is the damping matrix, $\mathbf{K}$ is the stiffness matrix, and $\mathbf{F}$ is the force vector. While n is defined as the number of nodes for all DOF, a finite number of mode shapes m are used to approximate the full characteristics of the structure. Rearranging Eq. 4.4.2 in state-space form:

$$\underbrace{\begin{bmatrix}\dot{\mathbf{q}}\\ \ddot{\mathbf{q}}\end{bmatrix}}_{\dot{\mathbf{x}}} = \underbrace{\begin{bmatrix}0 & 1\\ -\widetilde{\widetilde{\mathbf{M}}}^{-1}\widetilde{\widetilde{\mathbf{K}}} & -\widetilde{\widetilde{\mathbf{M}}}^{-1}\widetilde{\widetilde{\mathbf{C}}}\end{bmatrix}}_{\mathbf{A}} \underbrace{\begin{bmatrix}\mathbf{q}\\ \dot{\mathbf{q}}\end{bmatrix}}_{\mathbf{x}} + \underbrace{\begin{bmatrix}0\\ \widetilde{\widetilde{\mathbf{M}}}^{-1}\end{bmatrix}}_{\mathbf{B}} \underbrace{\widetilde{\mathbf{F}}}_{\mathbf{u}} \tag{4.4.3}$$

where $\mathbf{q}$, $\dot{\mathbf{q}}$, and $\ddot{\mathbf{q}}$, ($[\mathbf{q}, \dot{\mathbf{q}}, \ddot{\mathbf{q}}] \in \mathbb{R}^{m\times 1}$) are the generalised displacement, velocity and acceleration state vectors. The generalised mass matrix $\widetilde{\mathbf{M}} \in \mathbb{R}^{m\times m}$ and the generalised stiffness matrix $\widetilde{\mathbf{K}} \in \mathbb{R}^{m\times m}$ are given by:

$$\widetilde{\mathbf{M}} = \mathbf{\Phi}^T \mathbf{M} \mathbf{\Phi} \tag{4.4.4}$$

$$\widetilde{\mathbf{K}} = \mathbf{\Phi}^T \mathbf{K} \mathbf{\Phi} \tag{4.4.5}$$

where $\mathbf{\Phi} \in \mathbb{R}^{n\times m}$ is the mode shape matrix. The applied force vector $\mathbf{F}$ is transformed into normal coordinates $\widetilde{\mathbf{F}} \in \mathbb{R}^{m\times 1}$:

$$\widetilde{\mathbf{F}} = \mathbf{\Phi}^T \mathbf{F} \tag{4.4.6}$$

The generalised damping matrix $\widetilde{\mathbf{C}} \in \mathbb{R}^{m\times m}$ is calculated by assuming the following Rayleigh damping model:

$$\widetilde{\mathbf{C}} = a_0 \widetilde{\mathbf{M}} + a_1 \widetilde{\mathbf{K}} \tag{4.4.7}$$

where a_0 and a_1 are the damping coefficients that can be expressed as the following relation between damping ratio ζ and frequency ω [225]:

$$\zeta = \frac{a_0}{2\omega} + \frac{a_1 \omega}{2} \tag{4.4.8}$$

The relationship between damping ratio and frequency as expressed by Eq. 4.4.8 is presented in Figure 4.14. The two Rayleigh damping factors, a_0 and a_1 can be evaluated by the solution of a pair of simultaneous equations if the damping ratio ζ_m and ζ_n associated with two specific frequencies ω_m and ω_n are known [225], see Eq. 4.4.9.

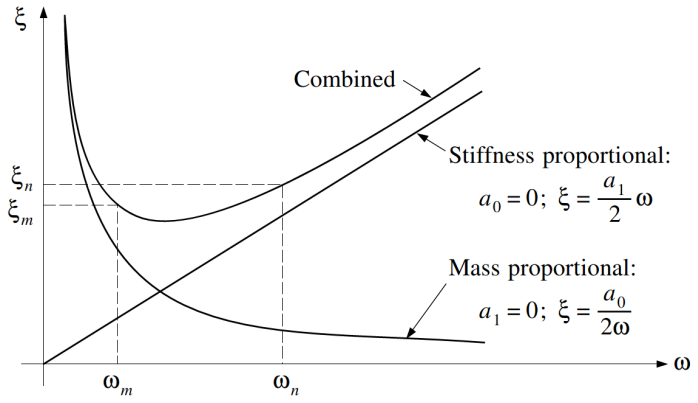

Figure 4.14: Relationship between damping ratio and frequency valid for Rayleigh damping (reproduced from Clough et al [225])

$$\begin{bmatrix} a_0 \\ a_1 \end{bmatrix} = 2\frac{\omega_m \omega_n}{\omega_n^2 - \omega_m^2} \begin{bmatrix} \omega_n & -\omega_m \\ -\frac{1}{\omega_n} & \frac{1}{\omega_m} \end{bmatrix} \begin{bmatrix} \zeta_m \\ \zeta_n \end{bmatrix} \tag{4.4.9}$$

where ω_m, and ω_n are associated to the damping ratios ζ_m and ζ_n. As detailed information about the variation of damping ratios associated with each frequency is seldom available, it can be assumed that ω_m and ω_n, such as $\zeta_m = \zeta_n = \zeta$. Therefore, Eq. 4.4.9 can be simplified:

$$\begin{bmatrix} a_0 \\ a_1 \end{bmatrix} = \frac{2\zeta}{\omega_m + \omega_n} \begin{bmatrix} \omega_m \omega_n \\ 1 \end{bmatrix} \tag{4.4.10}$$

Figure 4.15 demonstrates how the transient response varies as a function of the damping ratio ζ using Eq. 4.4.10. For ω_m and ω_n the first and eight frequencies were taken. In this case, the gravitational load was used as the input force. For further analysis, it was assumed that $\zeta = 0.1$ as the damping is very low obtained from initial inspections of the blade. The modal damping ratios were identified during testing (see Chapter 5) and the damping model updated as required.

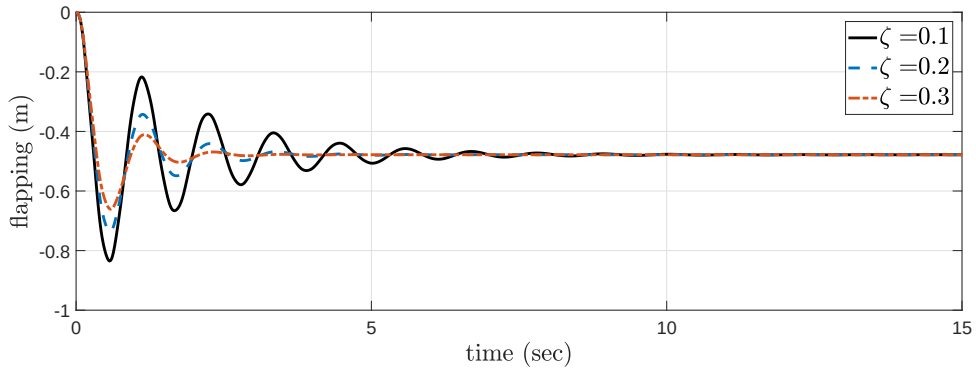

Figure 4.15: Flapping response due to damping ratio

Finally, to obtain the full state positions and velocities, the reduced states are multiplied by the jth mode shape ϕ_j. The response in geometric coordinates is then given by the following coordinate transformation:

$$\mathbf{d} = \sum_j \phi_j q_j \tag{4.4.11}$$

$$\dot{\mathbf{d}} = \sum_j \phi_j \dot{q}_j \tag{4.4.12}$$

where $\mathbf{d}$ is the structural displacement and $\dot{\mathbf{d}}$ is the structural velocity of each node in all degrees of freedom. For verification purposes, the steady-state response from the simulation was compared with results obtained through NASTRAN's linear static solver SOL 101. The first 12 modes were used to estimate the displacement. Figure 4.16 compares the blade tip displacement under gravitational load at t=100 seconds. For both, flap and lag, a small error of approximately 1.6% is obtained which is considered low enough to permit further analysis with the adopted state-space representation.

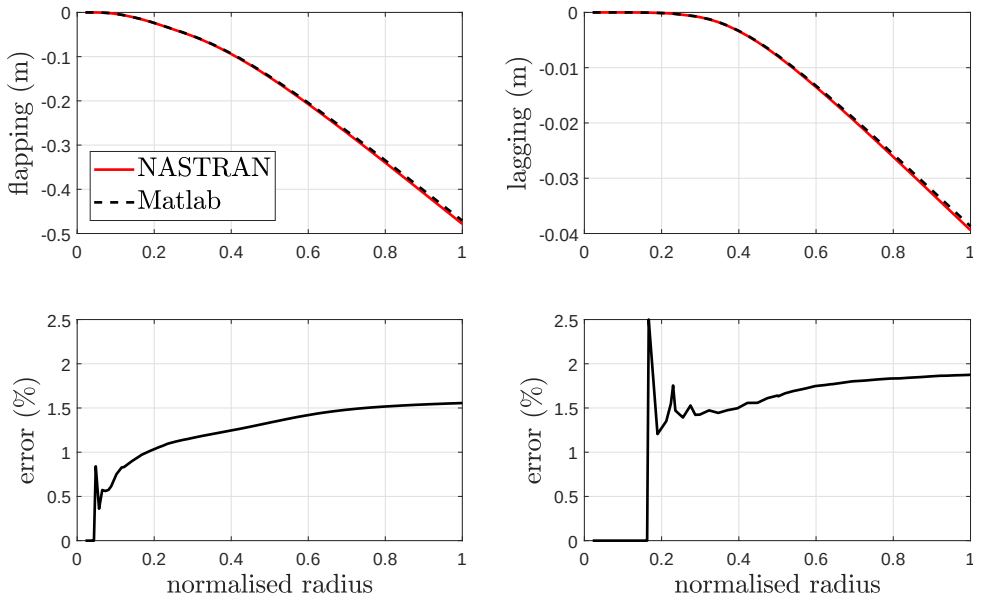

Figure 4.16: Comparison of steady-state response between NASTRAN and Matlab

4.4.3 Surface strain

Since the FBG sensors measure surface strain along their longitudinal axis, a mathematical expression is formulated that calculates the axial surface strain ϵ_T as a function of combined flapping and lagging displacement:

$$\epsilon_T(x,y,z,t) = -c_z(x,y,z)\frac{\partial^2 w(t)}{\partial y^2} + c_x(x,y,z)\frac{\partial^2 u(t)}{\partial y^2} \tag{4.4.13}$$

where c_z and c_x represent the distance between the location of the measurement and the neutral axis. A complete derivation of the surface strain can be found in Appendix D.2. Shear strain is neglected as it is assumed that the shape of the cross-sectional profile remains unaltered during deformation. The neutral axes position as presented in Figure 4.17 varies along the length of the rotor blade, but it is assumed to be close to the quarter chord line, while approximately centred between the upper and lower surfaces.

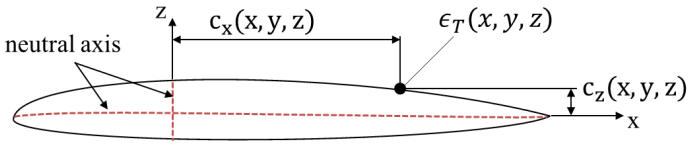

Figure 4.17: Approximate locations of the neutral axes across the blade cross section

Lack of knowledge about the exact position of the neutral axis leads to assumptions being made for the strain calculation and consequently leads to uncertainties in the mathematical model. Depending on where the neutral axis is located within the blade profile the structure experiences either compression (+) or tension (-) as described in Figure D.4. If the blade deforms in the $-z$ direction then positive strain (tension) is defined at the top surface. The jth axial surface strain mode shape ψ_{T_j} is obtained by replacing the curvature terms (second derivatives) in Eq. 4.4.13 with $\partial^2\phi_j/\partial y^2$:

$$\psi_{T_j}(x,y,z) = -c_z(x,y,z)\frac{\partial^2 \phi_{z_j}}{\partial y^2} + c_x(x,y,z)\frac{\partial^2 \phi_{x_j}}{\partial y^2} \tag{4.4.14}$$

where ϕ_{z_j} and ϕ_{x_j} are the jth mode shapes in z- and x-direction, respectively. For clarification, the terminology adopted within this thesis is as follows:

- *Surface strain* ϵ_T is obtained through a linear superposition of the curvature term in flap and lag directions multiplied by the distance between the surface point and the neutral axis.
- *Strain mode shape* ψ is defined as the second spatial derivative of the displacement mode shape, while the location of both is coincident with the FE beam model.
- The *surface strain mode shape* ψ_T takes into account a linear superposition of strain mode shape in the flap and lag direction, also multiplied by the distance between the surface point and the neutral axis.

Figure 4.18 shows the surface plot for the first eight normalised surface strain mode shapes. Modes 1L and 2L each have a predominant lagging component, which is evident from the high strain values at the trailing edge resulting from the separation between surface point and the neutral axis. The expected shape change in the surface strain at 20% radius (caused by the junction of the cuff with the blade) is very noticeable in all modes. Furthermore, Mode 1T shows a dominant flapping component because the surface strain is assumed to be a linear superposition due to flap and lag movement. For the experimental test data comparison (see Chapter 5.2.3 and 6.3), the numerical values are interpolated at the measurement positions.

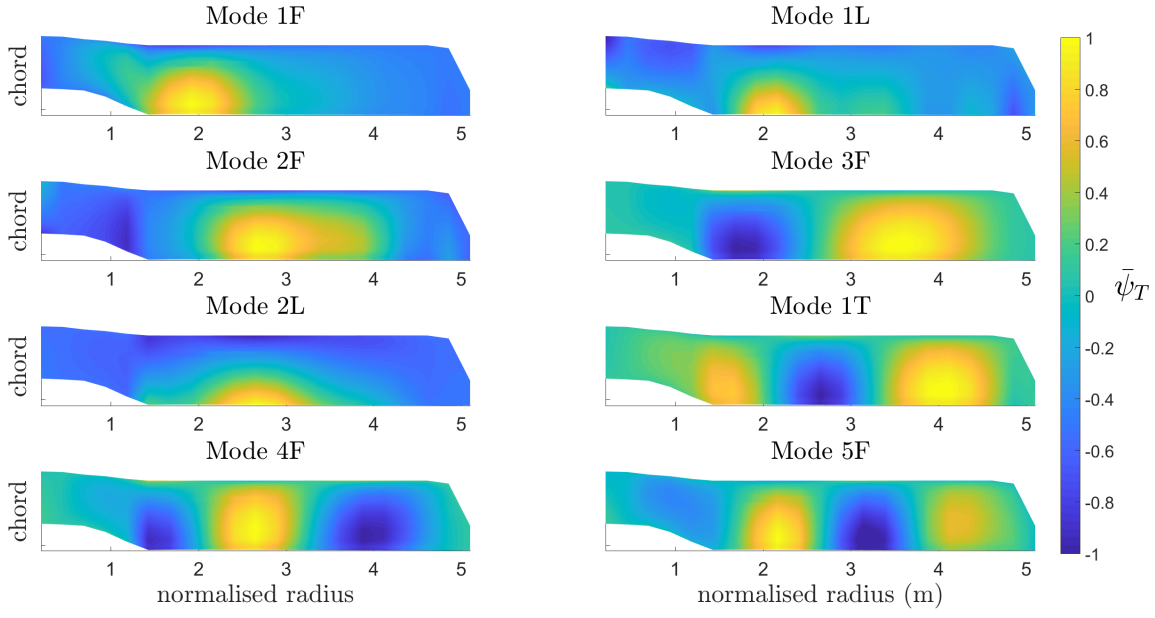

Figure 4.18: Normalised surface strain mode shapes $\bar{\psi}_T$

As shown in Eq. 4.4.13 axial surface strain ϵ_T can be calculated by differentiating the flapping and lagging displacement twice with respect to the spanwise length. A different approach can be taken to determine ϵ_T by using a finite number of strain mode shapes that

allows the approximation of strain of the structure. This is achieved by the summation of their mode shapes that are weighted by the corresponding generalised coordinates q_i:

$$\epsilon_T(x,y,z,t) = \sum_{i=1}^{n} \left[\left(-c_z(x,y,z)\frac{\partial^2 \phi_{z_j}}{\partial y^2} + c_x(x,y,z)\frac{\partial^2 \phi_{x_j}}{\partial y^2} \right) q_i(t) \right] \tag{4.4.15}$$

In both cases (Eq. 4.4.13 and Eq. 4.4.15), the curvature term needs to be calculated. Depending on the method numerical errors can be introduced. This is described and compared using (1) a variety of interpolations methods, (2) Chebyshev functions and (3) finite difference formulation. Before the curvature term is calculated the data points (displacement or mode shape) have to be interpolated so that each point is equidistant because the FE spanwise node distribution is not uniform. It is necessary to obtain a smooth and continuous curve since small discontinuities are amplified after formulating the second derivative. The Matlab function `fnder` was used to determine the second derivative in combination with `ppval` to evaluate each piecewise polynomial at the query point. Figure 4.19 shows that the strain mode shape ψ is dependent on the number of interpolation points p, as well as the interpolation method, such as *linear*, *pchip*, or *spline*. *Linear* and *pchip* interpolation methods yield large discontinuities for a high number of p. The spline interpolation, on the other hand, is less affected by the number of interpolation points and yields improved result for the strain mode shape approximation. Yet, for $n = 50$ or $n = 100$ there is a discontinuity observable at around 27% rotor radius that is the transition between cuff and aerofoil profile.

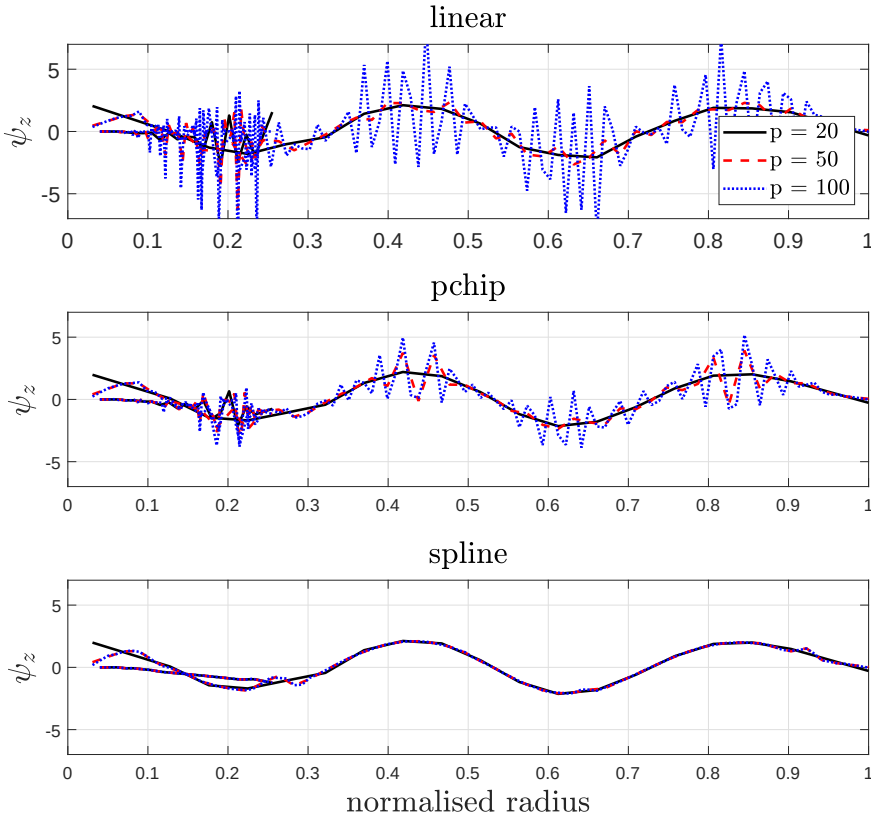

Figure 4.19: Dependency of strain mode shape ψ (Mode 5F) on the interpolation method and number of interpolation points p

Instead of applying Matlab's interpolation toolbox, the displacement mode shapes can be approximated with an open-source software application *Chebfun* [226]. The mathematical basis of *Chebfun* is a piecewise Chebyshev expansions [227]. The `polyfit` command was applied to the original data points, and as highlighted in Figure 4.20 its approximate reconstruction is dependent on the order of polynomials. For a more accurate calculation boundary conditions were introduced at each end, such that both have a curvature of zero because the strain is expected to be zero at the root and tip. The boundary conditions are as follows: $\psi(\bar{y}) = 0$ and $\psi(\underline{y}) = 0$ where $y \in [\bar{y}, \underline{y}]$ in which $\bar{y} = 0.11$ m (2.2% rotor radius) represents the blade root and $\underline{y} = 5.1$ m (100% rotor radius) reflects the blade tip. It was not possible to manually introduce this boundary condition to the *Chebfun* toolbox. This issue was circumvented by linearly extending each end so that the curvature would be as close as possible to zero. After approximating the displacement mode shape with *Chebfun* it was differentiated twice with respect to the span. The resulting strain mode shape (Mode 5F) is presented in Figure 4.21 for a number of interpolation points, highlighting the robustness of the result with regards to the number of interpolation points. The largest discrepancy is evident between 0-30% rotor radius.

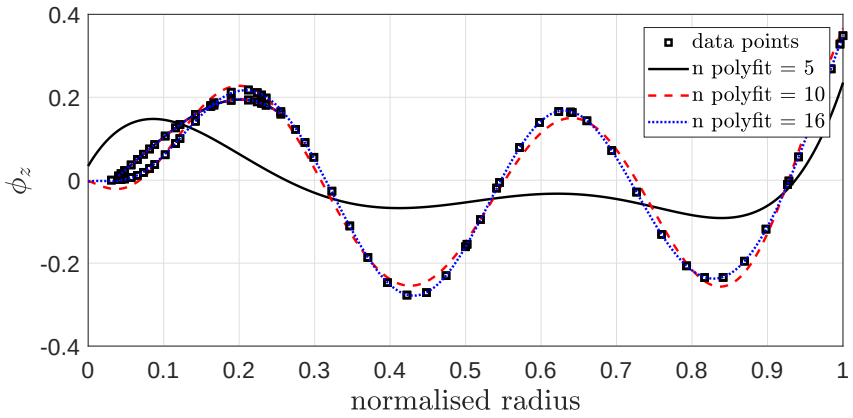

Figure 4.20: Displacement mode shape ϕ (Mode 5F) approximation using *Chebfun* polynomials

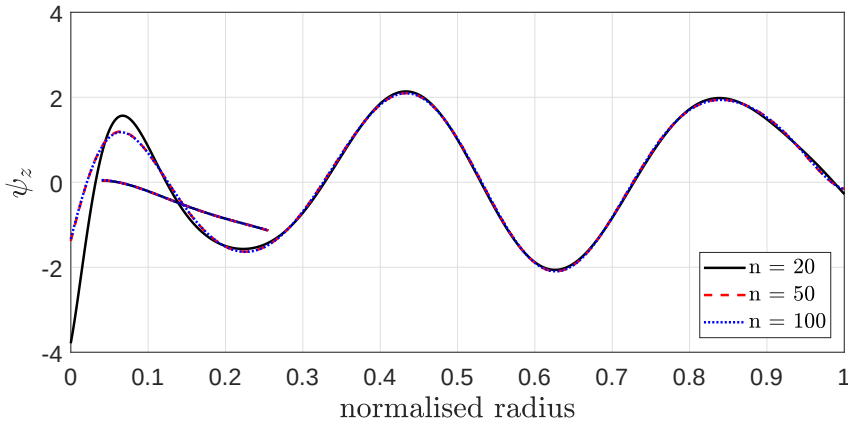

Figure 4.21: Dependency of strain mode shape ψ (Mode 5F) on number of interpolation points p using *Chebfun*

Another method for calculating the second derivative is through the central difference formulation (CDF). The benefit of this method is that the surface strain can be imple-

mented directly in the **C**-Matrix, which is the output matrix of the state-space formulation ($\mathbf{y} = \mathbf{Cx} + \mathbf{Du}$). The general definition of CDF is given by:

$$g''(x_0) = \frac{g(x_0 - \Delta x) - 2g(x_0) + g(x_0 + \Delta x)}{(\Delta x)^2} \tag{4.4.16}$$

where $g''(x_0)$ is the second derivative of function g calculated at point x_0, where Δx is the distance between adjacent backwards and forward nodal point. This method proved to be very efficient computationally. Figure 4.22 presents a schematic diagram of the variables for the derivation of strain with CDF. The second derivative is calculated at the query point i that is also the FE nodal point, while $i-1$ represents the nodal point before the query point, and $i+1$ is the nodal point after the query point. Because Δy is a constant value and the FE nodal points are non-uniform, a distance Δy is defined that is a small perturbation around the query point with $k-1$ and $k+1$. It should be noted that the spanwise position y and the displacement d values at any given nodal point i are known from the state-space solution.

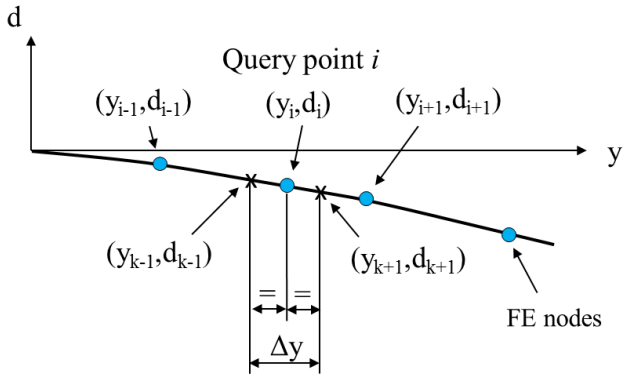

Figure 4.22: Definition of variables for CDF

The second derivative at at the query point (y_i, d_i) is given by:

$$\frac{\partial^2 d_i}{\partial y^2} = \frac{d_{k-1} - 2d_i + d_{k+1}}{(\Delta y)^2} \tag{4.4.17}$$

where d_{k-1} is the perturbed backward point and d_{k+1} the forward point, that were calculated adopting linear interpolation methods. With the assumption of linearity ($d = \beta y$) the backward displacement d_{k-1} can be calculated as follows:

$$\frac{d_{k-1} - d_{i-1}}{d_i - d_{i-1}} = \frac{\beta(y_{k-1} - y_{i-1})}{\beta(y_i - y_{i-1})} = \frac{y_{k-1} - y_{i-1}}{y_i - y_{i-1}} \tag{4.4.18}$$

where

$$y_{k-1} = y_i - \frac{1}{2}\Delta y \tag{4.4.19}$$

Substituting Eq. 4.4.19 into Eq. 4.4.18 and rearranging, d_{k-1} can be written:

$$d_{k-1} = d_{i-1} + (d_i - d_{i-1}) \underbrace{\left(\frac{y_i - \frac{1}{2}\Delta y - y_{i-1}}{y_i - y_{i-1}} \right)}_{y_b} \tag{4.4.20}$$

Similarly, the forward displacement d_{k+1} is derived:

$$\frac{d_{k+1} - d_i}{d_{i+1} - d_i} = \frac{y_{k+1} - y_i}{y_{i+1} - y_i} \tag{4.4.21}$$

where

$$y_{k+1} = y_i + \frac{1}{2}\Delta y \tag{4.4.22}$$

Substituting Eq. 4.4.22 into Eq. 4.4.21 and rearranging d_{k+1} is such that:

$$d_{k+1} = d_i + (d_{i+1} - d_i) \underbrace{\left(\frac{\frac{1}{2}\Delta y}{y_{i+1} - y_i} \right)}_{y_f} \tag{4.4.23}$$

Now, replacing displacement d with flapping displacement w and lagging displacement u in Eq. 4.4.17, and substituting Eq. 4.4.18 and Eq. 4.4.21 in Eq. 4.4.13, the surface strain ϵ_T is given by:

$$\begin{aligned} \epsilon_T = &- c_z \frac{w_{i-1} + (w_i - w_{i-1})y_b - 2w_i + w_i + (w_{i+1} - w_i)y_f}{(\Delta y)^2} \\ &+ c_x \frac{u_{i-1} + (u_i - u_{i-1})y_b - 2u_i + u_i + (u_{i+1} - u_i)y_f}{(\Delta y)^2} \end{aligned} \tag{4.4.24}$$

and after simplifying the equation becomes:

$$\begin{aligned} \epsilon_T = &- c_z \frac{w_{i-1}(1 - y_b) + w_i(y_b - 1 - y_f) + w_{i+1}y_f}{(\Delta y)^2} \\ &+ c_x \frac{u_{i-1}(1 - y_b) + u_i(y_b - 1 - y_f) + u_{i+1}y_f}{(\Delta y)^2} \end{aligned} \tag{4.4.25}$$

The equation above can now be written in matrix form ($\mathbf{y} = \mathbf{Cx}$), see Eq. 4.4.26. Finally, the various methods for computing the second derivative due to decoupled flapping and lagging displacement (gravitational case) are compared in Figure 4.23. The solid line represents the curvature term based on Eq. 4.4.13 using *Chebfun*, while the dotted line (CDF) utilises Eq. 4.4.17. The dashed line represents a summation of the mode shapes (MS) weighted by its generalised coordinate q_i (Eq. 4.4.15), also applying *Chebfun*.

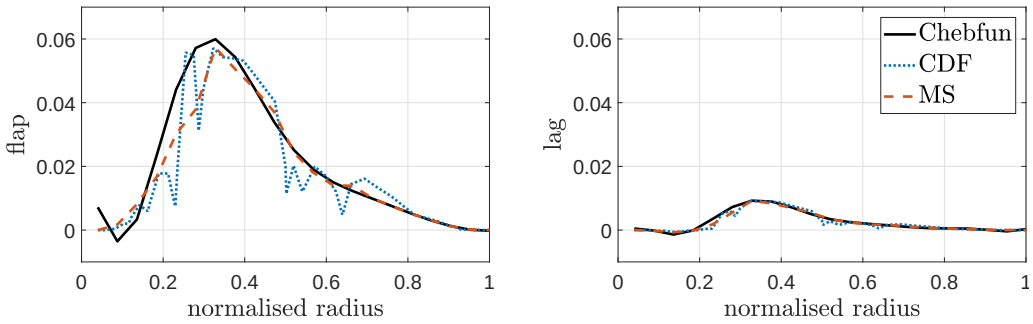

Figure 4.23: Comparison of curvature

The figure shows a variation in amplitude between the solid and dashed line, as well as a spanwise shift for the maximum peak. The CDF contains large discontinuities due to the non-uniform structural node distribution. Furthermore, a drop is observable at around 27% rotor radius for the dashed line. This stems from the discontinuity of the mode shapes between pitch control cuff and aerofoil section as a consequence of the adopted FE modelling principle: primary beam for flexbeam and aerofoil section and secondary beam for pitch control cuff. Each beam element experiences its dynamics, particularly evident for the higher modes, causing a discontinuity at the transition area between cuff and aerofoil section. As an outcome of this comparison the *Chebfun* based on Eq. 4.4.13 is used for the remainder of this work.

$$\mathbf{y} = \begin{bmatrix}
\frac{c_x(1-y_b)}{(\Delta y)^2} & 0 & 0 & 0 & 0 & 0 & \frac{c_x(y_b-1-y_f)}{(\Delta y)^2} & 0 & 0 & 0 & 0 & 0 & \frac{c_x y_f}{(\Delta y)^2} & 0 & 0 & 0 & 0 & \cdots \\
0 & 0 & 0 & 0 & 0 & 0 & 0 & 0 & 0 & 0 & 0 & 0 & 0 & 0 & 0 & 0 & 0 & \cdots \\
0 & 0 & -\frac{c_z(1-y_b)}{(\Delta y)^2} & 0 & 0 & 0 & 0 & 0 & -\frac{c_z(y_b-1-y_f)}{(\Delta y)^2} & 0 & 0 & 0 & 0 & 0 & -\frac{c_z y_f}{(\Delta y)^2} & 0 & 0 & \cdots \\
0 & 0 & 0 & 0 & 0 & 0 & 0 & 0 & 0 & 0 & 0 & 0 & 0 & 0 & 0 & 0 & 0 & \cdots \\
0 & 0 & 0 & 0 & 0 & 0 & 0 & 0 & 0 & 0 & 0 & 0 & 0 & 0 & 0 & 0 & 0 & \cdots \\
0 & 0 & 0 & 0 & 0 & 0 & 0 & 0 & 0 & 0 & 0 & 0 & 0 & 0 & 0 & 0 & 0 & \cdots \\
0 & 0 & 0 & 0 & 0 & 0 & \frac{c_x(1-y_b)}{(\Delta y)^2} & 0 & 0 & 0 & 0 & 0 & \frac{c_x(y_b-1-y_f)}{(\Delta y)^2} & 0 & 0 & 0 & 0 & \cdots \\
0 & 0 & 0 & 0 & 0 & 0 & 0 & 0 & 0 & 0 & 0 & 0 & 0 & 0 & 0 & 0 & 0 & \cdots \\
0 & 0 & 0 & 0 & 0 & 0 & 0 & 0 & -\frac{c_z(1-y_b)}{(\Delta y)^2} & 0 & 0 & 0 & 0 & 0 & -\frac{c_z(y_b-1-y_f)}{(\Delta y)^2} & 0 & 0 & \cdots \\
0 & 0 & 0 & 0 & 0 & 0 & 0 & 0 & 0 & 0 & 0 & 0 & 0 & 0 & 0 & 0 & 0 & \cdots \\
0 & 0 & 0 & 0 & 0 & 0 & 0 & 0 & 0 & 0 & 0 & 0 & 0 & 0 & 0 & 0 & 0 & \cdots \\
0 & 0 & 0 & 0 & 0 & 0 & 0 & 0 & 0 & 0 & 0 & 0 & 0 & 0 & 0 & 0 & 0 & \cdots \\
0 & 0 & 0 & 0 & 0 & 0 & 0 & 0 & 0 & 0 & 0 & 0 & \frac{c_x(1-y_b)}{(\Delta y)^2} & 0 & 0 & 0 & 0 & \cdots \\
0 & 0 & 0 & 0 & 0 & 0 & 0 & 0 & 0 & 0 & 0 & 0 & 0 & 0 & 0 & 0 & 0 & \cdots \\
0 & 0 & 0 & 0 & 0 & 0 & 0 & 0 & 0 & 0 & 0 & 0 & 0 & 0 & -\frac{c_z(1-y_b)}{(\Delta y)^2} & 0 & 0 & \cdots \\
0 & 0 & 0 & 0 & 0 & 0 & 0 & 0 & 0 & 0 & 0 & 0 & 0 & 0 & 0 & 0 & 0 & \cdots \\
0 & 0 & 0 & 0 & 0 & 0 & 0 & 0 & 0 & 0 & 0 & 0 & 0 & 0 & 0 & 0 & 0 & \cdots \\
\vdots & \vdots & \vdots & \vdots & \vdots & \vdots & \vdots & \vdots & \vdots & \vdots & \vdots & \vdots & \vdots & \vdots & \vdots & \vdots & \vdots & \ddots
\end{bmatrix}
\begin{bmatrix}
u_{i-1} \\ v_{i-1} \\ w_{i-1} \\ \rho_{i-1} \\ \eta_{i-1} \\ \mu_{i-1} \\ u_i \\ v_i \\ w_i \\ \rho_i \\ \eta_i \\ \mu_i \\ u_{i+1} \\ v_{i+1} \\ w_{i+1} \\ \rho_{i+1} \\ \eta_{i+1} \\ \mu_{i+1} \\ \vdots
\end{bmatrix} \tag{4.4.26}$$

4.4.4 Sensitivity study

The uncertainty of some structural properties as well as software limitations led to assumptions being made during the FE model development. A sensitivity study is presented that demonstrates the effect of material properties and structural centre locations on the dynamic characteristics. It should be noted, that each term is treated in isolation and does not reflect a true physical meaning of each spanwise element. Additionally, upper and lower uncertainty bounds are calculated for the surface strain due to the uncertainty of the neutral axis position.

By differentiating Eq. D.1.3 (see Appendix D.1.1) with respect to an updating parameter, and pre-multiplying by the mass normalised ϕ_j^T a expression for the eigenvalue sensitivity is obtained [228, 229]:

$$\frac{\partial \lambda_j}{\partial p_i} = \phi_j^T \left[\frac{\partial \mathbf{K}}{\partial p_i} - \lambda_j \frac{\partial \mathbf{M}}{\partial p_i} \right] \phi_j \tag{4.4.27}$$

where $p_i (i = 1, 2, ..., n)$ is the updating parameter and n is the number of structural nodes, $\lambda_j = \omega^2$ is the jth eigenvalue, ϕ_j is the jth mode shape. From Eq. 4.4.27 the eigenvalue sensitivity matrix $\mathbf{S}_\lambda$ can be obtained [228]:

$$\mathbf{S}_\lambda = \begin{bmatrix} \frac{\partial \lambda_1}{\partial p_1} & \frac{\partial \lambda_1}{\partial p_2} & \dots & \frac{\partial \lambda_1}{\partial p_n} \\ \frac{\partial \lambda_2}{\partial p_1} & \frac{\partial \lambda_2}{\partial p_2} & \dots & \frac{\partial \lambda_2}{\partial p_n} \\ \vdots & \vdots & \ddots & \vdots \\ \frac{\partial \lambda_m}{\partial p_1} & \frac{\partial \lambda_m}{\partial p_2} & \dots & \frac{\partial \lambda_m}{\partial p_n} \end{bmatrix} \tag{4.4.28}$$

where m is the number of used eigenvalues. A direct comparison between the sensitivity of each structural parameter to its mode can be obtained by scaling the sensitivity matrix by p_0/λ_0, where the original values are donated by the index '0' [228]:

$$\bar{\mathbf{S}}_\lambda = \begin{bmatrix} \frac{\partial \lambda_1}{\partial p_1} \frac{p_{0,1}}{\lambda_{0,1}} & \frac{\partial \lambda_1}{\partial p_2} \frac{p_{0,2}}{\lambda_{0,1}} & \dots & \frac{\partial \lambda_1}{\partial p_n} \frac{p_{0,n}}{\lambda_{0,1}} \\ \frac{\partial \lambda_2}{\partial p_1} \frac{p_{0,1}}{\lambda_{0,2}} & \frac{\partial \lambda_2}{\partial p_2} \frac{p_{0,2}}{\lambda_{0,2}} & \dots & \frac{\partial \lambda_2}{\partial p_n} \frac{p_{0,n}}{\lambda_{0,2}} \\ \vdots & \vdots & \ddots & \vdots \\ \frac{\partial \lambda_m}{\partial p_1} \frac{p_{0,1}}{\lambda_{0,m}} & \frac{\partial \lambda_m}{\partial p_2} \frac{p_{0,2}}{\lambda_{0,m}} & \dots & \frac{\partial \lambda_m}{\partial p_n} \frac{p_{0,n}}{\lambda_{0,m}} \end{bmatrix} \tag{4.4.29}$$

A similar study can be performed by investigating the influence of a change of structural parameter to its mode shape by applying the MAC sensitivity matrix $\mathbf{S}_{\Delta M}$:

$$\mathbf{S}_{\Delta M} = \begin{bmatrix} \frac{\partial \Delta M_1}{\partial p_1} & \frac{\partial \Delta M_1}{\partial p_2} & \dots & \frac{\partial \Delta M_1}{\partial p_n} \\ \frac{\partial \Delta M_2}{\partial p_1} & \frac{\partial \Delta M_2}{\partial p_2} & \dots & \frac{\partial \Delta M_2}{\partial p_n} \\ \vdots & \vdots & \ddots & \vdots \\ \frac{\partial \Delta M_m}{\partial p_1} & \frac{\partial \Delta M_m}{\partial p_2} & \dots & \frac{\partial \Delta M_m}{\partial p_n} \end{bmatrix} \tag{4.4.30}$$

where ΔM_m is the difference of analytical and experimental mode shape for m number

of identified modes. Again, the scaled MAC sensitivity $\bar{\mathbf{S}}_{\Delta M}$ was used to compare the impact of each structural parameter:

$$\bar{\mathbf{S}}_{\Delta M} = \begin{bmatrix} \frac{\partial \Delta M_1}{\partial p_1}\frac{p_{0,1}}{\Delta M_{0,1}} & \frac{\partial \Delta M_1}{\partial p_2}\frac{p_{0,2}}{\Delta M_{0,1}} & \cdots & \frac{\partial \Delta M_1}{\partial p_n}\frac{p_{0,n}}{\Delta M_{0,1}} \\ \frac{\partial \lambda_2}{\partial p_1}\frac{p_{0,1}}{\Delta M_{0,2}} & \frac{\partial \Delta M_2}{\partial p_2}\frac{p_{0,2}}{\Delta M_{0,2}} & \cdots & \frac{\partial \Delta M_2}{\partial p_n}\frac{p_{0,n}}{\Delta M_{0,2}} \\ \vdots & \vdots & \ddots & \vdots \\ \frac{\partial \Delta M_m}{\partial p_1}\frac{p_{0,1}}{\Delta M_{0,m}} & \frac{\partial \Delta M_m}{\partial p_2}\frac{p_{0,2}}{\Delta M_{0,m}} & \cdots & \frac{\partial \Delta M_m}{\partial p_n}\frac{p_{0,n}}{\Delta M_{0,m}} \end{bmatrix} \tag{4.4.31}$$

Both sensitivity terms provide some insight into the global properties and could be used for damage analysis [230]. Figure 4.24 shows the change of eigenvalue of the first eight modes caused by changes to the material properties, the torsional stiffness GJ, the out-of-plane bending stiffness EI_x, the in-plane bending stiffness EI_z, the longitudinal stiffness EA, the centre of mass cg, the neutral axis position na and, the non-structural mass moment of inertia NSI. For this study, the parameter values were increased in magnitude by Δp. The FE model consists of 80 structural nodes which are divided in flexbeam (nodes 1-23), aerofoil (nodes 24-59) and cuff (nodes 60-80). The cuff nodes are not shown due to a negligible effect. The eigenvalue sensitivities are all negative as $\partial \mathbf{K} = \mathbf{K} - \widehat{\mathbf{K}}$ and an increase in local stiffness results in a increased stiffness matrix $\widehat{\mathbf{K}}$, and hence, a negative $\bar{\mathbf{S}}_\lambda$.

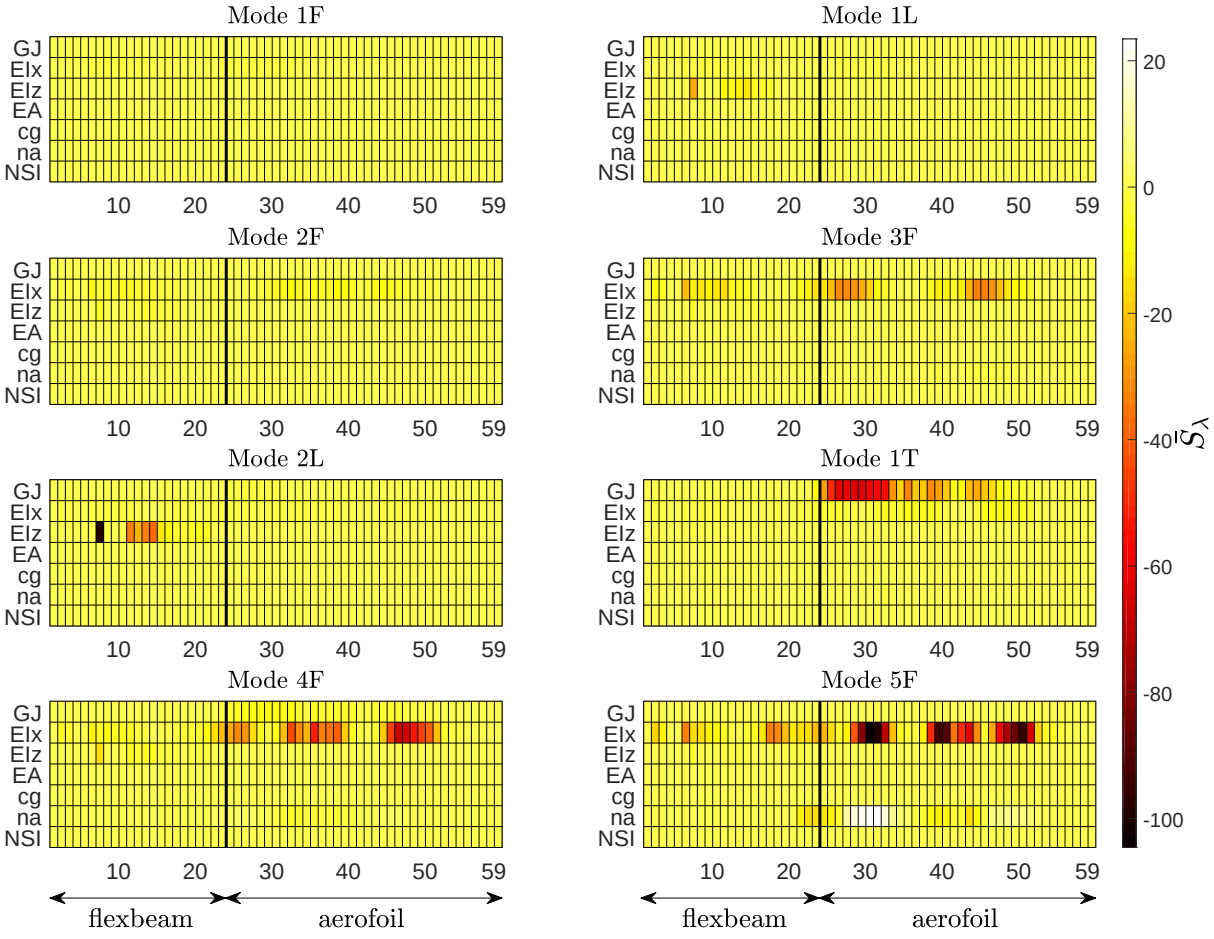

Figure 4.24: Scaled eigenvalue sensitivity $\bar{\mathbf{S}}_\lambda$

The results highlight that the structural properties are sensitive to a change in both bending stiffnesses and torsion stiffness, while changes in the location of the structural centres and the mass moment of inertias do not affect the eigenvalues significantly. In particular, out-of-plane bending stiffness EI_x affects Mode 3F-5F, while the first two flapping modes are barely affected. In comparison to the sensitivity of EI_z for the 2L mode at the flexbeam region, a change in GJ at the aerofoil section has a significant effect on Mode 1T. The increased eigenvalue sensitivity of 3F and 5F due to EI_x at the flexbeam positions indicates that the flapping hinge must be located between nodes 6-11, while the increased sensitivity of EI_z between node 11-16 points towards the lagging hinge position.

Some degree of similarity is noticeable between eigenvalue and MAC sensitivity analysis (Figure 4.25) because the eigenvalue is a function of the mode shape as stated in Eq. 4.4.27. The values obtained from the MAC sensitivity analysis are positive as $\partial \Delta M = MAC - M\hat{A}C$ for which MAC is assumed to be 1. Results suggest that the first three flapping and first lagging modes are very robust to structural variations, while a high sensitivity is evident for Mode 2L and 4F in particular to changes in cg location and GJ. The sensitivity of the modes due to torsion can be observed through the NSI input that contains the mass moment of inertia values, such as for 2L, 1T and 4F. In both sensitivity analyses, the structural properties are robust to longitudinal stiffness EA. Figure 4.25 also highlights the sensitivity of structural coupling behaviour, such as for Mode 2L that can be affected by changes in GJ. It is interesting to note that the modal properties are robust to a change of all the presented parameters in virtue of its high torsional stiffness in the pitch control cuff area, that is needed to transmit the required pitch angle due to pilot input.

Uncertainty in the neutral axis position leads to uncertainty in the total surface strain ϵ_T. It was assumed that the neutral axis of the rotor blade is located close to the quarter chord line, while approximately centred between the upper and lower surfaces. A sensitivity study was performed to calculate the upper and lower bounds if the neutral axis is shifted by a small percentage k along the x and z direction resulting in an increase or decrease of c_x and c_z. The sensitivity of the surface strain in flapping $\partial \epsilon_l / \partial d_{z_i}$ and lagging $\partial \epsilon_l / \partial d_{x_i}$ direction is calculated as follows:

$$\frac{\partial \epsilon_f}{\partial d_{z_i}} = -\frac{\partial c_{z_i}}{\partial d_{z_i}} \frac{\partial^2 w}{\partial y^2}, \quad \text{and} \quad \frac{\partial \epsilon_l}{\partial d_{x_i}} = \frac{\partial c_{x_i}}{\partial d_{x_i}} \frac{\partial^2 u}{\partial y^2} \tag{4.4.32}$$

Only variation of the neutral axes c_x and c_z in each ith nodal cross-section are considered and the curvature terms are assumed to be constant ensuring that the analysis is independent of the loading condition. The term ∂d_i is determined, such:

$$\partial d_{z_i} = c_{z_i} \pm \frac{k}{100} h_i, \quad \text{and} \quad \partial d_{x_i} = c_{x_i} \pm \frac{k}{100} c_i \tag{4.4.33}$$

where h_i is the thickness of the section and c_i is the chord at the ith cross-sectional nodal position. The upper and lower strain boundaries due to uncertainty in the neutral axis position are calculated as a function of rotor radius for ϵ_f and ϵ_l as shown in Figure 4.26(a) and Figure 4.26(b). A variation of $1\%h$ can result in a total error bound of above 500 $\mu\epsilon$, while a $0.04\%c$ yields an error bound of approximately 250 $\mu\epsilon$.

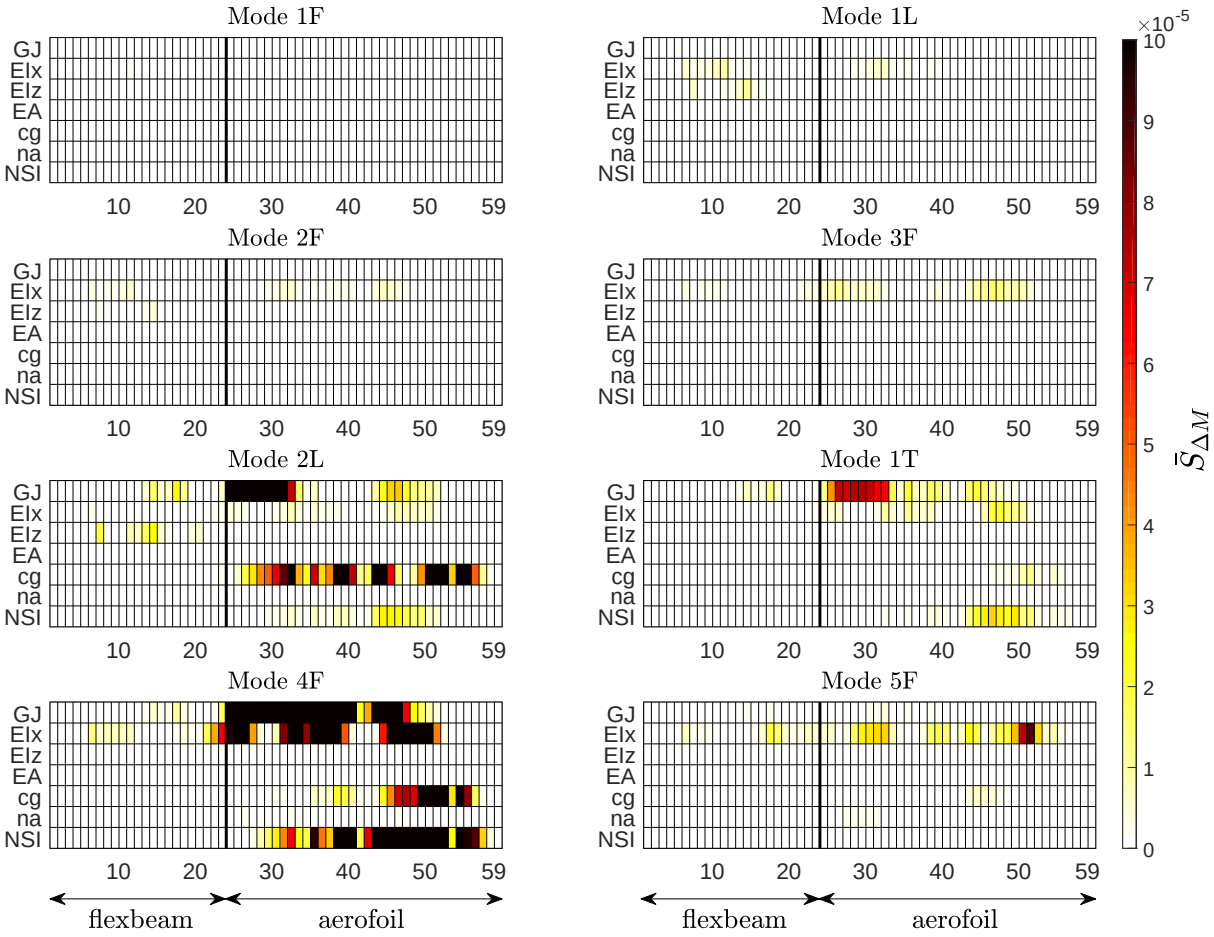

Figure 4.25: Scaled MAC sensitivity $\bar{\mathbf{S}}_{\Delta M}$

Further errors may be introduced during the sensor installation through misalignment in the chordwise direction. A study was undertaken by Suesse et al [9] who used a Monte-Carlo simulation to assess the sensitivity of the model's input to calculated bending moment or displacement. It was found that an error in the position of the FBG sensor had a considerable effect on bending stiffness and displacement results, while barely affecting the bending moment estimate. A simplified error analysis was performed in which the effect of sensor position error in the chordwise direction was calculated. Measurement errors of ± 4 mm was assumed, which includes errors due to marking the sensor position on the blade and positioning the ruler on the curved surface.

Figure 4.27 shows the upper strain error bound due to +4 mm and the lower bound due -4 mm sensor positioning. A sensor misalignment at the leading edge results in a higher error bound due to the gradient of the profile, while the error bound decreases at the quarter chordline of the profile. This stems from a nearly zero gradient at this location, and the neutral axis is assumed to be at this location. A jump of the upper error bound is observable at around 30% chord due to misalignment of the sensor of + 4 mm towards the trailing edge resulting in a profile gradient change.

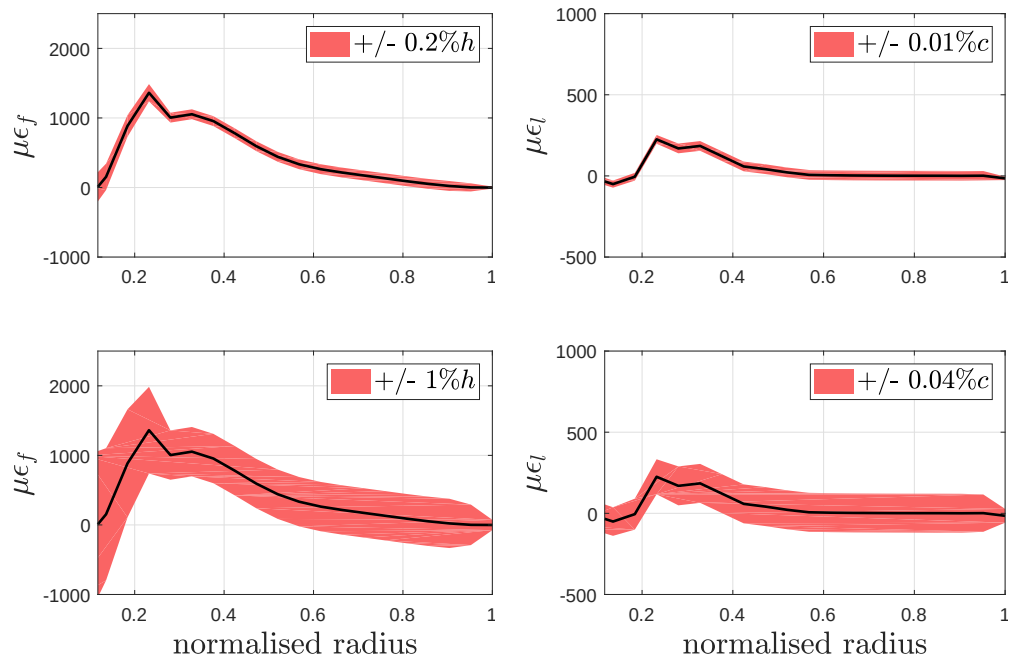

(a) Strain sensitivity due to neutral axis position in z-direction

(b) Strain sensitivity due to neutral axis position in x-direction

Figure 4.26: Strain sensitivity due to neutral axis location

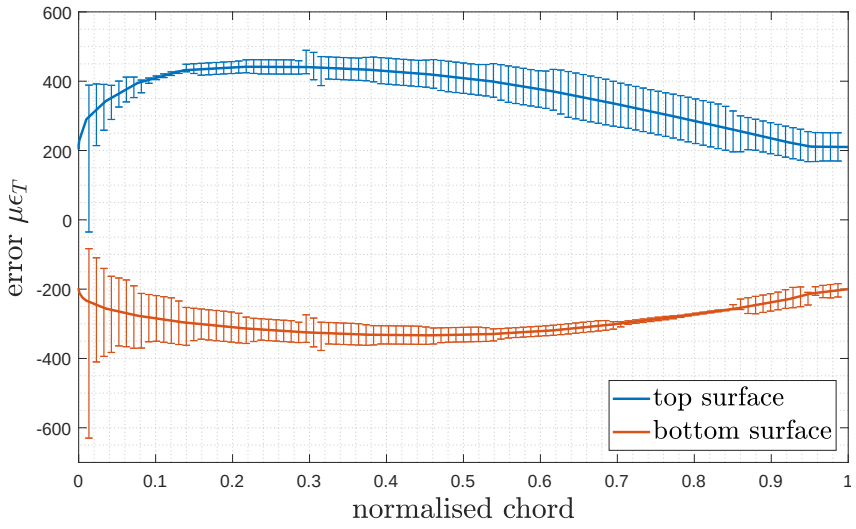

Figure 4.27: Effect of ±4 mm position error in chordwise direction

4.5 Aerodynamic model

An advanced inflow and aerodynamic model was developed to estimate the forces and moments for each blade element of the structural model. The model components and interconnections are outlined in Figure 4.28. Control input and blade dynamics are used as direct inputs from which the total pitch angle and total element velocities are determined. The induced inflow components are dependent on the rotor dynamics and are calculated from the total rotor forces and moments acting on the hub. Angles of

attack and inflow angles are determined with the use of geometric relationships alongside a linear model [79] based on blade element theory. Lift, drag and pitching moments are estimated using 2D aerofoil data, while lookup tables for the coefficient of lift, drag and pitching moment were created using the commercially available 2D aerodynamics program called VGK [231].

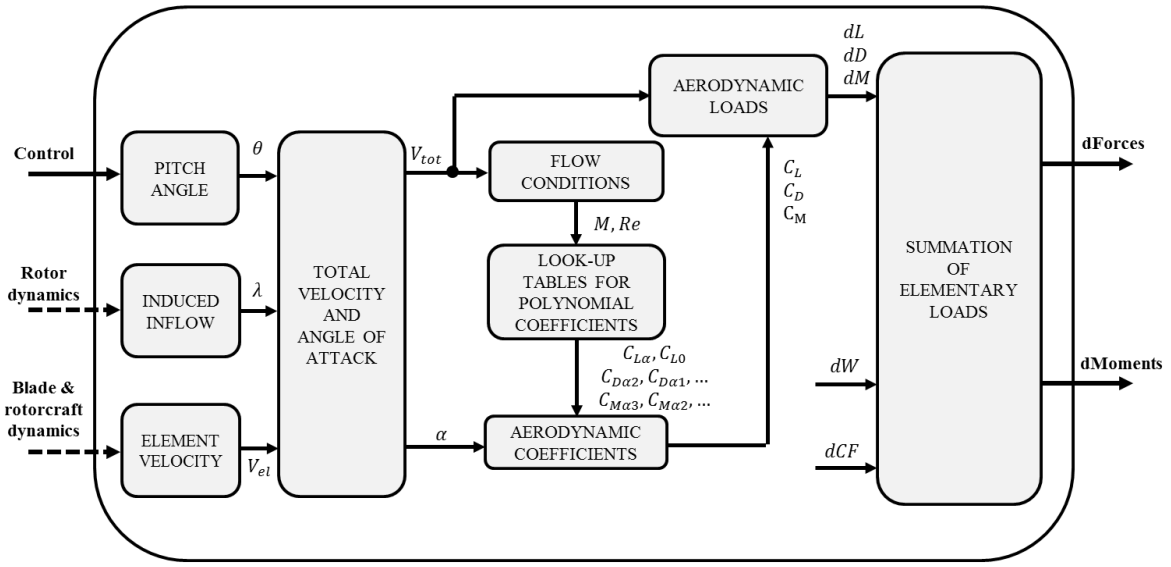

Figure 4.28: Flow chart of the aerodynamic analysis process

The induced inflow velocity is computed using the quasi-steady dynamic inflow model in combination with momentum theory developed by Pitt and Peters [81] and re-written by Peters and HaQuang [83] for practical applications, and corrected by Basset [232] to take into account tip loss and wake effects. The non-linear dynamic inflow with respect to the rotor disc plane is given by [83]:

$$\begin{bmatrix} \dot{\lambda}_0 \\ \dot{\lambda}_s \\ \dot{\lambda}_c \end{bmatrix} = -\mathbf{M}^{-1}\hat{\mathbf{L}}^{-1} \begin{bmatrix} \lambda_0 \\ \lambda_s \\ \lambda_c \end{bmatrix} + \mathbf{M}^{-1} \begin{bmatrix} C_T \\ C_{L_H} \\ -C_{M_H} \end{bmatrix} \tag{4.5.1}$$

where C_T, C_{L_H} and C_{M_H} are the instantaneous rotor thrust, roll and pitching moments coefficients in $\mathcal{F}_H$. $\mathbf{M}$ is defined as the matrix of apparent mass terms and $\hat{\mathbf{L}}$ is the inflow gains matrix. A derivation of the inflow model can be found in Appendix E. An example of the time domain behaviour of the uniform rotor inflow coefficients for hover is presented in Figure 4.29. The lateral inflow λ_s and longitudinal inflow λ_c are not shown as they are null for hover condition. Goaonkar [100] showed that a typical value for the uniform inflow is approximately 0.07, while a value of 0.054 is obtained here for trimmed hover condition.

Before the angle of attack on each blade element is determined, the element velocities relative to free-stream are calculated. Figure 4.30 shows a schematic diagram of the different velocity components due to blade dynamics (V1), tangential velocity on rotor blade (V2), rigid-body velocities in the hub reference system (V3), and the tangential velocity due to rigid-body angular rates (V4).

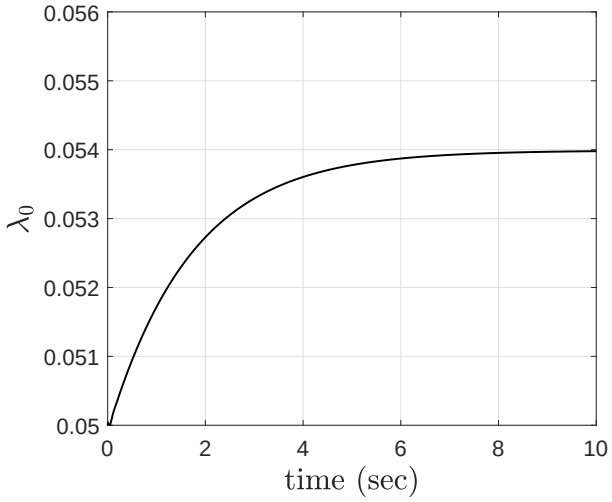

Figure 4.29: Variation of inflow coefficients in hover (pitch angles: $\theta_0 = 7.4°, \theta_{1s} = 0°, \theta_{1c} = 0°$)

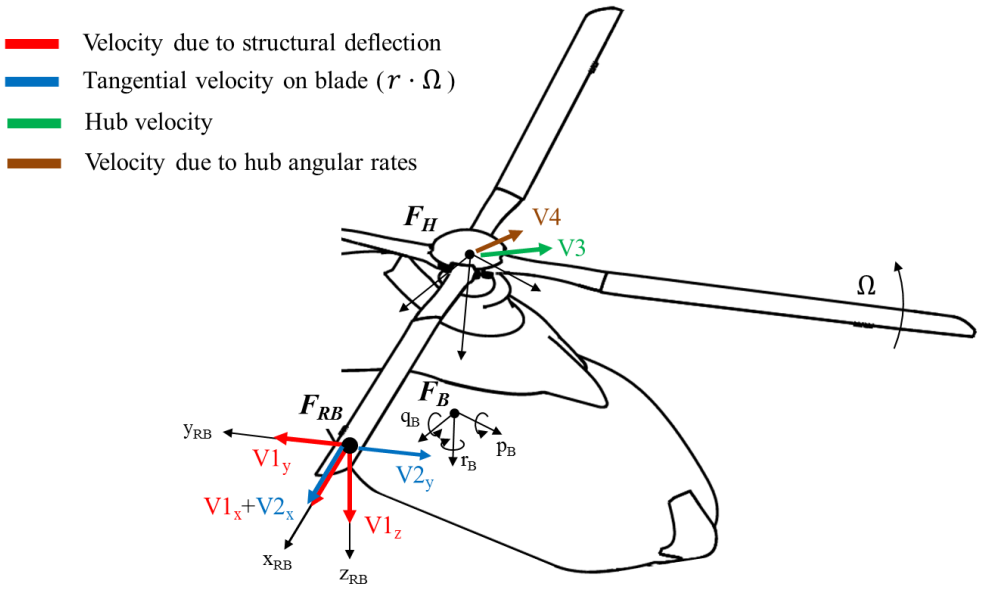

Figure 4.30: Schematic breakdown of velocities acting on main rotor

The overall total element velocity $V_{el_{RB}}$ is calculated at the aerodynamic node located at the centre of each blade element and is expressed as follows:

$$V_{el_{RB}} = V_{el_{RB_1}} + V_{el_{RB_2}} + V_{el_{RB_3}} + V_{el_{RB_4}} \tag{4.5.2}$$

The velocity $V_{el_{RB_1}}$ stems from each node's structural deformation:

$$V_{el_{RB_1}} = \begin{bmatrix} V_{el_x} \\ V_{el_y} \\ V_{el_z} \end{bmatrix} \tag{4.5.3}$$

where V_{el_x}, V_{el_y}, V_{el_z} are the structural velocity at each aerodynamic node. $V_{el2_{RB}}$ represents the dominant velocity term that results from the tangential velocity due to main rotor rotation:

$$V_{el_{RB_2}} = -\begin{bmatrix} r + u_{el_{RB}} \\ v_{el_{RB}} \\ w_{el_{RB}} \end{bmatrix} \times \begin{bmatrix} 0 \\ 0 \\ -\Omega \end{bmatrix} \tag{4.5.4}$$

where r is the radial position for each node, while $u_{el_{RB}}$, $v_{el_{RB}}$, $w_{el_{RB}}$ are the structural deformation on each node, and Ω is defined as the rotor idle speed. The sign convention in Eq. 4.5.4 ensures that the velocity vector V_{el2_y} of the rotating blade points in the direction as shown in Figure 4.30, which corresponds to the direction of the moving blade. The third term $V_{el_{RB_3}}$ stems from the body velocity converted into hub velocity in $\mathcal{F}_H$. The following equation is used to transform V_H to $\mathcal{F}_{RB}$ using Eq. 4.2.2:

$$V_{el_{RB_3}} = D_H^{RB} V_H \tag{4.5.5}$$

The last term $V_{el_{RB_4}}$ of Eq. 4.5.2 is the tangential velocity due to the fixed body's angular rates, roll rate, p, pitch rate, q, and yaw rate, r, transferred to $\mathcal{F}_{\mathcal{RB}}$.

$$V_{el_{RB_4}} = -\left\{ \begin{bmatrix} r + u_{el_{RB}} \\ v_{el_{RB}} \\ w_{el_{RB}} \end{bmatrix} + D_H^{RB} \overline{O_{\mathcal{F}_B} O_{\mathcal{F}_H}} \right\} \times D_H^{RB} \begin{bmatrix} p_H \\ q_H \\ r_H \end{bmatrix} \tag{4.5.6}$$

where $\overline{O_{\mathcal{F}_B} O_{\mathcal{F}_H}}$ is the distance from the body centre of gravity to the centre of the hub. Once all velocity components are determined and summed up to $V_{el_{RB}}$, these are referred to $\mathcal{F}_N$ using the following transformation:

$$V_{el_N} = D_{RB}^N V_{el_{RB}} \tag{4.5.7}$$

The induced inflow is given by [40]:

$$v_i = \lambda_i \Omega R \tag{4.5.8}$$

and substituting into Eq. E.0.13. The induced inflow velocity v_{i_H} is a function of the inflow coefficients λ_0, λ_s, and λ_c obtained from the dynamic inflow model:

$$v_{i_H} = \left(\lambda_0 + \lambda_s \frac{r}{R} \sin(\Psi + \Delta) + \lambda_c \frac{r}{R} cos(\Psi + \Delta) \right) \Omega R \tag{4.5.9}$$

and referred to $\mathcal{F}_N$:

$$v_{i_N} = D_{RB}^N D_H^{RB} \begin{bmatrix} 0 \\ 0 \\ v_{i_H} \end{bmatrix} \tag{4.5.10}$$

The element inflow angle ϕ_i and the element angle of attack α_i can be determined now. Figure 4.31 illustrates the relationship between the velocities and loads on an aerofoil. The elementary lift force dL is perpendicular and the elementary drag force dD is parallel to the total velocity V. These forces, as well as the elementary pitching moment dM, are acting on the aerodynamic centre that is the quarter chord line of an aerofoil.

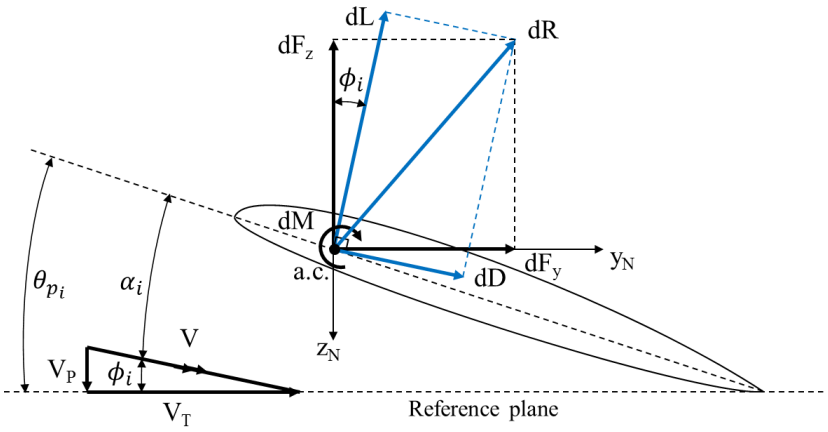

Figure 4.31: Conditions at the blade element (reproduced from Reference [79])

The resultant speed V on the blade element at each radial station from the centre of rotation has an out-of-plane component V_P that is calculated as follows:

$$V_P = V_{el_{N_z}} - v_{i_{N_z}} \tag{4.5.11}$$

The in-plane component V_T is given by:

$$V_T = V_{el_{N_y}} - v_{i_{N_y}} \tag{4.5.12}$$

Finally, the resultant blade velocity V for each node can be written as:

$$V = \sqrt{V_P^2 + V_T^2} \tag{4.5.13}$$

From simple geometrical relationships the inflow angle ϕ_i is defined:

$$\phi_i = \tan^{-1}\left(\frac{V_P}{V_T}\right) \tag{4.5.14}$$

and the effective angle of attack α is:

$$\alpha_i = \theta_{p_i} - \phi_i \tag{4.5.15}$$

Figure 4.32 presents the model predicted angle of attack over one revolution of the blade. Figure 4.32(a) shows the angle of attack due to a collective pilot input η_1, corresponding to a hover case assuming 0° shaft tilt angle. A uniformly circular outboard distributed

angle of attack is observed meaning that the same amount of force is produced by each blade for each moment of time. It should be noted that the wake of the preceding blades is ignored. Figure 4.5(b) shows the angle of attack after a combined cyclic longitudinal η_{1s} and lateral pilot input η_{1c} is introduced. As already demonstrated in the pilot map a coupled input is necessary to obtain a pure pitch or roll control of the helicopter [40]. Figure 4.5(b) demonstrates that the highest angle of attack is concentrated at the left of the rotor disc plane, at around 280° azimuth position. From the description about phase lag phenomena in Section 4.3, it is clear that the blade response will act approximately 90° later, which produces a nose-down attitude of the helicopter and therefore, a tilt of the tip path plane in the forward direction. Figure 4.33 illustrates that the rotor thrust T is always perpendicular to the rotor disc and a forward component F_x is produced. This is responsible for the forward flight motion of the helicopter.

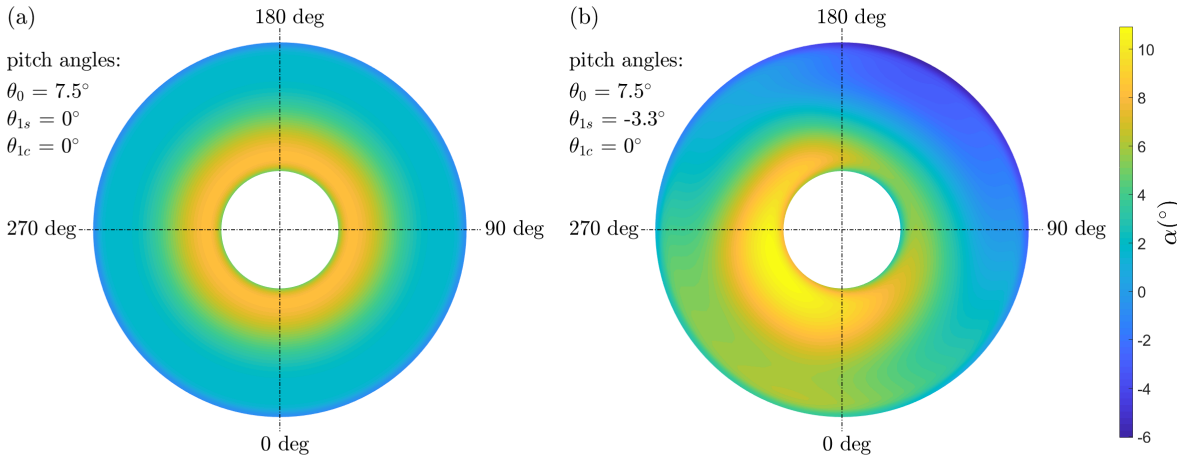

Figure 4.32: Azimuthal variation of α

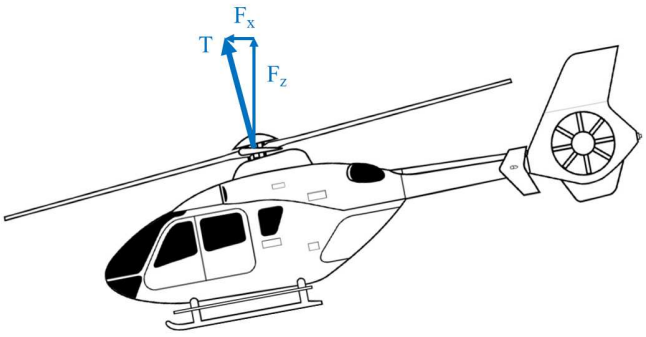

Figure 4.33: Force components on rotor hub in forward flight

The aerodynamic coefficients, such as $C_l(\alpha)$, $C_d(\alpha)$ and $C_m(\alpha)$, are calculated relative to the effective angle of attack, such that:

$$C_l(\alpha) = C_{l_\alpha}\alpha + C_{l_0} \tag{4.5.16}$$

$$C_d(\alpha) = C_{d_{\alpha 2}}\alpha^2 + C_{d_\alpha}\alpha + C_{d_0} \tag{4.5.17}$$

$$C_m(\alpha) = C_{m_{\alpha 3}}\alpha^3 + C_{m_{\alpha 2}}\alpha^2 + C_{m_{\alpha 1}}\alpha + C_{m_0} \tag{4.5.18}$$

These aerodynamic coefficients are dependent on Mach and Reynolds numbers and change with density, velocity, and fluid viscosity. The relationship between Reynolds number and Mach number is given by:

$$Re = \frac{\rho c V}{\mu} \tag{4.5.19}$$

where ρ is the air density, c is the chord, V is total velocity and, ν represents the dynamic viscosity of the air. The highest values occur at the blade tip with Ma = 0.58 and Re = $4 \cdot 10^6$. The values for C_l, C_d, and C_m were created with the open-source software VGK [231], which is a two-dimensional computational fluid dynamics method for predicting aerodynamic characteristics of an aerofoil in a subsonic free stream. It includes the effects of viscosity (boundary layers) and shock waves. Lookup tables were created ensuring the coverage of a wide range of data points [233], followed by linear interpolation to obtain the polynomial coefficients for each flow condition. Figure 4.34 shows the variation of the aerodynamic coefficients with angle of attack. For clarity, data corresponding to $M = 0.3$ is plotted in red. As expected, the lift coefficient C_l increases for high Mach numbers and for high angles of attack and the pitching moment coefficient C_m is negative as a cambered aerofoil is used [79]. For low angles of attack and small Mach numbers the absolute value of drag coefficient C_d and pitching moment coefficient C_m increase.

The divergence of C_d and C_m for high angles of attack arise from the polynomial coefficient approximations as shown in Figure 4.35. Note, that the calculated data point for $\alpha = 6°$ is faulty. Although stall is not taken into account, it is assumed that at $\alpha = 8.5°$ the flow starts to separate because VGK can only produce results for attached flow. Leishman [79] shows that for cambered aerofoils, such as SC 1095, the maximum lift coefficient C_l is obtained for $\alpha = 15°$. Finally, the elementary lift force dL, drag force dD, and pitching moment dM are calculated:

$$dL = \frac{1}{2}\rho V^2 l_{el} c C_l(\alpha) \tag{4.5.20}$$

$$dD = \frac{1}{2}\rho V^2 l_{el} c C_d(\alpha) \tag{4.5.21}$$

$$dM = \frac{1}{2}\rho V^2 l_{el} c^2 C_m(\alpha) \tag{4.5.22}$$

where l_{el} is the spanwise length of an element and c is the chord. These forces and moments act on the aerodynamic nodes that are centred between the element borders. Figure 4.36 shows the predicted lift force, drag force and pitching moment distributions normalised to the maximum lift. As expected the maximum lift is expected at around 90% of the rotor radius.

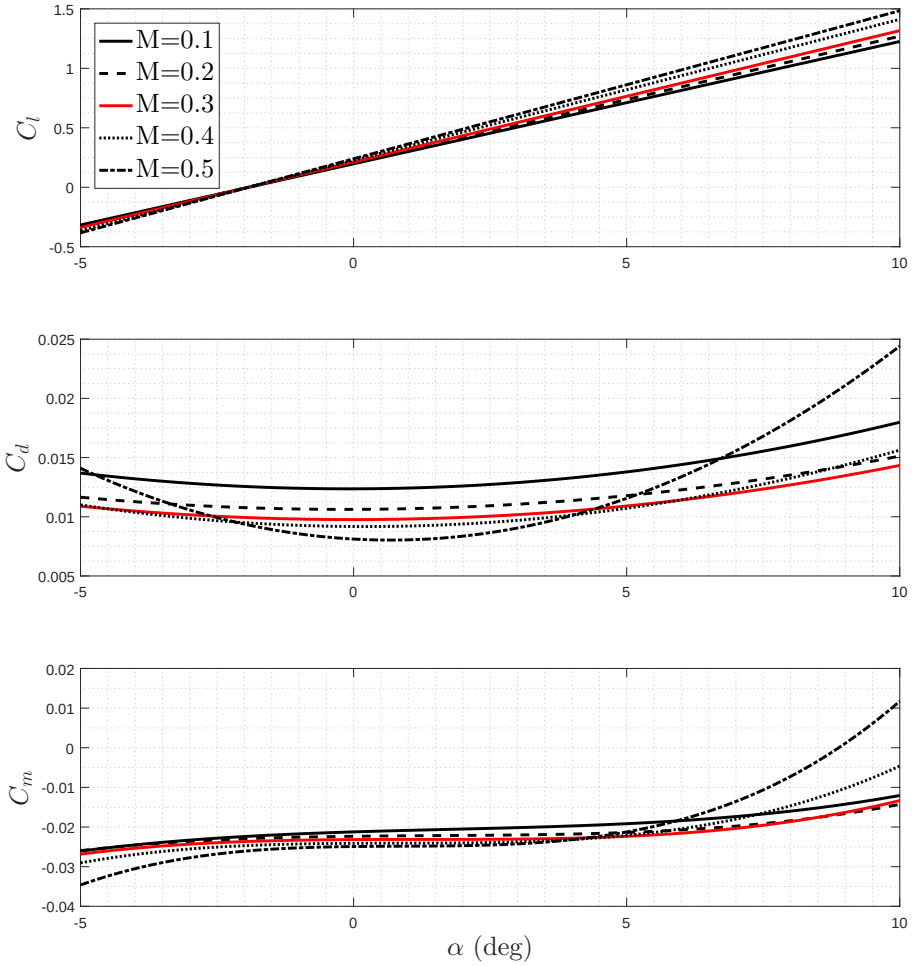

Figure 4.34: Variation of aerodynamic coefficients with the change of Mach numbers (data was reproduced from Reference [233])

The elementary lift and drag force has to be transformed to $\mathcal{F}_N$, with a rotation around the pitch axis (x-axis), such that:

$$\begin{bmatrix} 0 \\ dF_{N_y} \\ dF_{N_z} \end{bmatrix} = \begin{bmatrix} 1 & 0 & 0 \\ 0 & \cos\phi_i & -\sin\phi_i \\ 0 & -\sin\phi_i & -\cos\phi_i \end{bmatrix} \begin{bmatrix} 0 \\ dD \\ dL \end{bmatrix} \tag{4.5.23}$$

The pitching moment is not affected by this rotation because it is a moment around the pitch axis. Then the forces and pitching moment are expressed in $\mathcal{F}_{RB}$:

$$\begin{bmatrix} dF_{RB_x} \\ dF_{RB_y} \\ dF_{RB_z} \end{bmatrix} = (D_{RB}^N)^{-1} \begin{bmatrix} 0 \\ dF_{N_y} \\ dF_{N_z} \end{bmatrix} \tag{4.5.24}$$

and

$$\begin{bmatrix} dM_{RB_x} \\ dM_{RB_y} \\ dM_{RB_z} \end{bmatrix} = (D_{RB}^N)^{-1} \begin{bmatrix} dM \\ 0 \\ 0 \end{bmatrix} \tag{4.5.25}$$

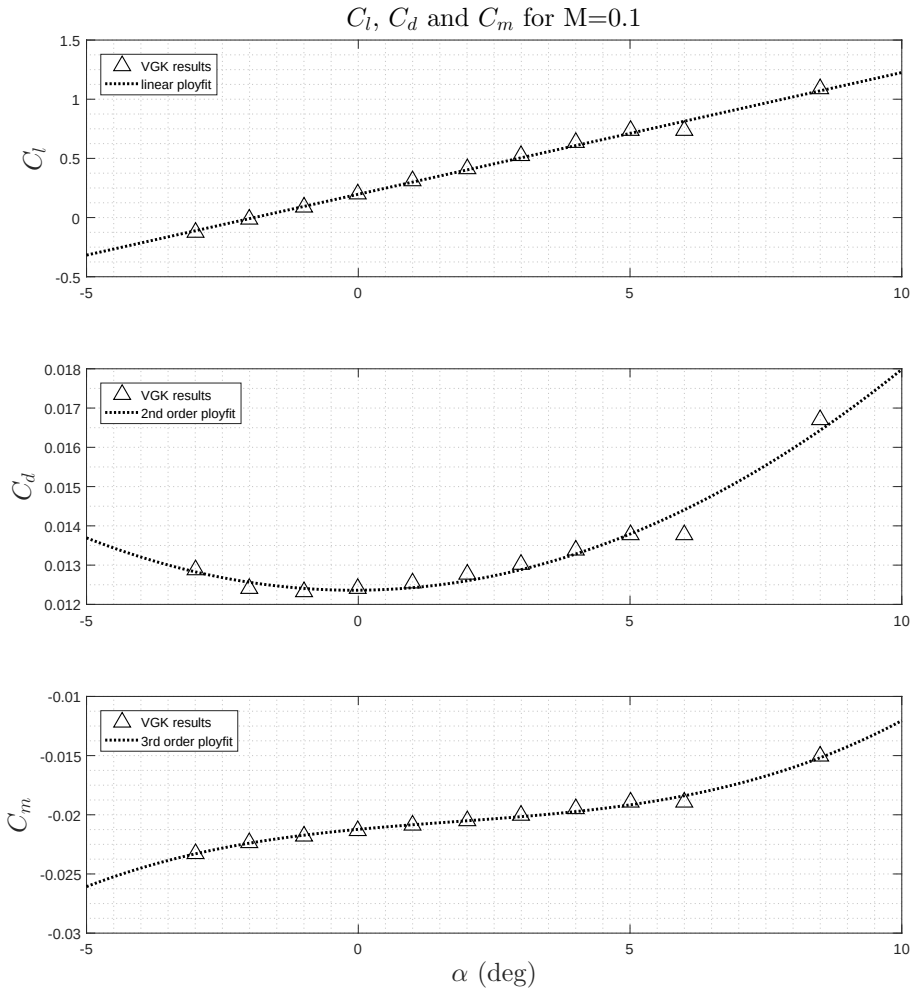

Figure 4.35: Polynomial coefficient approximations for $M = 0.1$ (data was reproduced from Reference [233])

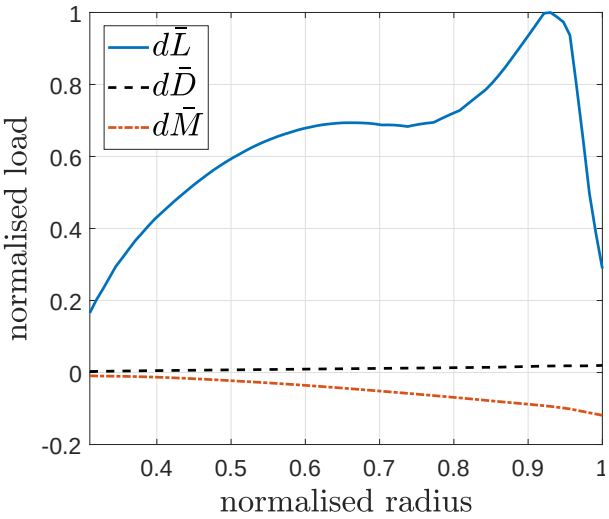

Figure 4.36: Normalised aerodynamic load distribution (pitch angles: $\theta_0 = 7.4°, \theta_{1s} = 0°, \theta_{1c} = 0°$, plotted at time $t = 10sec$)

4.6 Structural and aerodynamic coupling

The rotor blade structural, inertial, and aerodynamics must be coupled to analyse the blade dynamics. This was done through the time-domain inflow model, evaluated at the structural nodal points. The structural dynamics were obtained from the state-space representation as explained in Section 4.4.2. A trimmed state is obtained by adjusting the pilot control so that zero body forces and moments are maintained. One drawback with the implemented structural model is that although the aerodynamic forces and moments are calculated at each time step, the internal structural loading through pre-stressed modal analysis is not re-iterated as it would result in a high computational cost. However, it is assumed that this effect is relatively small for the hover condition.

4.6.1 Convergence study

A node adaption process was necessary as the structural and aerodynamic models have different node distributions. While the structural nodes are non-uniform as a consequence of the data set from AHD, a uniform node distribution was implemented for the aerodynamic model. The interaction between aerodynamics and structural mechanics are managed by transferring the load acting on each blade element from the structural to the aerodynamic node system. This is done before and after the inflow analysis. Figure 4.37 illustrates the definition of a structural section that is defined as the half distances of its two adjacent nodes. All aerodynamic nodes within this structural section are summed up and applied to its corresponding structural node.

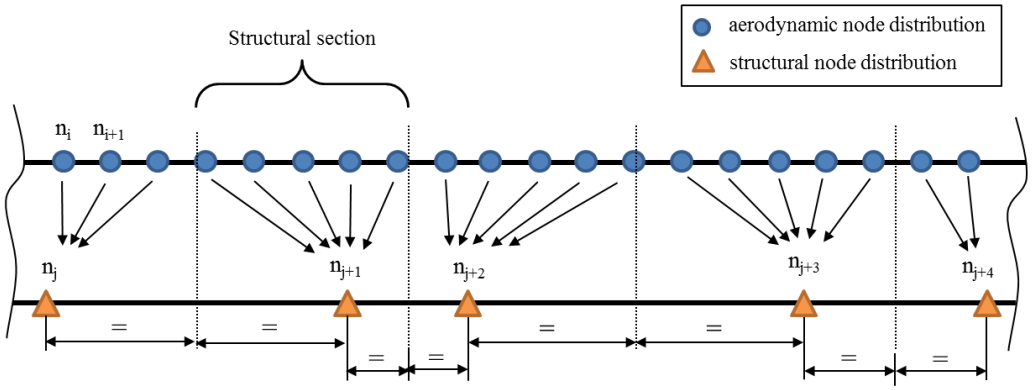

Figure 4.37: Node adaption process

Depending on the number of aerodynamic nodes, the nodal lift force within a particular structural section is not always constant. A convergence study was done to investigate the influence of the number of aerodynamic nodes N_{AD} on the overall predicted rigid body forces and moments (see Figure 4.38). For $N_{AD} > 40$ the solution converges and the resulting change of total load due to sparse and dense aerodynamic node distributions is negligibly small. This is confirmed in Table 4.2 which shows the percentage difference between the minimum and maximum predicted forces and moments. The highest variation between upper and lower bound for $N_{AD} > 40$ is 3.11 % for the F_y force.

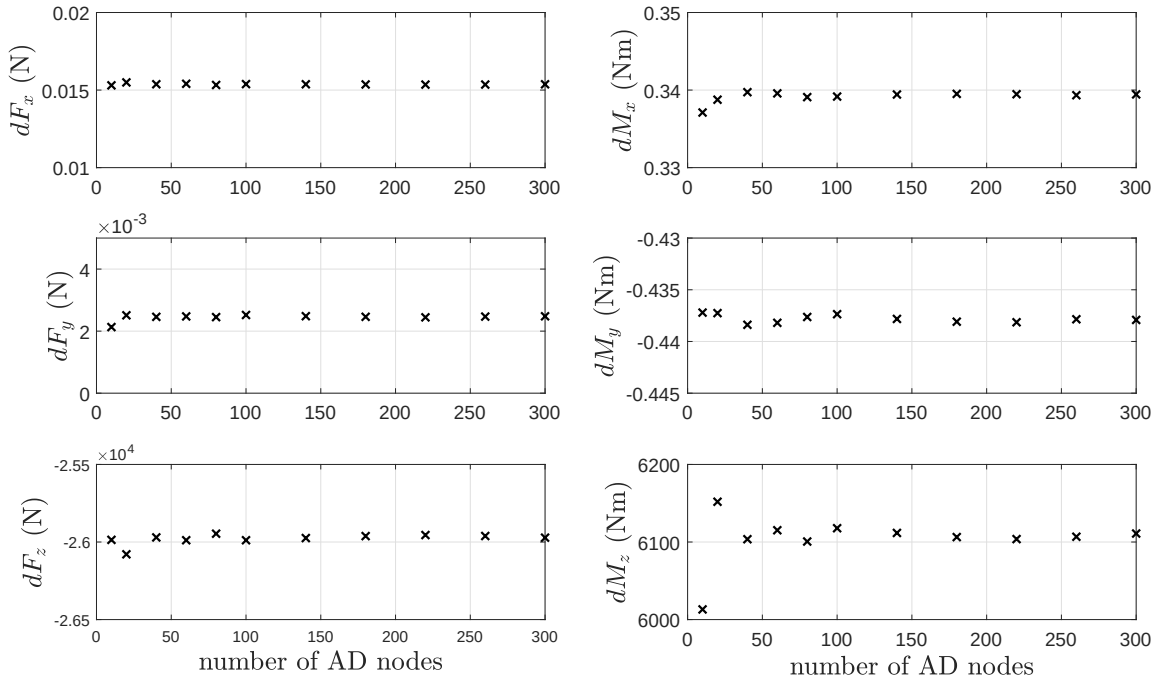

Figure 4.38: Investigation of impact of the number of aerodynamic nodes on overall forces and moments

Table 4.2: Percentage difference between the minimum and maximum load value

Load	Difference in %
dF_x	0.50
dF_y	3.11
dF_z	0.16
dM_x	0.14
dM_y	0.19
dM_z	0.28

A low number of aerodynamic nodes compared to a dense node distribution does not change the overall body forces and moments significantly. This finding is important to ensure a low computational cost for the simulation. A comparison of the structural load using 50, 60, 70 and 80 aerodynamic nodes is plotted in Figure 4.39. An overall trend is obtained, with large discontinuities depending on the number of aerodynamic nodes. A locally enhanced load could lead to different total structural deflections depending on the number of aerodynamic nodes. Results highlighted insignificant structural deviation due to the studied node distribution. From this outcome, 50 aerodynamic nodes were chosen.

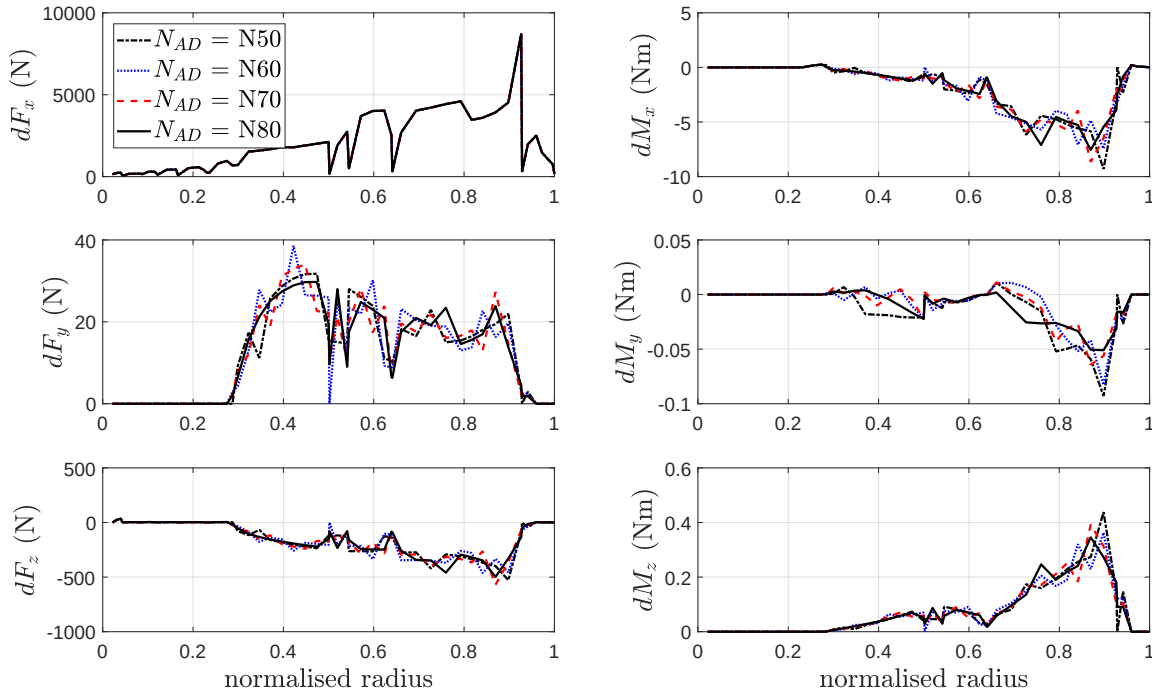

Figure 4.39: Impact of number of aerodynamic nodes on structural load

4.6.2 Summation of forces and moments

After the node adaptation process the elementary force due to gravitational force and centrifugal force is included. The distance between structural centre (which is equal to the shear centre and aerodynamic centre) and the centre of gravity is taken into account in order to apply force due to gravity effects:

$$dW_{RB} = D_H^{RB} D_B^H D_I^B \begin{bmatrix} 0 \\ 0 \\ gm_{el} \end{bmatrix} \tag{4.6.1}$$

where g is the gravitational constant and m_{el} is the mass of each blade element. In addition, a torsional moment due to the centre of gravity offset is included for each node:

$$dW_{M_{RB}} = d_y dW_{RB} \tag{4.6.2}$$

where d_y is the distance between shear centre and centre of gravity. The centrifugal force is calculated as follows:

$$dF_{C_{RB}} = rm_{el}\Omega^2 \tag{4.6.3}$$

The gravitational dW_{RB} and centrifugal forces $dF_{C_{RB}}$ are added to the forces dF_{RB} of each node:

$$dF_{RB} = dF_{RB} + dW_{RB} + dF_{C_{RB}} \tag{4.6.4}$$

and the structural moments are summed:

$$dM_{RB} = \begin{bmatrix} dM_{RB_x} \\ dM_{RB_y} \\ dM_{RB_z} \end{bmatrix} + \begin{bmatrix} dW_{M_{RB}} \\ 0 \\ 0 \end{bmatrix} \tag{4.6.5}$$

Due to the force acting on each node, a moment is induced as shown in Figure 4.40. This is given by:

$$dM_{F_{RB}} = \begin{bmatrix} r - x_{el_{RB}} \\ y_{el_{RB}} \\ z_{el_{RB}} \end{bmatrix} dF_{RB_z} \tag{4.6.6}$$

where r is the radial position for each node and where $x_{el_{RB}}$, $y_{el_{RB}}$, $z_{el_{RB}}$ are the structural deformation on each node.

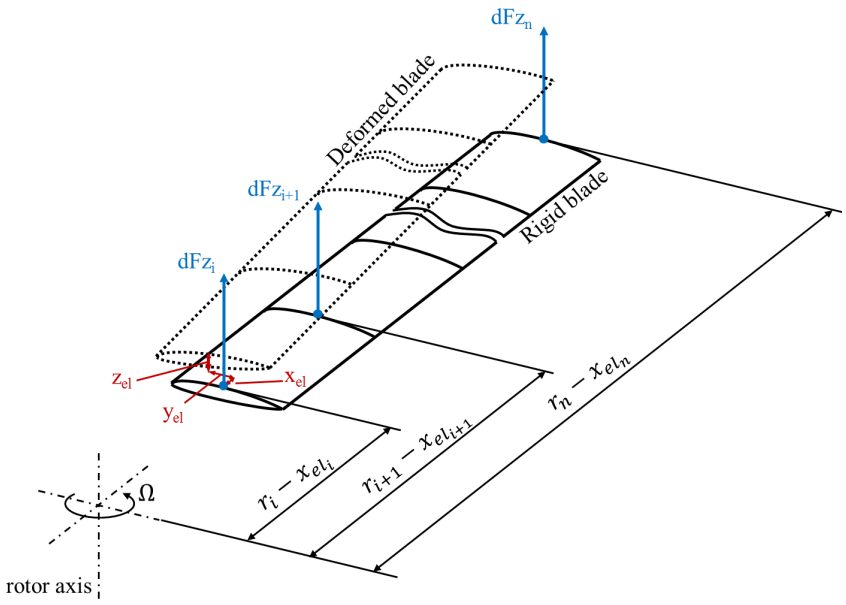

Figure 4.40: Calculation of moments induced by the elementary forces acting on the nodes

The overall hub moments are combined by summing the moments induced by the forces $M_{F_{RB}}$ and the moments at each blade element $M_{M_{RB}}$ and transferred to $\mathcal{F}_{\mathcal{H}}$:

$$M_H = \sum_{j=1}^{N_b} \left(\left(D_H^{RB}\right)^{-1} \sum_{i=1}^{n} \left(dM_{F_{RB_{ij}}} + dM_{RB_{ij}} \right) \right) \tag{4.6.7}$$

where n is the total number of nodes and N_b is the maximum number of blades. The total forces in the blade reference system $\mathcal{F}_{RB}$ are summed at the centre of gravity O_B in $\mathcal{F}_B$:

$$F_B = \left(D_B^H\right)^{-1} \sum_{j=1}^{N_b} \left(\left(D_H^{RB}\right)^{-1} \sum_{i=1}^{n} dF_{RB_{ij}} \right) \tag{4.6.8}$$

Similarly, the moments are transferred to $\mathcal{F}_\mathcal{B}$ using the following equation:

$$M_B = \left(D_B^H\right)^{-1} M_H + \overline{O_{\mathcal{F}_B} O_{\mathcal{F}_H}} \times F_B \tag{4.6.9}$$

The rotor thrust coefficient, C_{T_H}, roll coefficient, C_{L_H} and pitch coefficient, C_{M_H}, are calculated in the hub axis system [40] $\mathcal{F}_H$:

$$C_{T_H} = -\frac{F_H}{\rho(\Omega R)^2 \pi R^2} \tag{4.6.10}$$

$$C_{L_H} = \frac{M_{H_x}}{\rho(\Omega R)^2 \pi R^3} \tag{4.6.11}$$

$$C_{M_H} = \frac{M_{H_y}}{\rho(\Omega R)^2 \pi R^3} \tag{4.6.12}$$

where F_H is the total force in the hub reference system and M_{H_x} and M_{H_y} represent the hub moments. These coefficients are then used for the inflow analysis to calculate the various components of the inflow λ. For realistic aeroelastic analysis the aerodynamic damping has to be taken into account which plays a significant role for unsteady aerodynamics [60]. Since a quasi-steady aerodynamic model is adopted the aerodynamic damping value ζ_a is assumed to be constant. From the example in Section 3.1.2 a reduced frequency associated with aeroloads generated by the first mode at 70 % rotor radius results in a reduced frequency $k = 0.03$. The aerodynamic damping extracted using Figure 3.8 is approximately $\zeta_a = 0.07$ valid for incidence angles $0° \leq \alpha \leq 10°$. The constant aerodynamic damping value ζ_a was added to the structural damping $\zeta_s + \zeta_a$. Figure 4.41 shows how the flapping response varies as a function of different damping values for the hover condition.

The total rigid body forces and moments are shown in Figure 4.42 for an input of $\theta_0 = 7.4°$. Pilot input is given at time zero and it can be seen that a steady-state condition with aerodynamic damping $\zeta_a = 0.05$ is achieved after around 0.3 seconds. The shaft angle was set to zero to keep the F_x-component zero without the need for introducing additional longitudinal cyclic input. It can be seen that the F_x and F_y forces, as well as the M_x and M_y moments, are zero. The F_z force corresponds to the weight of the helicopter. Due to the torque produced by the rotation of the rotor blade, the yawing moment M_z would need to be compensated by the fin and the thrust force produced by the tail rotor, which is beyond the scope of this work.

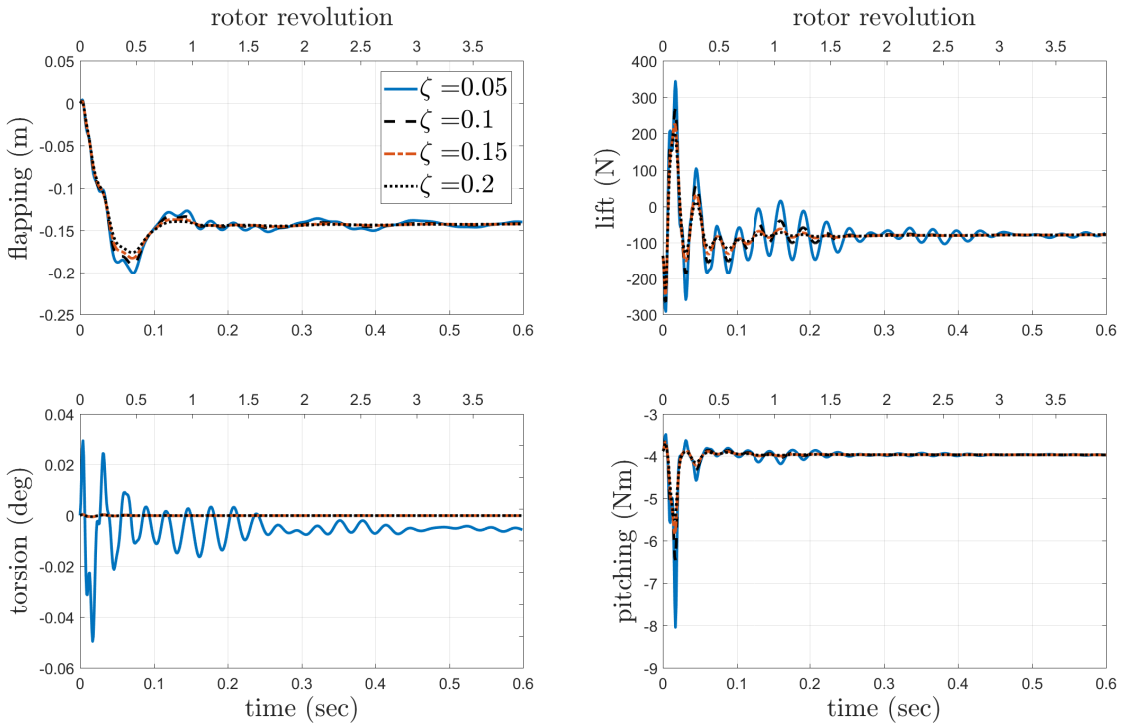

Figure 4.41: Impact of aerodynamic damping coefficients on aeroelastic tip response for hover (pitch angles: $\theta_0 = 7.4°, \theta_{1s} = 0°, \theta_{1c} = 0°$)

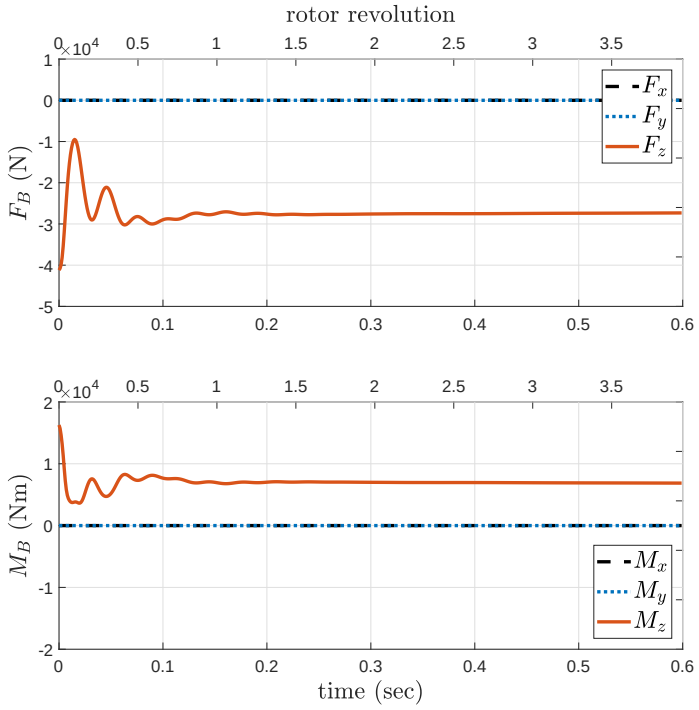

Figure 4.42: Total rigid body forces and moments (pitch angles: $\theta_0 = 7.4°, \theta_{1s} = 0°, \theta_{1c} = 0°$)

4.7 Summary

This framework lays the foundation for determining structural dynamics of a healthy blade that is needed for exploring theoretical instrumentation capabilities in the non-rotating and rotating frame. This was achieved with an industrial structural modelling approach that was linked with a quasi-steady dynamic inflow model together with blade element theory to predict the aerodynamic forces and moments arising from pilot inputs. Although a compromise had to be made between the versatility of modelling capabilities and the computational efficiency, it allows studying the first few aeroelastic blade modes in the hover condition. Several assumptions were made to simplify the modelling approach:

- No re-iteration of internal structural loading.
- Incompressible flow.
- Quasi-steady aerodynamics.
- Constant aerodynamic damping.
- Aerofoil stall neglected.
- Ground effect ignored.
- Coriolis force neglected.
- Other helicopter components not included such as the tail rotor, fuselage or empennage.

While some of the analysis focuses on the prediction of the structure's modal properties, the numerical surface strain was also calculated to allow a comparison with measurements taken from the surface-mounted FBGs (Chapters 5 and 6). Unavoidable numerical errors and lack of detailed structural knowledge highlighted the difficulties in predicting surface strain. A sensitivity study was carried out to determine the effects of changes in structural properties on structural dynamics and to estimate uncertainty bound for surface strain due to the uncertainty of the neutral axis position. The final chapter of this thesis (Chapter 7) uses this framework to investigate how damage changes the dynamic response of the blade and whether simulated strain (for FBG) and displacement (for DFOSS) measurements are suitable for damage detection.

CHAPTER 5

Structural model validation

Structural complexities and non-linear material properties are often simplified leading to approximate mathematical frameworks. Here, the need for experimental validation was identified due to (1) uncertainty of some material properties and, (2) NASTRAN software limitations (see Section 4.4). This chapter aims to describe efforts to prove that the proposed structural modelling approach has significant predictive capabilities. This was done by performing loading tests and experimental modal analysis (EMA) in a controlled environment. The resulting deformations were measured using a digital laser range finder together with surface-mounted FBG strain sensors, while accelerometers were used to extract modal properties from impact tests. Results were used to correct the neutral axis position and structural damping values. In addition, a common indirect finite element model updating technique was adopted to correlate the first torsional mode shape. Challenges associated with updating a model that contains a large parameter set and strongly coupled structural modes were addressed by trading off the achieved accuracy with computational costs.

5.1 Test environment

A test rig was developed in cooperation with Cranfield University and Airbus Helicopters UK (AHUK) that allowed static and dynamic testing of an H135 rotor blade in flap, lag and torsion direction. Several requirements were considered during the design, such as quick interchangeability between flapping (Figure 5.1(a)) and lagging test (Figure 5.1(b)). The test rig was also required to be rigid to avoid any coincidence of the resonances of the test rig structure with the bandwidth of interest for the ground vibration test (GVT). The overall rig height was chosen so that the blade could be mounted easily to the test rig and tests performed conveniently and safely. The test rig was fixed to the floor via screws and levelled during the installation.

Figure 5.1(c) illustrates the torsional test set-up that requires the blade to be mounted in a flapping test position. The support pillar is located underneath the rotor blade, while the associated clamp holds the blade tip in position. Both components are connected

via a hinge, ensuring that the blade is fixed in the out-of-plane direction, but allowing rotation around the feathering axis. With the use of the lever tube mounted on top of the clamp, a torsional moment can be applied by hanging a weight at either end. The entire assembly can be mounted at any chord or spanwise position of the blade.

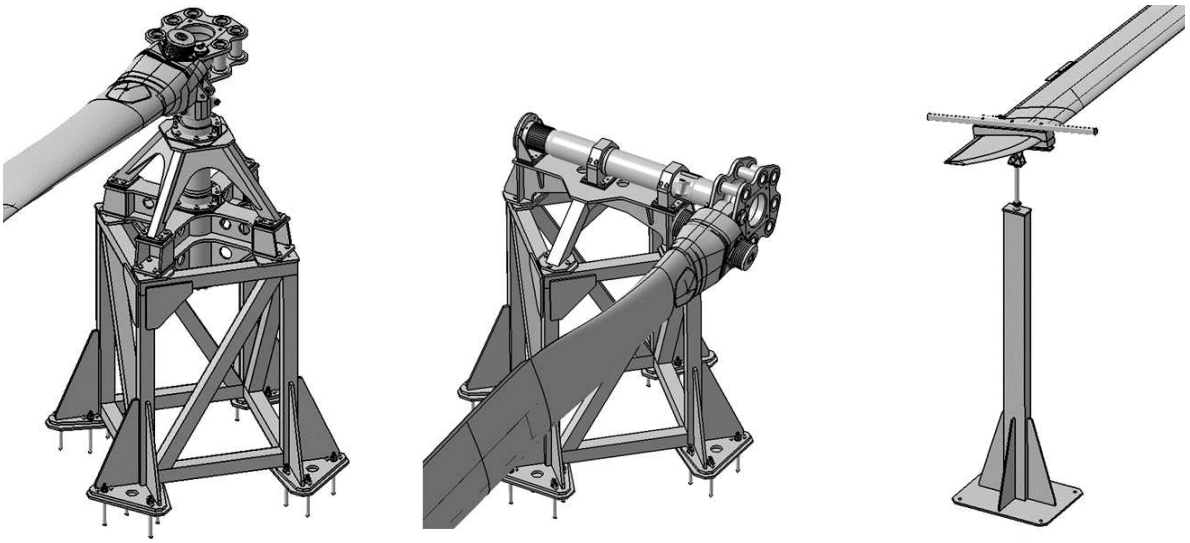

(a) Flapping test (b) Lagging test (c) Torsion test

Figure 5.1: Test rig design

5.2 Static testing

During static testing displacements of the rotor blade due to out-of-plane and torsion were measured under a variety of loading conditions. The analysis aimed to show that the piece-wise linear FE model could predict non-linear behaviour, although the implemented state-space model was valid for linear systems. It should be noted, that the test rig was insufficiently designed for the lagging test as the torsional degree of freedom could not be fixed. It was observed that without a pitch link the torsional stiffness of the pitch control cuff with respect to the flexbeam was relatively low so that a force in the lagging direction resulted in strong lag-torsion coupling. The lagging test was therefore neglected.

5.2.1 Out-of-plane tests

This test aimed to show that the FE model could capture a degree of non-linearity and for this, a significant out-of-plane displacement has to be generated. This was achieved by varying the applied load in location and magnitude. A range of weights was attached to the blade at locations A, B, and C listed in Table 5.1.

Table 5.1: Loading conditions

Test number	Position	Normalised radius (%)	Applied weight (kg)
1	-	-	0
2	C	0.87	10
3	C	0.87	7.5
4	C	0.87	5
5	B	0.66	10
6	B	0.66	7.5
7	A	0.40	10

The spanwise location of the load is illustrated in Figure 5.2 along with the 20 measurement points located on the bottom surface of the blade. Points 19 and 20 are at the blade tip (19 close to the leading edge and 20 close to the trailing edge). The further inboard the mass piece is applied, the higher the load has to be to obtain sufficient displacement. This is the reason why the blade was loaded with 10 kg only at position A.

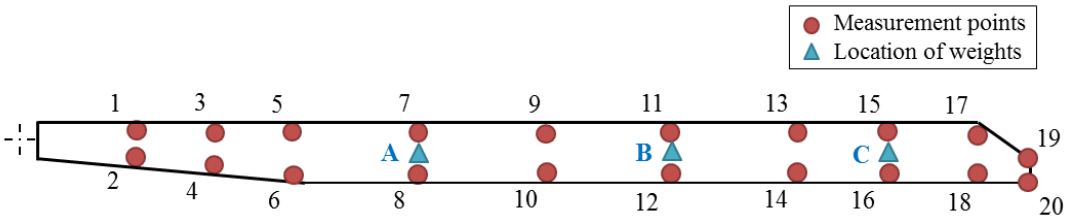

Figure 5.2: Layout of test grid

A typical test is shown in Figure 5.3, in which a mass of 10 kg is attached to location C underneath the quarter chordline. A string was used to attach the weights to the blade and fixed with tape to avoid any movement during the test. A laser range finder (see Appendix G.2) was used to take relative measurements from the floor. The measurements were repeated three times from which an average value and standard deviation were calculated.

Figure 5.3: Typical structural loading test set-up

The absolute displacement was obtained by subtracting the blade clamping height from the measurements (see Appendix G.2.1). The effect of the coning angle in-built into the blade must be correctly identified during the data analysis. When a blade is rotating a coning angle results from the lift and centrifugal force acting on the rotor blade. The blade root typically incorporates a 2-3° coning angle to reduce the bending moments at the rotor shaft [217]. Figure 5.4 shows that the inclination at the blade root is noticeable from the static test results.

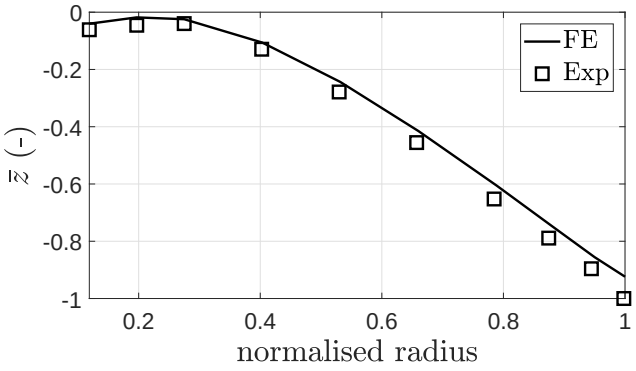

Figure 5.4: Displacement influenced by the in-built coning angle for load case: Position C 7.5 kg

This coning angle can be included in the initial conditions of the state-space formulation. The structural model is described through the linear state-space system ($\dot{x} = Ax + Bu$), and in general form can be described through the state evolution equation [234]:

$$\dot{x} = f(x(t), u(t), t) \tag{5.2.1}$$

where $f(x(t), u(t), t)$ is the vector of non-linear functions, $x(t)$ is the vector of the state variables as a function of time and $u(t)$ is the vector of the input vectors as a function of time t. Given a set of initial conditions and inputs for $t \geq t_0$, the state equations explicitly determine the derivatives of all the state variables. For continuous time $\dot{x}$ can be determined as:

$$\dot{x} = \frac{dx(t)}{dt} \tag{5.2.2}$$

The initial condition $x(t_0)$ stems from the Taylor series approximation:

$$\begin{aligned} x(t_0 + \delta) &\approx x(t_0) + \left(\frac{dx(t)}{dt}\right)_{t=t_0} \delta \\ &= x(t_0) + f(x(t_0), u(t_0), t_0)\delta \end{aligned} \tag{5.2.3}$$

where the second equation results from applying the state evolution equation (5.2.1). The initial value for displacement $x(t_0)$ is obtained by utilising a direction-cosine-matrix based on the in-built coning. Figure 5.5 compares the experimental displacements d_X with the numerically predicted displacements d_A for each loading condition. In all cases,

the standard deviation is smaller than ± 1.25 mm and hence, error bars are not shown. During testing creep was observed which resulted in a difference of 8 mm tip displacement after the load test[1]. This is explained in more detail in Section 5.2.4. The accuracy of the test results are then assessed by calculating the percentage error e:

$$e = \frac{d_X - d_A}{d_X} \tag{5.2.4}$$

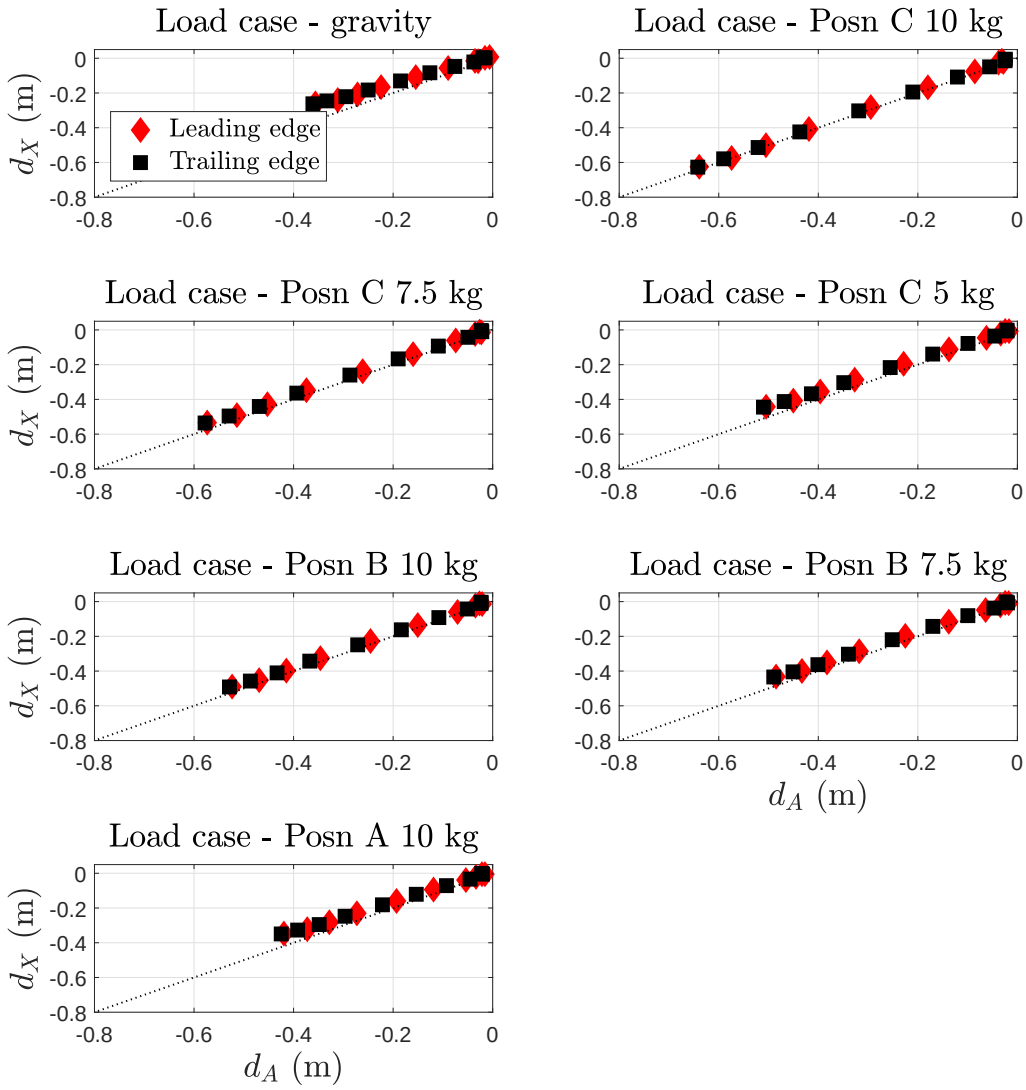

Figure 5.5: Comparison of out-of-plane displacement

The percentage error for each load case at measurement points 19 and 20 are shown in Table 5.2. The blade tip displacement at point 19 is within 11.5% agreement, while an average error of 12.3% is obtained for point 20. Creep has affected these results. The lowest percentage error was achieved for the first load case (test number 2), while the error increased for each further applied load. The complete removal of the weights at position C allowed for some relaxation of the residual tensions in the material, consequently resulting again in a decrease of percentage error for test case number 5.

[1]The tip displacement was 361 mm before and 369 mm after the loading test.

Table 5.2: Percentage error of out-of-plane displacements

Test number	Load case	e_d (%) Point 19	e_d (%) Point 20
1	Gravitation	26.4	27.4
2	Pos C, 10 kg	2.0	2.4
3	Pos C, 7.5 kg	6.6	7.3
4	Pos C, 5 kg	12.0	12.9
5	Pos B, 10 kg	6.1	7.1
6	Pos B, 7.5 kg	10.5	11.3
7	Pos A, 10 kg	16.7	17.8

The increased percentage error at the trailing edge can be explained by the fact that the rotational centre is approximately at the quarter chord line, and hence a higher discrepancy for the out-of-plane displacement at the trailing edge was obtained. This is demonstrated in Figure 5.6 that shows that both torsional distribution exhibit a similar trend at the aerofoil section (0.27%-0.88% rotor radius) with an offset of approximately 2°.

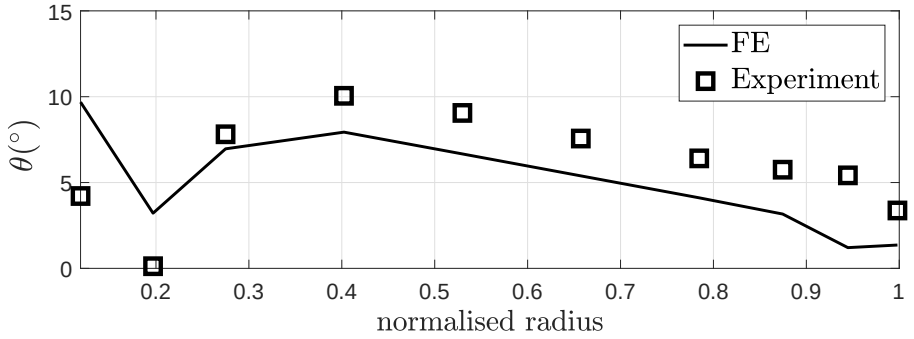

Figure 5.6: Comparison of twist

5.2.2 Torsional tests

Torsional testing was achieved by applying moments around the spanwise axis of the blade. The load was attached at location C and the height of the pillar adjusted so that the blade was horizontal. The clamp hinge allowed rotational movement in feather and was positioned underneath the quarter chord line. Out-of-plane displacement measurements were taken at the 20 measurement points for multiple torsional load cases. Figure 5.7 shows the set-up for each of the different load cases achieved by either varying the lever length or by increasing the applied weight.

After installing the loading equipment the blade settled to a rest position due to the additional weight introduced by lever and clamp. The measurements taken for this load (Figure 5.7(a)) was used as a baseline to correct the experimental results allowing a direct comparison with the numerical model. For load case 2 (Figure 5.7(b)), a total mass of 10 kg was suspended at the end of the lever towards the trailing edge which was mounted symmetrically to the clamp giving an applied moment of 45 Nm about the quarter chord. To obtain a higher torsional moment the length of the lever was increased by positioning

it off-centred on the clamp as shown in Figure 5.7(c). The final load case 4 suspended 17 kg close to the leading edge as shown in Figure 5.7(d). To obtain a significant change in the torsional movement compared to the baseline case, it was necessary to increase the mass substantially compared to the previous load cases.

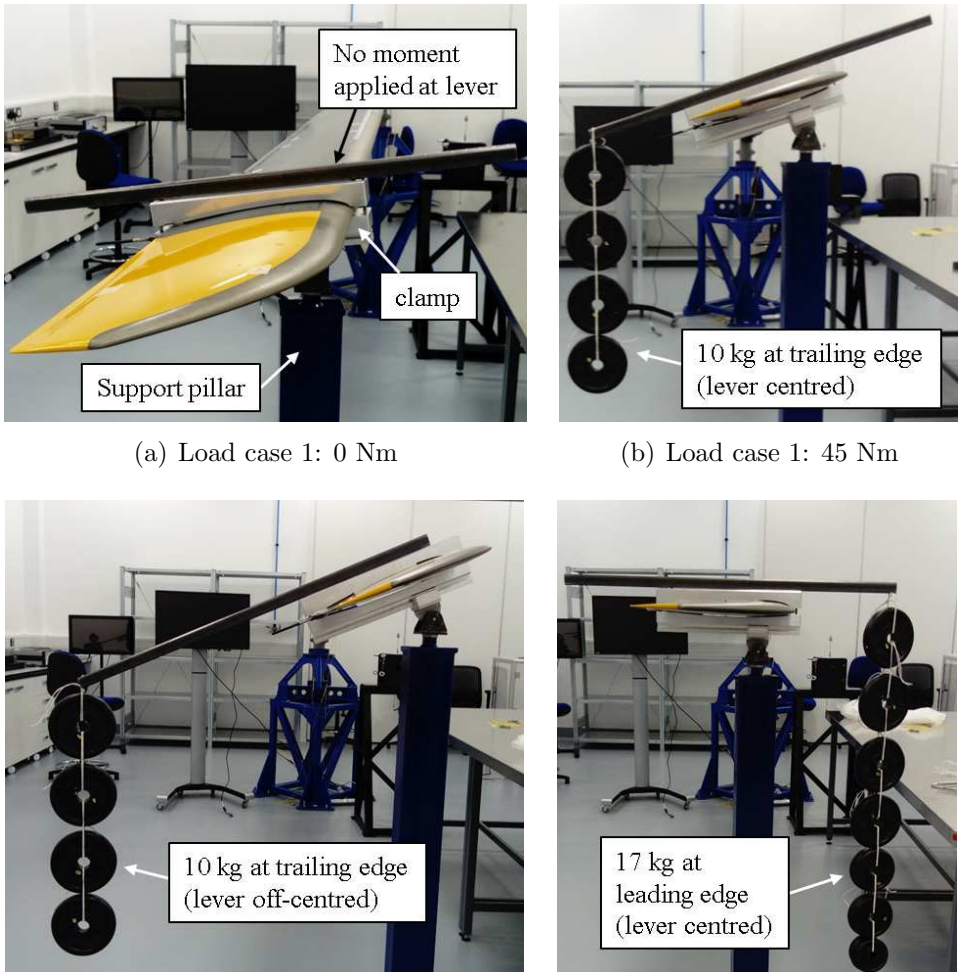

(a) Load case 1: 0 Nm

(b) Load case 1: 45 Nm

(c) Load case 3: 73 Nm

(d) Load case 4: 53 Nm

Figure 5.7: Torsional loading test set-up

Figure 5.8 compares the out-of-plane displacement at each measurement point with the analytical results. The natural twist is altered by the experimental set-up, and consequently, baseline measurements taken for load case 1 are used to correct the test results for the other load cases. A trend is evident in which the displacement at the leading or trailing edge is of a similar order of magnitude. The largest discrepancy is apparent for the blade tip, especially for load case 3 with a difference of more than 40 mm for the trailing edge. The test data exhibits an approximately constant and parallel behaviour for the trailing and leading edges, with the leading edge displacement close to zero because the blade is rotated around the quarter chord. This effect is not present in the numerical model, possibly due to the implementation of the in-built twist and errors in the data points used. Due to the design of the test equipment and assumptions made in the modelling framework, the test results might not be suitable for direct comparison.

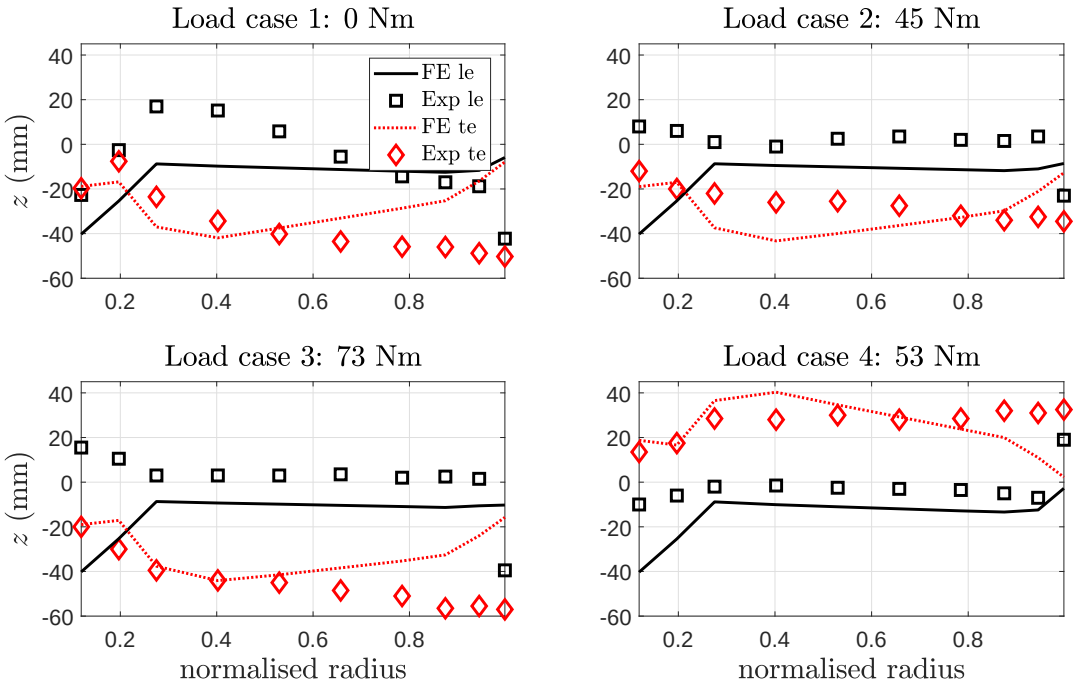

Figure 5.8: Comparison of out-of-plane displacement under torsional load

5.2.3 Static strain measurements

The strain model developed in Section 4.4 was validated by measuring static surface strain on the upper and lower surfaces using FBG sensors under loads applied at location C. This location was chosen to reduce the risk of damaging the fibre-optic cables. Throughout this validation work, two layouts of arrangements are used: four fibre optic cables containing seven FBG arrays (Figure 5.9(a)) are deployed in arrangement A), while in B) six fibre optic cables with each 9 FBG arrays were installed (Figure 5.9(b)). Each fibre optic cable was connected to a channel of the Smart Fibres Aero Interrogator using conventional patch cords. Four channels at one time could be recorded. For both arrangements, the FBG arrays were concentrated at the first 30% of the rotor radius, as the highest strain was expected in this area. The FBGs reflecting the wavelength band (1530-1563 nm) were fabricated in SMF-28 optical fibres and were attached to the blade using a cyanoacrylate adhesive and protected with a capping layer of 2-part epoxy. Correct bonding is very important for accurate strain transfer from the structure to the sensor. In order to protect the fibre optic cables, strips of aluminium speed tape (supplied by 3M) covered the length of the FBG array. During the installation, the rotor blade was placed on a workbench. In this condition, the rotor blade was unloaded ($\epsilon = 0$) which was needed for calibration purposes. After the rotor blade was mounted to the test rig, the wavelength deviations of the FBG reflection peaks were recorded as the blade came under gravitational load. This was taken as the baseline measurements. Then different loadings were applied and the change in wavelength at each FBG was recorded for 10 seconds to obtain an average value. Before the FBG data could be analysed, the recorded wavelength change from each FBG was converted to microstrain $\mu\epsilon$ using the following equation:

$$\mu\epsilon_i = (\lambda_i - \lambda_0) f = \Delta\lambda_i f \tag{5.2.5}$$

where $\Delta\lambda_i$ is the wavelength change in nano-meters with the subscript i representing the number of strain readings and 0 the baseline case, such as when the rotor blade is statically loaded under gravity. The factor f is the FBG wavelength strain coefficient, usually taken as 1.2 $\mu\epsilon$ pm^{-1} [156].

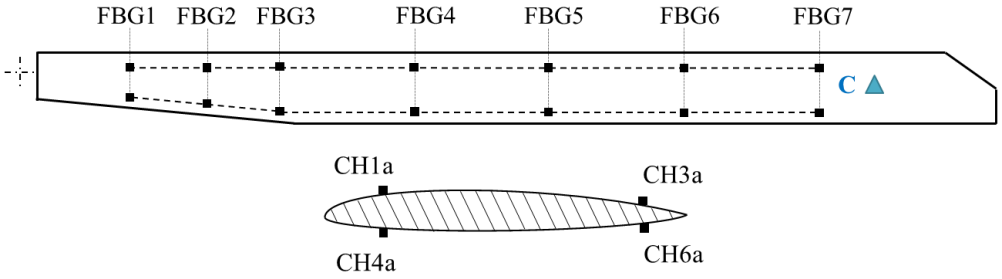

(a) Arrangement A: location of FBG arrays (7x) contained in each fibre optic cables (4x)

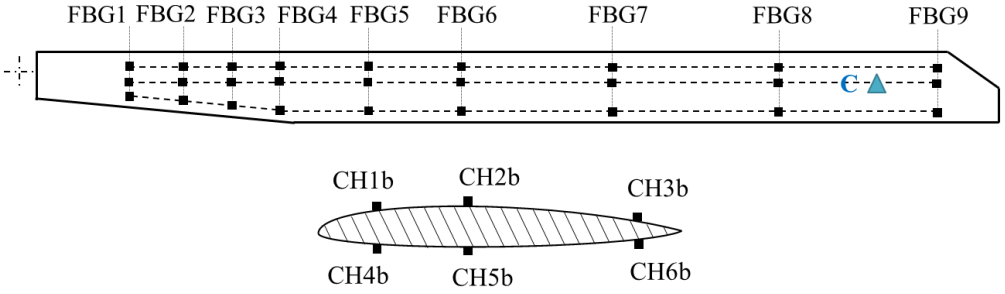

(b) Arrangement B: location of FBG arrays (9x) contained in each fibre optic cables (6x)

Figure 5.9: Location of FBG arrays

Figure 5.10 compares the strain readings along the length of the rotor radius measured for three load cases: 5kg, 7.5kg and 10kg. Tension on the surface due to bending results in a positive strain reading and compression at the bottom surface is reflected in negative strain values. Overall, a good match is obtained between both arrangements with a distinct peak magnitude difference. As the instrumentation system for arrangement B) was reinstalled after removal of arrangement A) errors could have been induced due to chordwise sensor positioning. Also, the data for the bottom leading edge comparison does not agree as some FBGs with the lower strain values were installed on top of the polyurethane tape while others did not work correctly. Also, the first FBG malfunctioned for arrangement A) and the last FBG at the top leading edge for arrangement B).

The measured strain readings are compared to the computed axial surface strain ϵ_T, while three methods are suggested in Section 4.4 to calculate the curvature terms:

1. Eq. 4.4.13: differentiation of displacement using the Chebyshev polynomial approximation,
2. Eq. 4.4.15: summation of the strain mode shapes weighted by its generalised coordinates,
3. Eq. 4.4.25: central difference formulation.

Problems with methods (2) and (3) discussed in Section 4.4 meant that only method (1) was used for further analysis. Figure 5.11 compares the experimental strain readings for

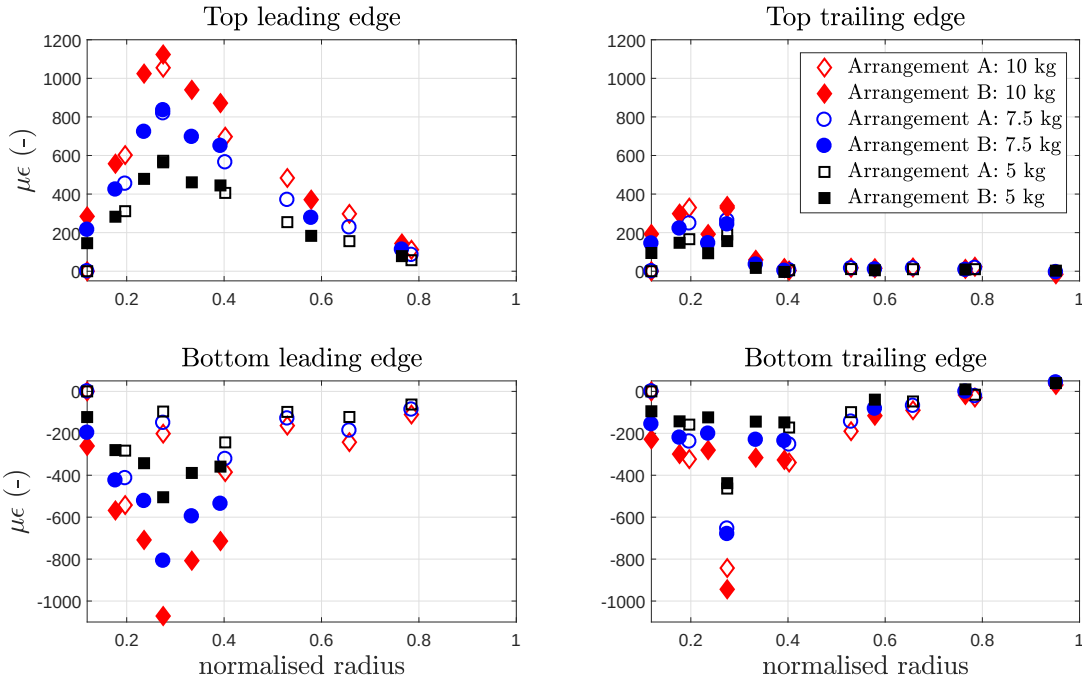

Figure 5.10: Experimental data from arrangement A and B

the different load cases compared to the analytical approach. While Figure 5.11(a) shows the actual trend over the rotor radius, the strain readings are plotted against each other in Figure 5.11(b). From the sensitivity analysis as discussed in Section 4.4.4 upper and lower bounds due to the uncertainty of neutral axis position of $\pm 0.2 c_z$ is included.

For the comparative analysis, it was assumed that the test blade does not deform in lagging direction, and therefore only the estimated strain in the out-of-plane direction ϵ_f is plotted against the experimental results. Furthermore, from the previous displacement analysis, it was shown that torsional movement was induced by attaching weights. The reason for the difference in peak magnitude, especially for the bottom trailing edge, was because the shear strain is neglected in the strain calculation. The data also gives some insight into the location of the neutral axis. As suggested by Ko and Richards [16] the neutral axis position c_i (defined from the top surface) can be calculated as follows:

$$c_i = \frac{\epsilon_{it}}{\epsilon_{it} - \epsilon_{ib}} h_i \tag{5.2.6}$$

where ϵ_{it} is the measured surface strain on the top surface at location i and ϵ_{ib} is the surface strain from the bottom surface at location i, and h_i is the full-depth at location i. Figure 5.12 compares the calculated neutral axis position from FBG arrangements with that from the FE analysis. From all three fibre optic cable positions, a general correlation is obtained. The scale of the plot is different for clarity reasons.

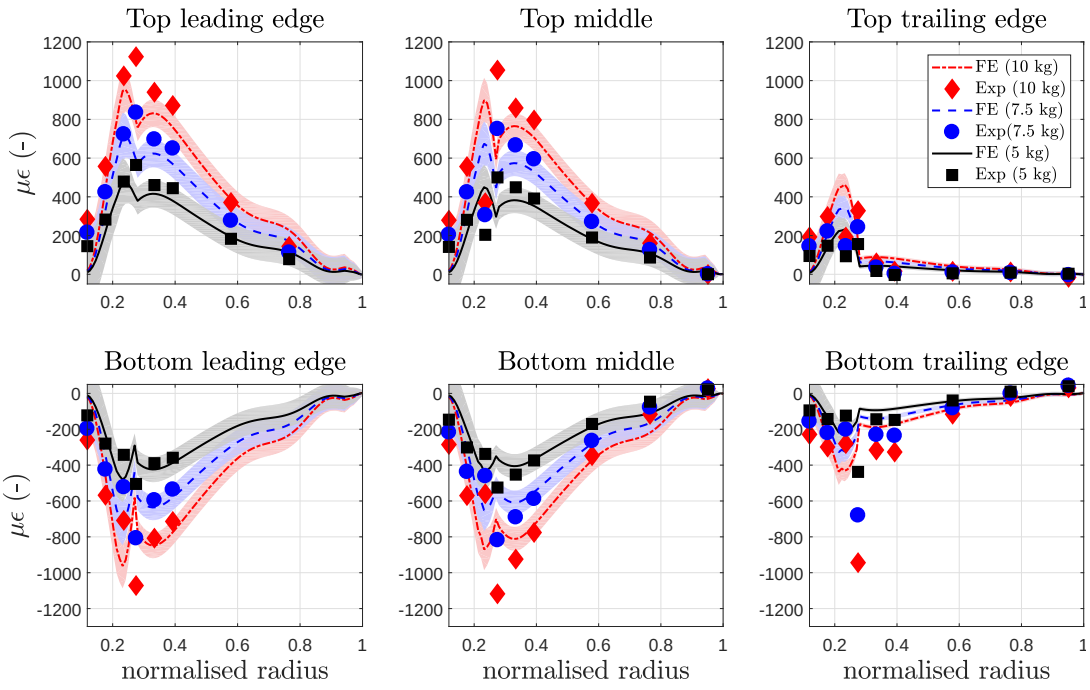

(a) Spanwise distribution

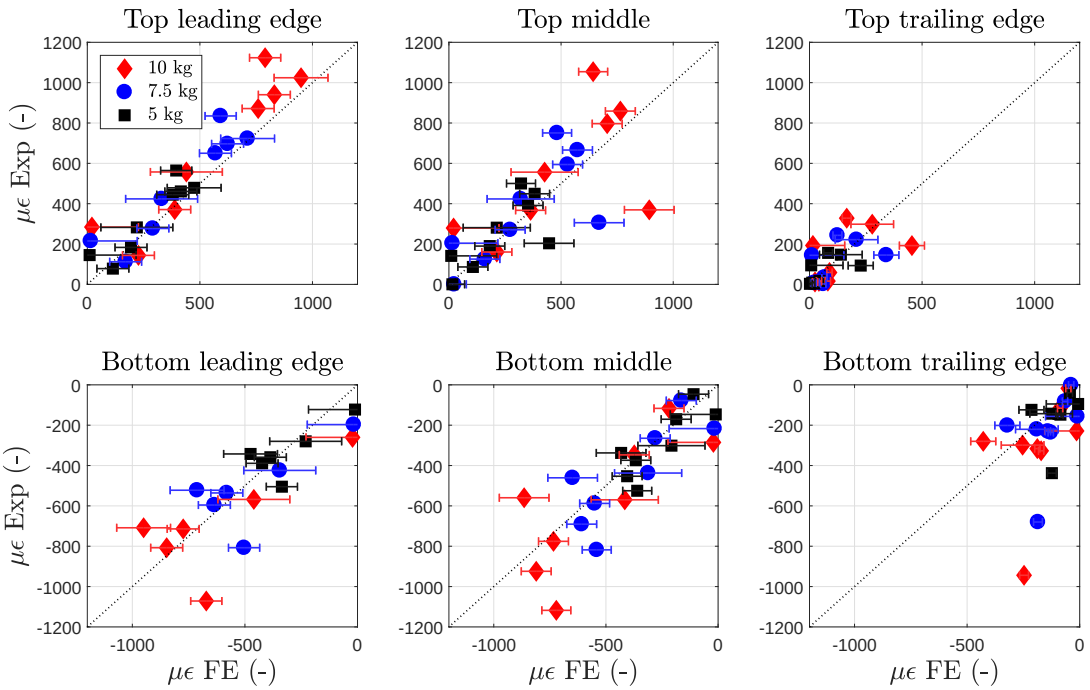

(b) Data correlation

Figure 5.11: Comparison of surface strain (arrangement B)

5.2.4 Sources of error

Errors during experimental testing can arise from several sources, such as human variability, instrumentation fluctuations, experimental design, or environment [235]. Some of these errors can be counteracted by repeating the measurements or calibration. Yet, some errors can be induced by the conducted test or by the test item, which is particularly the

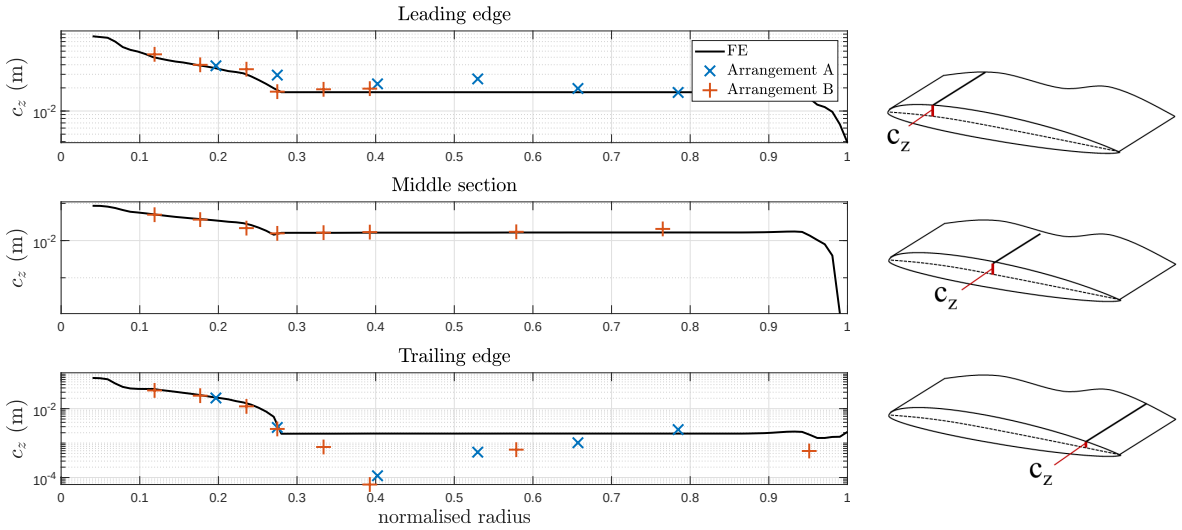

(a) Distance between neutral axis and surface, c_z

(b) Location of measurement

Figure 5.12: Comparison between experimental and FE neutral axis position

case for a composite rotor blade that has been in service for many years. Many unknown factors add to uncertainties about the structural behaviour, such as:

- Variation in the manufacturing processes
- Service history
- Unknown damages, or uncommented repairs
- Changes in ground handling procedures or storage environment
- Remaining service life

AHUK donated four H135T2[2] rotor blades that had remaining service life[3] as listed in Table 5.3. Before the structural loading test, the static deflection under gravitational load was measured for all blades. Two observations were also made during the test: 1) different vertical displacement for each sample blade, and 2) creep behaviour. Creep is an important aspect adding to measurement errors. Table 5.3 also highlights the total tip displacement of all four blades recorded after six hours settling time and over this period each blade had settled by 9 mm.

Table 5.3: Remaining service life of sample rotor blades and natural droop

Blade number	Serial number S/N	Remaining service life (hrs)	Tip displacement (mm)
1	1602	6652	269
2	1946	6302	262
3	985	3960	356
4	1751	1373	301

Table 5.3 shows that the blade with the lowest serial number (Blade 3) has the highest tip displacement. This could be due to the earlier manufacturing date of Blade 3 compared to

[2]The radius of the type T2 is 5.1 m.
[3]The service life of an H135 rotor blade is approximately 20,000 hours.

the other three sample blades suggesting changes in manufacturing techniques or changes caused by ageing. As Blade 3 was used for experimental testing its tip displacement settling time was recorded over several days. Figure 5.13 shows the relative measurements starting with zero when the blade was mounted to the rig and gravitational load started acting.

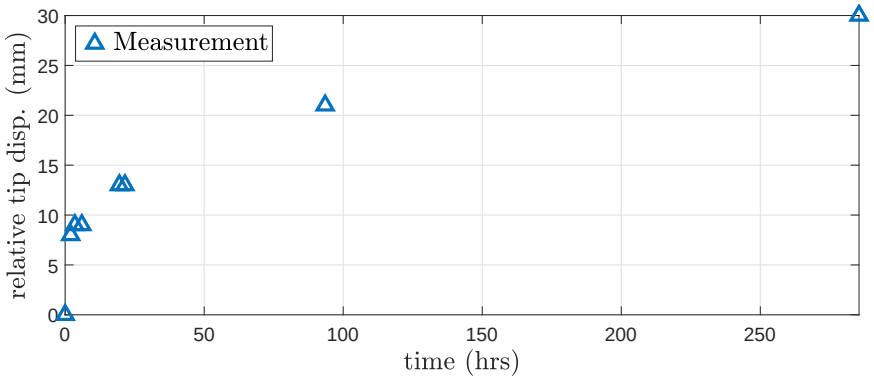

Figure 5.13: Creep of blade tip

After approximately 280 hours the blade tip has settled by a total of 30 mm. It is interesting to note that the blade also exhibited creep behaviour during torsional testing. For example, the effect of load case 2 resulted in a 7 mm movement of the trailing edge at the tip, load case 3 caused another movement of 6 mm, and the last load case caused 12 mm upwards movement. This behaviour introduced additional error. Using the information above, an uncertainty measure of tip displacement can be formed. From the measurements shown in Table 5.3 an average tip displacement of 297 mm can be calculated. The following equations are used to determine the uncertainty bound of the sample rotor blades:

$$\hat{u} = \max(y) - \frac{1}{4}\sum_{i=1}^{4} y_i \tag{5.2.7}$$

$$\check{u} = \min(y) - \frac{1}{4}\sum_{i=1}^{4} y_i \tag{5.2.8}$$

This yields an uncertainty bound of +59mm/-35mm. As the four blades were provided from one helicopter, it is assumed that this relatively large difference in static displacement has a minimal effect on the rotating environment. At full rotation, the blades experience centrifugal forces which reduce these differences in static deflection to a negligibly small amount. Any unwanted out-of-plane movement can be removed by the use of track and balance procedures (see Appendix F). A summary of sources of errors and aspects which add to uncertainties of structural behaviour during structural loading test is given in Appendix G.3.

5.3 Experimental modal analysis

Experimental modal analysis (EMA) was carried out to compare analytical and experimental modal properties. EMA was done on the H135 blade, using: ambient vibration testing (AVT) and impact hammer testing (IHT). Note that accelerometers are used for the model validation work, while fibre optic instrumentation systems are deployed for the characterisation study (Section 6.3). The tests were performed in a controlled environment so that the effects of temperature and humidity can be ignored. The presented work related to EMA, as well as the identification of modal properties with a stochastic subspace identification (SSI), are credited to Luca Zanotti Fragonara and Ivan Petrunin who provided the experimental equipment and expertise to carry out this work.

Two different arrangements with 9 triaxial accelerometers (ACC (3D)) were used to ensure that higher flapping modes, as well as torsional modes could be identified, see Figures 5.14 and 5.15. Only flap-wise and edge-wise channels have been recorded and one channel was aligned with the blade feathering. This resulted in a total of 19 acquisition channels and 1 input channel (hammer). For EMA 1 four high-sensitivity ACC (3D) (No. 6 - 9) were located near the blade root and the remaining five medium-sensitivity ACC (3D) (No. 1 - 5) were placed in an equal distance of 525 mm along the blade. The ACC (3D) were rearranged for EMA 2 and impact hammer locations were chosen off-centred to identify torsional modes. A National Instrument data acquisition NI-9234 module was used and the signals were acquired using standard Lab View software at a sampling frequency of 2560 Hz for the AVT and 10240 Hz for the IHT.

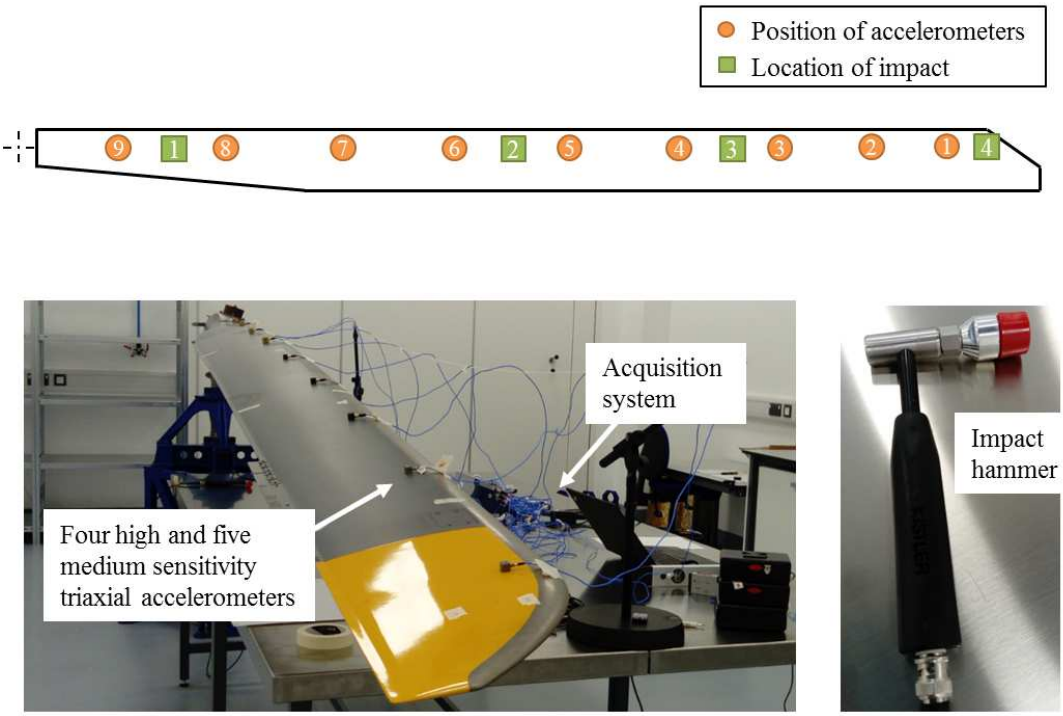

Figure 5.14: EMA arrangement 1

Figure 5.15: EMA arrangement 2

5.3.1 Data analysis and comparison

The experimental modal analysis was carried out in the time domain with an SSI algorithm (see Appendix G.1). A stabilisation diagram, using a segment of the correlation functions with a maximum length of L points, allowing to estimate a maximum system order j (where j is $19 * L/2$, being 19 the number of measured outputs). The stable poles from order n_{min} to n_{max} are determined based on different stabilisation criterion, in terms of frequency f, damping ζ and MAC. During the analysis poles having unrealistic damping ratios (negative or larger than 10%) were filtered out of the set of stable poles. In this set of tests the following stabilisation criteria were used [236]:

$$\delta f \leq 0.5\%, \delta\zeta \leq 10\%, (1 - MAC) \times \% \leq 5\% \tag{5.3.1}$$

The MAC is defined as follows:

$$MAC = \frac{|\phi_A^T \phi_X|^2}{(\phi_A^T \phi_A)(\phi_X^T \phi_X)} \tag{5.3.2}$$

where ϕ_A is the analytical mode shape and ϕ_X is the experimental mode shape. AVT allows the identification of most of the modal frequencies at once as all modes receive a similar excitation (assuming ambient noise is very close to white Gaussian noise). This procedure is often referred to as OMA, and typically is used for large structures [237]. Nonetheless, damping estimation under low amplitudes is often more difficult and input-output identification results should provide better estimates of the viscous damping coefficient.

The white noise signal had an acquisition length of 600 seconds and a sampling frequency of 2560 Hz. The expected dynamic modes of interests are all below 100 Hz according to the FE model thus pre-processing of the data involved de-trending using a 1st order polynomial (mean and linear trend removal) and subsampling with a factor of 8. Thus, the sampling frequency of the processed signals was reduced to 320 Hz. A stabilisation diagram (Figure 5.16) was created for each arrangement and the best regression order was selected by the operator based on the stability analysis.

Hammer tests were repeated several times to obtain consistent and robust results. Trial and error led to the decision to repeat after a free-decay phase of about 12 seconds.

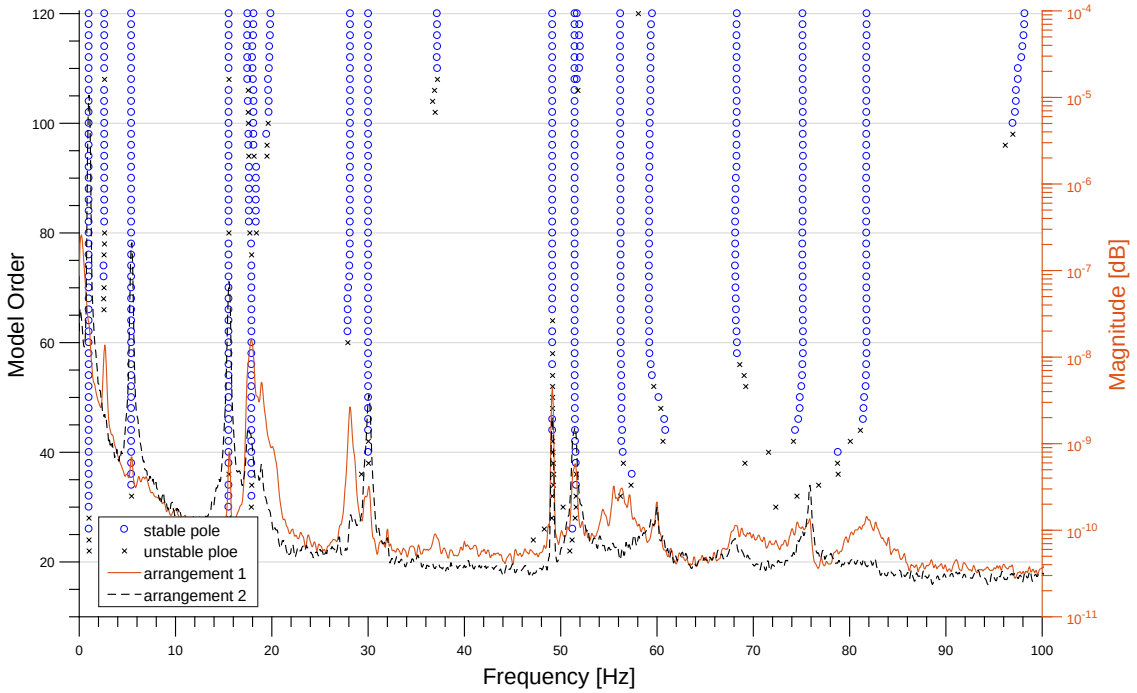

Figure 5.16: Stabilisation diagram for increasing order in the white Gaussian noise test (20 to 100) and $\delta f < 0.5\%, \delta\zeta < 10\%, (1 - MAC) \times \% < 5\%$. Signal length 100 seconds

This resulted in few oscillations of Mode 1F (frequency of about 1 Hz), thus leading to poor identification. The signals were processed all at once, discarding clipped impacts (over the threshold of the acquisition system). At least 10 impact response signals were included for the system identification. The force transducer in the tip of the hammer was used as an input signal, whilst the other 19 channels, measuring the accelerations form the output channels. A subsampling factor of 10 resulted in a reduced sampling frequency of 1024 Hz.

The first six experimentally determined mode shapes are shown in Figure 5.17. As with the analytical mode shapes, Mode 2L exhibits a lagging/torsion coupling whereas Mode 1T has a coupled torsion/flapping component. Table 5.4 shows the natural frequencies and damping values obtained from AVT, IHT 1 (using arrangement 1), and IHT 2 (using arrangement 2), while Table 5.5 compares the first eight analytical f_A and experimental natural frequencies f_X taken from AVT. The comparison between f_A and f_X shows a match with an average error of 10.26 %. The largest error is obtained for the natural frequency for Mode 1L and Mode 2L. This discrepancy could have occurred as a consequence of the difference in boundary conditions between the FE model and the experiment. This is schematically shown in Figure 5.18. No pitch link was used to fix the rotational degree of freedom of the pitch control cuff during the experiment, whereas in the FE model it was assumed that the pitch link is connected to the pitch horn using a rotational scalar spring element (see Section 4.4). The value of this spring constant indicates the stiffness of this kinematic linkage and how much force is required to rotate the pitch control cuff. Incorrect values of the scalar spring elements in flapping, lagging, and torsional direction have an impact on the natural frequencies and the structural mode shapes, as shown in Section 5.4.

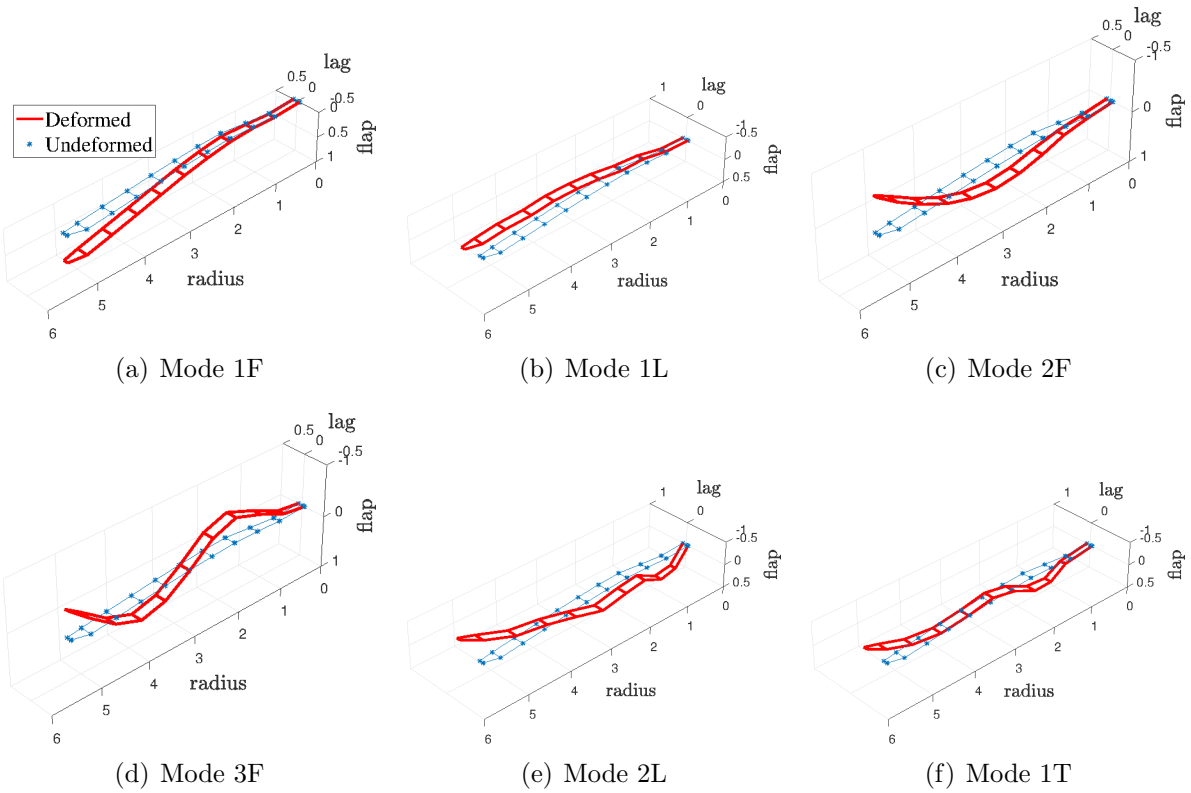

(a) Mode 1F (b) Mode 1L (c) Mode 2F

(d) Mode 3F (e) Mode 2L (f) Mode 1T

Figure 5.17: Experimental displacement mode shapes ϕ

Table 5.4: Experimental modal parameters obtained from AVT and IHT

Mode number	Mode type	Frequency (Hz)			Damping (%)		
		AVT	IHT 1	IHT 2	AVT	IHT 1	IHT 2
1	1st flapping	1.02	1.00	1.00	0.20	1.04	0.60
2	1st lagging	2.63	2.63	2.60	2.25	3.02	5.18
3	2nd flapping	5.43	5.40	5.41	0.44	0.87	0.64
4	3rd flapping	15.55	15.47	15.48	0.17	0.53	0.49
5	2nd lagging	17.80	18.66	18.70	1.18	3.18	2.00
6	1st torsion	28.17	27.96	27.90	1.00	1.21	1.02
7	4th flapping	30.04	30.07	30.05	0.26	0.42	0.40
8	5th flapping	51.49	51.46	51.59	0.31	0.50	0.48

After comparing the natural frequencies, it is essential to check how well the analytical and experimentally determined eigenvalues compare for the same physical mode. This can be achieved with the use of the MAC (see Eq. 5.3.2). A value of MAC close to 1 indicates a correct pairing of the modes. According to Ewins [196] a MAC value between 0.9 - 1 is obtained for well-correlated modes and a value of 0.1 is an indication of uncorrelated modes. Table 5.6 compares the computed MAC between analytical and experimentally determined mode shapes for both experimental arrangements. Arrangement 1 shows an overall mode shape correlation of MAC $>$ 0.8, except for Mode 1T which is MAC $=$ 0.24. It was expected that arrangement 2 gives an improved 1T mode shape correlation due to the off-centred location of the sensors and structural rotation around the shear centre. Compared to arrangement 1, the sensor positions located at the trailing edge

Table 5.5: Comparison of analytical with experimental (AVT) natural frequencies

Mode number	Mode type	f_A (Hz)	f_X (Hz)	e_f (%)
1	1st flapping	0.90	1.02	11.76
2	1st lagging	3.41	2.63	-29.66
3	2nd flapping	4.98	5.43	8.29
4	3rd flapping	15.28	15.55	1.74
5	2nd lagging	22.72	17.80	-27.64
6	1st torsion	28.59	28.17	-1.49
7	4th flapping	29.98	30.04	0.20
8	5th flapping	52.17	51.49	-1.32

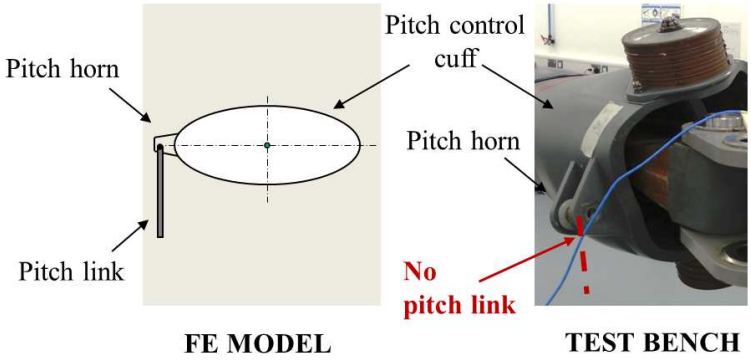

Figure 5.18: Difference in boundary condition

yield a 34.1 % improvement of the 1T mode shape correlation with MAC = 0.349. Using the ACC (3D) located at the quarter chord line very similar MAC values are achieved with arrangement and 1 and arrangement 2. However, using data from the ACC (3D) located close to the trailing edge a poor mode shape correlation for Mode 4F and Mode 5F mode shape is obtained with MAC < 0.1. One reason for this discrepancy could be due to the bending-torsion coupling in the higher modes, which could not be captured with only four sensors at the trailing edge.

Table 5.6: Comparison of MAC for both arrangements

Mode number	Mode type	Arrangement 1 quarter chord	Arrangement 2 quarter chord	Arrangement 2 trailing edge
1	1st flapping	0.990	0.988	0.957
2	1st lagging	0.949	0.898	0.947
3	2nd flapping	0.937	0.884	0.950
4	3rd flapping	0.951	0.960	0.747
5	2nd lagging	0.861	0.839	0.638
6	1st torsion	0.240	0.230	0.349
7	4th flapping	0.843	0.843	0.069
8	5th flapping	0.813	0.886	0.087

5.3.2 Sources of error

Several error sources have to be considered. These could have been induced by the test equipment, test arrangement, testing methodology and signal processing. The rigid test bench was designed to ensure that resonances in the bandwidth of interest were avoided. Yet, this might have led to over constraining the rotor shafts' dynamic characteristics. Figure 5.19 illustrates the difference between the test bench and the clamped condition on a real helicopter, in which the rotor shaft acts as a spring element as it is only attached at its end inside the gearbox.

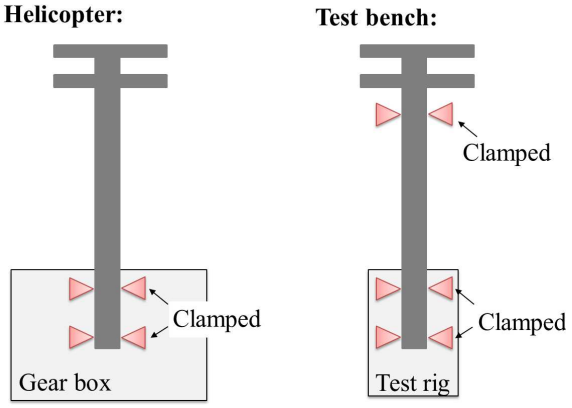

Figure 5.19: Schematic diagram of clamping locations of the rotor shaft

Within AHD, dynamic characteristics of a non-rotating blade are usually identified using all four blades on a whirl rig (non-rotating). This results in symmetric and asymmetric blade modes due to the rotor shaft's dynamic characteristics. Additional errors during the test could have occurred from the positioning of the ACC (3D) and their mounting on the curved aerofoil surface. Furthermore, human error has led to an inconsistent impact hammer testing. Also, the excitation through the hammer in the out-of-plane direction might have not been sufficient to excite the in-plane modes correctly.

5.4 Finite element model updating

The comparison between predicted and experimentally determined modal properties highlighted the need for finite element model updating (FEMU) due to the discrepancy of 1T mode shape correlation. Therefore, this section focuses on updating the structure in such a manner that only Mode 1T is affected since its associated natural frequency is within 1.5% agreement. FEMU can be a very demanding task and careful planning is required to get an understanding of which updating parameters achieve the best outcome in terms of matching mode shapes. FEMU can be performed by either adopting (1) an indirect or iterative updating method or (2) a direct updating procedure. The indirect or iterative updating method is achieved by minimising a cost function based on the difference between the experimental test data and analytical data. The advantage is that a wide choice of parameters can be included and weighting factors can be applied [229]. Direct updating methods, on the other hand, update the mass and stiffness matrix and often result in unrealistic elements in the system matrices which often have little physical meaning [229, 238].

Much research was done in the field of FEMU [196, 228, 229], and it was addressed for helicopter rotor blades in the past [239, 240]. Updating a structural rotor blade model requires a lot of effort because a strong bending and torsion coupling of modes is evident. For FEMU such coupling is computationally expensive and as proposed by Balis Crema [240] a two-step updating procedure reduces the computational time. In their work, the flapping stiffness was updated first for an AB-204 helicopter blade after using these partial results to optimise the torsional stiffness. This resulted in a better correlated dynamic finite element model [240].

For this work, two studies were carried out to determine which structural parameters have the greatest impact on improving the torsional mode shape: (1) impact of boundary conditions on modal properties, and (2) eigenvalue and MAC sensitivity analysis.

5.4.1 Impact of boundary conditions

This section examines how boundary conditions (BC) influence the structural modal parameters through two investigations:

1. impact on 1T mode shape correlation
2. impact on the lagging natural frequencies

The scalar spring rate (CELAS) was varied for flapping (c_f), lagging (c_l), and torsional degrees (c_t) of freedom. The outcome is shown in Figures 5.20 - 5.22 which show the change of natural frequency in percentage e_f and MAC as a function of $\bar{c}_f$, $\bar{c}_l$, and $\bar{c}_t$ normalised to its original value. Low c_f values influence f_A and MAC of the higher modes as shown in Figure 5.20. An improved 1T mode shape correlation could be obtained by using a small c_f value, yet high enough not to alter f_A. Figure 5.21 shows how the modal parameters vary with c_l. The analytical frequency for both Mode 1L and Mode 2L is higher, and hence the FE model exhibits a higher in-plane stiffness. Using a low c_l value f_A of Mode 1L could be adjusted to match the experimentally determined frequency which is 29.7% lower than the analytical frequency. However, this also impacts the modal parameters of Mode 5F significantly. Finally, a variation of c_t yields a deviation of the natural frequency of Mode 3F, Mode 2L, Mode 1T, and Mode 5F. Even though a small c_t value would realistically represent the test bench BC, yet it would not adjust both lagging frequencies. Although an increase of c_t does not affect the natural frequency of Mode 4F, it results in a decrease of MAC for the same mode and improvement of MAC for Mode 1T.

This analysis shows that the lagging frequencies cannot be adjusted by varying the stiffness values of the BC. Also, it is not the sole factor for insufficient 1T mode shape correlation. The outcome of this study was used to adjust the linear and rotational spring rates so that an improved 1T mode shape correlation was achieved. Although arrangement 2 gives a higher 1T mode shape correlation, arrangement 1 was used for the updating procedure, because Mode 4F and Mode 5F gave a higher MAC. Additionally, arrangement 1 provides a higher resolution of in-line measurement points. The flapping spring constant was reduced by 91.0% compared to the original value and the torsional spring rate was increased by 81.0%. Updated MAC and f_A results are presented in Table 5.7.

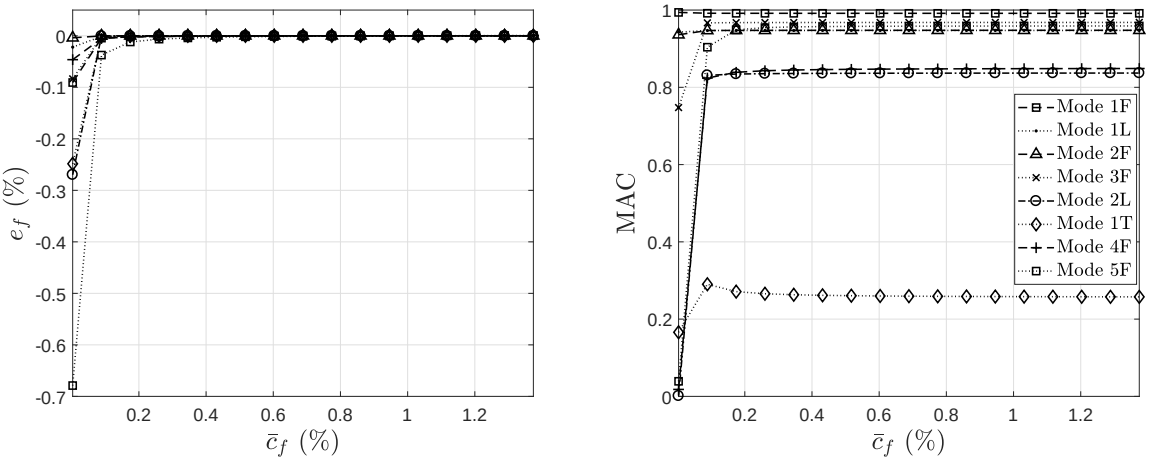

Figure 5.20: Impact of c_f on f_A and MAC

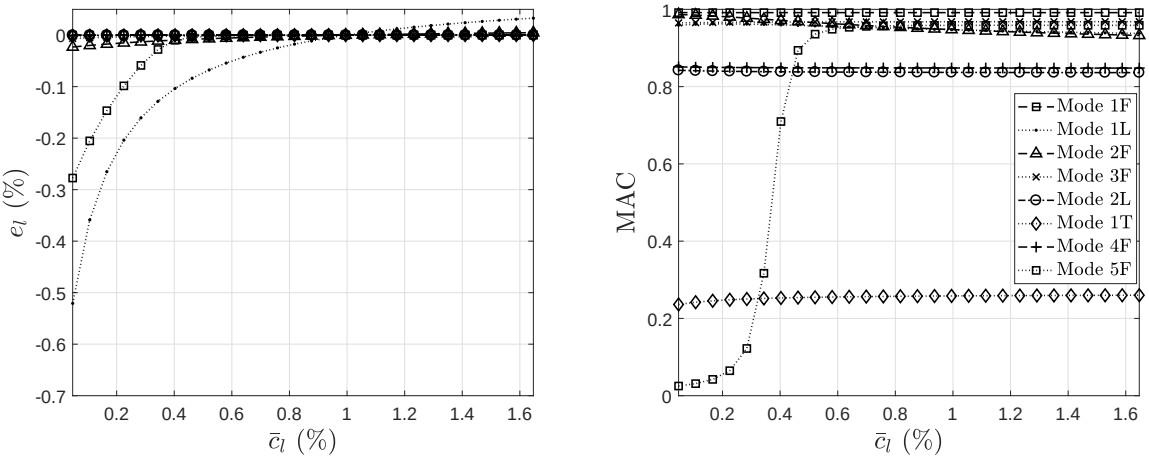

Figure 5.21: Impact of c_l on f_A and MAC

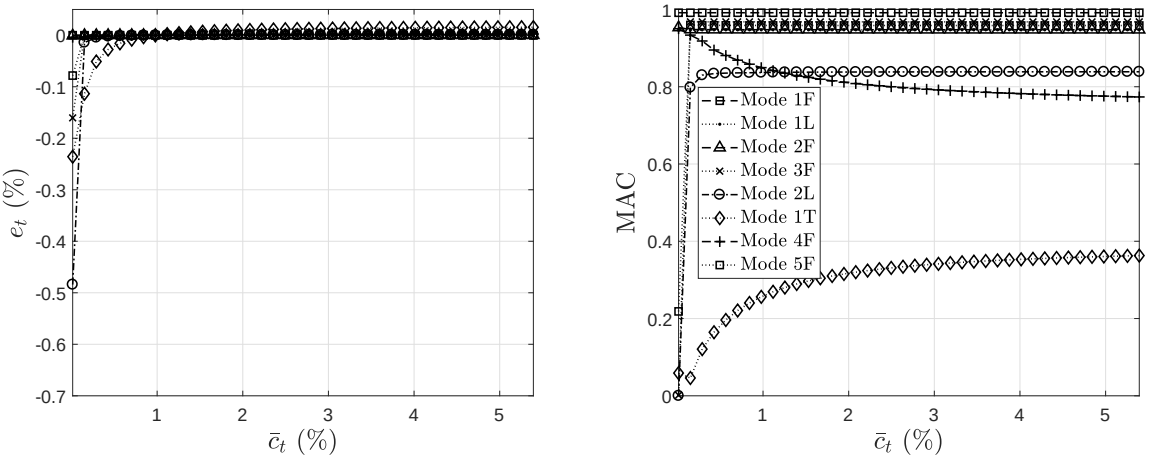

Figure 5.22: Impact of c_t on f_A and MAC

An improvement of 41.3% of Mode 1T MAC could be achieved with this initial updating method. Due to the strong bending and torsional coupling, the correlation of the Mode 4F was decreased by 16.3%, yet Mode 5F was improved by 10.1%. Results from the last column show that the experimental error in the natural frequency has not changed significantly after updating the BC. The values for the "before" column are repeated from

Table 5.7: MAC and f_A after updating BC

Mode number	Mode type	original MAC/f_A	updated MAC/f_A	Difference (%) MAC/f_A	Exp. error (%) before	after
1	1st flapping	0.990/0.90	0.992/0.90	0.20/0.00	11.76	11.76
2	1st lagging	0.949/3.41	0.947/3.40	-0.21/-0.29	-29.66	-29.28
3	2nd flapping	0.937/4.98	0.947/4.99	1.06/0.20	8.29	8.10
4	3rd flapping	0.951/15.28	0.967/15.27	1.65/-0.07	1.74	1.80
5	2nd lagging	0.861/22.72	0.833/22.72	-3.36/0.00	-27.64	-27.64
6	1st torsion	0.240/28.59	0.409/29.01	41.32/1.45	-1.49	-2.98
7	4th flapping	0.843/29.98	0.725/29.93	-16.28/-0.17	0.20	0.37
8	5th flapping	0.813/52.17	0.904/50.29	10.07/-3.74	-1.32	2.33

Table 5.5 for the reader's convenience. The initial average percentage error of 10.3% has only increased to 10.5% after updating. This is the reason why the adjustment of the BC was used for the updating procedure, as this increase in frequency was considered to be acceptable.

5.4.2 Eigenvalue and MAC sensitivity analysis

After using the BC to adjust the torsional mode shape correlation, it is necessary to identify which structural parameters (bending or torsional stiffness) achieve the best outcome. Since the BMR consists of around 80 structural nodes for flexbeam, pitch control cuff and aerofoil section, it is computationally very expensive to include all nodes in the updating procedure.

The FE model was developed based on assumptions for the bending stiffness, such as EI_x or EI_z and torsional stiffness GJ. Variations in these impacts either the geometrical properties of the blades' cross section (affecting the second moment of area I_x and I_y and mass) or the elastic modulus E. However, neither the second moment of area, shear modulus, nor the elastic modulus was known for any of the cross-sections. Consequently, it is not possible to ensure physical consistency throughout the updating process. Nevertheless, the product of material and geometrical properties, such as EI_x, EI_z, GJ were used for the updating procedure. It is assumed that the applied mass distribution and geometrical parameters are constant and were therefore not updated.

An eigenvalue and MAC sensitivity study was performed (see Section 4.4.4) to investigate the sensitivity of the modal properties due to torsional stiffness and bending stiffness. This allows the determination of how much the modal properties of the system are influenced by updating parameters at any node location. Here, the updated BC are included in the analysis and the outcome is plotted in Figures 5.23 - 5.24 for the flexbeam and aerofoil section. For both studies, the parameter value has increased in magnitude. As the local stiffness has increased, negative values for $\bar{S}_{\Delta M}$ indicate an improvement in the mode shape correlation. A change of GJ at the beginning of the aerofoil section mainly influences the eigenvalues and mode shapes of Mode 1T and 4F. The sign of $\bar{S}_{\Delta M}$ indicates that an increase in stiffness will result in an improvement of the 1T mode shape but in a deterioration of the 4F mode shape. This compromise has to be accepted. The structural eigenvalues of Mode 3F, 1T, 4F, 5F are sensitive to a change of EI_x in the

aerofoil region. Figure 5.24 shows that increased local stiffness EI_x in the aerofoil section would result in a degradation of 1T mode shape. This means that by decreasing the local stiffness EI_x an improvement could be achieved by this and could compromise the other mode shape correlations. The sensitivity study highlighted that the in-plane bending stiffness EI_z has no impact to the torsional mode shape correlation and therefore, is not considered for the updating procedure.

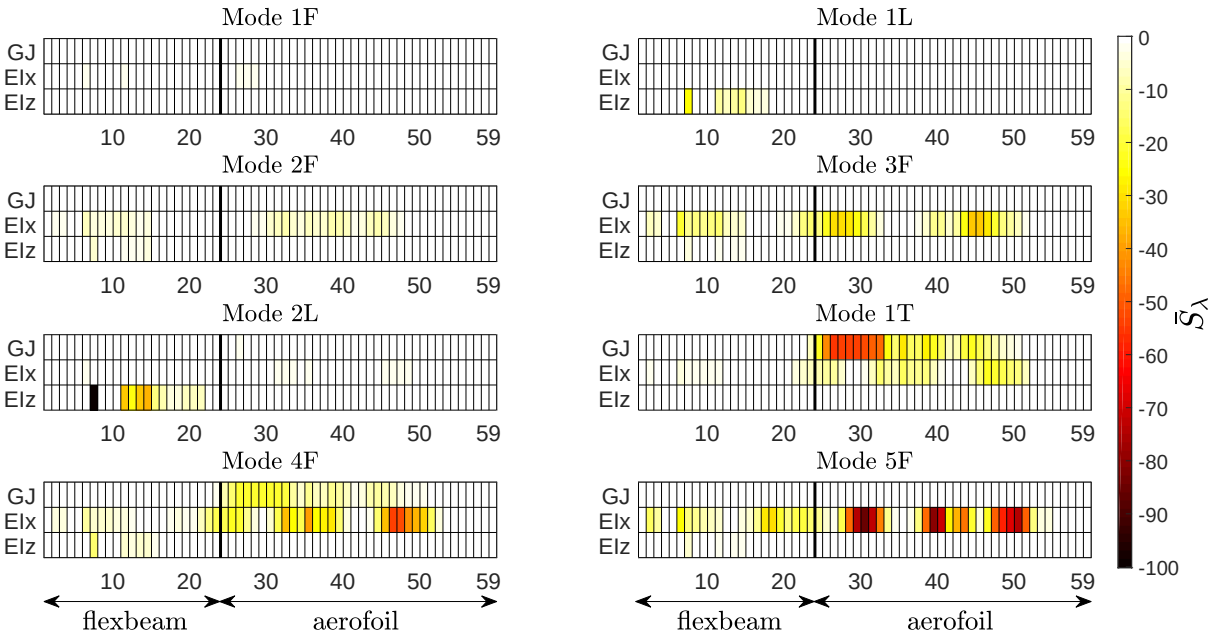

Figure 5.23: Eigenvalue sensitivity with updated BC

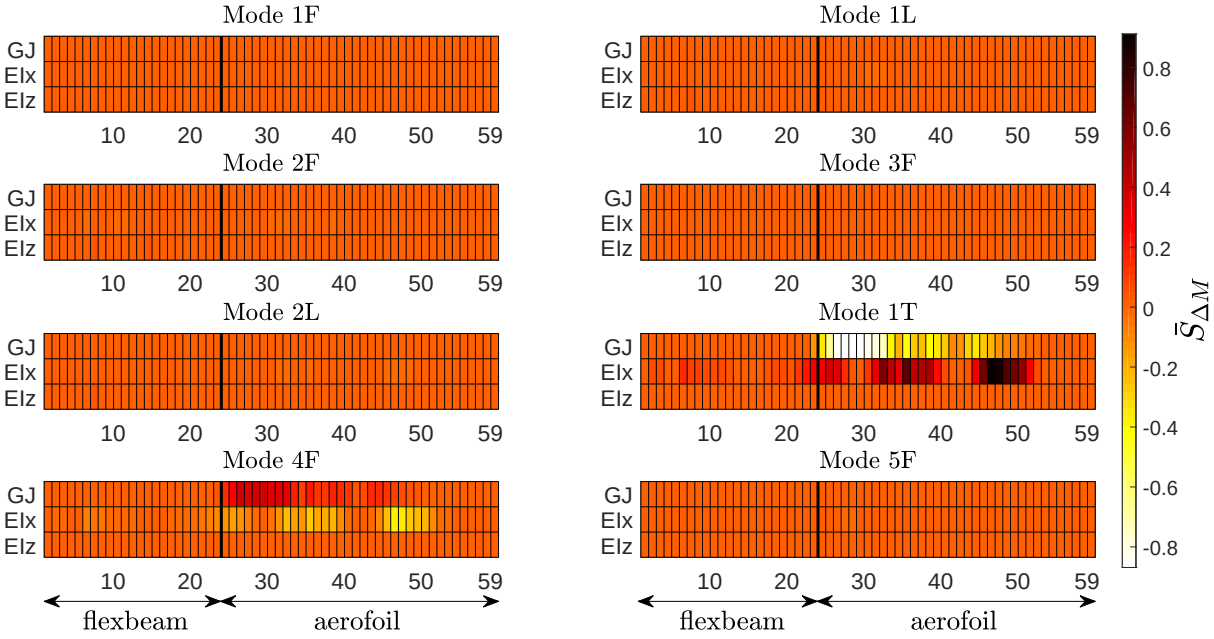

Figure 5.24: MAC sensitivity with updated BC

5.4.3 Updating structural parameters

The overall FEMU methodology is divided in a three-step procedure: (1) adjustment of BC, (2) updating the torsional stiffness GJ, followed by (3) updating the out-of-plane stiffness EI_x. As Step 1 was already performed in Section 5.4.1, the focus is put on the remaining indirect model updating process. Figure 5.25 shows the flow chart for the updating procedure starting from the initial FE model to the updated FE model with the use of experimental data. Incorporated criteria are used to end the updating procedure if the following accuracy is achieved for all target modes: $f < 15\%$, MAC > 0.8. The indirect model updating process uses two iterations, which includes updating GJ (Step 2) and EI_x (Step 3). If the criteria ($f < 15\%$, MAC > 0.8) is not reached the third iteration is introduced to relax the criteria by accepting a compromise between the updated modal parameters.

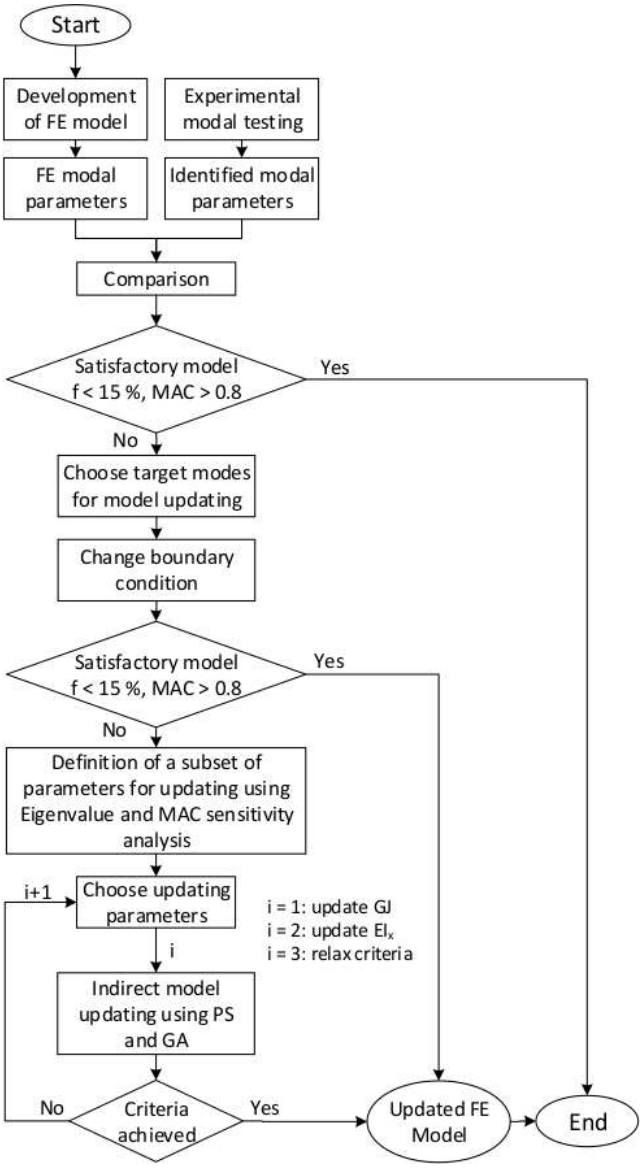

Figure 5.25: FEMU flow chart

Only a few structural nodes were updated to keep the computational cost as low as possible. If the structural updating parameter resulted in a MAC sensitivity change it

was considered for the updating procedure. Table 5.8 summarises the updating variables and range described as a percentage of the rotor radius R.

Table 5.8: Summary of updating parameters

Step	Description	Parameters	Rotor radius R (%)
1	scalar spring constant	c_f, c_t	5
2	torsional stiffness	GJ	28 - 76
3	out-of-plane stiffness	EI_x	24 - 92

Apart from choosing the updating parameters, a suitable optimisation algorithm has to be selected for this task. Genetic algorithms (GA) are often used for model updating problems because they can deal with continuous as well as discrete design variable problems [239, 241]. The GA approach uses large search spaces and it can find the global minimum amongst multiple local minima [241]. Another effective optimisation algorithm is the pattern search (PS). Findler [242] describes that PS *"generates and maintains multi-dimensional search directions"* to find a global minimum. A comparative study based on Basak et al [243] shows that PS finds the best value in a smaller search space and less computing time than GA. Other optimisation algorithms are utilised in FEMU, such as the particle swarm [238] or multi-objective algorithm [244]. Here, PS and GA were utilised and the results were compared with each other. The following cost function was implemented [245]:

$$J(p) = W^T r(p) \tag{5.4.1}$$

where p describes the updating structural parameters vector, r is the residual vector, and W is the weighting matrix:

$$W = \begin{bmatrix} \alpha \frac{1}{f_{X_1}^2} \\ \vdots \\ \alpha \frac{1}{f_{X_m}^2} \\ \beta \frac{1}{MAC_1^2} \\ \vdots \\ \beta \frac{1}{MAC_m^2} \end{bmatrix} \tag{5.4.2}$$

where m indicates the number of identified frequencies, α is the natural frequency weighting factor, β is the mode shape weighting factor. The weighting factors were chosen based on experience. For example the weighting factor for $\alpha = 0.2$ so that the natural frequencies were not altered significantly, yet, still allows some degree of adjustment for Mode 1L and 2L. $\beta = 0.8$ was selected as mode shape weighting factor to include the modes of interest in the updating process. To keep the total function value (error) as small as possible a weighting value of zero eliminates modes not being considered. The residual vector $r(p)$ can be written:

$$r(p) = \begin{bmatrix} r_e(p) \\ r_s(p) \end{bmatrix} = \begin{bmatrix} (f_{X_1} - f_{A_1})^2 \\ \vdots \\ (f_{X_m} - f_{A_m})^2 \\ 1 - MAC_1 \\ \vdots \\ 1 - MAC_m \end{bmatrix} \tag{5.4.3}$$

where r_e is the residual for eigenvalues and r_s is the residual for mode shape correlation. Finally, the cost function Eq. 5.4.1 can be minimised to find its optimal solution for the parameter vector p. Figure 5.26 compares the number of iterations required for each updating step for PS and GA. It can be seen that the function value for PS is decreasing and converging over a relatively short iteration time. A convergence is evident for GA, yet, a large design space is used to find the global minimum. The advantage of PS is that it reaches a quick convergence, especially if the function value is already close to the minimum. Using this method, the computational cost can be reduced significantly because the optimisation can be stopped manually when the function value is starting to converge. Even after 10000 iterations, the function value varies a lot and consequently care has to be taken when the optimisation process is terminated.

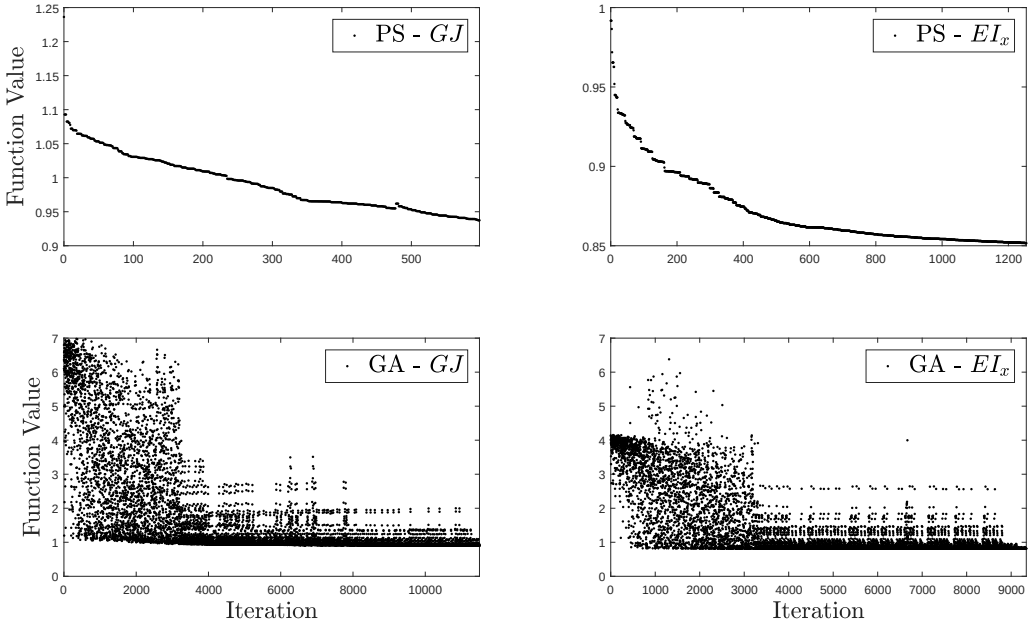

Figure 5.26: Iteration of optimisation algorithm

Comparable results are obtained with the early terminated PS optimisation algorithm and the much longer run of the GA algorithm. Tables 5.9 and 5.10 summarise and correlate the achieved MAC and frequency for each updating step for both optimisation algorithms. It can be seen that although the optimisation process was stopped before a global minimum was found the torsional mode shape correlation was improved by another 26.2% which results in a total improvement of more than 55% between initial and updated FE mode. Furthermore, as intended the first 5 MAC remained over a value of 0.8. Due to the strong coupling of the torsional bending components, the mode shape correlation of the 7th mode was degraded by more than 33%, whereas an improvement

of approximately 13% was achieved for the 8th mode shape correlation. As the average percentage difference is essentially the same the benefit of use PS over GA is confirmed.

Table 5.9: Comparison of MAC after each updating step

Mode number	Mode type	FE Before	Step 1 BC	Step 2 PS	Step 2 GA	Step 3 PS	Step 3 GA	Difference (%) PS	Difference (%) GA
1	1st flapping	0.990	0.992	0.992	0.992	0.992	0.993	0.20	0.30
2	1st lagging	0.949	0.947	0.947	0.947	0.931	0.946	-1.9	-0.32
3	2nd flapping	0.937	0.947	0.947	0.947	0.920	0.933	-1.85	-0.43
4	3rd flapping	0.951	0.967	0.967	0.967	0.960	0.941	0.94	-1.06
5	2nd lagging	0.861	0.833	0.834	0.833	0.824	0.828	-4.49	-3.99
6	1st torsion	0.240	0.409	0.480	0.493	0.535	0.554	55.14	56.68
7	4th flapping	0.843	0.725	0.676	0.666	0.632	0.625	-33.39	-34.88
8	5th flapping	0.813	0.904	0.904	0.904	0.933	0.934	12.86	12.96

The updating procedure aimed to keep the natural frequency constant. Table 5.10 shows the change in the natural frequency after each step. Comparing the outcome with the experimental (FE vs IHT) average percentage value of 10.3%, PS resulted in an increase of only 1.4% and GA in an increase of only 0.34%.

Table 5.10: Comparison of frequency (Hz) after each updating step

Mode number	Mode type	f_X	f_A	Step 1 BC	Step 2 PS	Step 2 GA	Step 3 PS	Step 3 GA	Exp. error (%) before	Exp. error (%) PS	Exp. error (%) GA
1	1st flapping	1.02	0.90	0.90	0.90	0.90	0.89	0.94	11.76	12.75	7.84
2	1st lagging	2.63	3.41	3.40	3.40	3.40	3.39	3.42	-29.66	-28.90	-30.04
3	2nd flapping	5.43	4.98	4.99	4.99	4.99	4.73	4.79	8.29	12.89	11.79
4	3rd flapping	15.55	15.28	15.27	15.27	15.27	15.21	15.36	1.74	2.19	1.22
5	2nd lagging	17.80	22.72	22.72	22.76	22.77	22.72	22.74	-27.64	-27.64	-27.75
6	1st torsion	28.17	28.59	29.01	29.20	29.23	29.21	29.27	-1.49	-3.69	-3.90
7	4th flapping	30.04	29.98	29.93	29.92	29.92	29.87	29.89	0.20	0.57	0.50
8	5th flapping	51.49	52.17	50.29	50.28	50.28	49.10	50.62	-1.32	4.64	1.69

The results presented in Tables 5.9 and 5.10 are reflected in the variation of mode shapes as depicted in Figure 5.27. The experimental mode shape is compared with the numerically obtained results highlighting the difference between the original and updated mode shape using PS and GA. The amplitude, as well as radius position of the mode shapes, are normalised to the outermost position for ϕ_x and to the amplitude at 50% rotor radius for ϕ_z. Figure 5.27(a) clearly shows that Mode 1T for both lagging direction ϕ_x and flapping direction ϕ_z has improved. This was already shown by the MAC value of achieving a 55% improvement. The discrepancy of the measurements of the first two nodes in ϕ_x direction could have been induced by the difference in BC between analytical and experimental environment. Figure 5.27(b) shows that the ϕ_z of Mode 4F has degraded compared to the initial mode shape. It is noted, that even though a large difference in iteration time for PS and GA is evident similar mode shape trends are achieved.

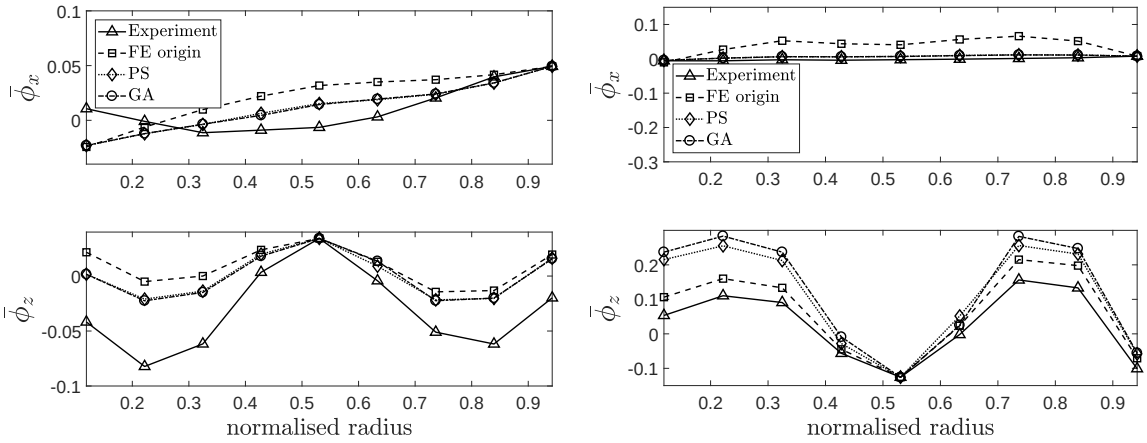

(a) Mode 1T (b) Mode 4F

Figure 5.27: Updated normalised displacement mode shapes $\bar{\phi}$

5.4.4 Updating damping coefficients

Finally, the structural damping model is updated using results from the experimental test data. A correct structural damping model is very important not only for predicting the life of a blade, but also for aeroelastic and stability analyses, such as ground or air resonance [246, 247]. IHT was needed to identify the blade's structural damping values as no quantitative values were known. The damping model was updated with the values obtained from IHT 1 by calculating the damping coefficients a_0 and a_i using Eq 4.4.9.

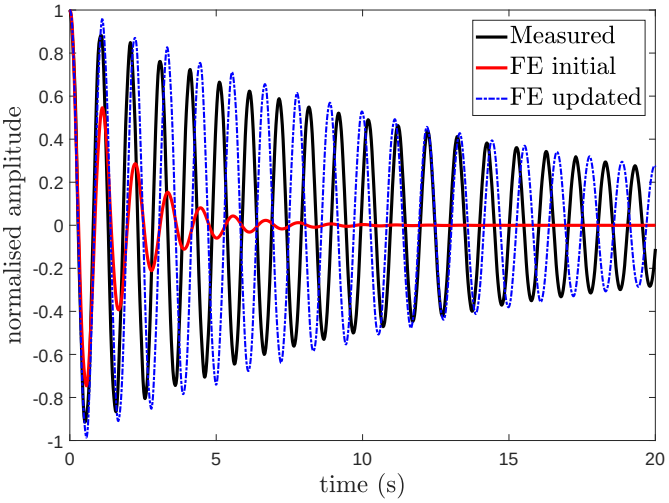

Figure 5.28: Tip motion - Mode 1F

Figure 5.28 shows a comparison of the normalised transient response measured at the blade tip under Mode 1F frequency excitation, with the initial and updated model. It is apparent that the initial assumption of ζ=0.1 overestimated the structural damping. A small difference in the logarithmic decrement and the modal frequency can still be observed.

5.5 Summary

This chapter summarises results obtained from structural loading tests and EMA utilising AVT and IHT. Despite uncertainties in material properties and simplifications within the structural modelling approach, experimental testing showed significant predictive capabilities for both displacement and strain estimation. While a correlation for the natural frequencies with an average percentage value of 10.26% was achieved, all MAC values were above 0.8, except that of the 1st torsional mode which was 0.24. This discrepancy highlighted the need for FEMU and structural modal properties were updated in virtue of experimental test results. A multi-step indirect FEMU approach was proposed that targeted the modes of interests in isolation via specific weighting factors. An assessment of updating parameters was carried out by adopting a modal assurance criterion sensitivity in addition to the commonly used eigenvalue sensitivity. Challenges associated with updating a finite element model defined by a large parameter set and strongly coupled structural modes were addressed by trading off the achieved accuracy with the computational cost. Although another set of experimental tests should have been performed to validate the updated FE model, the presented outcome provides the baseline for investigating the capabilities of the fibre optic instrumentation systems.

This page is intentionally left blank.

CHAPTER 6

Characterisation of blade dynamics

While the previous discussions have focused on the development of the computational framework and validating the FE model, this chapter explores the capabilities of highly advanced fibre optic sensors, such as multiplexed arrays of FBGs and the novel DFOSS system. This chapter begins by presenting the reader with a numerical exploration study of shaker input design and adopted post-processing methods required for the experiments. This is followed by the presentation of an error minimisation sensor placement approach that is valid for a range of sensor types and aims to recover displacement and strain mode shapes from the structure. The assessment of fibre optic sensor performance was carried out via a series of ground vibration tests using the full-scale H135 rotor blade to prove the suitability and pinpoint benefits of each instrumentation system for capturing blade structural dynamics. The chapter concludes by discussing optimal FBG strain sensor locations from a theoretical and practical point of view in light of the collected data set. The outcome of this chapter is later used for the assessment of sensor performance for damage detection.

6.1 Input design

Input design for experimental testing is an important pre-test step and is required to ensure that correct shaker settings are selected. This is necessary for safe execution of the test and to ensure test equipment limitations are not exceeded (maximum shaker travel range ± 12.7 mm) of the available modal exciter type[1]. The structure's response was studied by applying a frequency sweep at several spanwise stations and under a variety of shaker drive forces. The logarithmic frequency sweep input s is multiplied by the force input vector (see Eq. 4.4.3) and can be described mathematically by [248]:

$$s(i) = \sin(\varphi(i)) \tag{6.1.1}$$

[1]The modal exciter is type 4825 from Brüel & Kjær (a summary of the experimental equipment can be found in Appendix G.2.3).

$$\varphi(i) = \omega_0 t(i) + c_2(\omega_1 - \omega_0)\left[\frac{T}{c_1} e^{c_1 t(i)/T} - t(i)\right] \tag{6.1.2}$$

where $t(i) = i\Delta t$ is the product of $i = 0, 1, 2, ..., N-1$ and the sampling time Δt. T is the time length, $T = (N-1)\Delta t$, and $[\omega_0, \omega_1]$ rad/s is the frequency band. The coefficients $c_1 = 4$ and $c_2 = 0.0187$ have been found to work well in practice [248, 249]. Figure 6.1 demonstrates how the displacement z_i at the ith excitation input location varies with a shaker drive force ranging from 1-50 N. Non-linear behaviour is evident in particular for higher drive forces.

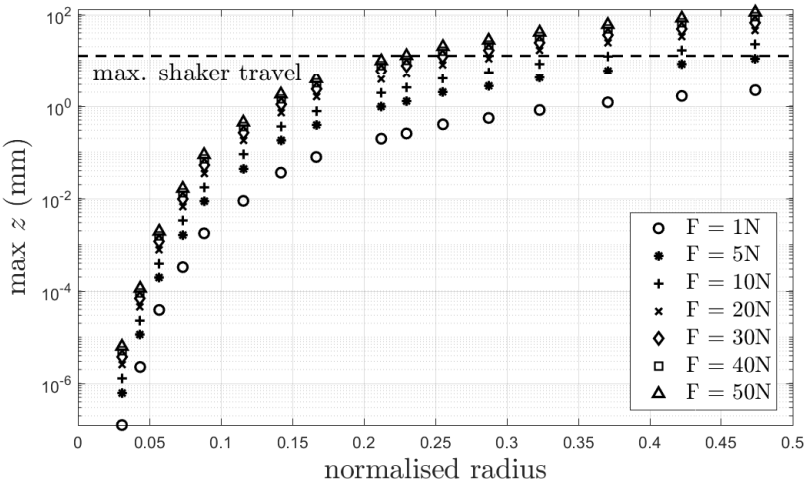

Figure 6.1: Estimated structural response at excitation input

The maximum shaker travel of ± 12.7 mm is indicated by the horizontal line in Figure 6.1. Possible drive force size versus location was also investigated and for safety reasons took into account the maximum travel range together with a criterion for which the blade tip displacement is less than 100 mm. Results are presented in the matrix plot in Figure 6.2, highlighting that an admissible excitation location is close to the blade root.

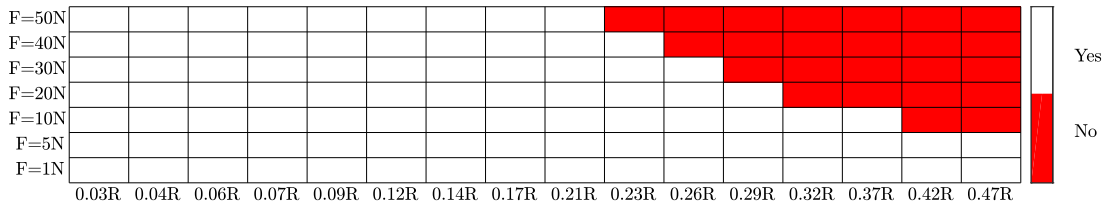

Figure 6.2: Permissible shaker drive force size and location

Methods for extracting modal parameters were investigated in the simulation environment before the tests were carried out. A frequency sweep from 0 Hz to 50 Hz was applied to examine the numerical modal response. Mode shapes were extracted using an output-only methodology based on time-domain decomposition (TDD) as proposed by Kim et al [250]. Time histories of flap acceleration a_z and lag acceleration a_x of each node was transformed into the frequency domain with a Fast Fourier transform (FFT) and is illustrated in Figure 6.3. The frequency spectra are presented as a function of rotor radius and clearly highlight the structure's natural frequencies; recognisable through the areas

of resonance. This magnitude shows the dominance of each mode. For instance, the resonant mode at 15 Hz was identified as Mode 3F because a significantly higher magnitude is observable from the flapping acceleration than from the lagging component. Although a clear lagging mode is evident at 23 Hz, the structural coupling is also evident for most of the modes. This surface plot gives additional information about the corresponding nodal points, such as for Mode 3F. These are located at 55% and 90% rotor radius. This can be further verified with the 3F mode shape in Figure 6.4. These mode shapes were extracted via TDD from time history data at five accelerometer positions, arbitrarily chosen to be at 20%, 40%, 60%, and 100% rotor radius. This outcome demonstrates the suitability of this methodology for extracting modal properties because the experimental mode shapes match well with the FE model for noise-free conditions.

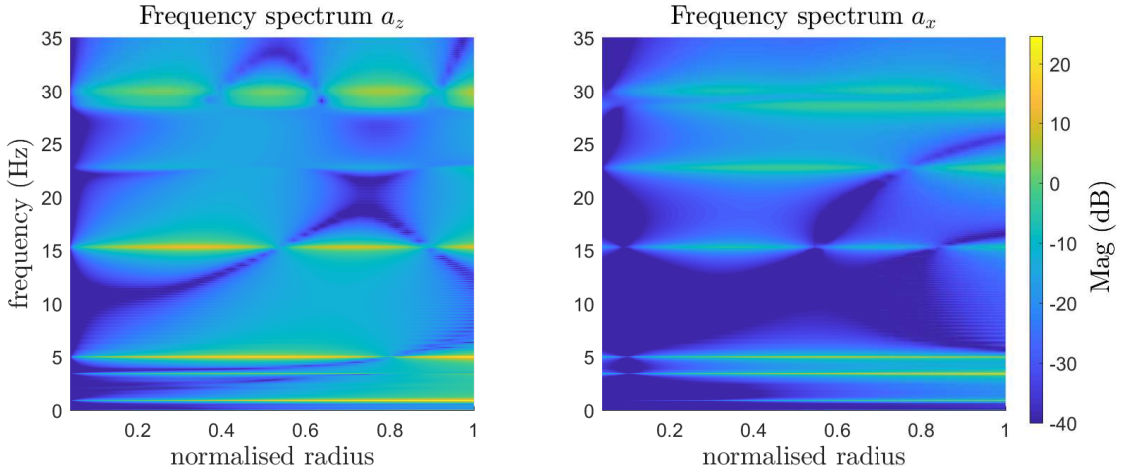

Figure 6.3: Surface plot of frequency spectra

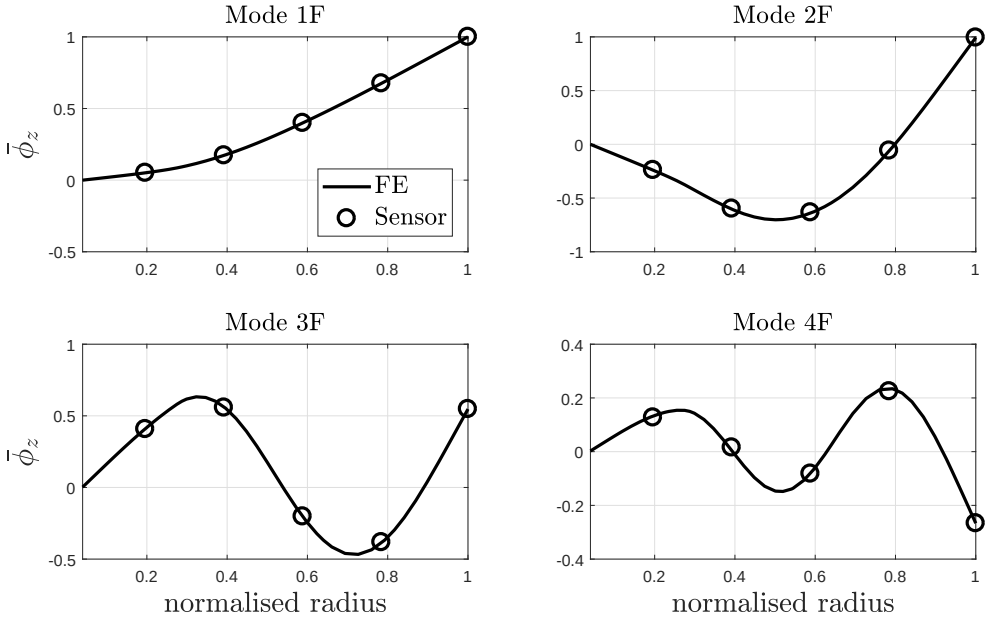

Figure 6.4: TDD extracted normalised blade flap displacement mode shapes $\bar{\phi}_z$

6.2 Sensor placement

The correct choice of sensor positions is important if the accurate frequency and mode shape extraction are to be achieved with a minimum number of sensors. A methodology is proposed that produces an "optimal" one-dimensional sensor distribution valid for either accelerometer, displacement or strain sensors.

6.2.1 Placement based on visual inspection

The simplest method for identifying suitable sensor positions is by visually inspecting the mode shapes and placing the sensors at points with large amplitude. This approach provides a quick estimate of the maximum number of sensors, while in the relevant literature it is suggested that at least the same number of sensors as a number of modes should be considered [15]. Figure 6.5 shows the first seven displacement mode shapes of the blade. The maximum number of sensors can be determined by assuming the availability of triaxial accelerometers, that was placed at the highest amplitude of each mode shape and then mapped to the blade planform.

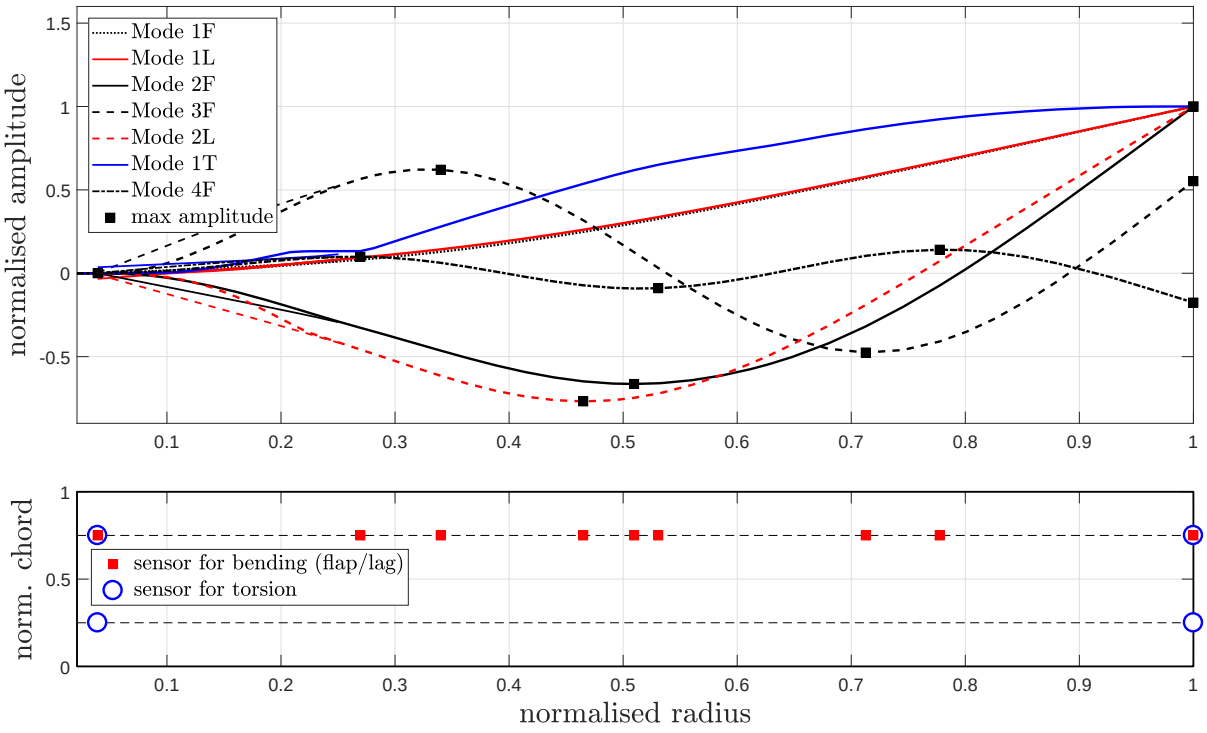

Figure 6.5: Visual inspection method using the H135 rotor blade

For determining the torsional mode shape the accelerometers have to be placed off-centre, which leads to a requirement for eleven accelerometers. This sensor mapping exercise shows the need for a small concentration of accelerometers at around 50% radius, because the highest amplitude for Mode 2F, 2L and 4F is expected in this area. To reduce the number of sensors the three accelerometers can be replaced by only one to capture the local amplitude of these three modes if a compromise in accuracy is accepted.

It also could be argued that nine instead of eleven sensors do not significantly change the data acquisition data nor duration of post-processing time. However, if the sensors

are used for continuous health monitoring over extended periods of time this needs to be considered. For instance, under the assumption that the recording of 10 sensors with a sampling rate of 1250 Hz over 1 min leads to a 10 MB dataset, a data size of 600 MB is obtained per hour. For this reason, the number of sensors should be kept to a minimum.

6.2.2 Placement based on error minimisation

This methodology aims to minimise the total error between the theoretical mode shape ϕ_{ij} and measured mode shape $\hat{\phi}_{ij}$ with $j = 1, 2, ..m$, where m is the maximum number of mode shapes to be identified, and $i = 1, 2, ..n$, where n is the total number of nodal points. Assuming that the sensors are located at spanwise positions y_k with $k = 1, 2, ..p$, where p is the maximum number of sensors, the measured mode shape $\hat{\phi}_{ij}$ is obtained by linearly interpolating between the nodal points y_i of the theoretical mode shape ϕ_{ij}. This is schematically shown in Figure 6.6.

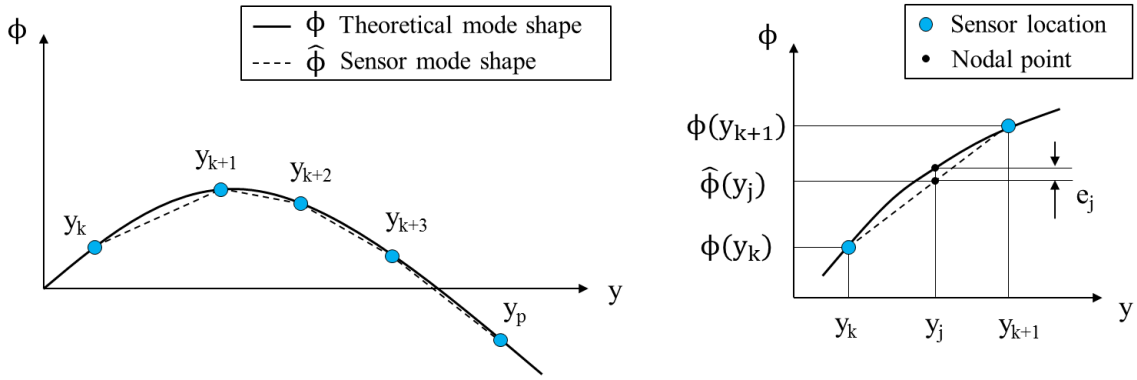

Figure 6.6: Schematic representation of sensor placement approach

To calculate the error e_{ij} $(= \phi_{ij} - \hat{\phi}_{ij})$ between the measured mode shape $\hat{\phi}_{ij}$ and the theoretical model shape ϕ_{ij} at each nodal point i for the jth mode, the following equation is used to interpolate between two sensor positions y_k and y_{k+1}:

$$\hat{\phi}_{ij} = \frac{\phi_{iy_k}(y_{k+1} - y_j) + \phi_{iy_{k+1}}(y_j - y_k)}{(y_{k+1} - y_k)} \tag{6.2.1}$$

The sensors at position y_k are identified by minimising the following cost function:

$$J = \sqrt{\frac{1}{n}\sum_{i=1}^{m}\sum_{j=1}^{n}(\phi_{ij} - \hat{\phi}_{ij})^2} \tag{6.2.2}$$

Although method is computationally efficient for identifying the optimal sensor position in a one-dimensional manner, it requires an accurate structural model and any uncertainties within the model will consequently lead to inaccurate sensor positions. Each mode shape is treated with equal importance that is essential for recovering experimental mode shapes of interest. Furthermore, this method is suitable for accelerometers, displacement

or strain sensors and only requires displacement or mode shape matrix to be provided as an input to the algorithm. The accuracy of the experimentally extracted mode shapes is dependent on the number of sensors and the number of numerical mode shapes considered for optimisation. This is proven in Figure 6.7 that shows J as a function of sensors and mode shapes highlighting that at least the same number of sensors as mode shapes should be deployed to keep the total error J to a minimum.

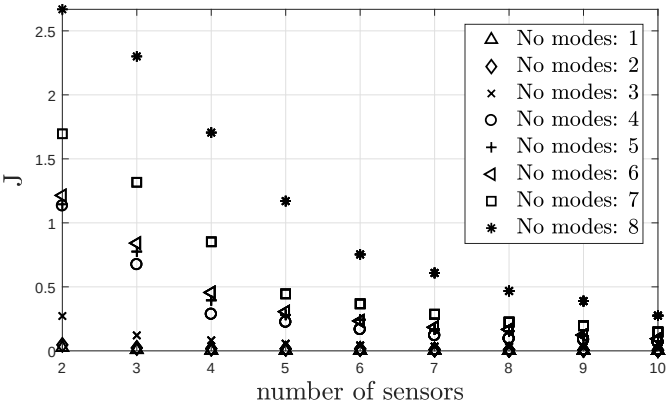

Figure 6.7: Variation of the cost function with number of sensors and modes

Although this methodology works well for determining local flapping and lagging modes, a two-dimensional sensor placement approach is needed for identifying the torsional mode. The torsional component can be measured by mounting displacement or accelerometers at the leading and trailing edges, or by mounting strain sensors at 45° with respect to longitudinal axis [8] to measure the shear strain due to torsion. However, the focus of this work was limited to the identification of flapping and lagging components due to simplifications and assumptions in the structural model.

6.2.3 Validation of sensor placement method

A test case using a cantilevered aluminium strip was prepared to validate the sensor placement based on error minimisation. Before the optimisation was carried out a numerical model was developed in Nastran using the material properties and dimensions in Table 6.1. The estimated normalised displacement mode shapes and associated natural frequencies are shown in Figure 6.8. The spanwise sensor locations for five uni-axial accelerometers (ACC (1D)) in Figure 6.9(a) were optimised considering the first five bending mode shapes. The result is shown in Table 6.2, while it can be observed that the initial guess (random position) was an effective starting point for reconstructing the first five mode shapes.

For the experimental testing, the strip was clamped to a rigid structure as shown in Figure 6.9(b) and the accelerometers were placed at the random and optimised positions. The strip was excited with a Random on Random (RoR) vibration in the frequency range of 0.5-200 Hz, while the input was introduced via a stinger that was adhered to the underside of the strip. It was found that the stinger excitation point (located at 22% length) restricted the free oscillation of the first mode, and hence, this mode could not be identified. The stinger position was limited by the rig structure and sizing of the stinger housing. After collecting the time history, TDD was applied to extract mode shapes and

Table 6.1: Properties of cantilever aluminium strip

Properties	Values
Length	0.9 m
Width	0.085 m
Thickness	0.0025 m
Young's Modulus	69 $\times 10^9$ N/m^2
Density	2700 kg/m^3
Poisson's ratio	0.334

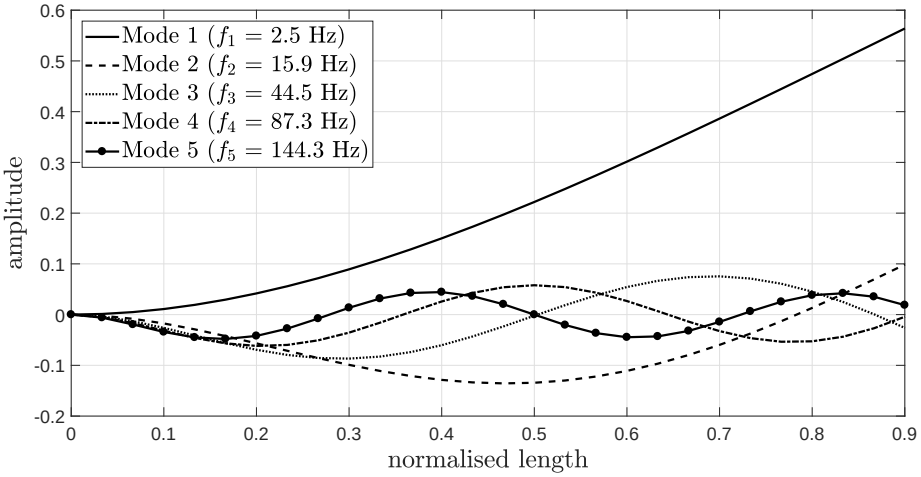

Figure 6.8: Displacement mode shapes ϕ of cantilever strip (out-of-plane bending)

Table 6.2: Accelerometer positions on aluminium strip

Sensor number	Initial guess (m)	Optimised position (m)
1	0.10	0.14
2	0.30	0.33
3	0.50	0.53
4	0.70	0.71
5	0.90	0.89

natural frequencies. Figure 6.10 presents the experimental mode shapes, while Figure 6.11 outputs the local error obtained for each interpolated nodal point. Results yield a total error reduction from $e_R = 5.7\%$ to $e_O = 3.8\%$ for the optimal solution. Besides this quantitative evaluation, the MAC provides another measure for validating the results for the optimal sensor locations. Table 6.3 presents the computed MAC for analytical and experimental mode shapes, resulting in an average MAC of 0.98 for the initial guess and 0.99 for the optimal solution.

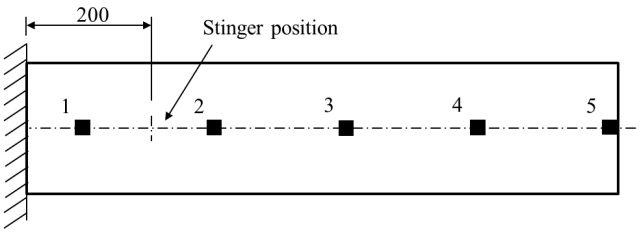

(a) Accelerometer positions randomly distributed

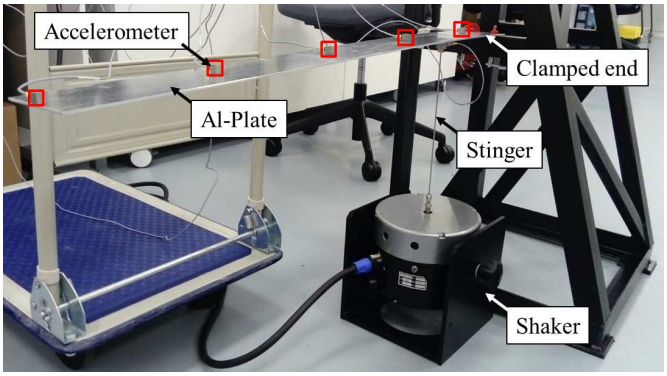

(b) Test bench

Figure 6.9: Experimental set-up of aluminium cantilever strip

Table 6.3: Comparison of mode shape pairing of aluminium cantilever strip

Mode number	Mode type	MAC Initial guess	MAC Optimal	MAC improvement (%)
2	2nd bending	0.979	0.991	1.2
3	3rd bending	0.986	0.986	0.0
4	4th bending	0.972	0.979	0.7
5	5th bending	0.987	0.991	0.4

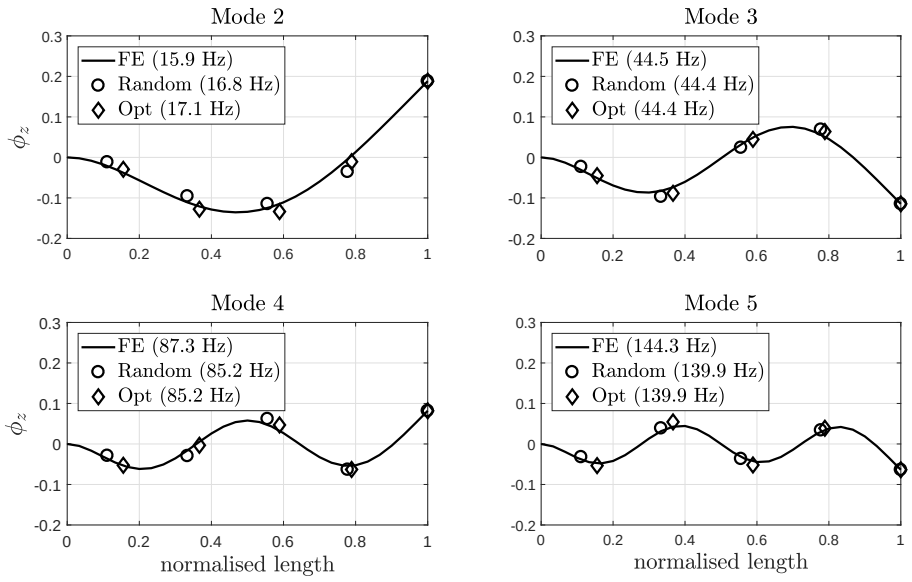

Figure 6.10: Comparison of experimental and numerical displacement mode shapes

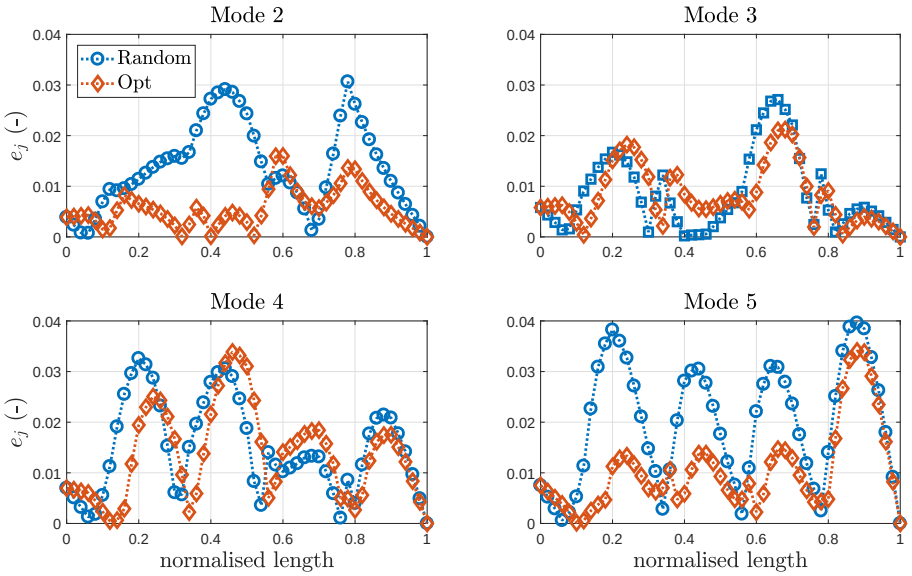

Figure 6.11: Error analysis of sensor placement approach

6.3 Fibre optic instrumentation

The novel DFOSS system together with FBGs was deployed on the H135 rotor blade to collect experimental strain and blade deformation data. Here, comparisons and assessments are carried out against ACC (1D) and the validated FE model. This allows the shape sensing technology to be validated while pinpointing the pros and cons of each instrumentation system for characterising blade dynamics.

6.3.1 Experimental methodology

OMA was carried out on the rotor blade through a series of GVTs. For each test, the blade was excited either for 60 seconds using an RoR excitation waveform over a frequency range of 0-100 Hz or at a single frequency (dwell test). The test set-up as presented in Figure 6.12(a) shows that the excitation was introduced to the blade by a shaker via a stinger that was adhered to the pitch control cuff. Although it would have been ideal to excite the structure inboard of the equivalent flapping hinge, however, because of space limitations the stinger could only be attached at approximately 13% rotor radius. Figure 6.12(b) shows the sensing elements, comprising ACC (1D), FBG sensor arrays and the DFOSS sensing cable, mounted on the blade.

Five ACC (1D) as shown in Figure 6.13(a), each with its measurement axis oriented normal to the top surface of the blade, were located along the aerofoil quarter chord line, as was the DFOSS system. The accelerometer positions were based on the method described in Section 6.2.2, while both fibre optic instrumentation systems with embedded reflectors and gratings were pre-manufactured. For strain measurement, a total of six optical fibres were used, three mounted on the top surface of the blade and three on the bottom surface, where corresponding fibres on the top and bottom surfaces were located at identical chordwise positions. Each optical fibre contained an array of nine

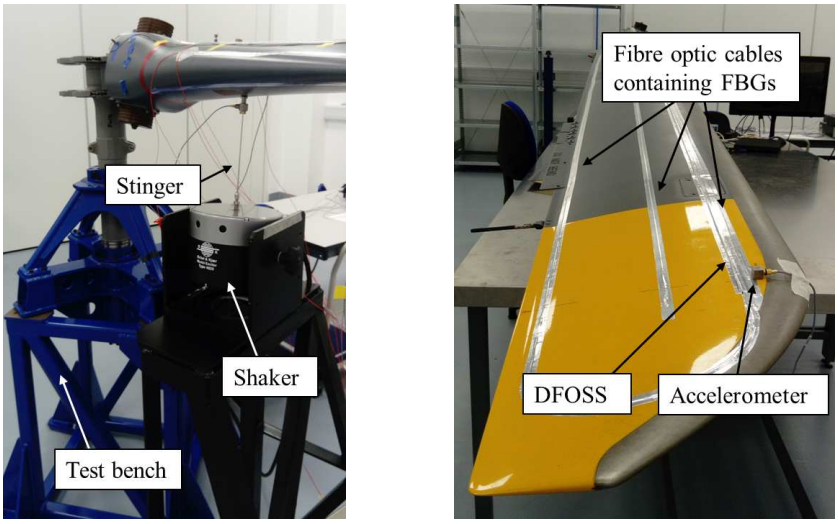

(a) Test bench (b) Location of instrumentation

Figure 6.12: Experimental arrangement

wavelength-division multiplexed FBGs (see Figure 6.13(b)). The chordwise locations of the optical fibres were close to the leading edge at the quarter chord line, at the half chord position, and close to the trailing edge. The FBG strain sensors were interrogated using a Smart Fibres SmartScan interrogator, which is capable of interrogating four FBG arrays with up to 16 gratings each at a data rate of 2.5 kHz, allowing four of the sensor arrays mounted on the blade to be monitored simultaneously. The FBGs, with centre wavelengths distributed in the 1528-1568 nm wavelength band, were fabricated in hydrogen loaded SMF-28 optical fibre. Correct bonding is important for the FBG sensors to ensure appropriate strain transfer from the structure to the sensor. The sections of fibre containing the FBG sensors were attached to the blade using a cyanoacrylate adhesive and, in order to protect the optical fibres, strips of aluminium speed tape were used to cover the length of each FBG array. Figure 6.13(d) shows a cross section of the installation of the optical fibres on the blade.

The DFOSS system as explained in Section 3.3.2.3 within each of the three optical fibres broadband low-reflectivity FBGs act as in-fibre reflectors R1 to R7 that define the boundaries of six fibre segments that form long gauge-length interferometric strain sensors. The three fibres were mounted in a custom-designed 3D printed support structure constructed to hold the fibres in the triangular arrangement, depicted in Figure 6.14(a) and 6.14(b). Care was taken to ensure that the corresponding reflectors R1 to R7 in all three fibres were co-located along the length of the support structure. Appropriate processing of the differential strains experienced by the corresponding fibre segments in the three fibres allows the direct independent measurement of the slope angle in the flapping and lagging directions [19], which is sampled at reflector locations R2 to R7 in Figure 6.13(c). The slope angles are determined relative to the angle of the measurement origin of the system, which is located at reflector R1 [19]. The only assumption required to obtain the desired shape deformation data from the measured slope angle data is the use of an interpolation (using a cubic spline) between the sample points to permit spatial integration of the slope angle. Note that this interpolation method does not require knowledge of the underlying structure. For continuously bending structures like a rotor

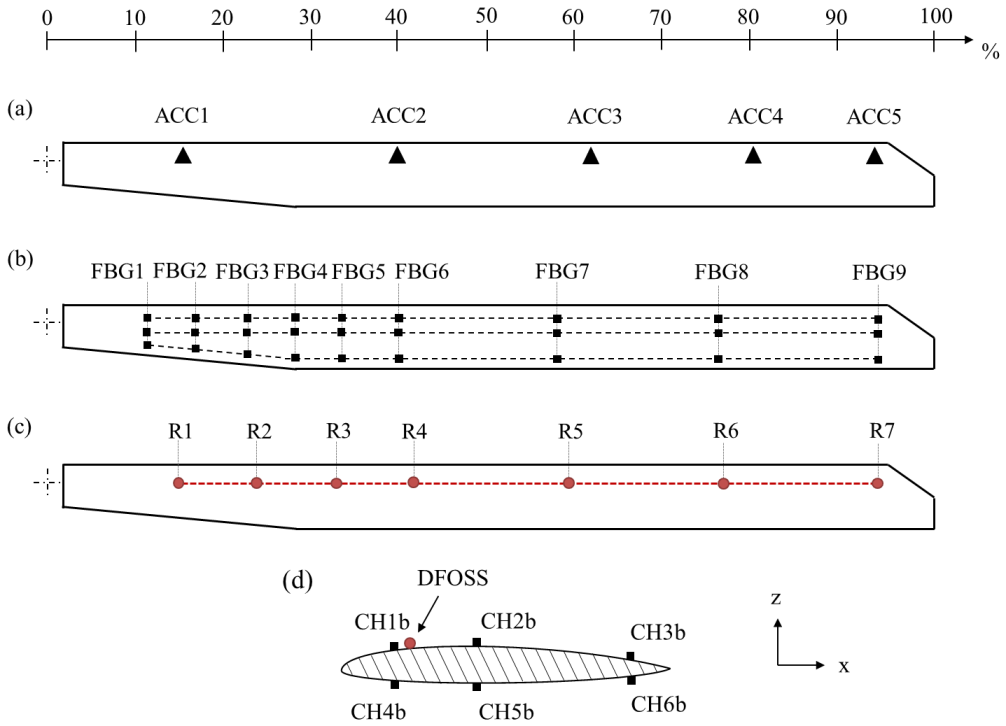

Figure 6.13: The positions of the five ACC (1D) are shown in (a), while the location of FBG arrays is shown in (b). The DFOSS cable with the positions of the reflectors defining the measurement sample points is shown in (c). Finally, (d) shows the the cross section of the blade.

blade, the only consideration involved in defining the numbers of reflectors required is analogous to the Nyquist sampling theorem in electrical engineering, requiring that the spatial density of sample locations is sufficient to follow the expected structural bending curves. The strains experienced by the fibre segments are interrogated using the range resolved interferometry concept detailed in [191]. The fully-enclosed interrogation unit, capable of acquiring data at rates up to 49 kHz, is depicted in Figure 6.14(c). In each of the three fibres forming the cable, Figure 6.14(a), the seven low reflectivity broadband FBGs in each fibre were arranged, as shown in Figure 6.13(c) such that the first three segments were each of length 0.46 m length and the remaining three segments were length 0.92 m. A smaller spacing towards the root of the blade, where the flexbeam was connected to the main blade, was chosen because higher slope angle changes were expected in this region. The fibre support structure was secured to the upper surface of the blade using aluminium speed tape. Given the geometry of the fibres in the support structures and the strain resolution of the system, the angular measurement resolution is $\approx 0.2 \times 10^{-6\,\circ} Hz^{-0.5}$, approximately constant across all reflector locations R2 to R7.

6.3.2 Modal frequency comparison

Initially, the performances of the DFOSS, the FBG strain sensors and the ACC (1D) were compared during a GVT. Each acquisition system recorded the structural response as a time series, where the sampling frequencies were 0.25 kHz for the accelerometers, 2.5 kHz for the FBGs and 1.5 kHz for the DFOSS system. Each sensor outputs data in a different

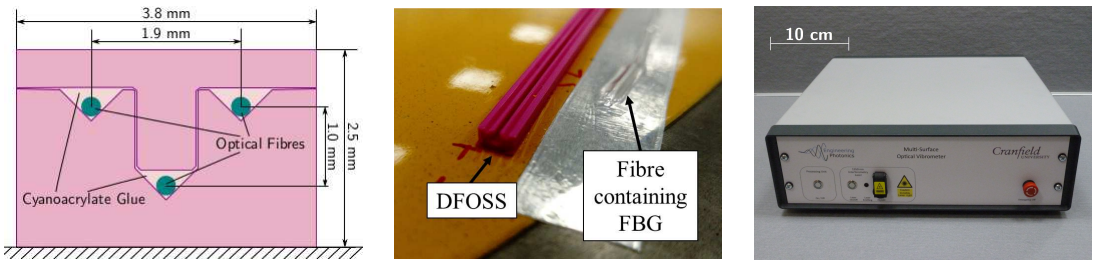

(a) Cross section of the sensor cable

(b) 3D printed DFOSS sensor rod prior to installation together with an FBG sensor

(c) Fully-enclosed interrogator unit

Figure 6.14: Detail of DFOSS system

physical unit: the accelerometers in m/s^2, the FBG data comprises the wavelength shift experienced by the grating, which is converted into strain using the conversion factor of 1.2 $\mu\epsilon$ pm^{-1} [156], while DFOSS provides slope angle measurements that are converted to local displacement in m using spatial integration of the interpolated slope angle curve.

The power content of the frequency spectra of the data from each technology was estimated using Welch's power spectral density (PSD) [251]. To investigate the sensitivity of each system, in all cases an RoR shaker drive force density of 0.1 N^2/Hz was chosen with a flat distribution across the chosen frequency bandwidth of 100 Hz, equating to a drive force of approximately 3 N RMS. As the blade was very flexible due to the absence of centrifugal loading, this drive force was sufficient to obtain adequate data quality from the measurements. Figure 6.15 compares the different PSDs obtained from sensors located on the top surface at the quarter chord line at approximately 40% and 60% of the rotor radius. While sensors ACC2 and FBG6 were used for the 40% rotor radius comparison, ACC3 and FBG7 provided measurements at approximately 60% rotor radius, see Figure 6.13 for exact locations. Note that the deformations curve for the DFOSS results can be obtained at arbitrary spatial resolution as a result of the continuous slope angle interpolation. Therefore, the evaluation locations of 40% and 60% could be directly selected.

The DFOSS data was separated into vertical and horizontal components, measuring flapping and lagging movements respectively. A total of nine resonance frequencies can be observed, exhibiting agreement of the resonance frequencies determined from each sensing system. At approximately 60% rotor radius, the peaks of the ACC3 and DFOSS system are more pronounced, while FBG6 is better able to capture structural modes at approximately 40% rotor radius. Only flapping components could be detected by the uni-axial accelerometers ACC1, ACC3, ACC4 and ACC5, while ACC2 also detected the torsion Mode 1T. The FBG sensor array located on the quarter chord line was able to measure only flapping modes, because the horizontal distance between the neutral axis and the surface is close to zero. The DFOSS system, on the other hand, was able to detect all nine resonance peaks due to its sensitivity to angular shapes (rather than surface strain), exhibiting its ability to measure biaxial components. Although exhibiting a small power content for Mode 1T, the DFOSS system was still able to detect the frequency of this mode at both radial locations. Comparing the vertical and horizontal components of the DFOSS system, a coupling between the structural modes is evident. Furthermore, a significant flapping/lagging coupling of Mode 1F was measured, which could have been

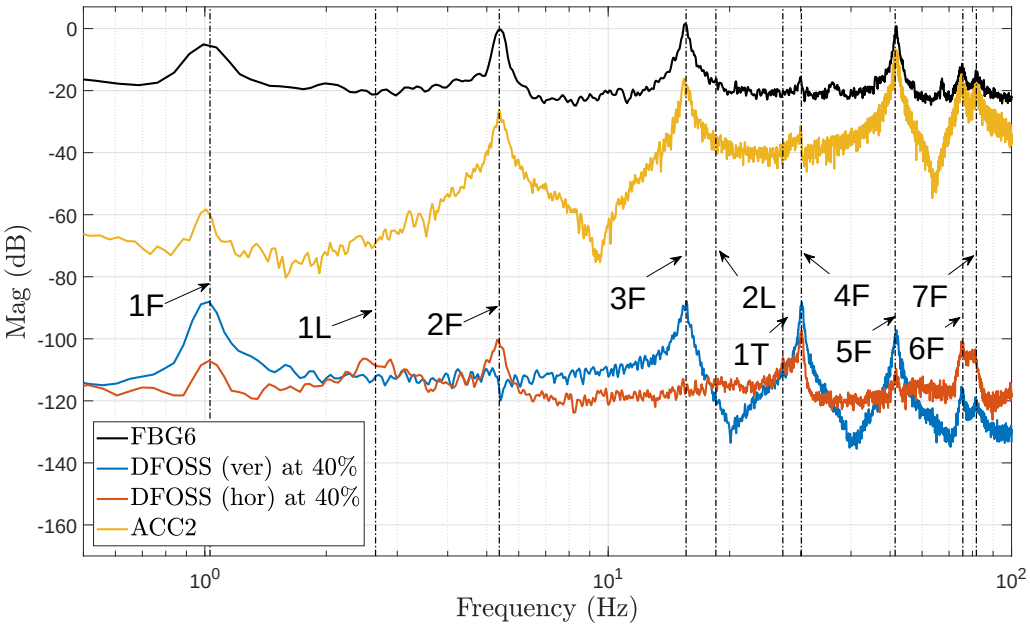

(a) Measurements taken at approximately 40% rotor radius

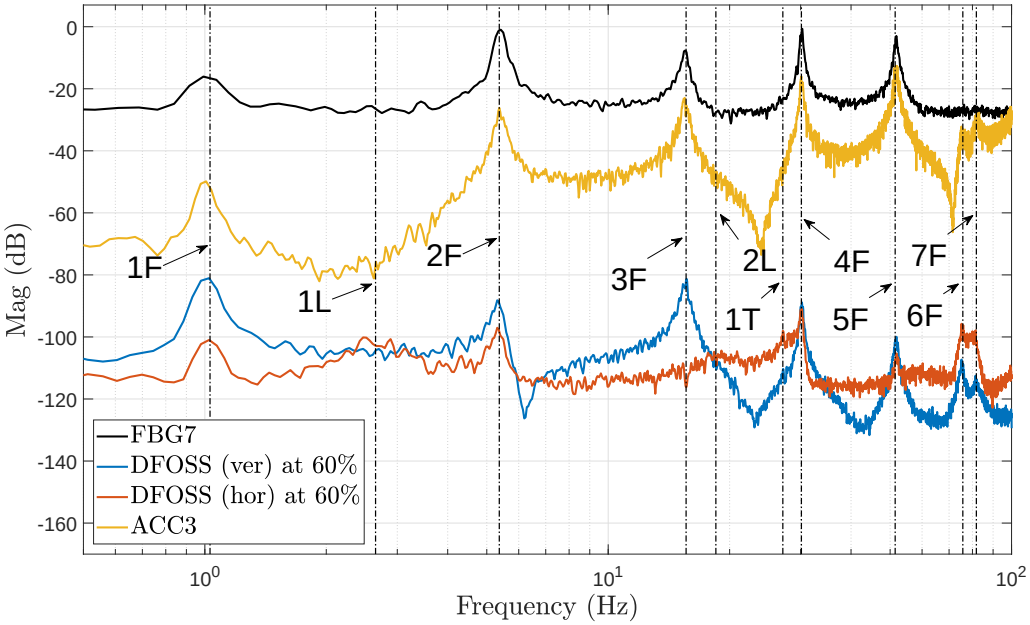

(b) Measurements taken at approximately 60% rotor radius

Figure 6.15: Comparison of PSD measured on the top surface at quarter chord line where the FBG (CH1b), ACC (1D), and DFOSS spectra

induced by a horizontal component of the movement of the stinger. Although the lagging and torsional modes could not be detected by the FBGs located at the quarter chord line in Figure 6.15, improved results were obtained from the FBGs mounted at the half chord or close to the trailing edge, as can be seen in Figure 6.16. Measurements at the trailing edge, CH3b and CH6b, show that both lagging and torsional modes can be captured. On the other hand, at the half chord position, CH2b and CH5b, Modes 1L and 1T are barely observable. This is expected from Eq. 4.4.13, which shows that the measured strain is a function of the distance from the sensor to the neutral axis. This outcome also verifies

the assumption that the neutral axis position for horizontal movement is approximately at the quarter chord line. A summary of the PSD for all FBG position can be found in Appendix H. The results indicate the potential of the use of the DFOSS sensing system for capturing the resonance frequencies of all modes within the relevant frequency range by collecting data at one span-wise location. It also shows the importance of distributing the FBG arrays optimally over the surface.

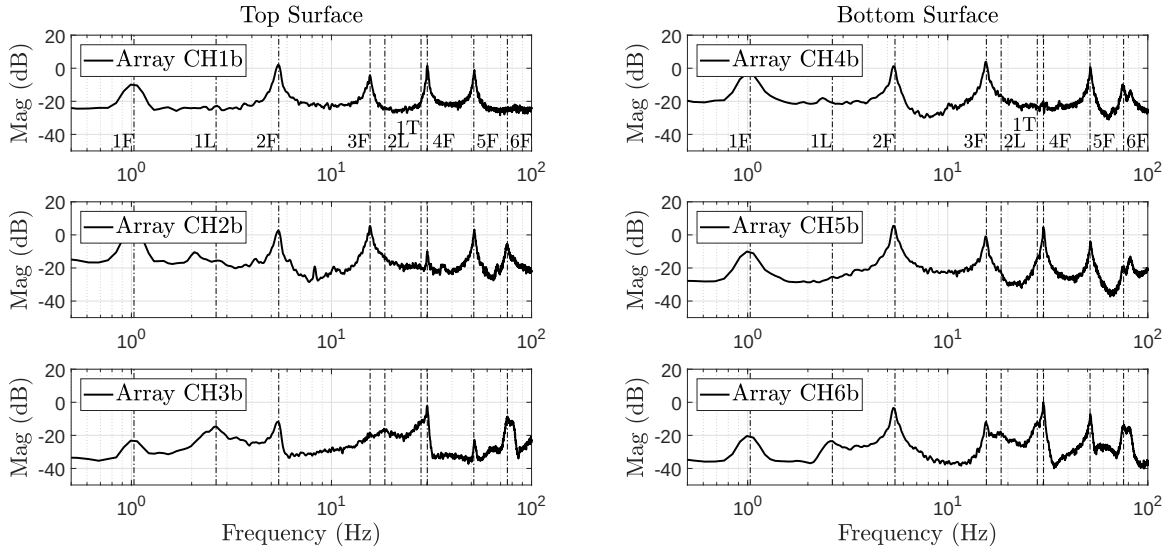

(a) Top surface (b) Bottom surface

Figure 6.16: PSDs of three FBGs (FBG7) at both the top and bottom surfaces in chord-wise direction at approximately 60% rotor radius

Accelerometers are known to have increased sensitivity for higher frequencies, while the DFOSS system and the FBGs exhibit a flat frequency characteristic. Therefore, it can be observed that at low frequencies the DFOSS system had the highest signal-to-noise ratio, while ACC (1D) offered improved performance at high frequencies. A dwell shaker test, in which the blade was excited with a constant input of 3 N at the 3rd flapping frequency of 15.72 Hz, was performed to compare the signal-to-noise ratios. The data obtained using the three technologies on the quarter cord line at 60% rotor radius on the top surface are shown in Figures 6.17 and 6.18. It should be noted that, in this case, the ACC (1D) sampling frequency was fixed at 20kHz due to software limitations. Typical time series measurements over 0.2 seconds are presented in Figure 6.17, while Figure 6.18 shows a comparison of the PSDs calculated for this case. At this frequency, the signal-to-noise ratios of both the ACC (1D), at 76 dB, and the DFOSS (vertical), at 79 dB, are comparable, while the signal-to-noise ratio of the FBG, at 51 dB, is considerably lower, as is also evident from Figure 6.17.

The natural frequencies determined experimentally and calculated from the FE model are given in Table 6.4. As part of the uncertainty analysis, each measurement was repeated five times, from which a mean value was formulated and error bounds calculated. While the obtained standard deviation is below ± 0.15 Hz for most cases, there are a few exceptions visible from the ACC (1D) and FBG results. Nevertheless, this outcome contributes to the confidence in both, the FBG and DFOSS measurements. Furthermore, from Table 6.4 it is evident that both FE lagging frequencies deviate from the experimentally determined values. This discrepancy has to be further investigated, yet, it could

have occurred as a consequence of the modelling approach, the test bench set-up, the excitation direction or the age and unknown service history of the test blade.

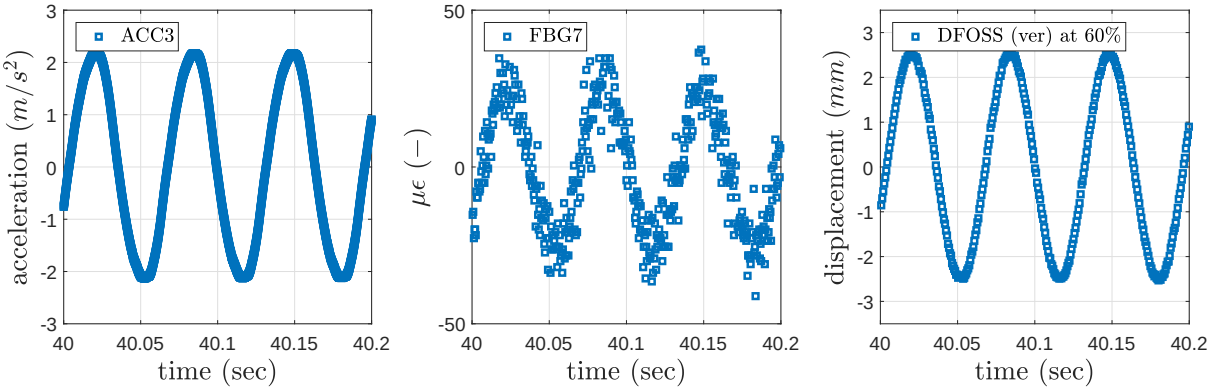

Figure 6.17: Time history of raw data of 3F frequency input collected at approximately 60% rotor radius

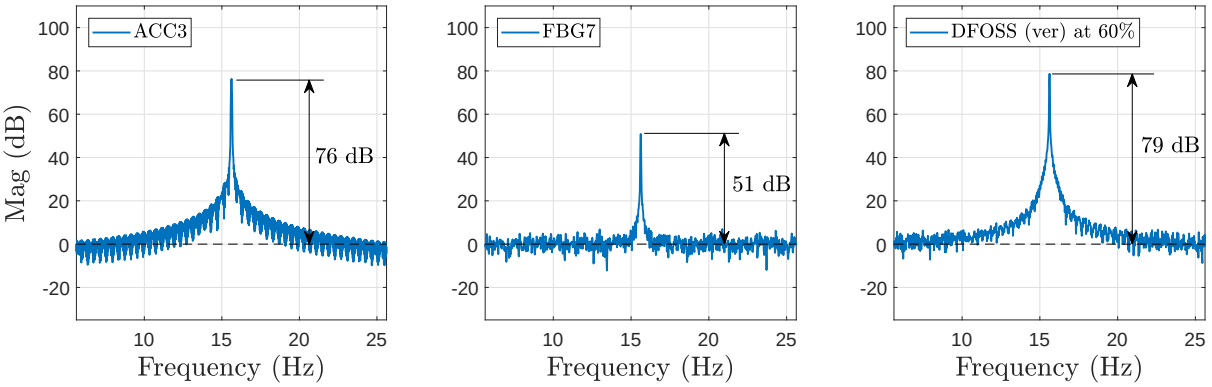

Figure 6.18: Comparison of PSD for the 3F mode measured at approximately 60% rotor radius

Table 6.4: Comparison of natural frequencies, along with standard deviation over 5 repeat measurements

Mode number	Mode type	Natural frequencies (Hz) FE	ACC (1D)	FBG (CH2)	DFOSS
1	1st flapping	0.90	0.98 ±0.00	0.99 ±0.00	1.02 ±0.00
2	1st lagging	3.41	-	2.59 ±0.00	2.66 ±0.03
3	2nd flapping	4.98	5.41 ±0.08	5.41 ±0.02	5.47 ±0.02
4	3rd flapping	15.28	15.72 ±0.18	15.58 ±0.03	15.55 ±0.05
5	2nd lagging	22.72	-	18.56 ±0.23	18.51 ±0.03
6	1st torsion	28.59	28.43 ±0.00	28.11 ±0.04	28.09 ±0.04
7	4th flapping	29.98	30.03 ±0.00	30.16 ±0.04	30.17 ±0.04
8	5th flapping	52.17	51.97 ±0.31	51.77 ±0.13	51.69 ±0.15

The determined natural frequencies from the FBG and DFOSS systems are compared against ACC (1D). Only those modes that contain a flapping component could be compared, which highlights the need for triaxial accelerometers for future testing. The relative errors between the measured frequencies are listed in Table 6.5. All natural frequencies

are in agreement with a percentage error of less than 4.00%. With the ACC (1D) data as the reference measurement, an average percentage error of 0.65% for the FBG system, compared to that of 1.38% for the DFOSS system, suggests that the FBG system is able to characterise the natural frequencies more accurately.

Table 6.5: Natural frequency error of FBG and DFOSS instrumentation systems relative to the ACC (1D) measurements

Mode number	Mode type	Error (%) FBG vs ACC (1D)	Error (%) DFOSS vs ACC (1D)
1	1st flapping	1.01	3.90
2	1st lagging	-	-
3	2nd flapping	0.00	1.10
4	3rd flapping	0.90	-1.09
5	2nd lagging	-	-
6	1st torsion	-1.14	-1.21
7	4th flapping	0.43	0.46
8	5th flapping	-0.39	-0.54

6.3.3 Mode shape extraction

Both operational displacement and surface strain mode shapes were extracted using TDD, while the FE displacement mode shapes and calculated strain mode shapes were used for comparison and analysis. For the DFOSS mode shapes, an additional post-processing step was required, because the origin of the measurement at the first reflector R1 is located on the pitch control cuff, which can move relative to the blade mount. Unlike the FE model and the ACC (1D) measurements, which determine the shape of the blade relative to the fixed laboratory reference frame, the DFOSS reference frame with its origin on the pitch control cuff itself can be moving, which results in mode shapes that are apparently distorted. This is analogous to a camera that is mounted on the moving pitch control cuff pointing along the blade and where the changes of the camera pointing angle resulting from movement of the cuff would result in the extraction of apparently distorted mode shapes, compared to an external camera viewing the blade from a fixed position. Therefore, the angle of the origin at R1 in the laboratory reference frame is unknown and has to be fitted as part of the correction procedure. In future implementations of this technique, it would be advantageous to locate the origin reflector R1 of the DFOSS sensing cable directly on the blade mount to avoid this additional processing step.

The measured DFOSS mode shapes extracted directly from TDD are plotted in Figure 6.19 as solid lines. Here, the unknown angle of the origin expresses itself though a distortion in the mode shapes that increases linearly with the blade radius. Through a visual fit with the FE model-generated mode shapes, shown in Figure 6.19, the value of the slope angle of a straight line through the origin for each mode is found, which is subsequently subtracted from the measured mode shape to correct for the movement of the reference frame. The adjusted mode shapes and the straight lines used for the correction are shown in Figure 6.19. It should be noted that this post-processing step is a

natural consequence of the movement of the reference frame and would not be necessary if R1 had been fixed. In future applications of the DFOSS method, the measurements will be referenced to a basis with a fixed angle, for example by mounting R1 on top of the rotor shaft, providing a stable origin.

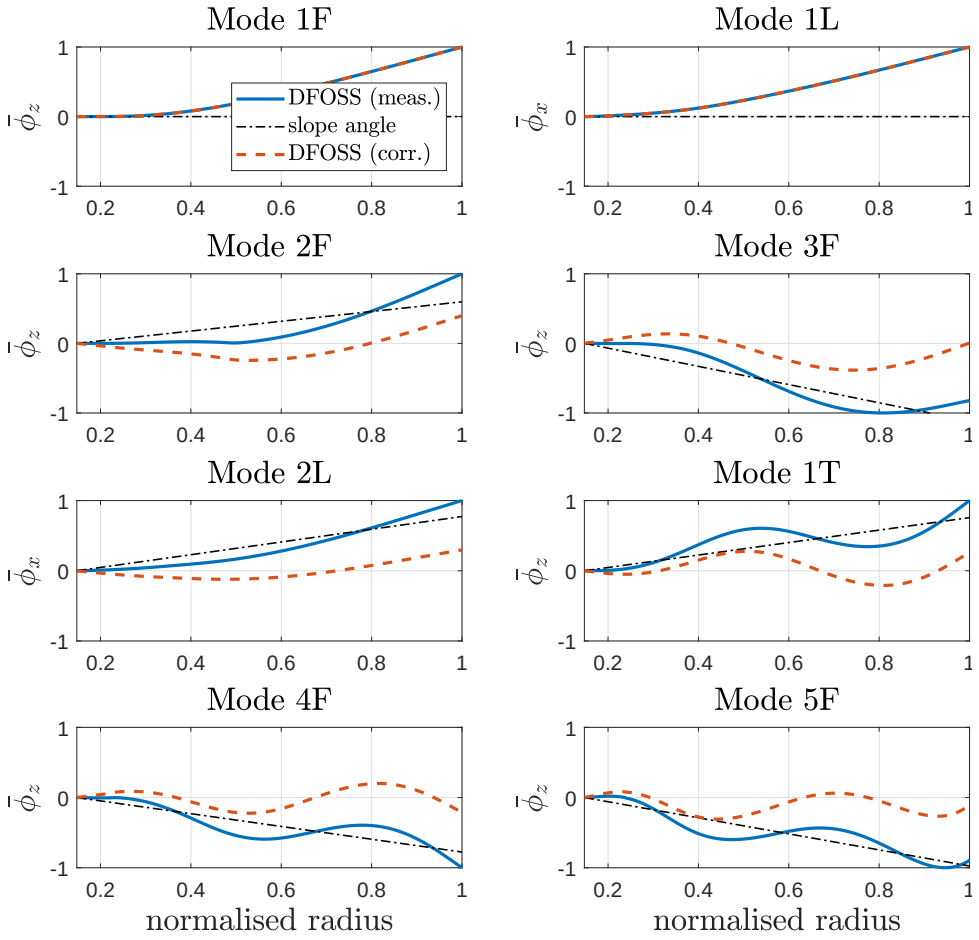

Figure 6.19: Measured versus corrected DFOSS displacement mode shapes

Figure 6.20 compares the displacement mode shapes predicted by the FE model with the corrected mode shapes obtained from the DFOSS system and the mode shapes determined from the ACC (1D) data. All mode shapes are normalised with respect to its maximum amplitude. Generally, an agreement between the model and the measurements can be observed. For the higher order modes, particularly for Mode 5F, the agreement seems to be reduced, with a phase shift of the mode shape visible at higher rotor radius values.

Closer investigation shows that this phase shift is a consequence of the spatial resolution of the DFOSS measurement and the error arising from the implemented spline interpolation in the DFOSS algorithm [19]. As previously mentioned, the output of the DFOSS system is the integration of interpolated slope angle curve, so the spatial resolution of the slope angle measurement needs to be sufficiently high to capture all relevant angular information. Figure 6.21 compares the angle measurements and the interpolated slope angle curve with the first derivative of the FE mode shape. The plot shows that the actual angle measurements at locations R2 to R7 agree very well with the calculated local FE slope values, however, the interpolated slope angle curve deviates from the FE model between measurement points. It can, therefore, be concluded from Figure 6.21 that, in

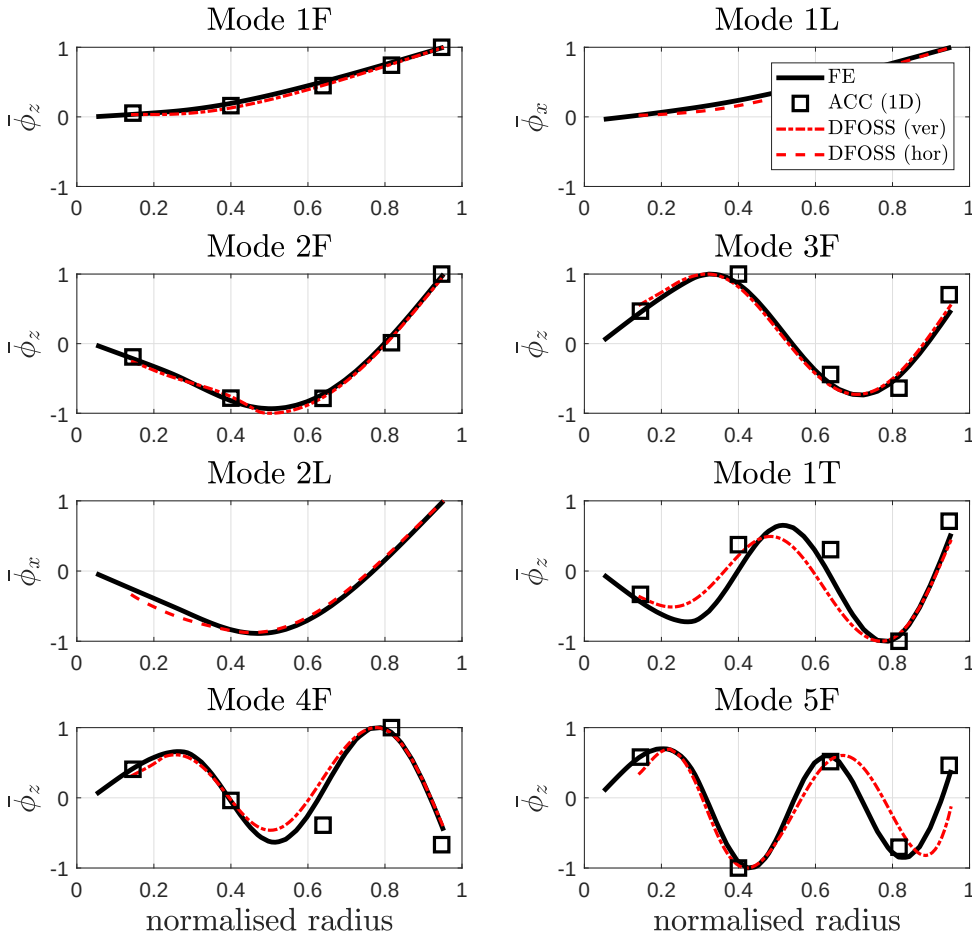

Figure 6.20: Comparison of normalised displacement mode shapes $\bar{\phi}$

the case of Mode 5F, the observed phase shift in Figure 6.20 is a result of an interpolation error due to the limited number of measurement points. The spatial resolution of the DFOSS measurement is therefore insufficient and that the density of reflectors would need to be increased to confidently reproduce this mode shape.

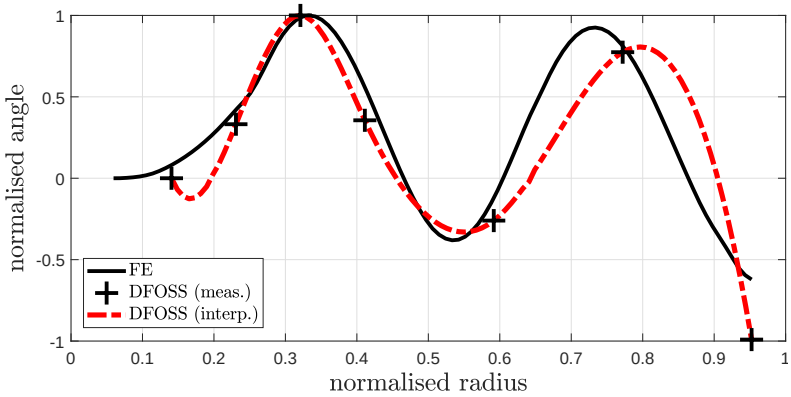

Figure 6.21: Comparison of angle measurements, the chosen slope angle interpolation and the slope angle curve calculated from the FE model for Mode 5F

Although all natural frequencies can be identified with one straight DFOSS cable it does not allow for full identification of the torsional mode shape. Figure 6.22 shows the local flapping and lagging component of Mode 1T. It should be noted that both mode

contributions in the figure are approximately equal. At least two DFOSS fibre optic cables are required, ideally installed at the leading and trailing edges, to determine the torsional component of Mode 1T. For surface mounting, this is only applicable in the laboratory environment, due to the potential impact of aerodynamic flow.

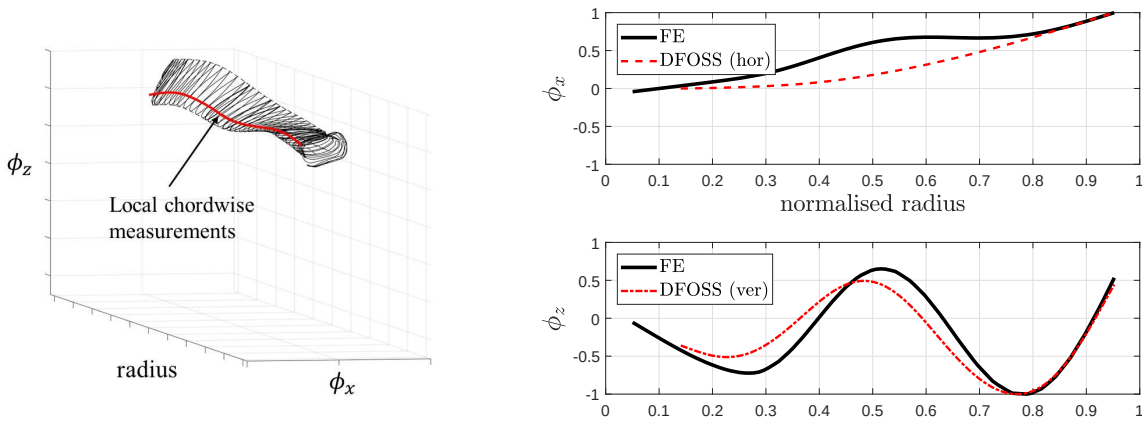

Figure 6.22: Local lagging ϕ_x and flapping ϕ_z components of Mode 1T

The FBG array mounted on the lower surface on the mid-chord line (CH5b in Figure 6.13(d)) was used to obtain the flapping and torsional strain mode shapes, while the array on the lower surface trailing edge (CH6b in Figure 6.13(d)) was used to obtain the lagging strain mode shapes, as these provided the highest signal-to-noise ratios. Figure 6.23 presents the comparison of the FBG-derived strain modes shapes with the strain mode shapes $\bar{\psi}$ determined from the FE model, where both strain mode shapes were normalised to their maximum amplitude. General agreement can be observed, despite some discontinuities that could be due to numerical errors generated from the second spatial differentiation of the calculated mode shapes. This strain mode shape comparison also validates the numerical approach as described in Section 4.4.3. Furthermore, a sudden change in strain mode shape is evident, in particular for Mode 3F at 24% rotor radius, approximately the location where the pitch control cuff merges with the main structure of the blade. This behaviour is well captured by both the analytical and experimental mode shapes and demonstrates the sensitivity of strain measurements to the exact sensor location. This highlights the need to exercise caution when selecting the locations for the FBG sensors and the need to verify the correct placement of the sensors on the blade.

Table 6.6 compares the MAC computed using FE and the experimentally determined mode shapes from ACC (1D), FBG and, DFOSS systems. A match between ACC (1D) determined mode shapes and the FE model is obtained with MAC values greater than 0.8. From the FBG measurements, an overall agreement is attained with a pairing of MAC>0.77, except for Mode 1T where MAC=0.58. Reasons for this discrepancy, in particular for the first strain measurement at approximately 10% rotor radius, could be due to the FBGs ability to measure shear strain, while this is neglected for the FE model as explained in Section 4.4. The mode shape pairing achieved with the DFOSS system resulted in a MAC$\geq$0.89 discounting the lower MAC value of MAC=0.78 for Mode 5F due to the insufficient spatial resolution as previously explained.

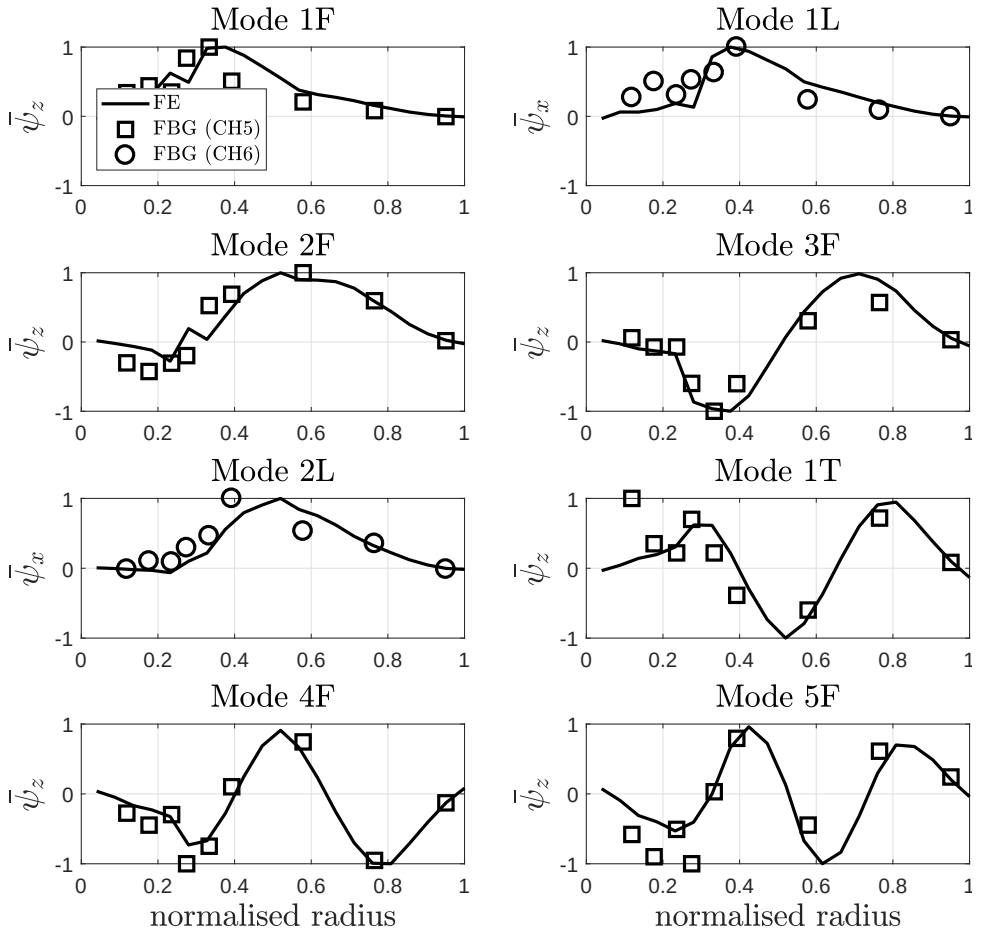

Figure 6.23: Comparison of normalised surface strain mode shapes $\bar{\psi}_T$ determined by the FBG strain measurements and the output from the FE model

Table 6.6: Comparison of mode shape pairing with FE model

Mode number	Mode type	MAC ACC (1D)	MAC FBG	MAC DFOSS
1	1st flapping	1.00	0.83	0.99
2	1st lagging	-	0.77	0.99
3	2nd flapping	1.00	0.80	1.00
4	3rd flapping	0.96	0.94	0.99
5	2nd lagging	-	0.81	0.99
6	1st torsion	0.81	0.58	0.89
7	4th flapping	0.83	0.94	0.97
8	5th flapping	0.98	0.78	0.78

6.4 Effect of position on measurement noise

In the preceding section, it was shown that a high signal-to-noise ratio of strain measurements is paramount when reconstructing the vibrational modes of interest. Measurements close to the trailing edge yielded an improved signal-to-noise ratio for lagging modes while flapping modes can be particularly well captured using measurements close to the quarter chord line. Figure 6.24 shows the mode shapes reconstructed from an ideal simulation

with added Gaussian noise. The frequency spectra show clear peaks up to 30 Hz for the ideal system, while only the first three resonance peaks are noticeable from the noisy data. It is evident that this affects the accurate reconstruction of the higher modes, such as Mode 3F.

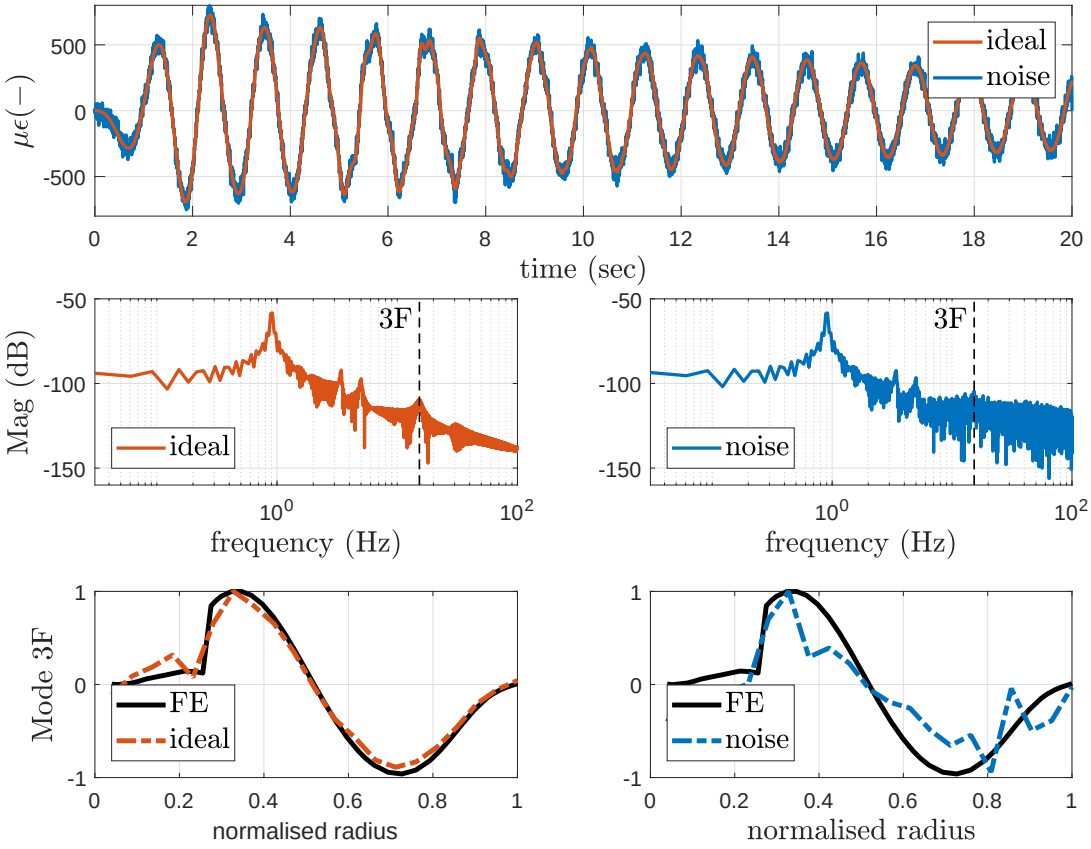

Figure 6.24: Comparison of structural response with and without Gaussian noise (ideal)

Many OSP algorithms exist to calculate the optimal sensor position, yet what seems optimal in an analytical sense does not seamlessly translate into practice. Unless experimental testing is carried out, the noise level associated with a particular acquisition system can only be estimated. Figure 6.25 shows a comparison between frequency spectra from data collected at the quarter chord line at 30% rotor radius for the simulated response including Gaussian noise and the experimental results. While the resonance peak for Mode 1L is visible in the simulated frequency response, it is hidden in the experimental data due to the low signal-to-noise ratio. This comparison demonstrates the importance of quantifying the experimental measurement noise to avoid unfavourable sensor locations.

An engineering-based approach is proposed for determining the optimal chordwise strain sensor location in virtue of measurement noise. It must be ensured that the sensor is positioned where the signal-to-noise ratio is the highest. This will occur at locations with the maximum distance between the sensor and the neutral axis. The aim is to place the sensors so that both flapping and lagging modes can be identified. The proposed optimisation is a two-step approach, that first calculates all possible spanwise sensor positions at each chordwise location by applying the error minimisation approach (see black dots in Figure 6.26). This is followed by selecting a weighting w_α and w_β for the importance of each mode, that is then incorporated into a cost function J to determine its chordwise position:

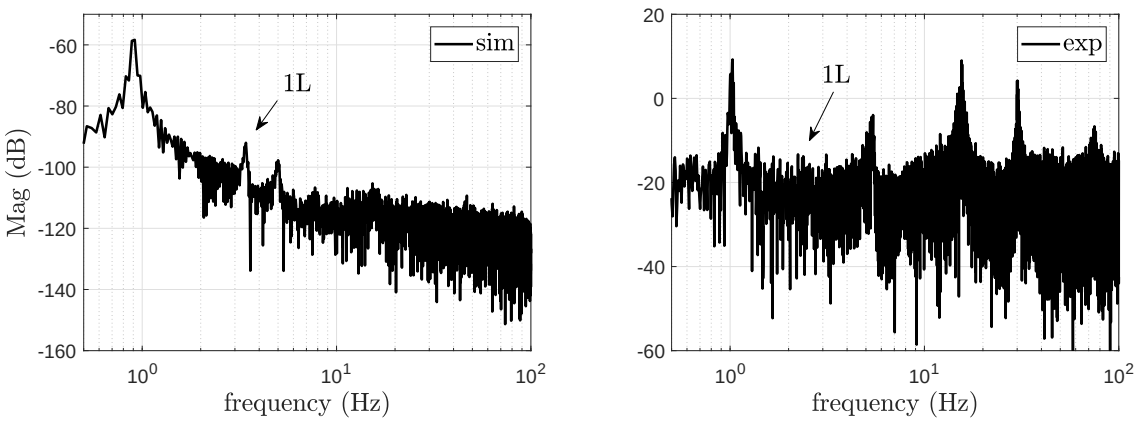

Figure 6.25: Comparison of frequency spectra with simulated Gaussian noise versus experimental results (CH1b) at 30% rotor radius

$$J = (w_\alpha \bar{c}_z - w_\beta \bar{c}_x)^2 \tag{6.4.1}$$

where the distance c_z and c_x are normalised ensuring that the ratio is equal:

$$\bar{c}_z = \frac{c_z}{\max(c_z(x))} \quad \bar{c}_x = \frac{c_x}{\max(c_x(x))} \tag{6.4.2}$$

If only flapping modes are of interest then w_β should be set to zero for which the sensor would be located at the quarter chord line. Figure 6.26 displays the determined chordwise sensor positions with w_α and w_β are set to unity.

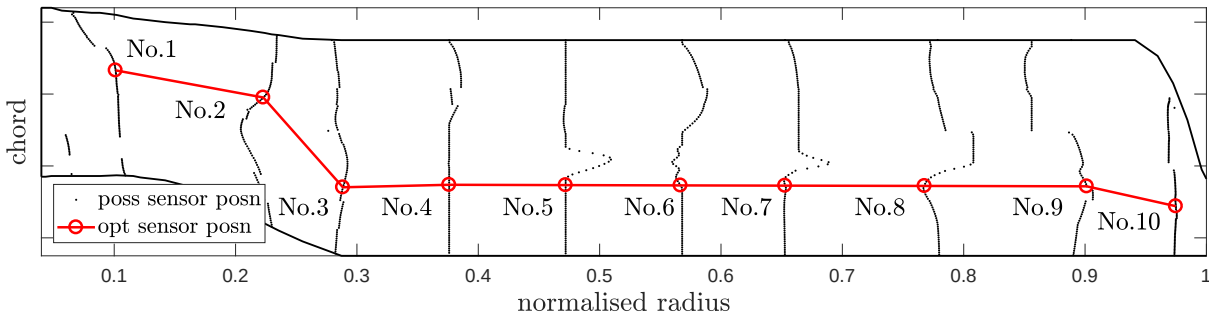

Figure 6.26: Spanwise and chordwise sensor position using 10 sensors, $w_\alpha = 1$, $w_\beta = 1$

For this case, these positions are referred to as "optimal" for the remainder of this work. This weighting results in a compromise ensuring that both flapping and lagging mode shapes can be recovered. The final suggested distribution is given in Table 6.7, in which the chordwise position is presented as a percentage of chord from the leading edge. This outcome could not be validated experimentally. However, comparing these results with the strain measurements from the GVT it is clear that the highest signal-to-noise ratio is obtained with fibre optic cables on the rear half of the blade. It should also be noted that attaching the FBGs at the identified location at the bottom surface is only practical in a controlled environment, yet in-flight this might lead to undesirable effects on the blade aerodynamics. A study on the impact of a fibre optic cable to the airflow around

an aerodynamic profile is provided in Appendix C. For future applications, it is highly desirable to embed the fibre optic cables with the blade structure.

Table 6.7: Optimised sensor position on the bottom surface

Sensor number	Spanwise position (%)	Chordwise position (%)
1	10.12	35.00
2	22.28	35.00
3	28.85	70.00
4	37.60	69.00
5	47.20	69.00
6	56.66	69.00
7	65.28	69.00
8	76.77	69.00
9	90.14	69.00
10	97.48	67.00

6.5 Summary

This chapter compared the performances of two state-of-the-art optical fibre-based techniques for characterising the structural dynamics of a helicopter blade, one based on the measurement of strain, and the other on the direct measurement of slope angle, from which the shape could be determined. This was achieved through a series of GVT, using accelerometers and an FE model as references. It was found that for FBG-based strain measurements the sensitivities to the modes were dependent upon the location of the sensor element relative to the neutral axes of the structure, suggesting that full modal identification would require careful optimisation of the distribution of the sensors, with knowledge of the underlying structure. DFOSS, on the other hand, by virtue of its high sensitivity and the two-dimensional measurement capability, allowed the natural frequencies of the flapping, lagging and torsional modes to be measured using a single sensing cable. Furthermore, the results showed that the signal-to-noise ratio of the FBG is considerably lower than that of the DFOSS and ACC (1D) measurements. The high repeatability of the experimentally determined natural frequencies contributes to the confidence in both FBG and DFOSS systems for characterising structural dynamics. While the natural frequencies obtained from FBG and DFOSS are in good agreement with a percentage error of less than 4.00%, FBG measurements provided the more accurate results when benchmarked against the natural frequencies obtained from ACC (1D) data. On the other hand, a closer match between FE-calculated mode shapes and the DFOSS system of MAC$\geq$0.89 (for the first seven modes) was achieved, compared to results obtained from the FBG sensors. Although the FBG strain mode shapes in flapping and lagging direction are in agreement of MAC$>$0.77, a lower value of MAC=0.58 for Mode 1T resulted from the FE model limitation that neglected shear strain. The obtained strain measurements highlighted the importance of choosing the optimal strain sensor location to minimise measurement noise and thus achieve the highest possible signal-to-noise ratio. Based on this finding a sensor placement algorithm was developed that

allowed a two-dimensional spatial distribution. This outcome will be further assessed in the rotating frame in Chapter 7. While the DFOSS system exhibits promising features for vibration characterisation, it is yet to be determined which instrumentation system is more sensitive for damage detection. Therefore, the presented experimental data set of a healthy blade will be used as a baseline case for exploring the instrumentation system's suitability of detecting damage (see Chapter 7).

CHAPTER 7

Health monitoring capabilities

Current rotor health monitoring capabilities adopted theoretical model-based methods that are linked to measured data from track and balancing systems. Despite previous efforts in formulating frequency-based damage indices [8], this chapter focuses on the exploration of fibre optic instrumentation capabilities to facilitate exploitation for future health and usage monitoring. This was done by bringing together the methods and numerical models developed in previous chapters. The first part concentrates on the structural identification of a healthy blade which forms the baseline case for a damage study. Theoretical instrumentation capabilities are explored in the rotating frame while demonstrating that the optimal strain sensor (OSS) positions (identified in Section 6.4) provide improved results compared to randomly distributed strain sensors (RSS). Structural response due to damage is examined in the second part, while damage indices are formulated based on the outcome of a parametric damage study. This chapter concludes through experimental testing in the static environment, for which damage is applied to the test blade to allow a complete discussion of the benefits of each instrumentation system in virtue of the collected data set.

7.1 Baseline study - healthy blade

7.1.1 Input design

The main rotor model as discussed in Chapter 4 is set for ground run simulations. Strain and displacement parameters are used to simulate FBG and DFOSS measurements to determine structural health. The DFOSS system is presented through its biaxial displacement components in flap and lag directions. The suitability of each measurement type is discussed in the following section. The blade was excited with a pulse or frequency sweep in collective pitch θ_0. For ground testing in practice, the pulse input is a realistic option because a frequency sweep, especially towards the higher frequency end, is hardly executable by the pilot. Both input and output responses obtained from data at the quarter chord line at 75% rotor radius are compared in Figures 7.1 and 7.2. For the pulse input a

collective input $\eta_0 = 1\%$ was chosen that translates to a pitch deflection $\theta_0 = 3.7°$, while for the frequency sweep an amplitude of $\theta_0 = 1°$ over a frequency range 0-100 Hz was applied for 5 seconds. Time histories of simulated displacement and strain measurements were converted to the frequency domain using the FFT algorithm. Since the aerodynamic damping is high, blade dynamics reach a steady-state condition 2 seconds after the pulse input as demonstrated by the displacement and strain measurements. The displacement response due to pilot frequency sweep input is only noticeable for the lower frequencies, while the response is negligibly small at higher frequencies, as reflected in Figure 7.2.

The mode order of the rotating system was investigated by comparing the resonance peaks with frequencies calculated through NASTRAN by examining the resonance peaks of flap displacement d_z and lag displacement d_x (indicated through the vertical dashed line). The first resonance peak observable from d_z is the first rotor harmonic, occurring at 6.58 Hz, and the first peak from d_x is the first lagging frequency. The obtained results are confirmed through the Campbell diagram that was presented earlier in Figure 4.13 and is illustrated in a simplified form for convenience in Figure 7.3.

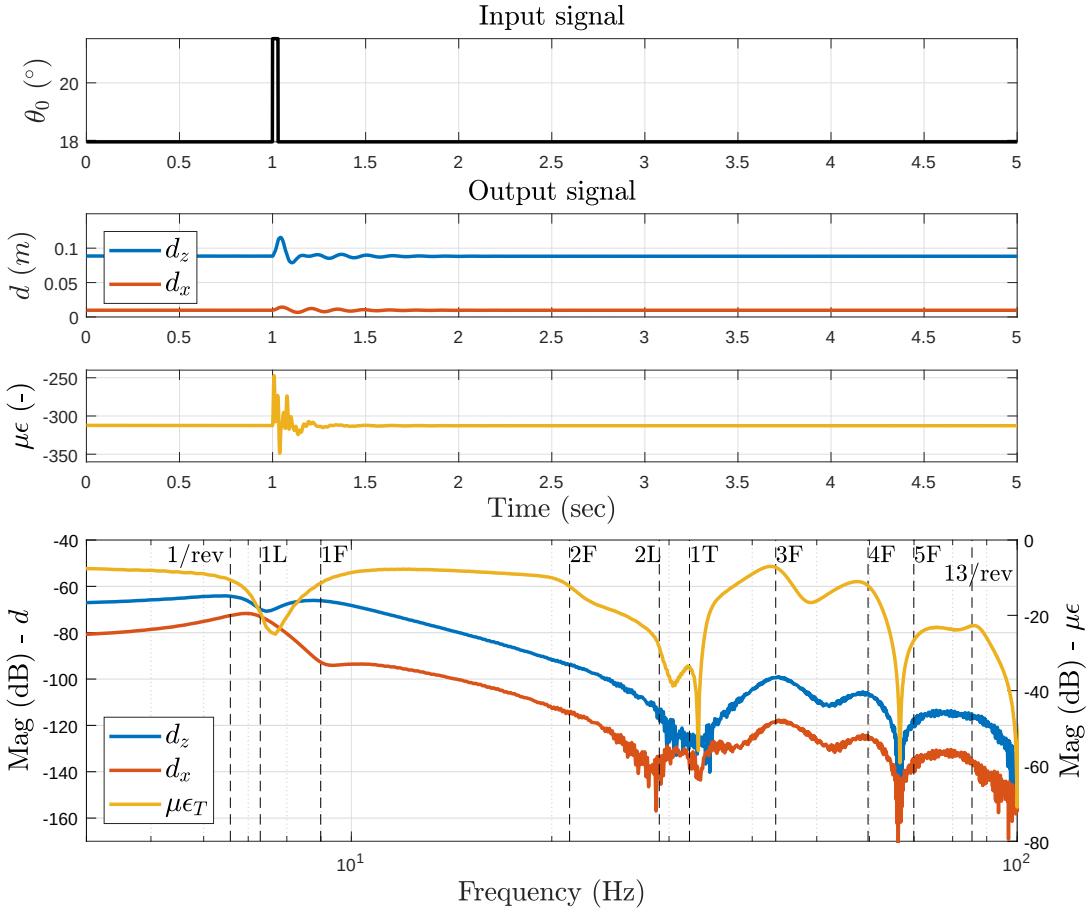

Figure 7.1: Input and output responses due to pulse input taken from simulated measurements at 40% chord and 75% rotor radius

A change in mode order for 1F and 1L is expected at around 50% RPM, while a significant switch is predicted for Mode 3F with 2L and 1T in a range between 60-70% RPM. Despite the high aerodynamic damping, which is also the cause for a low resonance peak for Mode 1F, the pulse input provided sufficient energy to excite the lower modes. This is confirmed by Rammer [221] who states that for real applications this mode may not

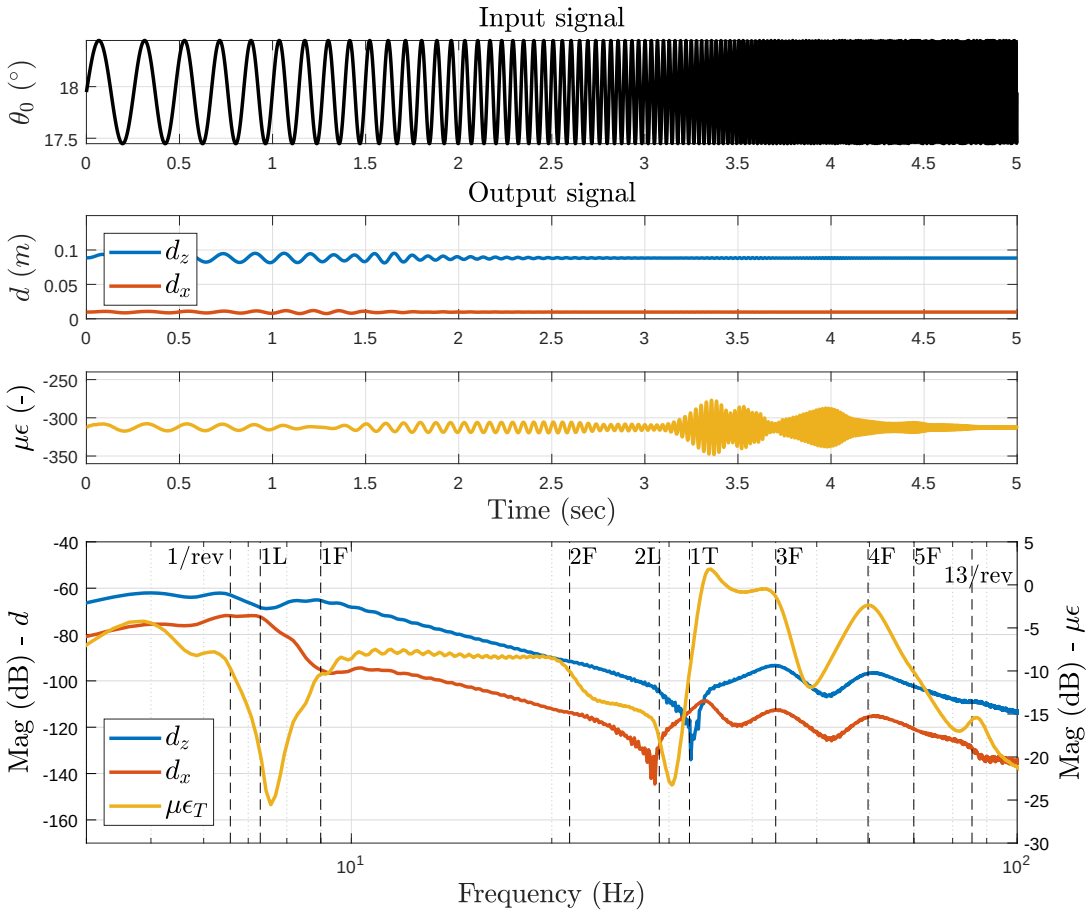

Figure 7.2: Input and output responses due to frequency sweep input taken from simulated measurements at 40% chord and 75% rotor radius

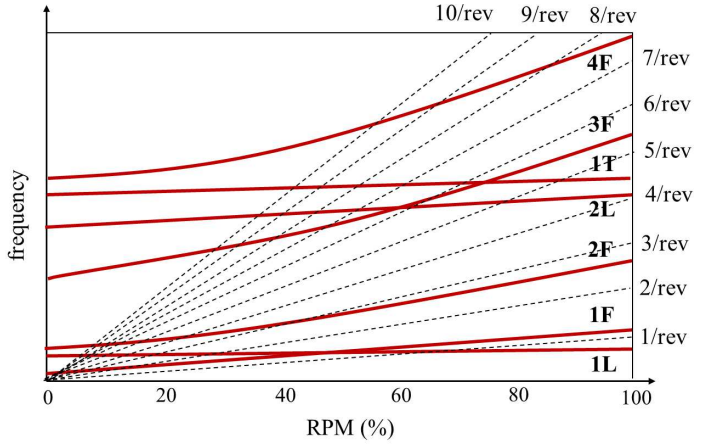

Figure 7.3: Simplified Campbell diagram

be identified due to the large aerodynamic damping. In contrast to the pulse input, the frequency sweep maintains the power content and therefore, an improved frequency spectrum was achieved. Although estimations were performed in an ideal environment (no noise) the simulation introduced discrepancies for the identified frequencies. Clear peaks are observable for Mode 1T, 3F and 4F, there is also a peak that coincides with the 13/rev rotor harmonic. Mode 1T has shifted possibly due to the periodic change of

pitching moment. The frequency sweep will be used for further analysis. Apart from being able to obtain combined local flap and lag information, strain is inherently more sensitive compared to displacement measurements. The quality of the strain measurement is again dependent on the chordwise strain sensor position. Figure 7.4 demonstrates that at different spanwise locations (30% and 75% rotor radius) and chordwise positions some of the modes are captured better than others. A clear resonance peak is perceived at 30% rotor radius at the 60% chord position, while the Mode 4F peaks are more pronounced at other chordwise locations. At 75% rotor radius strain readings at 60% and 80% chord capture both lagging modes (Mode 1L and 2L), while other modes are less pronounced (Mode 1F and 3F). This outcome demonstrates the need for locating strain sensors at suitable chordwise positions.

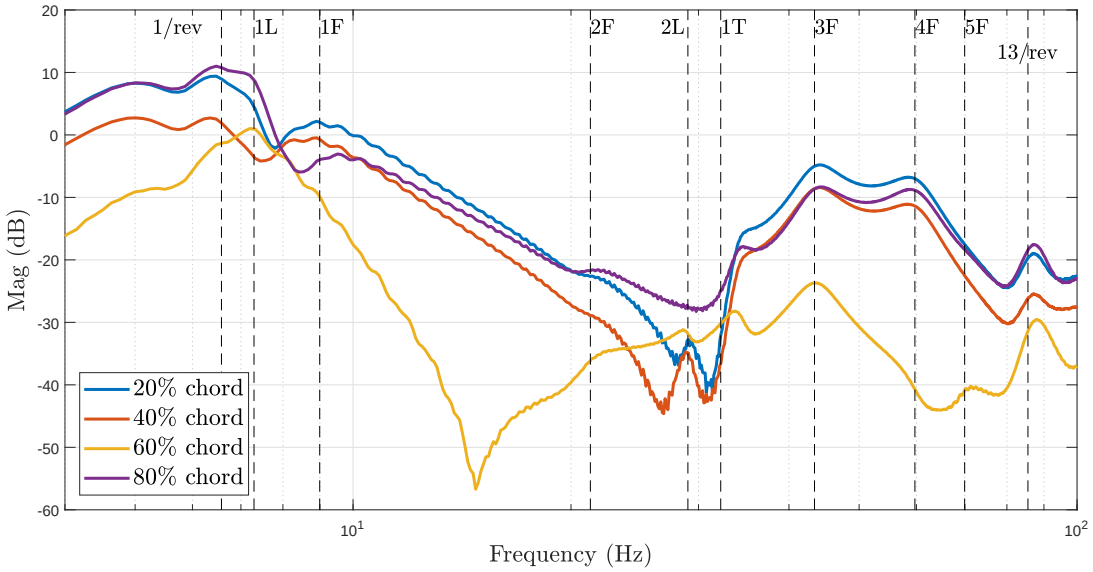

(a) Measurements taken at 30% rotor radius

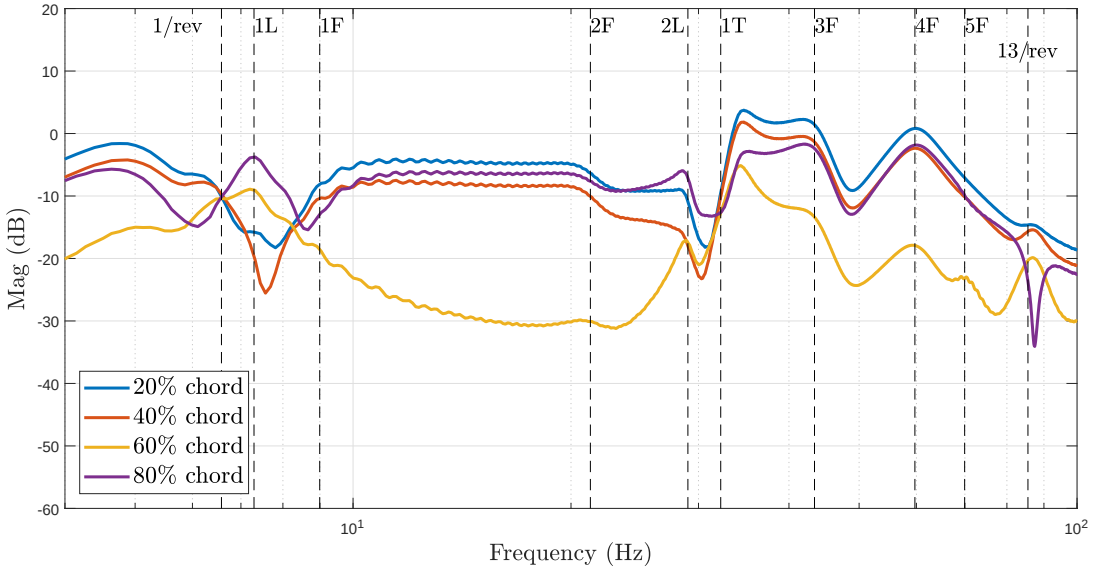

(b) Measurements taken at 75% rotor radius

Figure 7.4: Frequency spectra of simulated strain measurements

7.1.2 Analysis of modal properties

Frequencies were estimated from time histories using the subspace identification algorithm developed by Yusuf [252], while mode shapes were obtained with the TDD tool. Stabilisation diagrams were produced (see Figure 7.5) for numerical displacement and strain measurements taken at 40% rotor radius. A comparison is done between RSS and OSS positions. RSS reads numerical data from the quarter chord line in a straight line along the entire span, while OSS positions were determined in the previous Chapter (see Figure 6.26).

The stabilisation diagrams only show the stable poles also called physical poles, while the unstable ones are omitted. The latter stem from numerical errors through the mathematical algorithm [252]. Despite this, no unstable poles can exist as the blade is aeroelastically stable in hover. From Figure 7.5(b) it is evident that most stable poles for modes of interest are found from the OSS measurements, while a relatively high number of unstable poles are obtained for d_x and RSS positions. Although a clear peak is noticeable in the FFT plot for higher modes, the small amplitude of the measured time history[1] leads to numerically unstable poles. From the strain readings, on the other hand, stable poles are obtained for all modes of interest, particularly for OSS. From the d_z stabilisation diagram a higher number of stable poles are obtained for the first rotor harmonic than for the first flapping mode, while highlighting that Mode 1L, 2L and 1T cannot be clearly identified.

A comparison of extracted frequencies with estimation errors are shown in Table 7.1 demonstrating that the selected chordwise sensor positions allow 4.8% more accurate estimation of modal frequencies. Although similar results are obtained from both numerical strain readings, it is expected that the accuracy of measurements taken at 40% chord will decrease in the realistic noisy environment. Although these results show the importance of selecting the correct sensor positions in virtue of neutral axis distance, the determined strain sensors as shown in the previous chapter are valid only for the non-rotating case. Centrifugal stiffening considerably alters the modal properties. For the deployment of permanent fibre optic instrumentation systems the sensor positions need to be suitable for static and rotating cases if the structural health is to be determined. An example of how identified strain sensor positions change with increasing RPM is demonstrated in Figure 7.6. Furthermore, mode shapes will continuously change due to variable aerodynamic loading environment. Therefore, defining an optimal set of sensor locations will be valid only for a certain set of flight conditions. The problem is further exacerbated because, over a certain period of time, the structure will undergo changes due to ageing, loss of stiffness of composite material and potential damage.

[1]The full-time history is needed as input to the subspace identification algorithm.

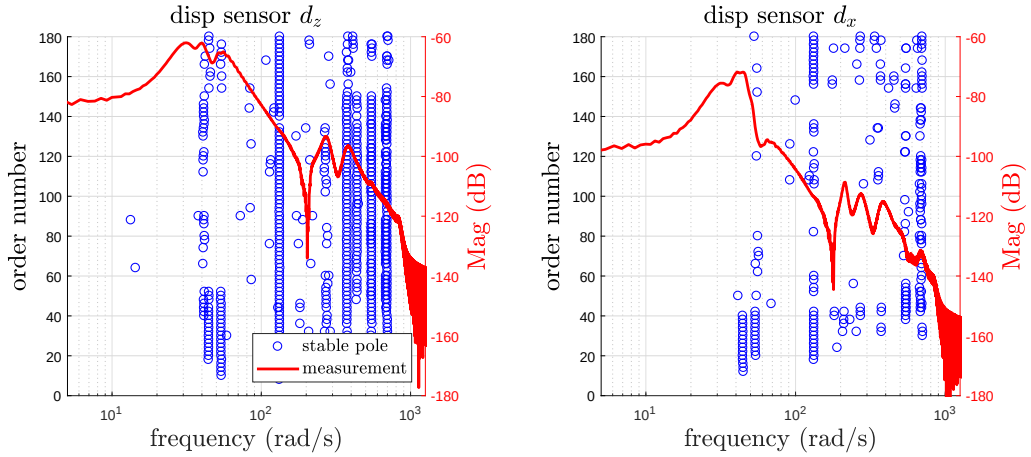

(a) Displacement measurements d_z and d_x

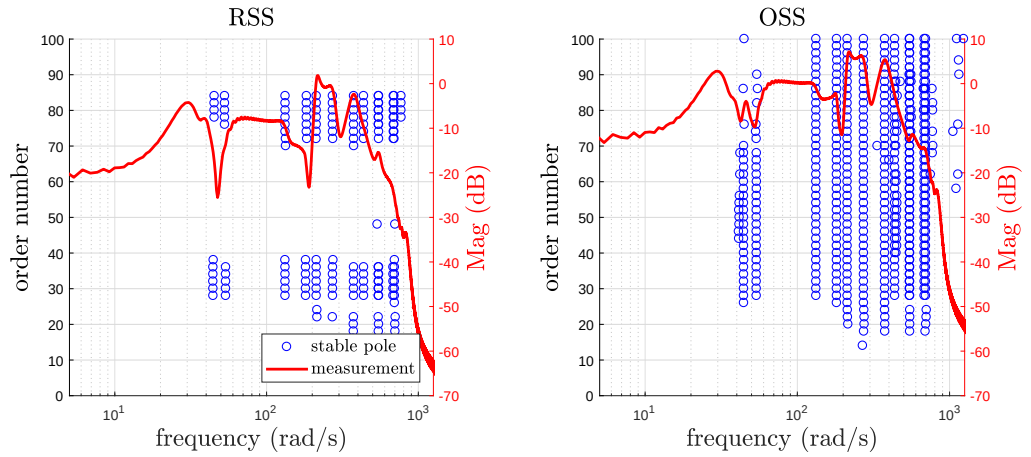

(b) Strain measurements $\mu\epsilon_T$

Figure 7.5: Stabilisation diagrams of simulated displacement and strain measurements (only stable poles are shown)

Table 7.1: Comparison of identified rotating natural frequencies from simulation

Mode number	Mode type	Frequency (Hz)				Error (%)		
		FE	Disp.	RSS	OSS	Disp.	RSS	OSS
1	1st lagging	7.30	-	7.23	7.10	-	-0.90	-2.80
2	1st flapping	8.99	8.60	8.46	8.61	-4.53	-6.21	-4.50
3	2nd flapping	21.27	21.19	21.22	21.20	-0.38	-0.24	-0.32
4	2nd lagging	29.01	-	29.32	28.96	-	1.06	-0.15
5	1st torsion	32.20	-	34.05	34.03	-	5.45	5.39
6	3rd flapping	43.39	44.24	43.55	43.58	1.92	0.37	0.45
7	4th flapping	59.71	60.05	60.02	59.98	0.57	0.52	0.46
8	5th flapping	69.94	69.87	69.77	69.83	-0.10	-0.24	-0.16
					average	|1.50|	|1.87|	|1.78|

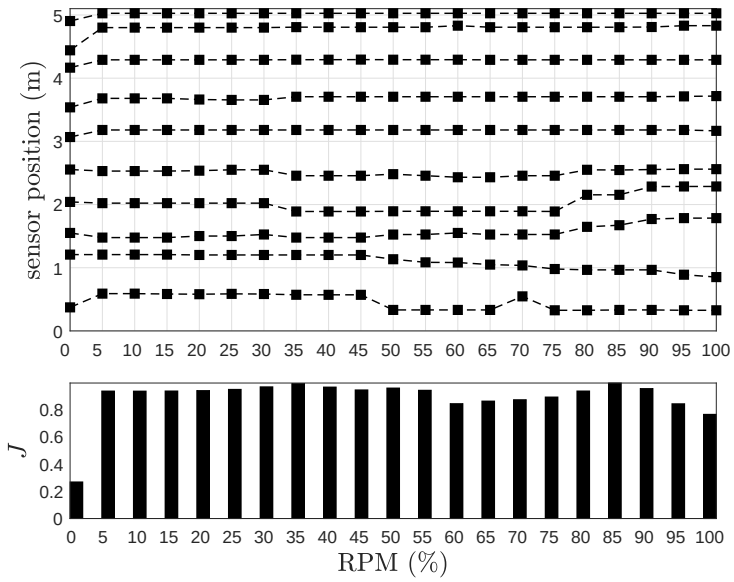

Figure 7.6: Sensor placement locations under the effect of centrifugal stiffening

7.2 Parametric damage study

Lack of experimental operational in-flight data makes it difficult to extract a meaningful damage index. Relevant literature focuses on the development of algorithms for damage localisation, while only a few researchers have adopted criteria for rating a blade as damaged, based on rotor track and balance procedures [117]. Since such data is incorporated into HUMS and is one of the few factors that allow the classification of a faulty blade, it appears to be the only available measure that could be used as a damage criterion. Malfunctions are detected during periodic inspection, especially that of the rotor blade and replaced as necessary. This can be achieved by following these steps:

1. identification of damaged blade,
2. localisation of damage and,
3. determination of whether the blade is still serviceable.

As reported by the survey participants in Chapter 2, damage caused by FOD or erosion was often not noticeable in flight. This fact poses some interesting challenges for the instrumentation systems and post-processing: whether the instrumentation system is sensitive enough to detect small structural changes and if it is distinguishable? While a number of common damage types are reported in Chapter 2, water ingress was selected for this study and was modelled through lumped masses. The survey highlights that water ingress was experienced 10 times out of the 105 reported damage events and in all 10 cases, the pilot was aware of the damage. Furthermore, this type of defect can be easily recreated in a controlled laboratory environment without impairing the blade. The lumped masses were located at the quarter chord line and varied along the length of the blade while increasing the ingress levels size from 0.01 - 0.51 kg. Since the FE model is a piece-wise linear approximation, while the real test blade is non-linear, an over prediction of the structural response is expected. Although the weight of the simulated water is exaggerated, it provides a map highlighting which damage combination would

result in a classified faulty blade, determined through a damage criterion. This was achieved by investigating the following:

1. change of modal properties for the static and rotating environment and,
2. structural response characteristics in the rotating environment.

It was assumed that one blade is damaged, while the others remain healthy.

7.2.1 Impact of damage on structural response

Modal analyses for the static and rotating environment were carried out for each damage case to determine the frequency sensitivity Δf with the following equation [253]:

$$\Delta f = \left(\frac{f^*}{f} \right) - 1 \tag{7.2.1}$$

where f is the healthy natural frequency, while f^* is the natural frequency of the damaged structure. In the following study, the subscript s stands for non-rotating frequency, while r represents the frequencies of the stiffened structure caused by centrifugal and aerodynamic loading. Figure 7.7 shows the change of non-rotating frequency with damage size and location for the first eight modes. It is evident that the changes in frequency are highly non-linear in particular for the higher modes (4F and 5F). In the rotating frame, it is noticeable that Mode 1F and 5F are considerably stiffened by centrifugal force. A similar trend is seen for Mode 3F and 4F in the rotating frame. Mode 1T exhibits an increased change in the area 20-50% rotor radius compared to the non-rotating frequency due to the applied pitching moment.

Investigation of structural response characteristics in the rotating environment are calculated through the absolute difference in tip deviation δz_{tip}:

$$\delta z_{tip} = z_{tip} - z^*_{tip} \tag{7.2.2}$$

where z_{tip} is the total dip displacement for the healthy case, and z^*_{tip} represents the damaged case. Figure 7.9 also shows that the change in tip deviation is also highly non-linear with damage size and location, especially for the higher load cases towards the blade tip. This trend is similar as the frequency variation for the higher modes. The analysis also shows that some damage cases result in decreased rather than increased tip displacement.

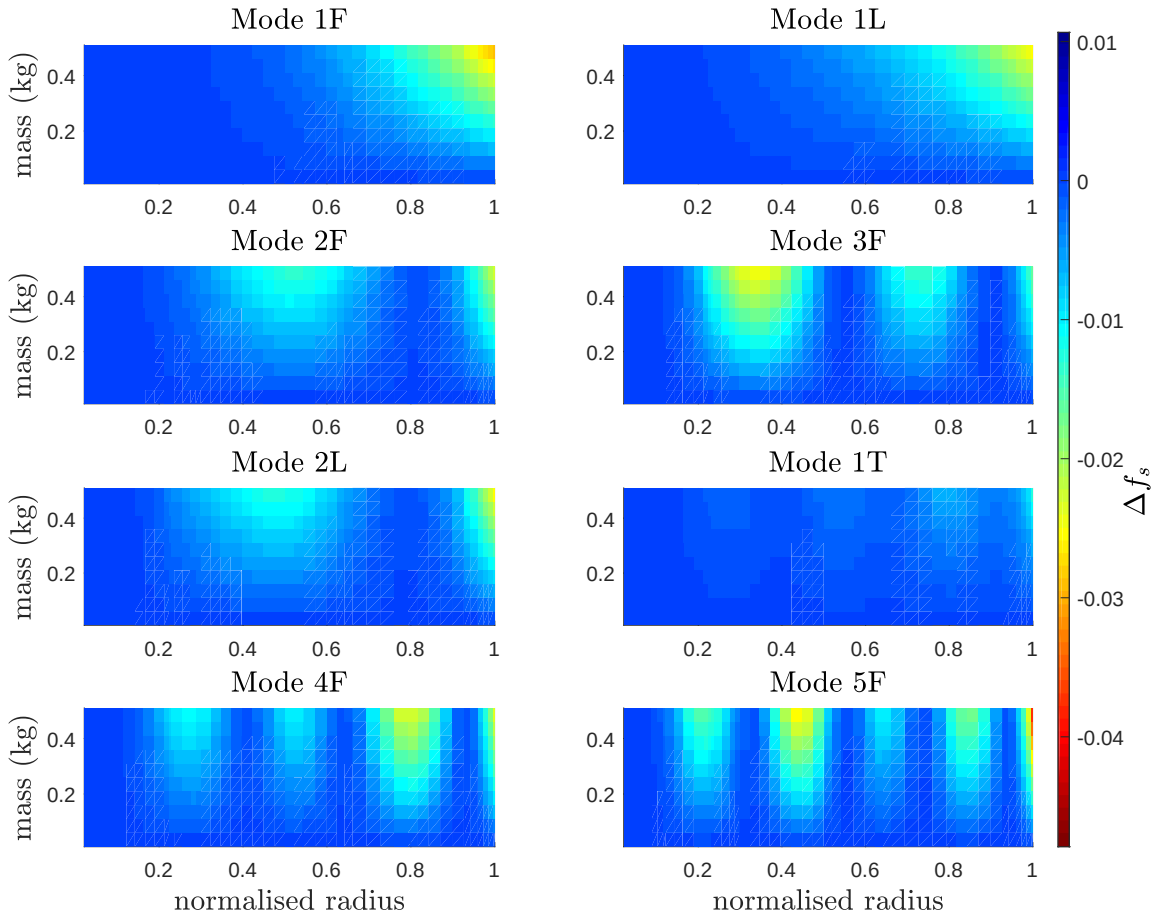

Figure 7.7: Non-rotating frequency change Δf_s with damage size and location

7.2.2 Effect of damage on sensor configuration

The purpose of OSP algorithms is to recover strain or displacement mode shapes as accurately as possible. OSP based on the healthy state will differ from that obtained when damage occurs. This consequently would lead to a decrease in accuracy of reconstructed mode shapes of the damaged structure. Figure 7.10 compares the change of Mode 4F surface strain mode shape for the smallest and largest damage cases. Little change was observed for the other modes.

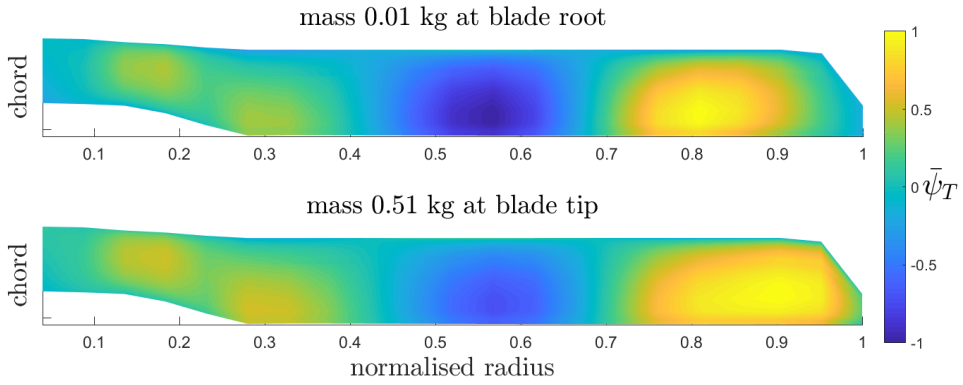

Figure 7.10: Comparison of Mode 4F normalised surface strain mode shape $\bar{\psi}_T$

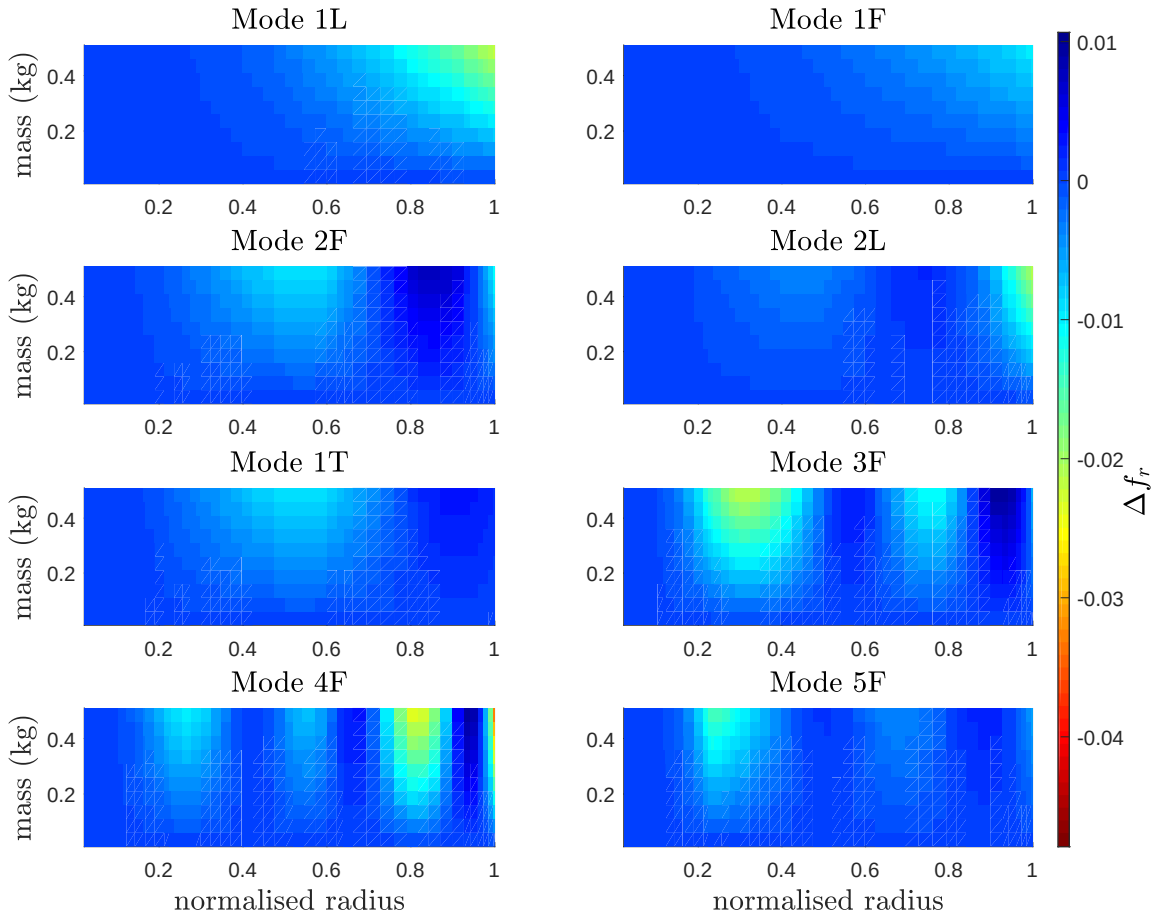

Figure 7.8: Pre-stressed (centrifugal and aerodynamic loading) frequency change Δf_r with damage size and location

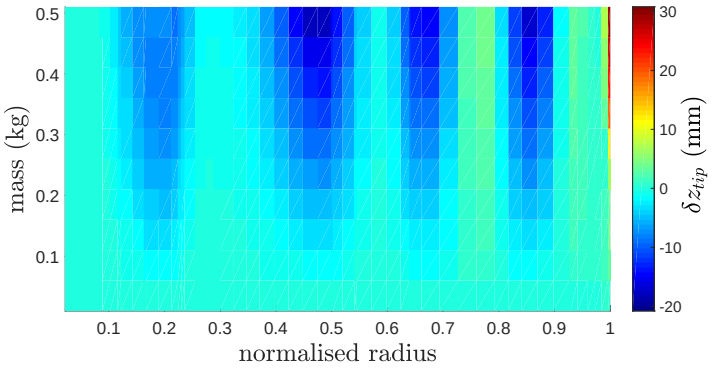

Figure 7.9: Blade tip response with damage size and location

Figure 7.11 summarises the variations for each of the ten sensor positions. Overall the effect of damage to change in optimal sensor configuration is negligibly small, yet a trend is observable for sensors 6 - 8. It is envisaged that small structural defects would not alter the optimal sensor position significantly. Large defects would be noticed by the pilot through changes in vibrations or noise (see Chapter 2).

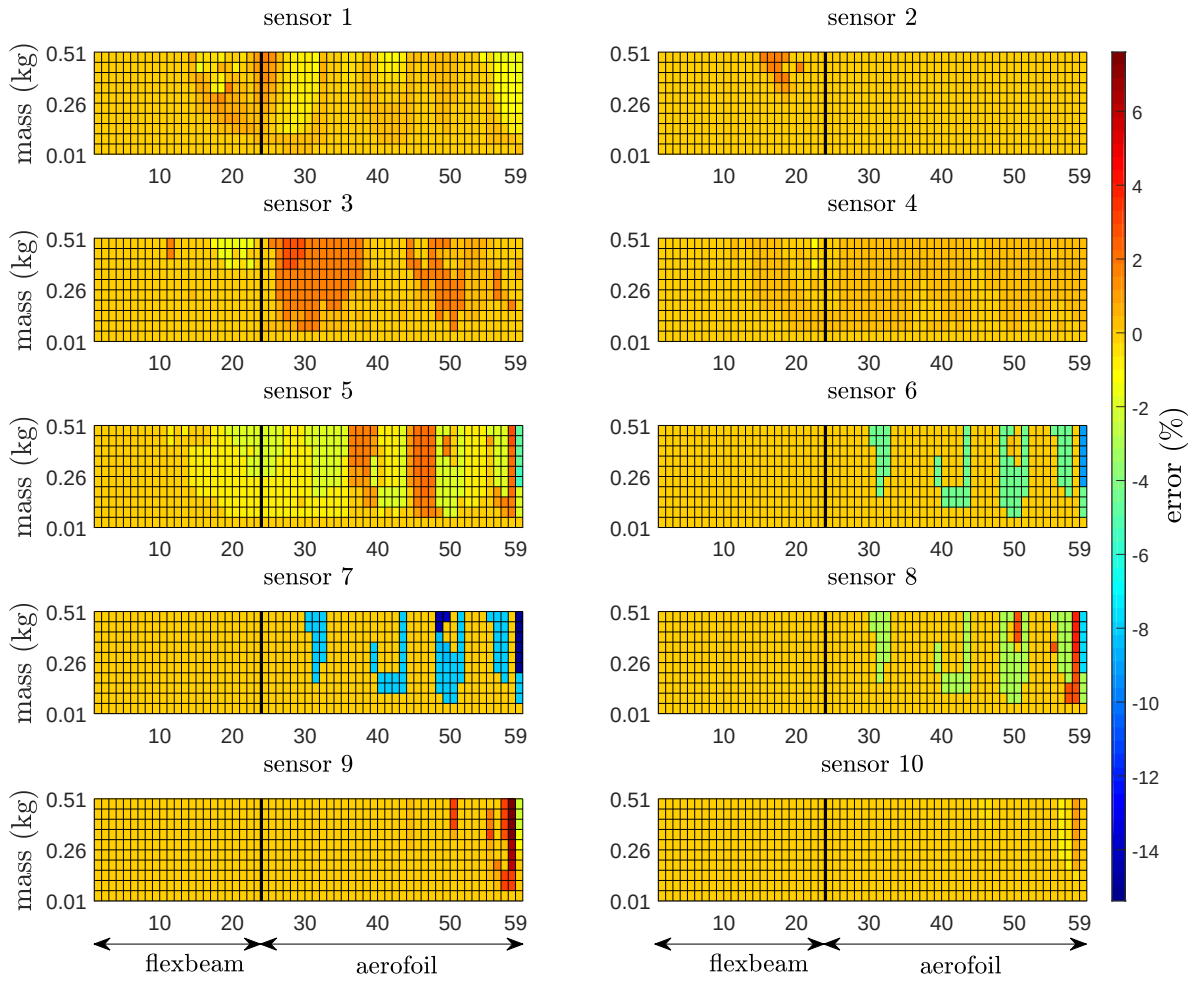

Figure 7.11: Variation of strain sensor position to damage

7.2.3 Structural identification of blade damage

The numerical example presented within this section uses modal property data from the damage case where 0.51 kg was attached at the blade tip. A change in modal properties was investigated from numerical strain and displacement readings. Figure 7.12 compares the frequency spectra for each simulated deflection in the flap and lag directions and axial surface strain. A shift in frequency is evident, in particular for Mode 1T. While changes to Mode 2L are noticeable from the strain measurements, a pronounced peak is observable from both displacement measurements.

Figure 7.13 presents the stabilisation diagram and a similar trend to the healthy case is obtained with the difference that Mode 2L can be determined, while Mode 3F and Mode 5F contain a large number of unstable poles. This result is also reflected in Table 7.2 in which the error between the identified and FE frequencies is determined. Furthermore, the absolute average error from the selected strain sensor positions results in the smallest value. Figure 7.14 compares the displacement mode shapes obtained from the peaks, while the mode shapes for the remaining modes could not be identified due to the same reasons as explained in the preceding section. A comparison of mode shapes at the random sensor locations is shown in Figure 7.15. A visual inspection and comparison of both displacement and strain mode shapes makes it evident that strain is more sensitive

to the damage, while not all displacement modes could be identified through subspace identification algorithms.

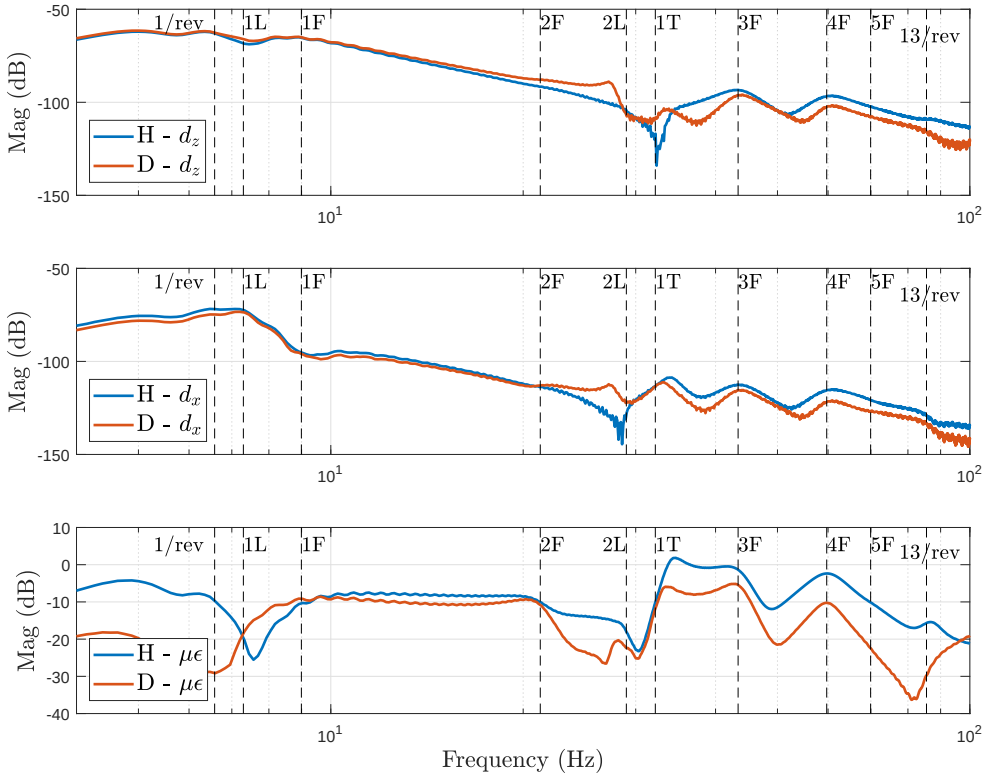

Figure 7.12: Comparison of frequency spectra for damaged and healthy case taken from simulated measurements at 40% chord and 75% rotor radius

Table 7.2: Comparison of identified rotating natural frequencies with damage case 0.51 kg attached to blade tip

Mode number	Mode type	Frequency (Hz)				Error (%)		
		FE	Disp.	RSS	OSS	Disp.	RSS	OSS
1	1st lagging	7.12	-	7.30	7.24	-	2.40	1.66
2	1st flapping	8.90	8.57	8.56	8.58	-3.85	-3.86	-3.69
3	2nd flapping	21.00	21.21	21.22	21.21	0.99	1.00	0.98
4	2nd lagging	28.31	27.58	27.54	27.54	-2.65	-2.79	-2.78
5	1st torsion	32.25	-	33.10	33.06	-	2.58	2.74
6	3rd flapping	42.97	-	43.52	43.54		1.27	1.30
7	4th flapping	57.12	58.71	59.89	59.85	2.71	4.63	4.57
8	5th flapping	69.46	-	69.77	69.80	-	0.44	0.49
					average	|2.55|	|2.37|	|2.24|

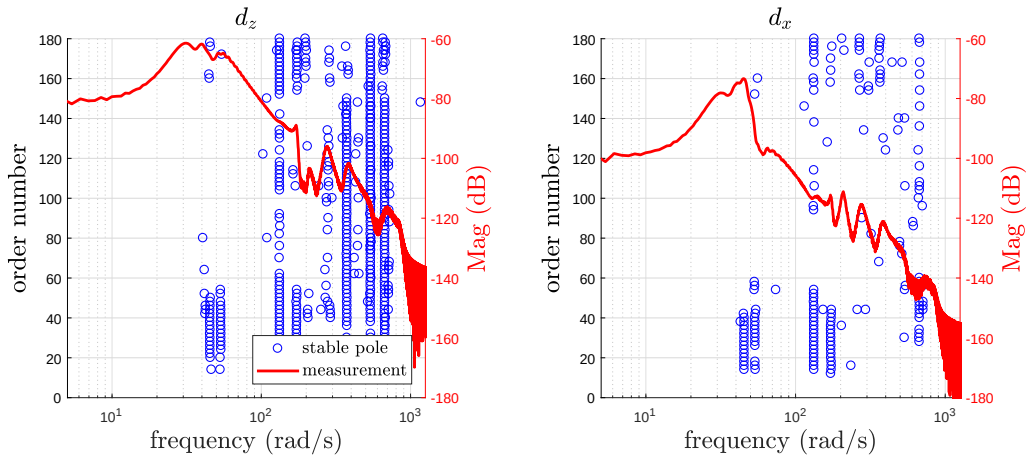

(a) Displacement measurements d_z^* and d_x^*

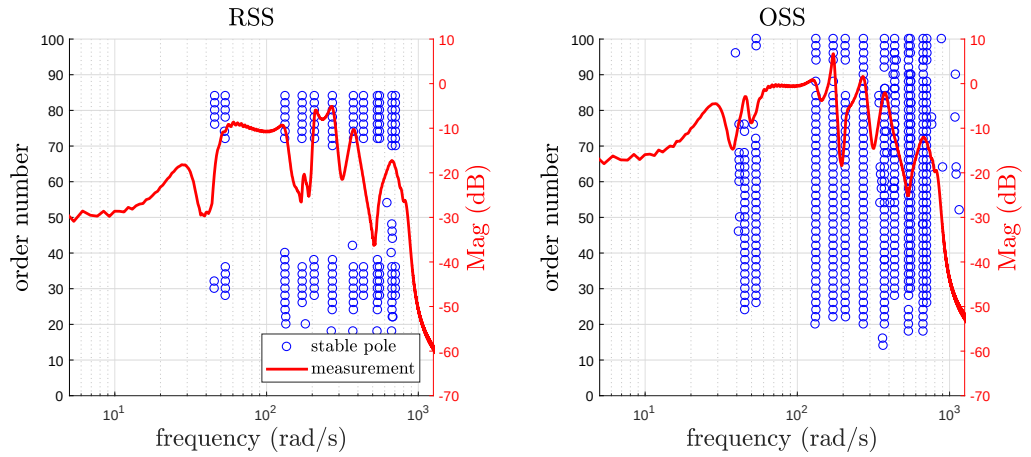

(b) Strain measurements $\mu\epsilon_T^*$

Figure 7.13: Stabilisation diagrams of simulated displacement and strain measurements of the damaged blade (only stable poles are shown)

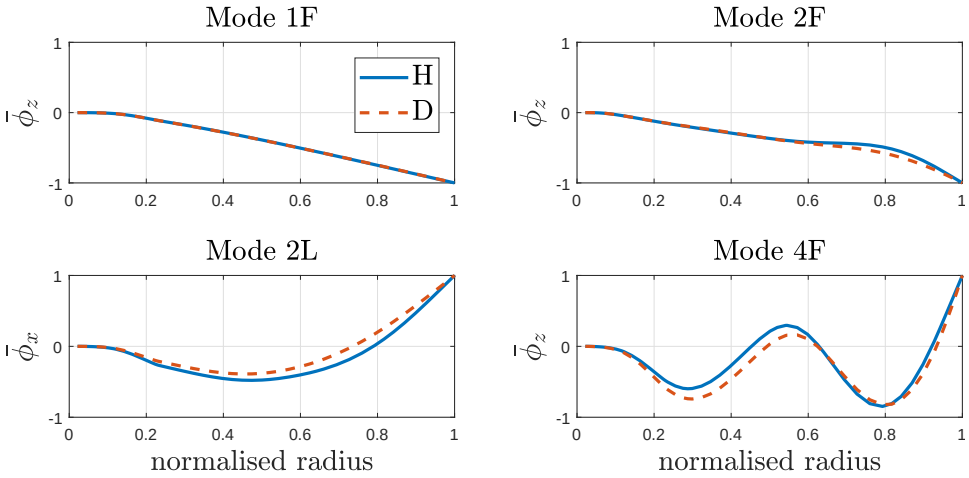

Figure 7.14: Comparison of numerical normalised displacement mode shape $\bar{\phi}$ for healthy and baseline case at 40% chord

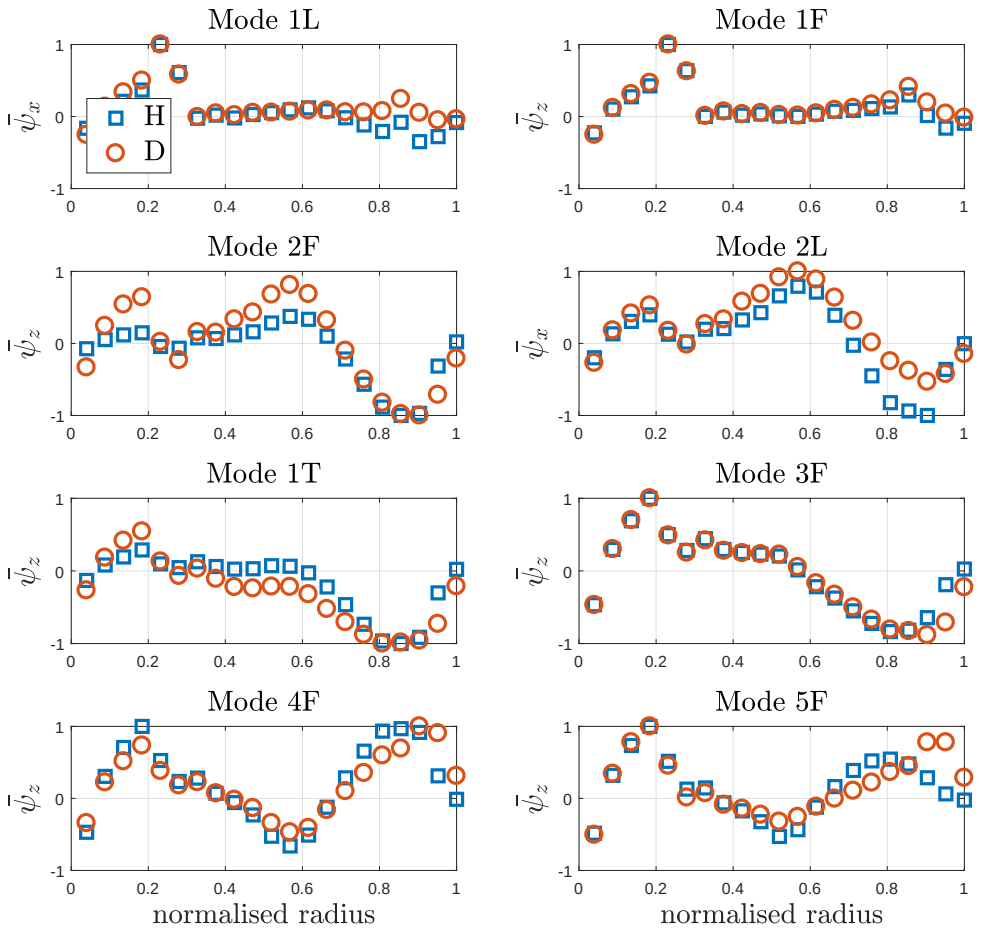

Figure 7.15: Comparison of numerical normalised surface strain mode shape $\bar{\psi}_T$ for healthy and baseline case at 40% chord

7.2.4 Definition of a damage index

The damage criterion used in this study is based on the H135 track and balancing procedure that specifies permissible tip height deviation of ± 5 mm for ground runs and hover close to ground [254]. A blade is considered as unsuitable for service if this track deviation limit is exceeded assuming that it is not possible to remove the problem by further track and balance work. Furthermore, it is considered that this criterion is valid for a set of blades that previously matched their dynamic characteristics. Further details of the track and balancing procedure are presented in Appendix F. Although relevant literature provides suggestions for damage detection, it is difficult to quantify damage for out-of-service conditions without experimental evidence. Here, an attempt is made to provide insight into different damage indicators, highlighting the most promising index. Adopting the chosen criterion a matrix plot was created that indicates which damage event caused the blade to exceed the aforementioned limits. Figure 7.16 highlights that even for 0.51 kg not all locations resulted in an out of limit condition. The reason for this behaviour stems from the highly non-linear frequency distribution especially that of Mode 3F and 4F.

Permanently installed sensors can permit the recording of strains or displacements over a period of time, from which modal properties could be extracted. Discussions in Chapter 3 highlight the effectiveness of curvature mode shapes or strain energy methods for damage

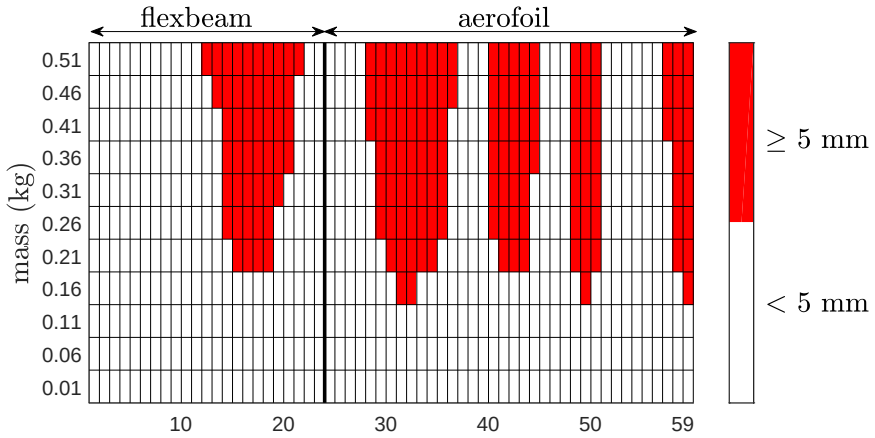

Figure 7.16: "Out-of-bound" map for selected damage criterion

localisation. Here, three damage metrics are proposed to achieve a distinction between damaged and healthy blades, related to changes in frequency, mode shapes and RMS calculated from time history data. The frequency damage index (FDI) is determined as follows:

$$\text{FDI} = \sum_{j=1}^{m} (100 \Delta f_j^2) \tag{7.2.3}$$

where j is the jth mode, m represents the total number of identified modes and Δf is obtained from Eq. 7.2.1. Although a damage index based on frequency change is not ideal (discussed in Chapter 3.2.2), the squared term ensures that only the sensitive modes dominate the index. A mode shape damage index (MDI) is introduced that calculates the differences in mode shapes between healthy and damaged cases:

$$\text{MDI} = \frac{1}{p} \sum_{k=1}^{p} \sum_{j=1}^{m} \left(\frac{\eta_{kj}^{*2} - \eta_{kj}^{2}}{\eta_{kj}^{*2}} \right) \tag{7.2.4}$$

where $\eta = \phi$ or ψ depending on which type of mode shape is being analysed and p is the maximum number of sensors. Finally, the variance damage index (VDI) is formulated using the RMS from the time history and is defined such that:

$$\text{VDI} = \sqrt{\frac{1}{p+N} \sum_{k=1}^{p} \sum_{t=1}^{N} \left(x_{kt} - \frac{1}{p+N} \sum_{k=1}^{p} \sum_{t=1}^{N} x_{kt}^{*} \right)^2} \tag{7.2.5}$$

where x is the healthy baseline time history measurement, while x^* represents the measurements on the damaged case. N is the total number of samples. These indices were calculated for each of the damage combinations and the results are presented in Figures 7.17 - 7.19 where the black lines indicate the area that resulted in the "out-of-bound" condition. The suitability of the proposed damage indices will be assessed by its ability to predict the out-of-bound area. For this study, it is assumed that the number of sensors is equal to the number of structural nodes. Figure 7.17 presents the FDI for static and

rotating case. In both cases, the out-of-bound area at the tip is predicted, yet for the rotating case, the effect on frequency is more pronounced. Frequency is a global structural property, and this outcome suggests that the change in frequency is negligibly small to detect out-of-bound behaviour. Hence, for this purpose, it is superfluous to investigate differences between frequencies obtained from displacement or strain measurements.

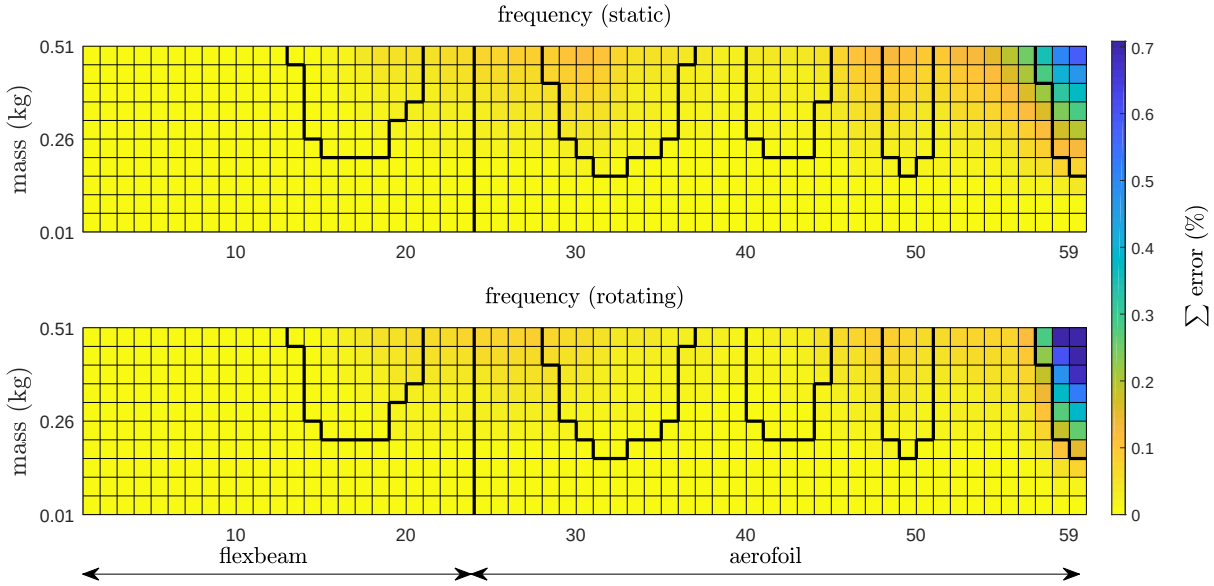

Figure 7.17: Frequency damage index, FDI

A similar trend as above is observed for the MDI for both displacement and strain measurements, while the strain mode shape seems to be more sensitive for damage at the tip. Figure 7.19 compares the VDI determined from displacement and strain measurements. It clearly points out that displacement measurements capture the out-of-bound area significantly better than strain readings, as the chosen criterion and displacement measurements have the same units.

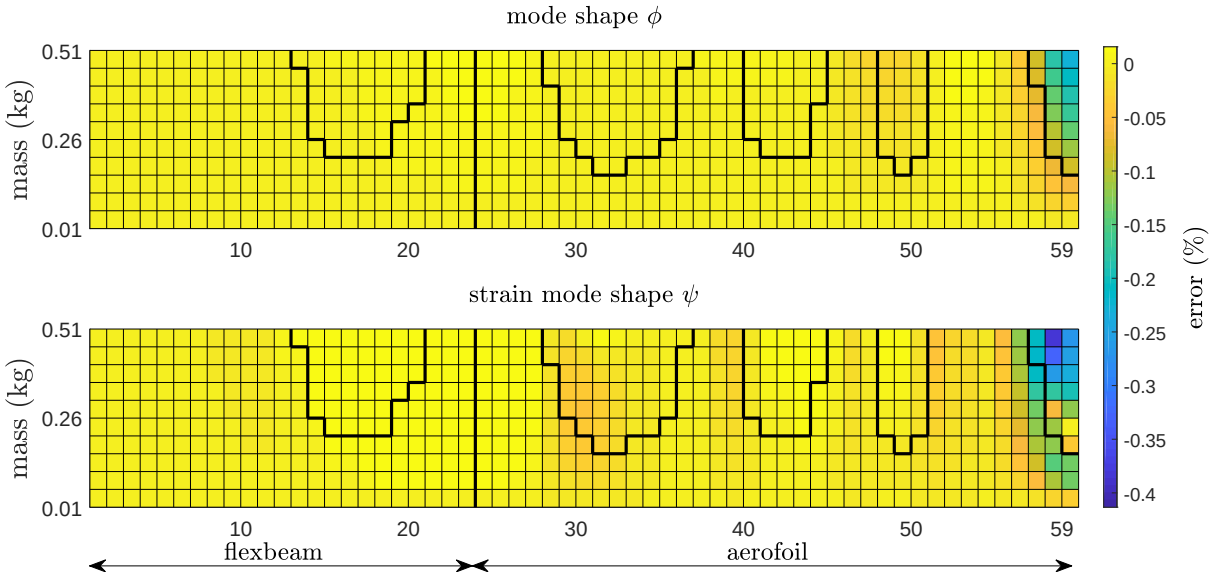

Figure 7.18: Mode shape damage index, MDI

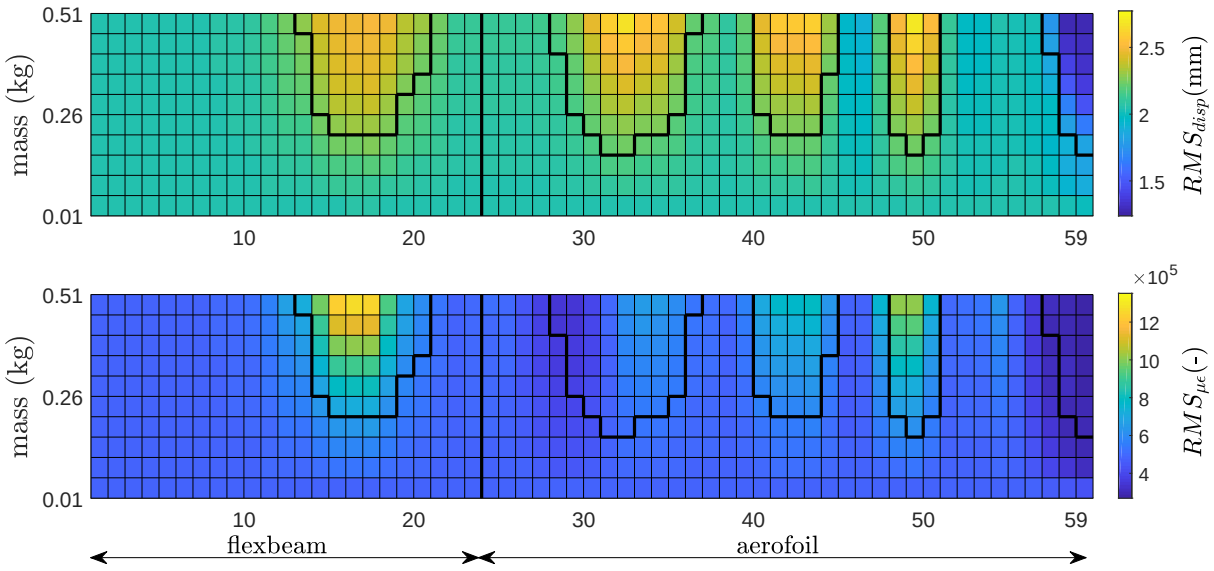

Figure 7.19: RMS of collected time history, VDI

7.3 Experimental damage test case

7.3.1 Sensor performance to damage

The final part of this research work aims to conclude some of the benefits of each instrumentation system in the experimental environment by linking it to results from the numerical damage study. Challenges, such as measurement uncertainty and measurement noise could lead to inaccurate interpretation of damage, that is particularly the case for small defects such as fibre breakage. A significant change in frequency shift has to be evident to confidently detect damage from a global perspective; if this is to be used as damage criteria. Therefore, it is important to formulate a meaningful and sensitive damage index. This section begins by providing some insight into global property change due to damage after the proposed damage indices are applied.

Damage was introduced to determine the instrumentation system's suitability for detecting a difference in dynamic characteristics. Two damage cases were applied by attaching a 0.5 kg mass piece at 75% rotor radius at the quarter chord line (damage case D1, Figure 7.20(a)) and close to the trailing edge at the same radius position (damage case D2, Figure 7.20(b)), as illustrated in Figure 7.20.

(a) Damage case 1

(b) Damage case 2

Figure 7.20: Schematic diagram of damage location using a mass piece of 0.5 kg located at 75% rotor radius

The RoR was repeated so that the damage events could be compared with the healthy baseline case as presented earlier. Due to the added mass, a frequency shift towards the

lower frequency spectrum is expected. It was found that the introduced damage predominately affected the higher frequencies, while the damage is not necessarily reflected in a mode shape change. Figure 7.21 shows the PSD covering the frequency range of Mode 1T and 4F recorded at 60% rotor radius. While a frequency shift is evident in particular for Mode 4F, a change in peak amplitude indicates a change in mode shape such as observable from the FBG measurements. From previous results, it is evident that FBGs located towards the trailing edge exhibit a higher signal-to-noise ratio for lagging and torsional modes. Therefore, the PSD obtained from FBG measurements (CH6b) indicating a frequency shift of Mode 1T, while only a small resonance peak is observable for the DFOSS system.

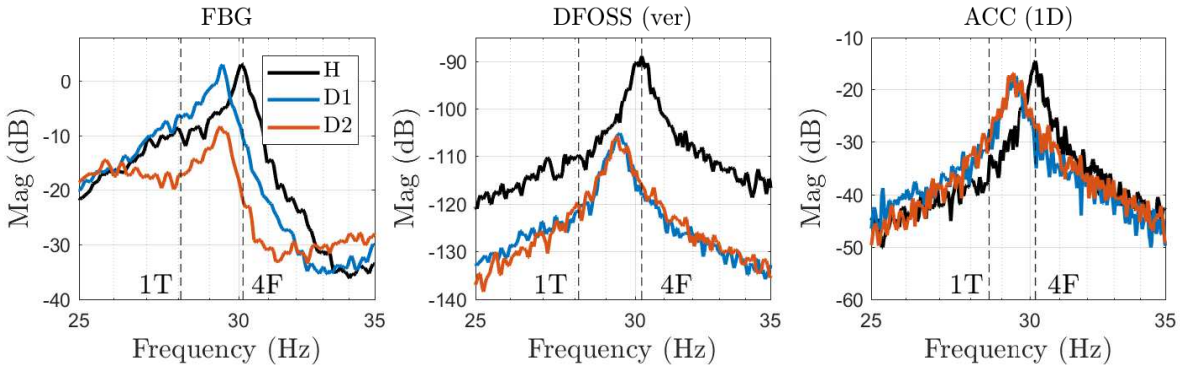

Figure 7.21: PSD limited to the frequency range between Mode 1T and Mode 4F at 60% rotor radius

Table 7.3 compares the change of frequency Δf for D1 and D2 and it is clear that the damage located close to the trailing edge introduces a higher torsional frequency change. Δf determined from all acquisition systems is in the same order of magnitude for Mode 4F, while there is a significant difference for the remaining modes. Changes for Mode 1L due to both damage cases are evident from the FBG and DFOSS measurements, while D1 mainly affects Mode 2L that is captured by both FBG and DFOSS. For D2 a significant frequency shift for Mode 1T is predicted from the FE model. This seems to be overpredicted by a factor of 1.6 based on measurements from the FBG system. This is expected through modelling assumptions, as explained in Section 7.2.

Table 7.3: Change of frequency due to damage case 1 and 2

Mode number	Mode type type	Δf (%) - D1				Δf (%) - D2			
		FE	ACC (1D)	FBG	DFOSS	FE	ACC (1D)	FBG	DFOSS
1	1st flapping	-1.33	0.00	0.00	0.00	-1.33	3.33	0.00	0.00
2	1st lagging	-1.27	-	5.88	-15.09	-1.27	-	5.88	-20.75
3	2nd flapping	-0.17	0.56	0.00	0.88	-1.40	-1.70	0.00	0.00
4	3rd flapping	-1.30	-0.40	-0.98	-1.79	-1.39	-0.20	-1.47	-1.49
5	2nd lagging	-0.08	-	2.94	-9.02	-0.33	-	1.68	-0.98
6	1st torsion	-0.66	0.00	-0.27	0.00	-6.20	-0.64	-3.80	-0.17
7	4th flapping	-2.40	-2.22	-2.28	-2.46	-2.38	-2.53	-1.77	-2.77
8	5th flapping	-0.56	-1.53	-1.03	0.56	-0.57	-0.59	0.15	0.93
	average	|0.97|	|0.79|	|1.67|	|3.73|	|1.86|	|1.50|	|1.84|	|3.39|

A change in MAC between the healthy and damaged case is calculated as follows:

$$\Delta M = (1 - \mathrm{mac}_{jj})100\% \tag{7.3.1}$$

where mac_{jj} is the diagonal term of the MAC matrix for the jth mode. Results as listed in Table 7.4 yield an overall small percentage change ΔM, while the FE model only predicts differences for Mode 2L, 1T and 4F. The mode shapes obtained from the FBG system (CH5b for flapping and torsional modes, and CH6b for lagging modes) result in an overall higher difference of mode shape correlation. Since FBGs measure strain along their longitudinal axis, they are capable of measuring shear strain that could be induced due to torsion. The favourable FBG measurement location close to the trailing edge results in high sensitivity for this type of damage. On the contrary, the ACC (1D) and DFOSS systems are located close to the quarter chord line which is also approximately the centre of rotation of the structure and hence, little change in mode shape is evident.

Table 7.4: Change of MAC due to damage case 1 and 2

Mode number	Mode type type	ΔM (%) - D1				ΔM (%) - D2			
		FE	ACC (1D)	FBG	DFOSS	FE	ACC (1D)	FBG	DFOSS
1	1st flapping	0.00	0.25	5.86	0.00	0.00	0.22	6.32	0.00
2	1st lagging	0.00	-	19.05	0.02	0.00	-	19.96	0.04
3	2nd flapping	0.00	0.00	1.68	0.00	0.00	0.00	1.27	0.00
4	3rd flapping	0.00	0.04	2.29	0.02	0.00	0.15	2.16	0.01
5	2nd lagging	0.12	-	7.18	1.45	0.50	-	11.49	0.93
6	1st torsion	0.74	1.93	2.28	0.97	24.97	5.06	4.26	1.31
7	4th flapping	0.06	1.96	1.19	1.26	6.34	0.04	1.87	1.13
8	5th flapping	0.00	0.36	1.73	2.32	0.00	0.15	3.79	1.68
	average	|0.12|	|0.76|	|5.16|	|0.76|	|3.98|	|0.94|	|6.39|	|0.64|

The change of strain mode shape is presented in Figure 7.22 comparing both damage cases with the healthy baseline case (H) and to the numerical model, labelled as FE H. Other than the frequency shift that is a global damage indicator, strain mode shape provides some insight into local structural change. A spanwise shift in maximum amplitude from 40% to 30% rotor radius is evident from both lagging modes that are a result of the added weight at 75% rotor radius. This change is also reflected by ΔM but it does not give any indication about the size and location of the damage. The displacement mode shapes obtained from ACC (1D) and DFOSS systems are shown in Figure 7.23 highlighting the largest difference for Mode 1T and 4F.

The damage case study showed that FBG sensors are more sensitive to damage predominantly because of its measurement location and ability to measure shear strain. The performance of the DFOSS system needs to be investigated further by mounting it to different chordwise locations. The presented data proves that the instrumentation system is capable of detecting a global system property change due to damage, although some damage detection algorithms have to be used for identifying its location. However, the aim of such an instrumentation system for in-flight operation is to provide information about overall system behaviour, while at the same time collect valuable information for the wider research community. Furthermore, the instrumentation system needs to be applied to a full-scale helicopter to demonstrate the capability of this technology in a realistic rotating environment.

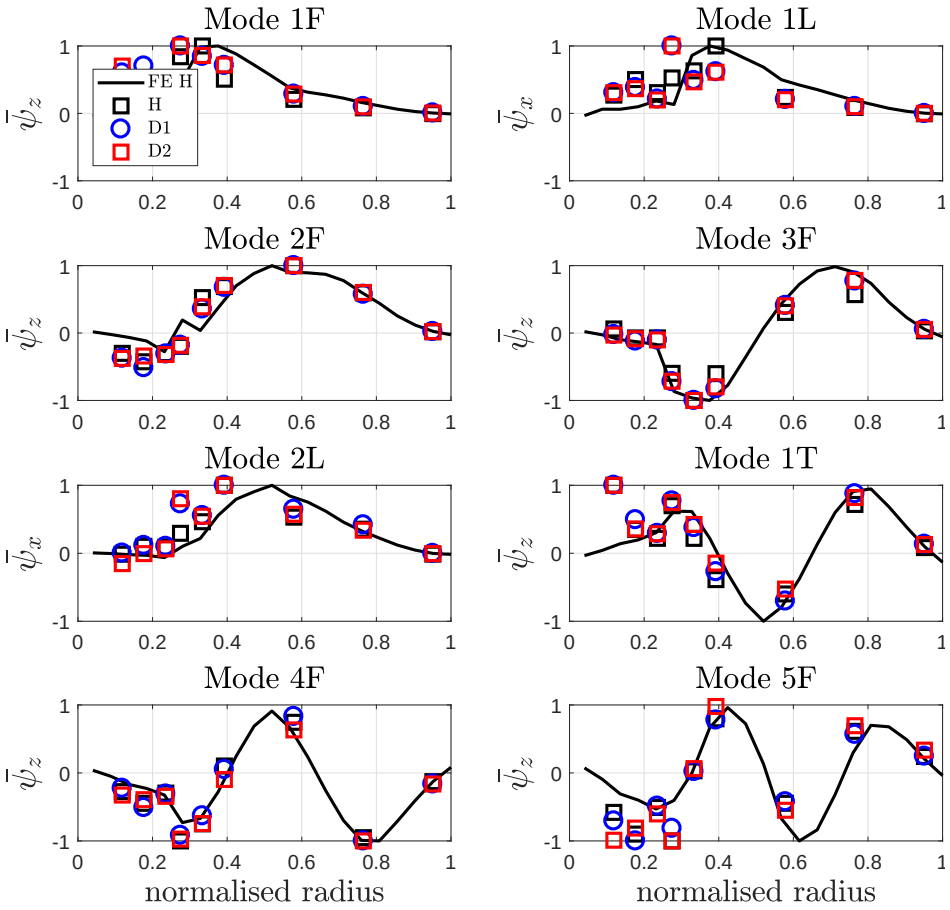

Figure 7.22: Normalised surface strain mode shape $\bar{\psi}_T$ due to damage

7.3.2 Application of damage index

The damage indices proposed earlier were calculated using the measurements taken from the experimental damage cases. Only FDI and MDI are determined and are listed in Table 7.5. Since experimental data was collected under RoR excitation input, VDI would not provide any meaningful results unless a large database for healthy configuration is collected. From these results, one can determine which instrumentation system is the most sensitive one for the specific damage. Currently, no clear conclusion can be made for which damage index is more suitable for damage detection. Instead, an analogy has to be made with previously analysed data, while linking it with results from the parametric study.

Table 7.5: Comparison of FDI and MDI for damage test case 1 and 2

	Sensor system	Damage type D1	D2
FDI	FBG	54.98	53.82
	DFOSS	313.75	435.02
MDI	FBG	0.117	0.133
	DFOSS	0.0271	0.0181

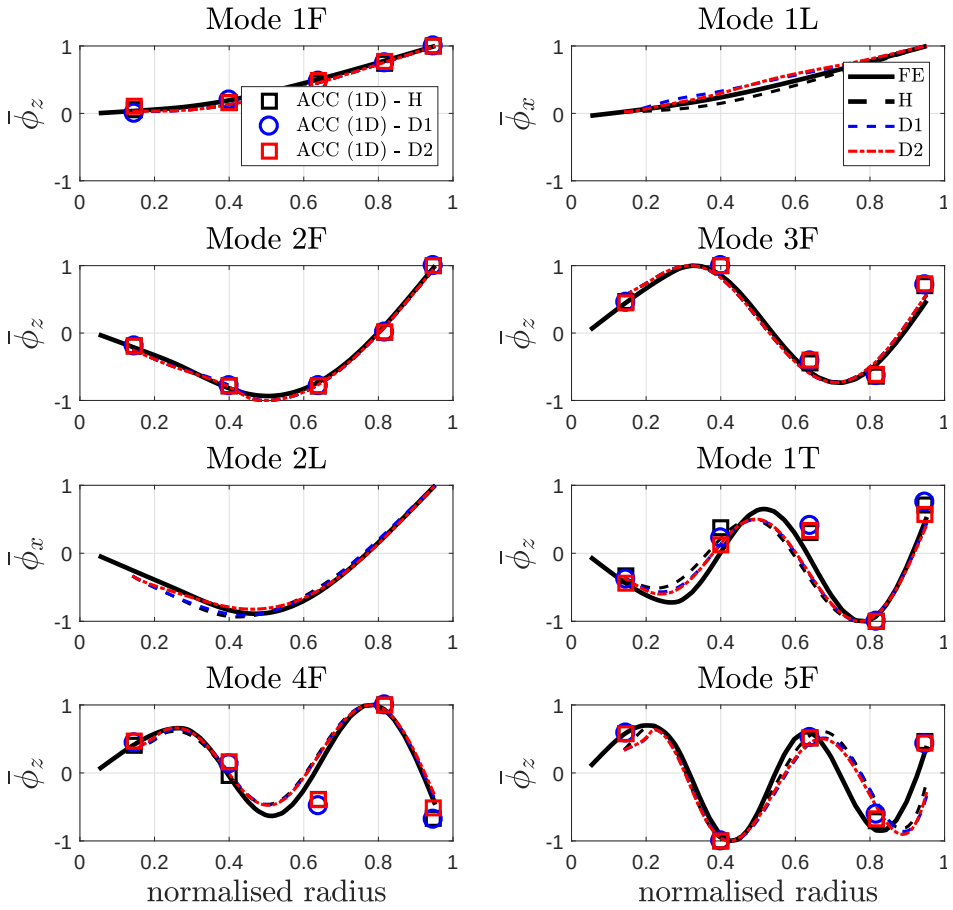

Figure 7.23: Normalised displacement mode shape $\bar{\phi}$ due to damage

Some interesting results are obtained that are already reflected to a certain degree in Tables 7.3 and 7.4. The large FDI value for DFOSS system implies that it is more sensitive in picking up frequency changes, while a lower signal-to-noise ratio of FBG measurements could have influenced the results. Any large deviation is amplified through the squared term in Eq. 7.2.3. Results obtained for MDI indicate that the DFOSS value is an order of magnitude smaller than from the FBG, demonstrating the high sensitivity of strain mode shapes to damage. This finding is also confirmed to some extent through the parametric study. As an outcome of this damage study, it is concluded that DFOSS is more suitable for detecting a change of frequency, while it is evident from the numerical and experimental studies that strain mode shapes are more sensitive to damage than displacement mode shapes. This suggests a hybrid DFOSS and FBG system for future health and usage monitoring systems.

Yet, the presented study is a preliminary and simple case. For practical applications, unsteady flight conditions associated with unsteady aerodynamics and asymmetric rotor blade loading will make the determination of blade health far more challenging. However, it is anticipated that an in-depth study using real data will open up future pathways for determining substantial damage indices.

7.4 Summary

The beginning of this chapter explored the theoretical challenges of deploying both fibre optic instrumentation systems in the rotating environment, for a healthy and damaged case. This was followed by a parametric damage study that showed a highly non-linear behaviour of modal properties to damage, particularly for the higher frequency modes. Modal property identification was discussed based on simulated displacement and strain measurements. It was found that the small time history amplitude of displacement measurements (compared to strain) resulted in difficulties of identifying all modes of interests. Furthermore, numerical results demonstrated that the optimal strain sensor positions provided improved results compared to random distribution for the rotating frame. Challenges associated with optimal sensor placement under the effect of centrifugal stiffening or damage through added mass were studied. This underlines the limitation that optimal sensor positions are only valid for a particular loading condition.

Although it is difficult to quantify damage indices without experimental evidence, this work utilised model-based methods by focusing on the exploration of different damage indicators for future data collection. These were based on the outcome of the parametric damage case study by adopting a damage criterion based on admissible tip deviation taken from standard track and balancing procedures. Numerical (rotating frame) and experimental (static frame) investigation of these damage indices demonstrated a high sensitivity of strain mode shapes to damage, while the DFOSS was more suitable for detecting changes in frequencies. Therefore, the outcome of this research work suggests a hybrid DFOSS and FBG system for future health and usage monitoring capabilities.

CHAPTER 8

Conclusions and future work

Technological advancements and improved safety regulations in helicopter design over the last century have led to helicopter operations becoming significantly safer. A low statistical accident rate involving main rotors is reflected through the rigorous approach the rotorcraft design community has enforced for rotor blades in combination with advanced modelling techniques. Nevertheless, researchers and practitioners spend much effort in integrating theoretical methods with rotor health monitoring systems by using the limited data available from track and balancing procedures and flight tests. Since the maintenance sector still relies on traditional servicing methods, it is believed that rotor HUMS could be a promising tool for supporting the maintenance actions, and further contribute to condition-based maintenance for reducing operational cost and improving aircraft availability. It is evident that all technical areas lack operational in-flight blade deformation data that is limiting today's rotorcraft design community from making significant improvements. Yet, technological advancements in fibre optic sensor technology are now presenting an opportunity to monitor blade dynamics in operational environments and in doing so, potentially furthering our understanding of blade dynamics. Therefore, the aim of the work presented in this thesis was to explore the capabilities of fibre optic instrumentation systems to facilitate exploitation for future health and usage monitoring.

The purpose of this chapter is to summarise the key conclusions and discuss their implications in the wider context of the aims of this research. Areas of future work and the key contributions to knowledge are also presented together with a list of how the results from this research effort were disseminated.

8.1 Summary of findings

A survey carried out to obtain a view of main rotor blade damage occurring in service and their impact on today's helicopter operations highlighted the reliability of rotor blades in the harsh operating environment. Feedback presented from the participants confirmed widely accepted beliefs, such as the fact that visually identifiable rotor blade damage

is often directly sensed by the pilot through increased vibration or noise, while internal damage often goes unnoticed in flight and can be hard to detect, even during maintenance.

The outcome of this survey together with statistical data highlighted the dichotomy faced by designers and rotorcraft engineers who have a choice: to either follow a reactive strategy based on operational experience or a preventative approach based on technological trends. Nevertheless, a review of historic and current research efforts spent towards blade health monitoring, advanced mathematical modelling and instrumentation techniques suggested a growing interest in the rotorcraft community for operational in-flight blade measurements. Currently, only a limited amount of operational data collected during track and balancing procedures can be linked with model-based methods for damage identification and prognostics for rotor HUMS. It was found that most measurement systems are only applicable in controlled laboratory environments or usable for a limited number of flight tests, while recent advances in fibre optic instrumentation show potential for in in-service operation applications. Furthermore, the need for shape measurements was identified due to the extensive research interest in converting strain to displacement, while eliminating dependence on structural information.

Based on a review of existing aeroelastic modelling techniques, a compromise had to be made between the versatility of modelling capabilities and the computational efficiency, particularly for detailed damage study. An industrial structural modelling approach was proposed that was linked with a quasi-steady dynamic inflow model together with blade momentum theory. Unavoidable numerical errors and lack of detailed structural knowledge highlighted the difficulties in accurately predicting surface strain. Despite uncertainties in material properties and simplifications within the structural modelling approach, experimental testing showed significant predictive capabilities for both displacement and strain estimation. A sensitivity study was carried out to predict the effects of changes in structural properties on structural dynamics and to estimate uncertainty bound for surface strain due to the uncertainty of the neutral axis position.

Structural modal properties were updated in virtue of experimental test results. A multi-step indirect finite element model updating approach was proposed that targeted the modes of interests in isolation via specific weighting factors. An assessment of updating parameters was carried out by adopting a modal assurance criterion sensitivity in addition to the commonly used eigenvalue sensitivity. Challenges associated with updating a finite element model defined by a large parameter set and strongly coupled structural modes were addressed by trading off the achieved accuracy with the computational cost.

The outcome of FBG and DFOSS measurements from a series of ground vibration tests showed the potential for measuring blade dynamics and provided a complete experimental data set characterising a healthy bearingless main rotor blade. The DFOSS measurement approach was also validated, while the capabilities of fibre optic sensors were addressed by pinpointing the benefits of each instrumentation system. Pros and cons identified through experimental testing are summarised in Table 8.1. Note that the limitations mentioned for DFOSS can be significantly improved by addressing these in the development of the next DFOSS generation.

The obtained strain measurements highlighted the importance of choosing the optimal strain sensor location to minimise measurement noise and thus achieve the highest possible signal-to-noise ratio. Based on this finding a sensor placement algorithm was developed that allowed a two-dimensional spatial distribution. Numerical and experimental

Table 8.1: Comparison of pros and cons of FBG and DFOSS

Description	FBG		DFOSS	
	YES	NO	YES	NO
detailed structural model is required	x			x
output of displacement in two dimensions		x	x	
prediction of structural loading	x			x
local torsion measurement	x			x
continuous measurements		x	x	
ease of installation (tape)		x	x	
straight fibre optic cable sufficient for characterising structural dynamics		x	x	
optimal distribution of sensors needed	x		x	

results demonstrated that the optimal strain sensor positions provided improved results compared to random distribution for both, static and rotating frame. Challenges associated with optimal sensor placement under the effect of centrifugal stiffening or damage through added mass were studied. This underlines the limitation that optimal sensor positions are only valid for a particular loading condition.

Having assessed the fibre optic instrumentation system in the static environment, theoretical capabilities were explored in the rotating frame for healthy and damaged cases. Modal property identification was discussed based on simulated displacement and strain measurements. It was found that the small time history amplitude of displacement measurements (compared to strain) resulted in difficulties of identifying all modes of interests. A parametric damage study showed a highly non-linear behaviour of modal properties to damage, particularly for the higher frequency modes. Although it is difficult to quantify damage indices without experimental evidence, this work utilised model-based methods by focusing on the exploration of different damage indicators for future data collection. These were based on the outcome of the parametric damage case study by adopting a damage criterion based on admissible tip deviation taken from standard track and balancing procedures. Numerical (rotating frame) and experimental (static frame) investigation of these damage indices demonstrated a high sensitivity of strain mode shapes to damage, while the DFOSS was more suitable for detecting changes in frequencies. A summary of damage detection capabilities is given in Table 8.2. Although Table 8.1 highlights the benefits of DFOSS, strain is very sensitive to damage especially due to its capability of measuring shear strain. Therefore, the outcome of this research work suggests a hybrid DFOSS and FBG system for future health and usage monitoring capabilities.

Table 8.2: Sensitivities of damage detection capabilities in the static and rotating frame

Damage index	Theoretical (rotating)				Experimental (static)			
	Strain		Disp.		FBG		DFOSS	
	YES	NO	YES	NO	YES	NO	YES	NO
FDI						x	x	
MDI	x			x	x			x
VDI		x	x					

8.2 Contributions to knowledge

The contributions to knowledge identified and attributed to the work presented here can be summarised as follows:

1. Foundations were laid by linking the need for rotor blade measurement systems between designer, maintainer and operator. This was achieved through a survey that provided a view of main rotor blade damage occurring in service and the corresponding impact on today's helicopter operations that was further complemented by an extensive literature review.

2. A multi-step indirect finite element model updating technique was proposed that targeted modes of interest in isolation. An assessment of updating parameters was carried out by adopting a modal assurance criterion sensitivity in addition to the commonly used eigenvalue sensitivity.

3. The novel DFOSS was deployed to a BMR blade to assess sensor performance in a non-rotating laboratory environment and compared with the FE model and other commercially available instrumentation systems.

4. The effect of chordwise strain measurements was investigated that allowed the selection of strain sensor locations from theoretical and practical points of view.

5. A discussion was given that pinpointed the benefits of FBG and DFOSS measurements for deployment on complex structures, both for numerical and theoretical exploration. Experimental data collection from GVTs of a healthy BMR blade was obtained. Recommendations were given with regards to the fibre optic instrumentation system's sensitivity to damage.

6. Future rotor HUMS based on fibre optic sensing technologies require the development of a hybrid FBG and DFOSS instrumentation system.

8.3 Recommendations for further work

The work carried out in this thesis has mainly focused on exploring fibre optic instrumentation systems in a laboratory environment. While promising results were obtained, it is crucial to test such systems in the rotating frame. Furthermore, the use of sophisticated simulation frameworks is essential for furthering the exploration of fibre optic instrumentation systems in a theoretical sense. The presented computational framework is based upon simplifications and assumptions and the main recommendation would be to improve the simulation fidelity. In general, this work provides a glimpse into the potential future health and usage monitoring, and throughout this research more questions were raised than answered. The key areas of further work are identified as follows:

1. A higher fidelity structural model should include shear strain for more accurate prediction of surface strain.

2. The aeroelastic modelling capabilities have to be improved by implementing a higher fidelity aerodynamic model, linking the current computational framework of the main rotor to other helicopter components, such as tail rotor or fin, and establish a full 6 DOF flight dynamic model.

3. Sophisticated aeroelastic and flight dynamic models would allow the exploration of how in-flight blade deformation measurements could impact wider research areas, such as the investigation of blade flexibility on rotorcraft flight dynamics discussed in Reference [255]. Moreover, the development of novel flight control design methods that take into account live blade information is another potential exploitation route.

4. For the realistic prediction of damage to the overall aircraft behaviour, aspects related to human factors need to be considered as explained in Chapter 2.

5. A two-dimensional theoretical sensor mapping approach is needed that considers the inclusion of shear strain. Measurement noise should be extracted and implemented for theoretical predictions. Furthermore, this research work did not consider the identification of torsional behaviour, so focus should be put into this area. Moreover, it is suggested that at least two DFOSS cables are deployed, ideally installed at the leading and trailing edges.

6. Testing of DFOSS and FBG in the rotating frame is necessary. This will be done as part of the project BladeSense [190] on a working helicopter during ground runs.

7. While the deployment of hybrid FBG and DFOSS for future rotor HUMS is needed, it is highly desirable to embed fibre optic instrumentation system inside the structure to avoid effects on blade aerodynamics. This poses new challenges in terms of installation, manufacturing processes and interfacing of acquisition systems with the aircraft systems. Particularly important is the repeatable and precise sensor installation within each rotor blade to avoid false damage detection. In addition, the current battery-driven interrogators will have to be replaced to remove the dependency on the external power source or battery-driven systems, for example by energy harvesting methods [256].

8. Operational in-flight data collection will open up new pathways for rotor health monitoring capabilities, especially for the determination of blade damage indicators. Such information could be implemented for rotor blade life extension programmes. Furthermore, challenges associated with collecting a large amount of data suggests the rotorcraft community needs to be ready for efficient analysis and storage of future in-flight data.

9. In practice, the helicopter is subject to scenarios that can lead to non-linear excitation and asymmetric rotor blade loading. The analysis of collected data sets during such complex flight conditions bring another challenge for health monitoring.

10. The formulation of damage indices should both consider damage identification and localisation for the rotating and static frames, while taking into consideration the differences in manufacturing tolerances.

8.4 Dissemination of results

8.4.1 Presentations at technical workshops and seminars

Implementation of rotating Timoshenko beam for simulation of in-flight rotor blade deformations
Royal Aeronautical Society Conference Advances in Simulation, London, June 2016

BladeSense - project overview
AIAA Special Session: "BladeSense - a novel approach for measuring helicopter rotor blade deformation", AIAA SciTech Forum, San Diego, California, January 2019

Structural model development of a bearingless main rotor
AIAA Special Session: "BladeSense - a novel approach for measuring helicopter rotor blade deformation", AIAA SciTech Forum, San Diego, California, January 2019

Application of novel direct fibre optic shape sensing approach to measure rotor blade structural dynamics
AIAA Special Session: "BladeSense - a novel approach for measuring helicopter rotor blade deformation", AIAA SciTech Forum, San Diego, California, January 2019

8.4.2 Conference papers

Impact of rotor blade aeroelasticity on rotorcraft flight dynamics
AIAA Atmospheric Flight Mechanics Conference 2017, AIAA SciTech Forum, Grapevine, Texas, January 2017
This paper presents a study of how variations in blade flexibility can affect flight dynamics and therefore, handling qualities. An in-house flight simulation model has been developed using a reduced-order beam model together with a dynamic inflow model to take into account aeroelasticity effects. A pilot's control map has been implemented to effectively predict aerodynamic loading and dynamic movement of the blade for any flight condition. For this work only hover case is considered. Using a short pulse input, time histories predict the dynamic response of the helicopter in roll and yaw direction, as well as manoeuvre quickness for a range of blade stiffnesses. Results linking roll and yaw quickness to blade stiffness and damping are presented together with a comparison with data available in literature.

Fast computational aeroelastic analysis of helicopter rotor blades
AIAA Aerospace Sciences Meeting, Kissimmee, Florida, January 2018
The use of a new aeroelastic computer framework called Flexit is described and the framework is used to analyse the dynamic aeroelastic behaviour of a four-bladed helicopter main rotor. Flexit implements a loose coupling between unsteady vortex lattice method (UVLM) and numerical solution of the inhomogeneous Euler-Bernoulli partial differential equation (PDE). The framework is fast because most of the intensive computational functionality is performed on GPU using NVIDIA CUDA technology, and this makes it suitable for use in the early design stages. The UVLM algorithm uses a free wake model, and solution of the Euler-Bernoulli PDE is approximated using a finite difference

algorithm that includes a term to take account of centrifugal forces. The results of simulations are compared with analysis performed with CFD and FSI tools.

BladeSense a novel approach for measuring dynamic helicopter rotor blade deformation
44th European Rotorcraft Forum, Delft, September 2018
Technologies that allow accurate measurement of rotor blade dynamics can impact almost all areas of the rotorcraft sector; ranging from maintenance all the way to blade design. The BladeSense project initiated in 2016 aims to take a step in developing and demonstrating such a capability using novel fibre optic sensors that allow direct shape measurement. In this article the authors summarise key project activities in modelling and simulation, instrumentation development and ground testing. The engineering approach and associated challenges and achievements in each of these disciplines are discussed albeit briefly. This ranges from the use of computational aerodynamics and structural modelling to predict blade dynamics to the development of direct fibre optic shape sensing that allows measurements above 1kHz over numerous positions on the blade. Moreover, the development of the prototype onboard system that overcomes the challenge of transferring data between the rotating main rotor to the fixed fuselage frames is also discussed.

Measurement of rotor blade structural dynamics
44th European Rotorcraft Forum, Delft, September 2018
Initial results collected with optical fibre Bragg grating (FBG) strain sensors and with a novel direct fibre optic shape sensing approach during a series of ground vibration tests performed on a rotor blade are presented. A number of key benefits highlight the potential of applying the shape sensing system to complex rotor blade structures: (1) no information of the underlying structure is required to infer the shape and (2) the rotor blade structural characterization can be achieved with only one straight fibre optic cable that is mounted along the length of a rotor blade. An assessment of sensor performance has shown that the results are within 4% agreement with commercially available instrumentation systems. Limitations of the use of FBG-based strain gauges are discussed in terms of the dependency of strain measurements on the position of neutral axis.

Aeroelastic scaling for flexible high aspect ratio wings
AIAA Scitech 2019 Forum, , San Diego, California, January 2019
This paper provides an overview of the work conducted as part of the Cranfield BEAm Reduction and Dynamic Scaling (BEARDS) programme, which aims to develop a methodology for designing, manufacturing and testing of a dynamically scaled High Aspect Ratio (HAR) Wing inside Cranfield 8'x6' wind tunnel. The aim of this paper is to develop a methodology that adopts scaling laws to allow experimental testing of a conceptual flexible-wing planform as part of the design process. Based on the Buckingham π theorem, a set of scaling laws are determined that enable the relationship between a full-scale and sub-scale model. The dynamically sub-scaled model is manufactured as a combination of spar, skin, and added mass representing the stiffness, aerodynamic profile, and aeroelastic behaviour respectively. The spar was manufactured as a cross-sectional shape using Aluminium material, while the skin was manufactured using PolyJet technology. Compromises due to the manufacturing process are outlined and lessons learned during the development of the sub-scaled model are highlighted.

8.4.3 Journal articles

Recent experiences of helicopter main rotor blade damage
Journal of the American Helicopter Society, 2019
Results of a survey investigating commonly occurring minor rotor blade damage incidents are presented in this paper. Over 100 participants worldwide ranging from test pilots to commercial pilots and licensed engineers answered the survey. The focus of this work was to provide a user orientated context that can inform the decision making process for integrating state-of-the-art instrumentation systems for rotor blade health monitoring onboard operational helicopters. This paper highlights the dichotomy faced by designers who have a choice to either follow a reactive strategy based on operational experience or a preventative approach based on technological trends.

References

[1] B.D. Larder. Helicopter HUM/FDR: benefits and developments. *American Helicopter Society 55th Annual Forum*, pages 25–27, 1999.

[2] *HUMS extension to rotor health monitoring. CAA Paper 2008/05.* Civil Aviation Authority, 2008.

[3] M. Martinez, M. Yanishevsky, B. Rocha, R.M. Groves, N. Bellinger. *Maintenance and monitoring of composite helicopter structures and materials.* Elsevier Ltd., 2015.

[4] P.M. Pawar, R. Ganguli. Helicopter rotor health monitoring - a review. *Proceedings of the Institution of Mechanical Engineers, Part G: Journal of Aerospace Engineering*, 221(5):631–647, 2007.

[5] V. Giurgiutiu. Structural health monitoring (SHM) of aerospace composites. pages 449–507. Elsevier, 2014.

[6] D.C. Lombardo. Helicopter structures - a review of loads, fatigue, design techniques and usage monitoring. Technical Report ARL-TR-15, Department of Defence: Defence Science and Technology Organisation, Melbourne, Australia, 1993.

[7] K. von Gersdorff, K. Knobling. *Die deutsche Luftfahrt. Hubschrauber und Tragschrauber.* Bernard & Graefe Verlag, third edition, 1999.

[8] J. Serafini, G. Bernardini, I. Mattioni, V. Vezzari, C. Ficuciello. Non-invasive dynamic measurement of helicopter blades. *Journal of Physics: Conference Series*, 882, 2017.

[9] S. Süße, M. Hajek. Rotor blade displacement and load estimation with fiber-optical sensors for a future health and usage monitoring system. *AHS 74th Annual Forum, 14-17 May, Phoenix, USA*, pages 1–12, 2018.

[10] G.C. Foss, E.D. Haugse. Using modal test results to develop strain to displacement transformations. *Proc. SPIE Vol. 2460, Proceedings of the 13th International Modal Analysis Conference*, pages 112–118, 1995.

[11] A. Derkevorkian, S.F. Masri, J. Alvarenga, H. Boussalis, J. Bakalyar, W.L. Richards. Strain-based deformation shape-estimation algorithm for control and monitoring applications. *AIAA Journal*, 51(9):2231–2240, 2013.

[12] A. Derkevorkian, J. Alvarenga, S.F. Masri, H. Boussalis, W.L. Richards. Computational studies of a strain-based deformation shape prediction algorithm for control and monitoring applications. *Industrial and Commercial Applications of Smart Structures Technologies 2012, 12-13, California, USA*, 8343:1–10, 2012.

[13] G.C. Kirby, D.K. Lindner, M.A. Davis, A.D. Kersey. Optimal sensor layout for shape estimation from strain sensors. *Proceedings of SPIE 2444, Smart Structures and Materials 1995: Smart Sensing, Processing, and Instrumentation*, April, 1995.

[14] C.J. Li, A.G. Ulsoy. High-precision measurement of tool-tip displacement using strain gauges in precision flexible line boring. *Mechanical Systems and Signal Processing*, 13:531–546, 1999.

[15] L.H. Kang, D.K. Kim, J.H. Han. Estimation of dynamic structural displacements using fiber Bragg grating strain sensors. *Journal of Sound and Vibration*, 305(3):534–542, 2007.

[16] W.L. Ko, W.L. Richards. U.S. Patent application for "Method for real-time structure shape-sensing", 2009.

[17] M.J. Nicolas, R.W. Sullivan, W.L. Richards. Large scale applications using FBG sensors: determination of in-flight loads and shape of a composite aircraft wing. *Aerospace*, 3(3), 2016.

[18] G. Sun, Y. Wu, H. Li, L. Zhu. 3D shape sensing of flexible morphing wing using fiber Bragg grating sensing method. *Optik*, 156:83–92, 2018.

[19] T. Kissinger, E. Chehura, S.E. Staines, S.W James, R.P. Tatam. Dynamic fiber-optic shape sensing using fiber segment interferometry. *Journal of Lightwave Technology*, 36(4):917–925, 2018.

[20] As a courtesey of Airbus Helicotpers Deutschland (Obtained: September 2016).

[21] Special Study. Review of rotorcraft accidents 1977-1979. Technical Report NTSB-AAS-81-1, National Transportation Safety Board, Washington D.C., USA, 1981.

[22] U.S. helicopter accidents decrease. https://www.faa.gov/news/updates/?newsId =87406. Accessed: 10 April 2018.

[23] M. Amura, L. Aiello, M. Colavita, F. De Paolis, M. Bernabei. Failure of a helicopter main rotor blade. *Procedia Materials Science, 20th European Conference on Fracture*, 3:726–731, 2014.

[24] Accident report. https://www.ntsb.gov/investigations/AccidentReports/_layouts/ntsb.aviation/brief.aspx?ev_id=20001213X29709&key=1. Accessed: 11 April 2018.

[25] D.R. Hinson. Safety recommendation. Technical Report A-94-189, National transportation safety board., Washington D.C., USA, 1994.

[26] R. Kieselbach, G. Soyka. Failure of a helicopter rotor. *Technology, Law & Insurance*, 5(3/4):141–146, 2000.

[27] A. Romeyn. Engineered system failure analysis report. Main rotor blade fracture Robinson R22, VH-OHA occurence 200302820. https://www.atsb.gov.au/media/25106/aair200302820_002.pdf, 2005. Accessed on 11 April 2018.

[28] Aviation Investigation Report. In-flight separation of main rotor blade and collision with terrain. Technical Report A11O0205, Transportation Safety Board of Canada, Ontario, Canada, 2011.

[29] Report on the accident to Sikorsky S-76A + , G-BJVX near the Leman 49 / 26 Foxtrot platform in the North Sea, 16 July 2002. *Air Accidents Investigation Branch.*

[30] N.J. Lourenço, M.L.A. Graça, L.A.L. Franco, O.M.M. Silva. Fatigue failure in a military helicopter main rotor blade. http://www.metallum.com.br/20cbecimat/resumos/trabalhos_completos/315-015.doc, 2012. Accessed on 11 April 2018.

[31] EASA Certification Specification. CS-29: Easy access rules for large rotorcraft (amendment 4), 2018.

[32] Flightglobal. Data Insight. Helicopters 2015.

[33] Some significant wildlife strikes to civil aircraft. Technical report, FAA Wildlife Strike Database, Sandusky, USA, 2010.

[34] V.T. Nagaraj, I. Chopra. Safety study of wire strike devices installed on civil and military helicopters. Technical Report DOT/FAA/AR-08/25, Air Traffic Organization Operations Planning Office of Aviation Reserach and Development, Washington D.C., USA, 2008.

[35] I.A. Herrera, S. Habrekke, T. Krakenes, P.R. Hokstad, U. Forseth. Helicopter Safety Study 3. Technical Report SINTEF A15753, SINTEF Technology and Society, Trondheim, Norway, 2010.

[36] Sikorsky Helicopters. *Flight International*, 10 October:614–615, 1963.

[37] R.L. Bielawa. *Rotary Wing Structural Dynamics and Aeroelasticity.* American Institute of Aeronautics and Astronautics, Inc., USA, second edition, 2006.

[38] A.R. Collar. Rotor anisotropy as a blade damage indicator for wind turbine structural health monitoring systems. *Aerospace*, 5(2):12–20, 1978.

[39] D.A. Peters. Modeling of unsteady aerodynamics for rotary-wing aeroelasticity. *Mathematical and Computer Modelling*, 11:293–297, 1988.

[40] G.D. Padfield. *Helicopter flight dynamics.* Blackwell Publishing, United Kingdom, second edition, 2007.

[41] D.A. Peters, D.D. Boyd, C.J. He. Finite-state induced-flow model for rotors in hover and forward flight. *Journal of the American Helicopter Society*, 34(4):5–17, 1989.

[42] A.E.F. Love. *A treatise on the mathematical theory of elasticity.* Cambridge University Press, second edition, 1906.

[43] J.C. Houbolt, G.W. Brooks. Differential equations of motion for combined flapwise bending, chordwise bending and torsion of twisted nonuniform rotor blades. Technical report, 1957.

[44] D.H. Hodges, E.H. Dowell. Nonlinear equations of motion for the elastic bending and torsion of twisted nonuniform rotor blades. *NASA Technical Note D-7818*, 1974.

[45] D.H. Hodges. *Nonlinear composite beam theory*. American Institue of Aeronautics and Astronautics, Inc., USA, 2006.

[46] C.E.S. Cesnik, D.H. Hodges. VABS : a new concept for composite rotor blade modeling. *American Helicopter Society*, 2:1627–1640, 1995.

[47] O.A. Bauchau, N.K. Kang. A multibody formulation for helicopter structural dynamic analysis. *Journal of the American Helicopter Society*, 38:3–14, 1993.

[48] P.P. Friedmann, B. Glaz, R. Palacios. A moderate deflection composite helicopter rotor blade model with an improved cross-sectional analysis. *International Journal of Solids and Structures*, 46(10):2186–2200, 2009.

[49] I.G. Lim, I. Lee. Aeroelastic analysis of bearingless rotors using large deflection beam theory. *AIAA Journal*, 45(3):599–606, 2007.

[50] D.H. Hodges. A mixed variational formulation based on exact intrinsic equations for dynamics of moving beams. *International Journal of Solids and Structures*, 26(11):1253–1273, 1990.

[51] W. Johnson. *Rotorcraft Aeromechanics*. Cambridge University Press, 2013.

[52] P.R. Heyliger. When beam theories fail. *Journal of Mechanics of Materials and Structures*, 8(1):15–35, 2013.

[53] A. Labuschagne, N.F.J. van Rensburg, A.J. van der Merwe. Comparison of linear beam theories. *Mathematical and Computer Modelling*, 49(1-2):20–30, 2009.

[54] W. Yu, D.H. Hodges, V. Volovoi, C.E.S. Cesnik. On Timoshenko-like modeling of initially curved and twisted composite beams. *International Journal of Solids and Structures*, 39:5101–5121, 2002.

[55] T. Yokoyama. Free vibration characteristics of rotating Timoshenko beams. *International Journal of Mechanical Sciences*, 30(10):743–755, 1988.

[56] S.C. Lin, K.M. Hsiao. Vibration analysis of a rotating Timoshenko beam. *Journal of Sound and Vibration*, 240(2):303–322, 2001.

[57] K. Sarkar, R. Ganguli. Modal tailoring and closed-form solutions for rotating beams. *International Journal of Mechanical Sciences*, 88:208–220, 2014.

[58] MSC.Nastran Version 70. Advanced dynamic analysis. User guide, 2001.

[59] R. Clark, D. Cox, H.C. Curtiss Jr., J.W. Edwards, K.C. Hall, D.A. Peters, R. Scanlan, E. Simiu, F. Sisto, T.W. Strganac. Aeroelastic response of rotorcraft. chapter 7. Kluwer Academic Publishers, fourth edition, 2004.

[60] A.R.S. Bramwell, G. Done, D. Balmford. *Bramwell's Helicopter Dynamics*. Butterworth-Heinemann, Oxford, second edition, 2001.

[61] S.J.A. Malham. An introduction to Lagrangian and Hamiltonian mechanics, 2014.

[62] J.E. Marsden, T.S. Ratiu. *Introduction to mechanics and symmetry. A basic exposition of classical mechanical systems.* Springer, second edition, 1999.

[63] D.A. Danielson, D.H. Hodges. Nonlinear beam kinematics by decomposition of the rotation tensor. *Journal of Applied Mechanics*, 54:258–262, 1987.

[64] V. Berdichevsky. Variational-asymptotic method of constructing a theory of shells. *AIAA Journal*, 43(4):664–687, 1979.

[65] W. Yu, M. Blair. GEBT: a general-purpose nonlinear analysis tool for composite beams. *Composite Structures*, 94(9):2677–2689, 2012.

[66] D.H. Hodges. Unified approach for accurate and efficient modeling of composite rotor blade dynamics: the Alexander A. Nikolsky honorary lecture. *Journal of the American Helicopter Society*, 60(1), 2015.

[67] D.H. Hodges, A.R. Atilgan, C.E.S. Cesnik, M.V. Fulton. On a simplified strain energy funciton for geometrically nonlinear behaviour of anisotropic beams. *Composites Engineering*, 2(September 1991):513–526, 1992.

[68] V.Z. Vlasov. *Thin-walled elastic beams.* National Science Foundation and Department of Commerce, 1961.

[69] W. Yu, D.H. Hodges, V.V. Volovoi, E.D. Fuchs. A generalized Vlasov theory for composite beams. *Thin-Walled Structures*, 43:1493–1511, 2005.

[70] W. Yu, V.V. Volovoi, D.H. Hodges, X. Hong. Validation of the variational asymptotic beam sectional analysis. *AIAA Journal*, 40(10):2105–2112, 2002.

[71] H. Pollayi, W. Yu. Modeling matrix cracking in composite rotor blades within VABS framework. *Composite Structures*, 110:62–76, 2014.

[72] O.A. Bauchau, C.L. Bottasso, Y.G. Nikishkov. Modeling rotorcraft dynamics with finite element multibody procedures. *Mathematical and Computer Modelling*, 33:1113–1137.

[73] W. Johnson. Rotorcraft dynamics models for a comprehensive analysis. *54th Annual Forum Proceedings - AHS International, 20-22 May, Washington D.C., USA*, (May):1–21, 1998.

[74] W. Johnson. Technology drivers in the development of CAMRAD II. (January):1–17, 1994.

[75] H.A. Saberi, M. Khoshlahjeh, R.A. Ormiston, M.J. Rotkowski. RCAS overview and application to advanced rotorcraft problems. *'4th Decennial Specialists' Conference on Aeromechanics*, (January 21-23), 2004.

[76] T.Y. Chun, H. Ryu, H.C. Seong, S.J. Shin, Y.J. Kee, D.K. Kim. Structural analysis of a bearingless rotor using an improved flexible multibody model. *Journal of Aircraft*, 50(2):539–550, 2013.

[77] J.G. Leishman. Rotorcraft aerodynamics. *Encyclopedia of Aerospace Engineering*, 2010.

[78] K. Richter, A. Le Pape, T. Knopp, M. Costes, V. Gleize, A.D. Gardner. Improved two-dimensional dynamic stall prediction with structured and hybrid numerical methods. *Journal of the American Helicopter Society*, 56(4), 2011.

[79] J.G. Leishman. *Principles of helicopter aerodynamics*. Cambridge University Press, New York, second edition, 2006.

[80] J.R. Wright, J.E. Cooper. *Introduction to aircraft aeroelasticity and loads*. John Wiley & Sons, second edition, 2015.

[81] D.M. Pitt, D.A. Peters. Rotor dynamic inflow derivatives and time constants from various inflow models. *Ninth European Rotorcraft Forum, 13-15 September*, 1983.

[82] D.A. Peters G.H. Goankar. Effectiveness of Current Dynamic-Inflow Models in Hover and Forward Flight. *Journal of the American Helicopter Society*, 31(2):47–57, 1986.

[83] D.A. Peters, N. HaQuang. Technical note: dynamic inflow for practical applications. *Journal of the American Helicopter Society*, 33(4), 1988.

[84] A.J. Landgrebe. An analytical method for predicting rotor wake geometry. *Journal of the American Helicopter Society*, 14(4):20–32, 1969.

[85] D.R. Clark, A.C. Leiper. The free-wake analysis - a method for the prediction of helicopter hovering performance. *25th Annual Forum of the American Helicopter Society*, 1969.

[86] J.M. Greenberg. Airfoil in sinusoidal motion in a pulsating stream. *National Advisory Committee for Aeronautics*, (1326), 1947.

[87] P.P. Friedmann, C. Venkatesan. Finite state modeling of unsteady aerodynamics and its application to a rotor dynamics problem. *Eleventh European Rotorcraft Forum, London*, 1985.

[88] D.A. Peters, C.J. He. A closed-form unsteady aerodynamic theory for lifting rotors in hover and forward flight. *American Helicopter Society 43rd Annual Forum - Proceedings, Missouri, USA*, 2:839–865, 1987.

[89] D.A. Peters, C.J. He. Correlation of measured induced velocities with a finite-state wake model. *Journal of the American Helicopter Society*, 36(3):59–70, 1991.

[90] D.A. Peters, C.J. He. Finite state induced flow models part II - three-dimensional rotor disk. *Journal of Aircraft*, 32(2):323–333, 1995.

[91] D.A. Peters. Complete dynamic rotor wake model in state space. Technical report.

[92] K. Yu, D.A. Peters. Nonlinear state-space modeling of dynamic ground effect. *Journal of the American Helicopter Society*, 50(3):259–268, 2005.

[93] X. Shang, D.H. Hodges, D.A. Peters. Aeroelastic stability of composite hingeless rotors in hover with finite-state unsteady aerodynamics. *Journal of the American Helicopter Society*, 44:206–221, 1999.

[94] H. Lee, S.R. Viswamurthy, S.C. Park, T. Kim, S.J. Shin, D.K. Kim. Helicopter rotor load prediction using a geometrically exact beam with multicomponent model. *Journal of Aircraft*, 47(4):1382–1390, 2010.

[95] W.J. Eun, H.Y. Ryu, S.J. Shin, Y.J. Kee, D.K. Kim. Aerodynamics-structural coupled analysis of a bearingless rotor using a flexible multi-body model. *55th AIAA/ASMe/ASCE/AHS/SC Structures, Structural Dynamics, and Materials Conference - SciTech Forum and Exposition, 13-17 January, Maryland, USA*, pages 1–11, 2014.

[96] I. Goulos, V. Pachidis. Real-time aero-elasticity simulation of open rotors with slender blades for the multidisciplinary design of rotorcraft. *Journal of Engineering for Gas Turbines and Power*, 137(1), 2014.

[97] I. Goulos, V. Pachidis, P. Pilidis. Helicopter rotor blade flexibility simulation for aeroelasticity and flight dynamics applications. *Journal of the American Helicopter Society*, 59(4), 2014.

[98] J.G. Leishman, T.S. Beddoes. A semi-empirical model for dynamic stall. *Journal of the American Helicopter Society*, 34(3):3–17, 1989.

[99] J. Zhao, J.V.R. Prasad, D.A. Peters. Rotor dynamic wake distortion model for helicopter maneuvering flight. *Journal of the American Helicopter Society*, 49(4):414–424, 2004.

[100] G.H. Gaonkar, D.A. Peters. Review of dynamic inflow modeling for rotorcraft flight dynamics. *American Institute of Aeronautics and Astronautics*, (2):89–115, 1988.

[101] R.T.N. Chen. A survey of nonuniform inflow models for rotorcraft flight dynamics and control applications. Technical Report 102219, Ames Research Center, California, USA, 1989.

[102] P.P. Friedmann. Rotary-wing aeroelasticity: current status and future trends. *AIAA Journal*, 42(10):1953–1972, 2004.

[103] P.P. Friedmann. Aeroelastic instabilities of hingeless helicopter blades. *Journal of Aircraft*, 10(10):623–631, 1973.

[104] P.P. Friedmann, P. Tong. Dynamic nonlinear elastic stability of helicopter rotor blades in hover and in forward flight. Technical Report NASA CR-114485, Ames Research Center, California, USA, 1972.

[105] D.H. Hodges, R.A. Ormiston. Stability of elastic bending and torsion of uniform cantilever rotor blades in hover with variable structural coupling. Technical Report NASA TN D-8192, Ames Research Center and U.S. Army Air Mobility R&D Laboratory, California, USA, 1976.

[106] M.V. Fulton, D.H. Hodges. Aeroelastic stability of composite hingeless rotor blades in hover - part II: results. *Mathematical and Computer Modelling*, 18(3–4):19–35, 1993.

[107] K.A. Yuan, P.P. Friedmann. Aeroelasticity and structural optimization of composite helicopter rotor blade with swept tips. *NASA Contractor Report*, (NASA-CR-4665), 1995.

[108] I. Goulos, V. Pachidis, P. Pilidis. Flexible rotor blade dynamics for helicopter aeromechanics including comparisons with experimental data. 119(1213):301–342, 2015.

[109] I. Goulos, V. Pachidis, P. Pilidis. Lagrangian formulation for the rapid estimation of helicopter rotor blade vibration characteristics. *The Aeronautical Journal*, 118(1206):861–901, 2014.

[110] G.P. Guruswamy. Computational-fluid-dynamics- and computational-structural-dynamics-based time-accurate aeroelasticity of helicopter rotor blades. *Journal of Aircraft*, 47(3):858–863, 2010.

[111] D. Fleischmann, M.M. Lone, S. Weber, A. Sharma. Fast computational aeroelastic analysis of helicopter rotor blades. *AIAA Aerospace Sciences Meeting, 8-12 January, Kissimmee, USA*, 2018.

[112] P.J. Dempsey, D.G. Lewicki, D.D. Le. Investigation of current methods to identify helicopter gear health. *IEEE Aerospace Conference Proceedings, 3-10 March, Montana, USA*, pages 1–14, 2007.

[113] G.D. Bruckner. *Methods for expanding rotary wing aircraft health and usage monitoring systems to the rotating frame through real-time rotor blade kinematics estimation.* Phd thesis, North Carolina State University, 2015.

[114] *Helicopter vibration health monitoring (VHM). Guidance material for operators utilising VHM in rotor and rotor drive systems of helicopters.* Civil Aviation Authority, 2018.

[115] R. Ganguli, I. Chopra, D.J. Haas. Formulation of a helicopter rotor system damage detection methodology. *Journal of the American Helicopter Society*, 41(4):302–312, 1996.

[116] M. Yang, I. Chopra, D.J. Haas. Sensitivity of rotor-fault-induced vibrations to operational and design parameters. *Journal of the American Helicopter Society*, 49(3):328–339, 2004.

[117] R. Ganguli, I. Chopra, D.J. Haas. Simulation of helicopter rotor-system structural damage, blade mistracking, friction, and freeplay. *Journal of Aircraft*, 35(4):591–597, 1998.

[118] I. Tawk, J. Aubry, P. Navarro, J.F. Ferrero, S. Marguet, S. Rivallant, S. Lemaire, P. Rauch. Study of impact on helicopter blade. *Engineering Failure Analysis*, 24:38–45, 2012.

[119] K.C. Kim. Analytical investigation into the helicopter vibration resulting from main rotor blade (MRB) ballistic damage. Technical Report ARL-TR-1985, Army Research Laboratory, Maryland, USA, 1999.

[120] J. Fries. The effect of helicopter main rotor blade damage on the rotor disk (whole rotor) motion. Technical Report ARL-TR-2241, Army Research Laboratory, Maryland, USA, 2000.

[121] J. Fries. Helicopter forced response vibration analysis method RTVIB20. Technical Report February, 1993.

[122] M.E. Calvert, T.C. Wong. Aerodynamic impacts of helicopter blade erosion coatings. *30th AIAA Applied Aerodynamics Conference, 25-28 June, Louisiana, USA*, pages 1151–1163, 2012.

[123] A. Vagnot, Y. Chauveau, P. Brillant. Simulating ice impact on helicopter parts. *Presentation at HTC08*, pages 1–28, 2008.

[124] Z. Eren, S. Tataroglu, D. Balkan, Z. Mecitoglu. Modeling of bird strike to a composite helicopter rotor blade. *58th AIAA/ASCE/AHS/ASC Structures, Structural Dynamics, and Materials Conference, 9-13 January, Texas, USA*, page 11, 2017.

[125] D. Chandra Naik, R. Vijaya Kumar. Helicopter main rotor blade root end under high velocity bird impact. *7th International Conference of Materials Processing and Characterization, 17-19 March, India*, 5(2):4653–4668, 2018.

[126] P.M. Pawar, R. Ganguli. On the effect of progressive damage on composite helicopter rotor system behavior. *Composite Structures*, 78(3):410–423, 2007.

[127] N. Roy, R. Ganguli. Helicopter rotor blade frequency evolution with damage growth and signal processing. *Journal of Sound and Vibration*, 283(3-5):821–851, 2005.

[128] K. Worden, D.J. Inman. Modal vibration methods in structural health monitoring. *Encyclopedia of Aerospace Engineering*, pages 1–10, 2010.

[129] W. Fan, P. Qiao. Vibration-based damage identification methods: a review and comparative study. *Structural Health Monitoring*, 10(1):83–111, 2011.

[130] A.K Pandey, M. Biswas, M.M Samman. Damage detection from changes in curvature mode shapes. *Journal of Sound and Vibration*, 145(2):321–332, 1991.

[131] A. Messina, E.J. Williams, T. Contursi. Structural damage detection by a sensitivity and statistical-based method. *Journal of Sound and Vibration*, 216(5):791–808, 1998.

[132] F.L.M. dos Santos, B. Peeters, H. van der Auweraer, L.C.S. Góes. Modal-based damage detection of a composite helicopter main rotor blade. *54th AIAA/ASME/ASCE/AHS/ASC Structures, Structural Dynamics, and Materials Conference AIAA, 8-11 April, Boston, Massachusetts, USA*, pages 1–10, 2013.

[133] N. Stubbs, J.T. Kim, C.R. Farrar. Field verification of a non destructive damage localization and sensitivity estimator algorithm. *Proceedings of SPIE, Proceedings of the 13th International Modal Analysis Conference, 13-16 February, Tennessee, USA*, 2460(December 2013):210–218, 1995.

[134] J. Kiddy, D. Pines. An eigenstructure assignment technique for damage detection in rotating structures. *AIAA/ASME/ASCE/AHS/ASC Structures, Structural Dynamics and Materials Conference, 20-23 April, California, USA*, 4:3337–3346, 1998.

[135] J. Kiddy, D. Pines. Experimental validation of a damage detection technique for helicopter main rotor blades. *Proceedings of the Institution of Mechanical Engineers. Part I: Journal of Systems and Control Engineering*, 215(3):209–220, 2001.

[136] F.L.M. dos Santos, B. Peeters, H. van der Auweraer, L.C.S Góes. Modal strain energy based damage detection applied to a full scale composite helicopter blade. *10th International Conference on Damage Assessment of Structures, 8 - 10 July 2013, Dublin, Ireland*, 569-570:457–464, 2013.

[137] F.L.M. dos Santos, B. Peeters, H. van der Auweraer, L.C.S Góes, W. Desmet. Vibration-based damage detection for a composite helicopter main rotor blade. *Case Studies in Mechanical Systems and Signal Processing*, 3:22–27, 2016.

[138] N. Cheraghi, F. Taheri. A damage index for structural health monitoring based on the empirical mode decomposition. *Journal of Mechanics of Materials and Structures*, 2(1):43–62, 2007.

[139] R.R.K. Reddy, R. Ganguli. Structural damage detection in a helicopter rotor blade using radial basis. *Smart Materials and Structures*, 12(2):232–241, 2003.

[140] G. Bernardini, R. Porcelli, J. Serafini, P. Masarati. Shape sensing and structural health monitoring of rotor blades from strain analysis. *AHS International 73rd Annual Forum & Technology Display, 9-11 May, USA*, pages 1–9, 2017.

[141] D. Tcherniak. Rotor anisotropy as a blade damage indicator for wind turbine structural health monitoring systems. *Mechanical Systems and Signal Processing*, 74:183–198, 2016.

[142] R. Golub, W. McLachlan. In-flight measurement of rotor blade airloads, bending moments, and motions, together with rotor shaft loads and fuselage vibration, on a tandem rotor helicopter. Volume I. Instrumentation and in-flight recording system. Technical Report 67-9A, U.S. Army Aviation Materiel Laboratories, Virginia, USA, 1967.

[143] W.J. Grant, R.R. Pruyn. In-flight measurement of rotor blade airloads, bending moments, and motions, together with rotor shaft loads and fuselage vibration, on a tandem rotor helicopter. Volume II. Calibrations and instrumented component testing. Technical Report 67-9B, U.S. Army Aviation Materiel Laboratories, Virginia, USA, 1967.

[144] J. Riley, G.D Padfield, J. Smith. Estimation of rotor blade incidence and blade deformation from the measurement of pressures and strains in flight. *14th European Rotorcraft Forum, Milano, Italy*, 1988.

[145] W.K. Wilkie, P.H. Mirick, C.W. Langston. Rotating shake test and modal analysis of a model helicopter rotor blade. Technical Report 1389, U.S. Army Research Laboratory, Virginia, USA, 1997.

[146] A. Datta, I. Chopra. Validation of structural and aerodynamic modeling using UH-60A airloads program data. *Journal of the American Helicopter Society*, 51(1):43–58, 2006.

[147] R. Steijl, G.N. Barakos, K.J. Badcock. Computational study of the advancing-side lift-phase problem. *Journal of Aircraft*, 45(1):246–257, 2008.

[148] J. Sirohi, M.S. Lawson. Measurement of helicopter rotor blade deformation using digital image correlation. *Optical Engineering*, 51(4):1–8, 2012.

[149] R. Di Sante. Fibre optic sensors for structural health monitoring of aircraft composite structures: recent advances and applications. *Sensors*, 15(8):18666–18713, 2015.

[150] L.M. Bottasso, G. Sala, P., Bettini, P. Tagliabue, F., Corbani, E. Platini, A. Guerra, A. Anelli. A rugged fiber optics monitoring system for helicopter rotor blades. *44th European Rotorcraft Forum, 18-21 September, Delft, The Netherlands*, pages 1–16, 2018.

[151] N.J. Lawson, R. Correia, S.W. James, M. Partridge, S.E. Staines, J.E. Gautrey, K.P. Garry, J.C. Holt, R.P. Tatam. Development and application of optical fibre strain and pressure sensors for in-flight measurements. *Measurement Science and Technology*, 27(10):1–17, 2016.

[152] S.J. Buggy, S.W. James, S.E. Staines, R. Carroll, P.V. Kitson, D. Farrington, L. Drewett, J. Jaiswal, R.P. Tatam. Railway track component condition monitoring using optical fibre Bragg grating sensors. *Measurement Science and Technology*, 27(5), 2016.

[153] R.M. Groves, E. Chehura, W. Li, S.E. Staines, S.W. James, R.P. Tatam. Surface strain measurement: a comparison of speckle shearing interferometry and optical fibre Bragg gratings with resistance foil strain gauges. *Measurement Science and Technology*, 18(5):1175–1184, 2007.

[154] A. Cusano, A. Cutolo, J. Albert. *Fiber Bragg grating sensors: recent advancements, industrail applications and market exploitation.* Bentham Science Publishers, 2018.

[155] A. Goldbacher. Grundlagen der optischen Sensormessung mit Faser-Bragg-Gittern. Available at www.elektroniknet.de. (Accessed: 14 July 2015).

[156] Y.J. Rao. In-fibre Bragg grating sensors. *Measurement Science and Technology*, 8(4):355–375, 1997.

[157] C.V. Jutte, W.L. Ko, C.A. Stephens, J.A. Bakalyar, W.L. Richards, A.R. Parker. Deformed shape calculation of a full-scale wing using fiber optic strain data from a ground loads test. Technical Report NASA/TP-2011-215975, NASA Dryden Flight Research Centre, California, USA, 2011.

[158] S.B. Kim, D. Geiger, P.O. Bowles, C.G. Matalanis, B.E. Wake. Tip displacement estimation using fiber optic sensors for X2 technology^{TM} rotor blades. *AHS International 72nd Annual Forum, 16-19 May, West Palm Beach, Florida, USA*, 3:1914–1923, 2016.

[159] M. Hajek, S. Manner, S. Süße. Blade root integrated optical fiber Bragg grating sensors a highly redundant data source for future HUMS. *AHS International 71st Annual Forum, 5-7 May, Virginia Beach, Virginia, USA*, 3:1598–1605, 2015.

[160] S. Süße, M. Hajek. Dynamic rotor blade displacement tracking with fiber-optical sensors for a health and usage monitoring system. *Proceedings of the 18th AIAA/ISSMO Multidisciplinary Analysis and Optimization Conference, 5-9 June, Denver USA*, pages 1–15, 2017.

[161] H.I. Kim, L.H. Kang, J.H. Han. Shape estimation with distributed fiber Bragg grating sensors for rotating structures. *Smart Materials and Structures*, 20(3), 2011.

[162] H.I. Kim, J.H. Han, H.J. Bang. Real-time deformed shape estimation of a wind turbine blade using distributed fiber Bragg grating sensors. *Wind Energy*, 17(April 2013):657–669, 2014.

[163] S. Bosnyakov, A. Bykov, V. Coulech, S. Fonov, A. Morozov, V. Moskalik, L. Moskalik, V. Mosharov, A. Orlov, V. Radchenko, N. Tarassov. Blade deformation and PSP measurements on the large scale rotor by video metric system. *ICIASF Record, International Congress on Instrumentation in Aerospace Simulation Facilities, 29 Sept - 2 Oct 1997, California, USA*, pages 95–104, 1997.

[164] G.A. Fleming, S.A. Gorton. Measurement of rotorcraft blade deformation using Projection Moiré interferometry. *Shock and Vibration*, 7(3):149–165, 2000.

[165] O. Schneider, B.G. van der Wall, K. Pengel. HART II blade motion measured by Stereo Pattern Recognition (SPR). *American Helicopter Society 59th Annual Forum, 6-8 May, Arizona, USA*, pages 1–14, 2003.

[166] D.H. Kim, S.H. Kim, J.W. Park, J.H. Han. Blade deformation measurement of a model-scale rotor system using a SPR system with IR cameras. *39th European Rotorcraft, 3-6 September, Moscow, Russia*, pages 458–466, 2013.

[167] M.S. Lawson, J. Sirohi. Measurement of deformation of rotating blades using digital image correlation. *52nd AIAA/ASME/ASCE/AHS/ASC Structures, Structural Dynamics and Materials Conference, 4-7 April 2011, Colorado, USA*, (April):1–15, 2011.

[168] S. Rizo-Patron, J. Sirohi. Operational modal analysis of a rotating cantilever beam using high-speed digital image correlation. *57th AIAA/ASCE/AHS/ASC Structures, Structural Dynamics, and Material Conference, 4-8 January, California, USA*, pages 1–19, 2016.

[169] A.I. Abrego, L.E. Olson, E.A. Romander, D.A. Barrows, A.W. Burner. Blade displacement measurement technique applied to a full-scale rotor test. *68th American Helicopter Society International Annual Forum, 1-3 May, Texas, USA*, 4:2771–2794, 2012.

[170] D.A. Barrows, A.W. Burner, A.I. Abrego, E.O. Lawrence. Blade displacement measurements of the Full-scale UH-60A airloads rotor. *29th AIAA Applied Aerodynamics Conference, 27-30 June, Hawaii, USA*, pages 1–16, 2011.

[171] M. Ozbek, D.J. Rixen, T.W. Verbruggen. Remote monitoring of wind turbine dynamics by laser interferometry: phase 1. *27th Conference and Exposition on Structural Dynamics 2009, 9-12 February, Florida, USA*, pages 1–8, 2009.

[172] D.J. Rixen M.J.L van Tooren M. Ozbek, F Mengt. Identification of the dynamics of large wind turbines by using photogrammetry. *Conference Proceedings of the Society for Experimental Mechanics Series, 1-4 February, Florida, USA*, 1:351–359, 2011.

[173] B. Stasicki, F. Boden. Application of high-speed videography for in-flight deformation measurements of aircraft propellers. *28th International Congress on High-Speed Imaging and Photonics, 9-14 November, Canberra, Australia*, 7126:1–12, 2008.

[174] R. Boden, A. Torres, C. Maucher. Advanced optical rotor blade deformation measurements on a flying helicopter. *35th European Rotorcraft Forum, 22-25 September, Hamburg, Germany*, 1:218–227, 2009.

[175] C. Maucher, F. Boden. Blade deformation measurements with IPCT on an EC 135 helicopter rotor. 2013.

[176] T. Wolf, F. Boden. Vergleich von optischer Deformationsmessung mittels IPCT mit herkömmlichen Messverfahren bei Standschwingversuchen. *Deutscher Luft-und Raumfahrtkongress, 8-10 September, Aachen, Germany*, pages 1–8, 2009.

[177] F. Boden, B. Stasicki. Non-intrusive in-flight propeller blade deformation measurements by means of a rotating camera. *34th European Telemetry and Test Conference*, pages 58–63, 2014.

[178] F. Boden, B. Stasicki, K. Ludwikowski. Optical rotor-blade deformation measurements using a rotating camera. *38th European Test and Telemetry Conference, 26-28 June, Nuremberg, Germany*, pages 147–154, 2018.

[179] A. Fender, E.J. Rigg, R.R.J. Maier, W.N. MacPherson, J.S. Barton, A.J. Moore, J.D.C. Jones, D. Zhao, L. Zhang, I. Bennion, S. McCulloch, B.J.S. Jones. Dynamic two-axis curvature measurement using multicore fiber Bragg gratings interrogated by arrayed waveguide gratings. *Applied optics*, 45(36):9041–9048, 2006.

[180] P.M. Blanchard, J.G. Burnett, G.R.G. Erry, A.H. Geenaway, P. Harrison, B. Mangan, J.C. Knight, P.St.J. Russel, M.J. Gander, R. McBridge, J.D.C. Jones. Two-dimensional bend sensing with a single, multi-core optical fibre. *Smart Materials and Structures*, 2(9):132–140, 2000.

[181] T. Loutas, A. Bourikas. Strain sensors optimal placement for vibration-based structural health monitoring. The effect of damage on the initially optimal configuration. *Journal of Sound and Vibration*, 410(1):217–230, 2017.

[182] W.L. Ko, W.L. Richards, V.T. Tran. Displacement theories for in-flight deformed shape predictions of aerospace structures. Technical Report NASA/TP-2007-214612, NASA Dryden Flight Research Center, California, USA, 2007.

[183] W.L. Ko, V.T. Fleischer. Further development of Ko displacement theory for deformed shape predictions of nonuniform aerospace structures. Technical Report NASA/TP-2009-214652, NASA Dryden Flight Research Center, California, USA, 2009.

[184] W.L. Ko, W.L. Richards, V.T. Fleischer. Applications of KO displacement theory to the deformed shape predictions of the doubly-tapered Ikhana wing. Technical Report October, NASA Dryden Flight Research Center, 2009.

[185] I. Abdallah. *Advanced load alleviation for wind turbines using adaptive trailing edge geometry: sensoring techniques*. Msc thesis, Technical University of Denmark, 2006.

[186] H. Jiang, B. van der Veek, D. Kirk, H. Gutierrez. Real-time estimation of time-varying bending modes using fiber Bragg grating sensor arrays. *AIAA Journal*, 51(1):178–185, 2013.

[187] L. Li, W. Li, P. Ding, X. Zhu, W. Sun. Structural shape reconstruction through modal approach using strain gages. *Communications in Computer and Information Science*, 462:273–281, 2014.

[188] G. Lu, Z. Xiaojin, Z. Hesheng, G. Zhiyuan, L. Kaining. Optimal placement of FBG sensors for reconstruction of flexible plate structures using modal approach. *Proceedings of the 34th Chinese Control Conference,8 -30 July, Hangzhou, China*, 1(2):4587–4592, 2015.

[189] G. Bernardini, R. Porcelli, J. Serafini, P. Masarati. Rotor blade shape reconstruction from strain measurements. *Aerospace Science and Technology*, 79:580–587, 2018.

[190] S. Weber, D. Southgate, K. Mullaney, S.W. James, R.Rutherford, A. Sharma, M.M. Lone, T. Kissinger, E. Chehura, S. Staines, H. Pekmezci, L. Zanotti Fragonara, I. Petrunin, D. Willimas, I. Moulitsas, A. Cooke, N. Lawson, W. Rosales, R.P. Tatam, P. Morrish, M. Fairhurst, R. Atack, G. Bailey, S. Morley. BLADESENSE A novel approach for measuring dynamic helicopter rotor blade deformation. *44th European Rotorcraft Forum, 18-21 September, Delft, The Netherlands*, 2018.

[191] T. Kissinger, T.O.H. Charrett, R.P. Tatam. Range-resolved interferometric signal processing using sinusoidal optical frequency modulation. *Optics Express*, 23(7):9415–9431, 2015.

[192] T. Kissinger, R. Correia, T.O.H. Charrett, S.W. James, R.P. Tatam. Fibre segment interferometry for dynamic strain measurements. *Journal of Lightwave Technology*, 34(19):4620–4626, 2016.

[193] A. Mironov, P. Doronkin, A. Priklonsky, I. Kabashkin. Structural health monitoring of rotating blades on helicopters. *Aviation*, 20(3):110–122, 2016.

[194] M.I. Friswell, R. Castro-Triguero. Clustering of sensor locations using the effective independence method. *AIAA Journal*, 53(5):1388–1390, 2015.

[195] M. Papadopoulos, E. Garcia. Sensor placement methodologies for dynamic testing. *AIAA Journal*, 36(2):256–263, 1998.

[196] D.J. Ewins. *Modal testing - theory, practice and application*. Research Studies Press Ltd., Exeter, Great Britian, second edition, 2000.

[197] R.F. Guratzsch, S. Mahadevan. Structural health monitoring sensor placement optimization under uncertainty. *AIAA Journal*, 48(7):1281–1289, 2010.

[198] L. Li, B.S. Zhong, W.Q. Li, W. Sun, X.J. Zhu. Structural shape reconstruction of fiber Bragg grating flexible plate based on strain modes using finite element method. *Journal of Intelligent Material Systems and Structures*, 29(4):463–478, 2018.

[199] D.C. Kammer. Optimal sensor placement for modal identification using system-realization methods. *Journal of Guidance, Control, and Dynamics*, 19(3):729–731, 1995.

[200] D.C. Kammer, M.L. Tinker. Optimal placement of triaxial accelerometers for modal vibration tests. *Mechanical Systems and Signal Processing*, 18(1):29–41, 2004.

[201] W.L. Poston. *Optimal sensor locations for on-orbit modal identification of large space structures*. Msc thesis, George Washington University, Washington D.C., USA, 1991.

[202] A.R.M. Rao, K. Lakshmi, S. Krishnakumar. A generalized optimal sensor placement technique for structural health monitoring and system identification. *Procedia Engineering*, 86:529–538, 2014.

[203] D. Li, H. Li, C.P. Fritzen, B. Epureanu. Comments on "Clustering of Sensor Locations Using the Effective Independence Method". *AIAA Journal*, 54(6):2009–2010, 2016.

[204] A.R.M. Rao, K. Lakshmi, S. Krishnakumar. A generalized optimal sensor placement technique for structural health monitoring and system identification. *1st International Conference on Structural Integrity, ICONS-2014, Procedia Engineering, 4-7 February, India*, 86:529–538, 2014.

[205] M. Chang, S.N. Pakzad. Optimal sensor placement for modal identification of bridge systems considering number of sensing nodes. *Journal of Bridge Engineering*, 19(6):1–10, 2014.

[206] J. Peck, I. Torres. A DMAP program for the selection of accelerometer locations in MSC/NASTRAN. *Proceedings of the 45th AIAA/ASME/ASCE/AHS/ASC Structures, Structural Dynamics and Materials Conference, 19-22 April, California, USA*, 1:281–289, 2004.

[207] M. Reynier, H. Abou-Kandil. Sensors location for updating problems. *Mechanical Systems and Signal Processing*, 13(2):297–314, 1999.

[208] O. Menuzzi, J.S.O. Fonseca, E.A. Perondi, J.F. Gonçalves, E. Padoin, O.A.A. Silveira. Piezoelectric sensor location by the observability Gramian maximization using topology optimization. *Computational and Applied Mathematics*, 37:237–252, 2018.

[209] W. Geeraert, C. Stephan. CROR blade deformation, part 1: experimental results by strain pattern analysis. *International Forum on Aeroelasticity and Structural Dynamics, 28 June -2 July, Saint Petersburg, Russia*, pages 1–16, 2015.

[210] N.A. Samad, J.B. Siegel, A.G. Stefanopoulou, A. Knobloch. Observability analysis for surface sensor location in encased battery cells. *Proceedings of the American Control Conference, 1-3 July, Chicago, USA*, pages 299–304, 2015.

[211] G.C. Kirby, T.W. Lim, R. Weber, A.B. Bosse, C. Povich, S. Fisher. Strain-based shape estimation algorithms for a cantilever beam. *Proceedings of SPIE, Smart Structures and Materials 1997: Smart Structures and Integrated Systems, 3-6 March, California, USA*, 3041:788–798, 1997.

[212] E. Dyllong, A. Kreuder. Optimal reconstruction of mode shapes using nonuniform strain sensor spacing. *International Conference on Advanced Intelligent Mechatronics. Proceedings. 19-23 September, Georgia, USA*, pages 150–155, 1999.

[213] Y.H. Jung, S.U. Na, Y. Mok. Optimal FBG sensor deployment via Gaussian quadrature formula for measurement of displacement of laterally loaded piles. *Proceedings of the 18th International Conference on Soil Mechanics and Geotechnical Engineering, 2-6 September, Paris, France*, pages 2767–2770, 2013.

[214] I.A. Raptis, K.P. Valavanis. *Linear and nonlinear control of small-scale unmanned helicopters*. Springer Verlag, 2011.

[215] D.J. Price. *A practical investigation of helicopter longitudinal manoeuvre stability*. Msc thesis, Cranfield University, 1985.

[216] V.O. Payo. *Validation of a non-linear Lynx AH7 model using static stability test data*. Msc thesis, Cranfield University, 2012.

[217] S. Weber. *Rotornabenkonzepte zur Reduzierung der Mastmomentenkapazität für einen lagerlosen Hauptrotor*. Diploma thesis, University of Applied Sciences Munich, 2012.

[218] MSC Nastran 2001. Quick reference guide, 2001.

[219] K. Kampa, B. Enenkl, G. Polz, G. Roth. Aeromechanic aspects in the design of the EC135. *Journal of the American Helicopter Society*, 44(2):83–93, 1997.

[220] O. Stodieck, J.E. Cooper, P.M. Weaver. Interpretation of bending/torsion coupling for swept, nonhomogenous wings. *Journal of Aircraft*, 53(4):892–899, 2016.

[221] R. Rammer, M. Priems, P. Konstanzer. Modification of a four bladed main rotor impact on dynamics and vibrations. *39th European Rotorcraft Forum, 3-6 September 2013, Moscow, Russia*, pages 1–10, 2013.

[222] NX Nastran. Handbook of nonlinear analysis (solutions 106 and 129).

[223] D.W. Lobitz. A Nastran-based computer program for structural dynamic analysis of horizontal axis wind turbines. *European Wind Energy Conference, Hamburg, Germany*, pages 385–393, 1984.

[224] J. Watkinson. *The art of the helicopter*. Elsevier Butterworth-Heinemann, Great Britain, 2004.

[225] R.W. Clough, J. Penzien. *Dynamics of Structures*. Computers & Structures, Inc., Berkeley, CA, third edition, 1995.

[226] *Chebfun guide*. Pafnuty Publications, Oxford, first edition, 2014.

[227] L.N. Trefethen. Computing numerically with functions instead of numbers. *Communications of the ACM*, 58(10):91–97, 2015.

[228] J.E. Mottershead, M. Link, M.I. Friswell. The sensitivity method in finite element model updating: A tutorial. *Mechanical Systems and Signal Processing*, 25(7):2275–2296, 2011.

[229] M.I. Friswell, J.E. Mottershead. *Finite element model updating in structural dynamics*. Kluwer Academic Publishers, The Netherlands, 1995.

[230] Q.W. Yang, J.K. Liu, C.H. Li, C.F. Liang. A universal fast algorithm for sensitivity-based structural damage detection. *The Scientific World Journal*, 2013:1–8, 2013.

[231] IHS ESDU 96028. Transonic data memorandum VGK method for two-dimensional aerofoil sections. Part 2: User manual. Technical Report October, Endorsed by The Royal Aeronautical Society, 1996.

[232] P.M. Basset. Contributions à l'amélioration d'un modèle de simulation de la mécanique du vol des hélicoptères., 1996.

[233] X. Barral. *Implementation of a blade element aerodynamic model for aeroelastic coupling at the main rotor of a helicopter*. Msc thesis, Cranfield University, 2016.

[234] M. Dahleh, M.A. Dahleh, G. Verghese. Lectures on dynamic systems and control. Lecture Notes, Department of Electrical Engineering and Computer Sicence, Massachusetts Institute of Technology.

[235] N.J. Lawson. Lecture Notes. Advanced optical measurement techniques : Part 1 Errors, 2006.

[236] B. Cauberghe, P. Guillaume, P. Verboven, S. Vanlanduit, E. Parloo. On the influence of the parameter constraint on the stability of the poles and the discrimination capabilities of the stabilisation diagrams. *Mechanical Systems and Signal Processing*, 19(5):989–1014, 2005.

[237] E. Reynders. System identification methods for (operational) modal analysis: review and comparison. *Archives of Computational Methods in Engineering*, 19:51–124, 2012.

[238] L. Mthembu, T. Marwala, M.I. Friswell, S. Adhikari. Finite element model selection using particle swarm optimization. *28th IMAC, A Conference on Structural Dynamics, 1-4 February, Florida, USA*, 4:41–52, 2011.

[239] V.R. Akula, R. Ganguli. Finite element model updating for helicopter rotor blade using genetic algorithm. *AIAA Journal*, 41(3):554–556, 2001.

[240] L.B. Crema, G. Coppotelli. Output-only approach for finite element model updating of AB-204 helicopter blade. *46th AIAA/ASME/ASCE/AHS/ASC Structures, Structural Dynamics & Materials Conference, 18-21 April, Texas, USA*, 8:5587–5598, 2005.

[241] S.F. Lung, C.G. Pak. Updating the finite element model of the aerostructures test wing using ground vibration test data. *50th AIAA/ASME/ASCE/AHS/ASC Structures, Structural Dynamics, and Materials Conference, 4-7 May, California, USA*, (May), 2009.

[242] N.V. Findler, C. Lo, R. Lo. Pattern search for optimization. *Mathematics and Computers in Simulation*, 29(1):41–50, 1987.

[243] R. Basak, A. Sanyal, S.K. Nath, R. Goswami. Comparative view of genetic algorithm and pattern search for global optimization. *International Journal of Engineering and Science*, 3(4):9–12, 2013.

[244] E. Ntotsios, C, Papadimitriou. Multi-objective optimization algorithms for finite element model updating. *23rd International Conference on Noise and Vibration Engineering 2008, 15-17 September, Leuven, Belgium*, 4:1895–1909, 2008.

[245] G. Boscato, S. Russo, R. Ceravolo, L. Zanotti Fragonara. Global sensitivity-based model updating for heritage structures. *Computer-Aided Civil and Infrastructure Engineering*, 30(8):620–635, 2015.

[246] W.E. Baker. Inherent vibration damping of helicopter blades. *International Journal of Mechanical Sciences*, 13(2):157–158, 1971.

[247] G.C. Lee, Z. Liang, Q. Gan, T. Niu. Vibration reduction of helicopter blade using variable dampers - a feasibility study. Technical report, Multidisciplinary Center for Earthquake Engineering Research, New York, USA, 2002.

[248] V. Klein, E.A. Morelli. *Aircraft system identification. Theory and practice.* American Institute of Aeronautics and Astronautics, Inc., USA, 2006.

[249] M.B. Tischler. Frequency-response identification of XV-15 tilt-rotor aircraft dynamics. Technical Report NASA-TM-89428, Ames Research Center, California, USA, 1987.

[250] B.H. Kim, N. Stubbs, T. Park. A new method to extract modal parameters using output-only responses. *Journal of Sound and Vibration*, 282(1-2):215–230, 2005.

[251] P.D. Welch. The use of fast transform for the estimation of power spectra: a method based on time averaging over short, modified periodograms. *IEEE Transactions on Audio and Electroacoustics*, 15(2):70–73, 1967.

[252] S.Y. Yusuf. *On scaling and system identification of flexible aircraft dynamics.* Phd thesis, Cranfield University, UK, 2019.

[253] C.H. Jenkins, L. Kjerengtroen, H. Oestensen. Sensitivity of parameter changes in structural damage detection. *Shock and Vibration*, 4(1):27–37, 1997.

[254] Airbus. Measurement of track and unbalance - adjustment/test. *Aircraft Maintenance Manual (AMM) EC135*, (18-11-00).

[255] S. Weber, L. Ramos Valle, X. Barral, D. Hayes, M.M. Lone, A. Cooke. Impact of rotor blade aeroelasticity on rotorcraft flight dynamics. *AIAA Atmospheric Flight Mechanics Conference, 5-9 January, Texas, US*, pages 1–14, 2017.

[256] E. Mendoza, C. Kempen, Y. Esterkin, S. Sun. Energy harvesting , wireless fiber optic sensor (WiFOS^{TM}) structural health monitor system for helicopter rotors. *AIAC16 Sixteenth Australian International Aerospace Congress*, 2015.

[257] EC135 specifications. Available at http://airbushelicoptersinc.com/products/EC135-specifications.asp. (Accessed: 15 February 2016).

[258] H. Bansemir, S. Emmerling. Fatigue substantiation and damage tolerance evaluation of fiber composite helicopter components. *RTO AVT Specialists' Meeting on "Application of Damage Tolerance Principles for Improved Airworthiness of Rotorcraft", 21-22 April 1999, Corfu, Greece*, 1999.

[259] W. Bittner. *Flugmechanik der Hubschrauber*. Springer Verlag, Berlin, Germany, second edition, 2004.

[260] H. Bansemir, R. Müller. The EC135 - Applied Advanced Technology. *53rd Annual Forum Proceedings - AHS International, 29 April - 1 May, Virginia, USA*, 2:846–861, 1997.

[261] H. Strehlow, D. Teves, G. Polz. Applied helicopter aeroelastics - modelling and testing. *22nd European Rotorcraft Forum, 16 - 19 September, Brighton, UK*, pages 1–30, 1996.

[262] H. Barnerssoi, A. von Panajott, K. Pfeifer, R. Vorwerg. EC135 structural testing. *23rd European Rotorcraft Forum, 16-18 September, Dresden, Germany*, pages 16–18, 1997.

[263] W. Johnson. A history of rotorcraft comprehensive analyses. *69th American Helicopter Society International Annual Forum 2013, 21-23 May 2013, Phoenix, Arizona, USA*, (1):685–406, 2013.

[264] G.S. Bir, I. Chopra, K. Nguyen. Development of UMARC (University of Maryland Advanced Rotorcraft Code). *46th Annual Forum Proceedings of the American Helicopter Society. Part 1 (of 2), 21-23 May 1990, Washington D.C., USA*, (1):55–78, 1990.

[265] R. Sopher, D.W. Hallock. Time-history analysis for rotorcraft dynamics based on a component approach. *Journal of the American Helicopter Society*, 31(1):43–51, 1986.

[266] B. Benoit, A.M. Dequin, K. Kampa, W. von Grünhagen, P.M. Basset, B. Gimonet. HOST: A General Helicopter Simulation tool for Germany and France. *56th Annual Forum Proceedings of the American Helicopter Society, 2-4 May 2000, Virginia Beach, Virginia, USA*, (May), 2000.

[267] H. Schlichting. *Boundary Layer Theory*. Pergamon Press Ltd, second edition, 1955.

[268] R.C. Lock, B.R. Williams. Viscous-inviscid interactions in external aerodynamics. *Progress in Aerospace Sciences*, 24(2):51–171, 1987.

[269] J.E. Green, D.J. Weeks, J.W.F. Brooman. Prediction of turbulent boundary layers and wakes in compressible flow by a lag-entrainment method. Technical Report R. & M. No. 3791, Procurement Executive Ministry of Defence, London, UK, 1977.

[270] S.W. Tsai, H.T. Hahn. *Introduction to composite materials*. Technomic Publishing Co., Inc., USA, 1980.

[271] Airbus. Track and balancing - adjustment/test. *Aircraft Maintenance Manual (AMM) EC135*, (18-10-00).

[272] P. van Overschee, B. de Moor. *Subspace identification for linear systems: theory and implementation - applications*. Kluwer Academic Press, Dordrecht, The Netherlands, 1996.

[273] PLR 15 Laser Range Finder Bosch. Original instructions. Available at https://www.tooled-up.com/artwork/ProdPDF/0603672000.pdf. (Accessed: 27 June 2018).

APPENDIX A

Airbus Helicopters H135 specifications

A.1 General specifications

Figure A.1 provides the overall dimensions of an Airbus Helicopters twin-engine H135 T2 (formerly known as Eurocopter EC135). More detailed specifications can be found in Table A.1.

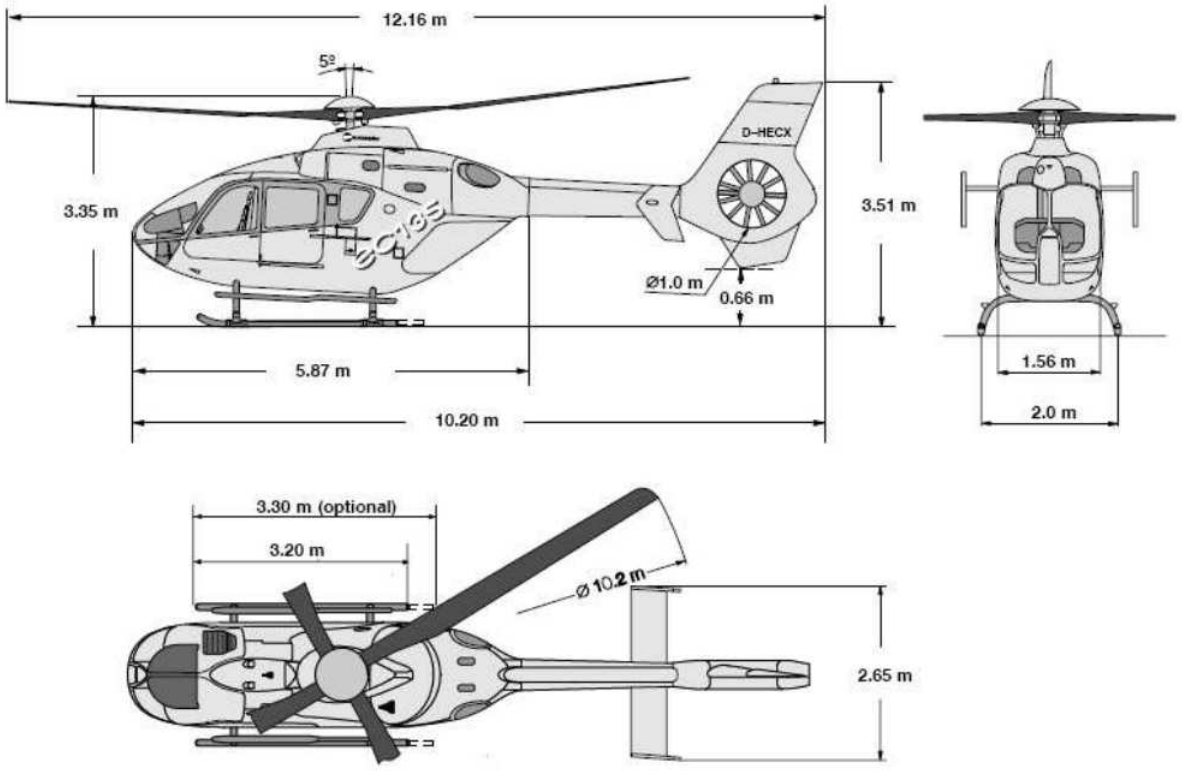

Figure A.1: Dimensions of an H135 (reproduced from Reference [257])

Table A.1: Airbus Helicopters H135 specification (reproduced from Reference [257])

Characteristic	Values
Max. useful load	1498 kg
Max take-off weight	3980 kg
Main rotor diameter	10.2 m
Number of rotor blades	4
Rotor speed	41.36 rad/s
Standard seating capacity	1 crew + 6/7 pax or 2 crew + 2/6 pax
Engines	2 Pratt & Whitney Canada PW206B2 or 2 Turbomeca Arrius 2B2
Hover out of ground effect ceiling	2012 m
Hover in ground effect ceiling	3048 m
Maximum Range (without fuel reserve)	309 km
Fast cruise speed	254 km/h
Never exceed speed	259 km/h

A.2 H135 bearingless main rotor blade

With improved material properties and advanced manufacturing technologies, the H135 BMR blade was developed by incorporating the conventional mechanical flapping, lead-lag and torsional hinges into a single flexible structure. This was achieved by using a complex composite layout with varying cross-sections. Today it is part of the family of modern advanced rotor configurations [76]. The BMR of an H135 is a fully composite design consisting of fiberglass and graphite-epoxy [258]. As shown in Figure A.2 the rotor blade consists of the pitch control cuff with an elastomeric lead-lag damper, aerofoil section, and a flexbeam.

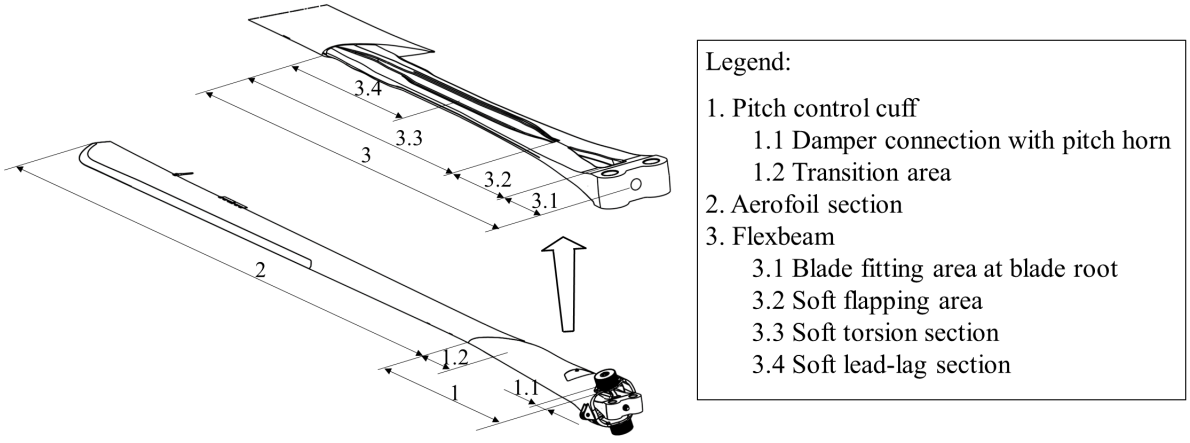

Figure A.2: H135 bearingless main rotor rotor blade (reproduced from Bansemir et al [258])

The pitch control cuff is merged with the aerofoil section over the transition area. The key element of the rotor blade is the flexbeam which incorporates the three required "hinges" within the structure. The attachment of the rotor blade is at the root of the flexbeam

which consists of two double lugs and a load path attachment. The blade is connected with only two bolts to the rotor hub thereby simplifying maintenance. The flat flapping hinge area is designed using a tapered section as shown in Figure A.2. The cruciform shape of the torsional element replaces the bearings. As explained by Bansemir et al [258] the design of "*the cross section results in an extremely low torsional stiffness of the flexbeam of 4.2 Nm/° without and of 7.2 Nm/° with centrifugal force*". This design has advantages, such as the avoidance of warping restriction and the independent tuning of flapping and lead-lag stiffnesses. Also, the static sag of the non-rotating rotor is reduced due to the relatively high flapping stiffness of the torsional element. Consequently, no blade stop is needed. Overall dimensions of the H135 T2 rotor blade are presented in Figure A.3, while a selection of cross sectional cuts provides some insight into the variation of the flexbeam.

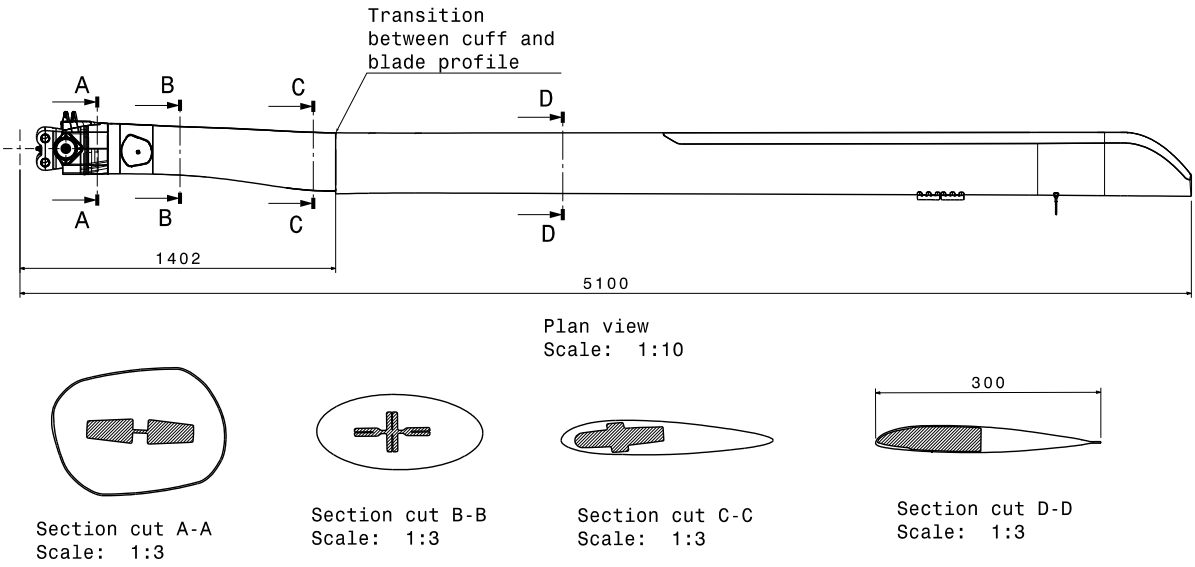

Figure A.3: Overall dimensions of H135 T2

This blade has an equivalent flapping hinge offset of about 9 % at rotor radius [219, 258]. A coning angle of 2.5° is in-built in the hub design to reduce the static flapwise bending loads in the flexbeam [219]. In comparison to its predecessor (BO105[1]), a weight reduction of 50 kg and a part count reduction of 40 % was achieved [258]. As the conventional mechanical bearings are redundant, the maintenance costs are significantly reduced. Another advantage of this blade design is that the build-up of the control moment starts from the blade root, which results in a more agile helicopter [259]. Disadvantages are mainly seen in the complicated design [258] and manufacturing process. For more information about the H135 the reader is referred to References [7, 219, 258, 260–262].

[1]The H135 main rotor was derived from the BO108 [258] which was a technology demonstrator developed based on the BO105 rotor [7]

This page is intentionally left blank.

APPENDIX B

Computational tools for rotorcraft analysis

A summary of the most common comprehensive modelling and techniques used for calculating rotorcraft performance and trim, blade motion, aerodynamic and structural loads, vibration, noise, aeroelastic stability and flight dynamics are listed below. An overview of the historical evolution of such methods and tools can be found in Reference [263].

- **UMARC** (University of Maryland Advanced Rotorcraft Code)
  - Adoption of a geometrically non-linear rotor blade model based on FE formulation [264].
  - Incorporation of a free-wake geometry model and capability of trim analysis.
- **CAMRAD II** (Comprehensive Analytical Model of Rotorcraft Aerodynamics and Dynamics, developed by Johnson Aeronautics)
  - Incorporation of multibody dynamics, non-linear finite-based elements and rotorcraft aerodynamics [73, 74].
  - CAMRAD II requires detailed input for numerical analysis and consequently may not be appropriate at a preliminary design stage of a helicopter [263].
- **RDYNE** (Rotorcraft System Dynamics Analysis, developed by Sikorsky)
  - Utilisation of dynamical substructures and non-structural components [265].
  - A single minimum variance controller is used to solve both the trim and vibration reduction problem [265].
- **HOST** (Helicopter Overall Simulation Tool)
  - Developed through the combined effort of Airbus Helicopter, DLR and ONERA [266].
  - Allows for consistent treatment of handling qualities, stability, load calculations, trim, and flutter tasks [263].

  - Capability of handling new rotor and aircraft configurations [263].

- **RCAS** (Rotorcraft Comprehensive Analysis System, developed by Advanced Rotorcraft Technology, Inc.)
  - Combination of FE structural and advanced aerodynamic model representation, and the adoption of a sophisticated control system [75, 263].
  - Inclusion of dynamic inflow and dynamic wake model.
  - Ability to analyse trim and flutter and large-motion manoeuvres [263].

- **DYMORE** (Developed at the Georgia Institute)
  - FE-based tool for analysis of non-linear, flexible multibody systems [72].
  - Ability of modelling complex configurations of arbitrary topology through the assembly of basic components. Those are chosen from an extensive library of elements that includes rigid and deformable bodies as well as joint elements [72].

APPENDIX C

Impact of surface fibre attachment on aerofoil aerodynamics

C.1 Background and boundary conditions

Bonding objects to a surface of an aerofoil can cause unwanted early flow separation and therefore, unexpected aeroelastic behaviour. Based on the definition of displacement thickness it can be argued that if the fibre attachment is smaller than the displacement thickness of the fluid, no early flow separation occurs. This context motivates a study of the aerodynamic properties of the aerofoil profile with fibre attachment, such as boundary layer thickness, displacement thickness, and pressure distribution.

For this analysis VGK was used; a computational fluid dynamics (CFD) method valid in the two-dimensional domain. As described in the user manual [231] the *"aerodynamic characteristics of a single-element aerofoil in a subsonic free stream, including the effects of viscosity (boundary-layers and wake) and shock waves"* can be predicted. VGK gives an approximation of the boundary layer properties, instead of adopting Navier-Stokes equation or Prandtl's method that satisfies the differential equations for each fluid particle within the boundary layer in a layer near the aerofoil surface [267]. This is known as von Karman's integral equation or the *momentum equation* of boundary layer theory. Schlichting [267] explained that *"in the remaining region of fluid in the boundary layer only a mean over the differential equation is satisfied, the mean being taken over the whole thickness of the boundary layer."* Figure C.1 shows the definition of the boundary layer thickness δ where the velocity at the edge of the boundary layer is reduced $U_e = 0.99U_\infty$.

The displacement thickness δ^* defines the distance by which the solid boundary would have to be displaced in a frictionless flow to provide the same mass deficit as the boundary layer. Hence, the momentum thickness θ is the thickness of a layer of fluid velocity U_∞ for which the momentum flux is equal to the deficit of momentum flux through the boundary layer. The momentum integral equation is expressed as [267]:

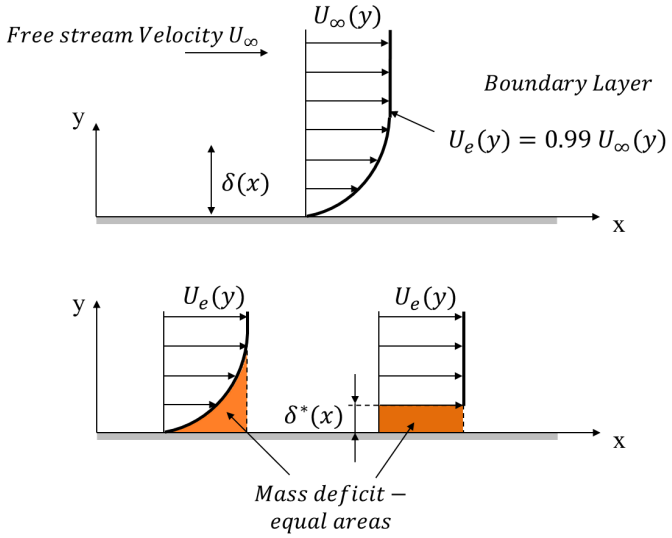

Figure C.1: Definition of boundary layer and displacement thickness

$$\frac{\partial \theta}{\partial x} + \frac{1}{U_e}\frac{\partial U_e}{\partial x}(2\theta + \delta^*) = \frac{\tau_w}{\rho_e U_e^2} = \frac{1}{2}C_f \tag{C.1.1}$$

where τ_w is the shearing stress on the wall, and the skin-friction coefficient C_f is given by:

$$C_f = \frac{\tau_w}{\frac{1}{2}\rho_e U_e^2} \tag{C.1.2}$$

with the the displacement thickness δ^* for compressible flow:

$$\delta^* = \int_0^\infty \left(1 - \frac{\rho U}{\rho_e U_e}\right) dy \tag{C.1.3}$$

and the momentum thickness θ:

$$\theta = \int_0^\infty \left(1 - \frac{U}{U_e}\right) \frac{\rho U}{\rho_e U_e} dy \tag{C.1.4}$$

Introducing the shape factor $H \equiv \delta^*/\theta$ such that the non-dimensional von Karman equation can be written as follows:

$$\frac{\partial \theta}{\partial x} + \frac{1}{U_e}\frac{\partial U_e}{\partial x}(2 + H) = \frac{1}{2}C_f \tag{C.1.5}$$

In VGK the value of the boundary layer shape factor $\bar{H}$ is calculated as follows:

$$\bar{H} = \frac{1}{\theta} \int_0^\infty \frac{\rho}{\rho_e} \left(1 - \frac{U}{U_e}\right) dy \tag{C.1.6}$$

As stated in Reference [268] for compressible flow the shape factor H should be replaced by the 'transformed' shape parameter $\bar{H}$. This was proven by Green et al [269]. Here, the displacement thickness is calculated at the maximum fluid velocity. It is assumed that the rotor disc is not tilted in forward flight and the blade is parallel with the air inflow. The maximum Mach number M_{max} occurs at the blade tip that is estimated as follows:

$$M_{max} = \frac{v_{tan}}{a} = \frac{\Omega R}{a} \tag{C.1.7}$$

where a is the speed of sound[1], v_{tan} is the tangential velocity on the blade tip, Ω is the rotor rotational speed, and R is the blade radius. The Reynolds number Re is defined as:

$$Re = \frac{\rho v c}{\mu} = \frac{v c}{\nu} \tag{C.1.8}$$

where ρ is the density of the fluid, v is the velocity of the fluid with respect to the object, c is the length of the object (chord in this case), μ is the dynamic viscosity of the fluid, and ν is the kinematic viscosity of the fluid. Two different flight cases are chosen, that are (1) a helicopter in ground run and, (2) hover out-of ground effect ceiling (see Table[2] C.1). The final study was carried out on the aerofoil section at 40 % rotor radius, due to limitations of VGK that only performs calculation below Ma = 0.63.

Table C.1: Flight condition for the 2D aerodynamic analysis

No.	Flight condition	Parameters	Values
1	Helicopter tethered on ground	Height (m)	0
		Forward speed (m/s)	0
		Tip speed of blade (m/s)	211
		Reynolds number (-)	4330000
		Mach number at blade tip (-)	0.62
2	Hover out-of ground effect ceiling	Height (m)	2012
		Forward speed (m/s)	0
		Tip speed of blade (m/s)	211
		Reynolds number (-)	3690000
		Mach number at blade tip (-)	0.63

[1]Data is taken from ISA (International Standard Atmosphere)
[2]Altitude is taken from Reference [257]

C.2 Results of 2D aerodynamic analysis

Due to limitations within VGK, the study was done for angles of attack ranging from $\alpha = -4$ to $+4°$. For higher angles of attack, the flow around the aerofoil is detached and VGK does not produce any results. The obtained pressure distribution C_p and Mach number indicate the location of shockwaves (see Table C.2 and Figure C.2) which vary with the angle of attack. For $\alpha > 2°$ a shockwave is expected around the quarter chord line, while for $\alpha < -2°$ shockwaves occur close to the leading edge. The flow separation beyond the shockwave could not be determined through VGK.

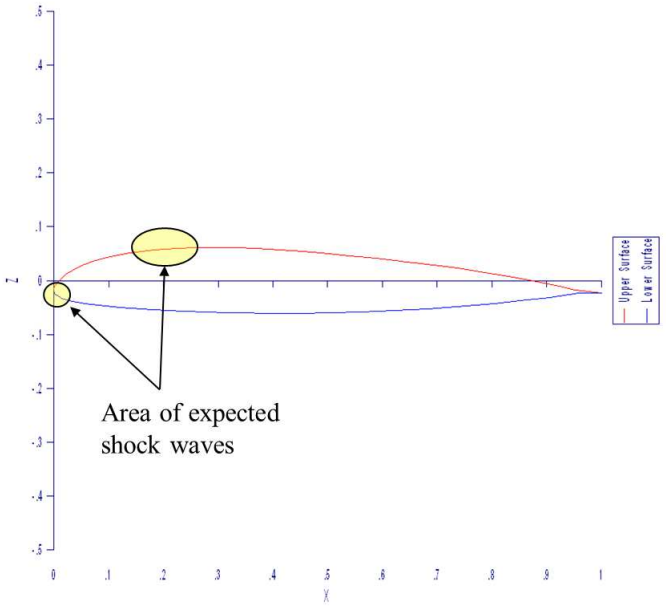

Figure C.2: Location of expected shockwave

Table C.2: Location of shockwaves

Angle of attack α (deg)	Upper surface normalised (-)	Lower surface normalised (-)
-4	n/a	0.03547
-3	n/a	0.02231
-2	n/a	0.00468
-1	n/a	n/a
0	n/a	n/a
1	n/a	n/a
2	0.16023	n/a
3	0.20174	n/a
4	0.23157	n/a

The coefficient of lift C_l and pitching moment C_m is presented in Figure C.3, while Figures C.4 - C.5 show the pressure distribution and variation of Mach number.

Figure C.6 shows the displacement thickness of upper and lower surfaces for several angles of attack for Condition 1 and Condition 2, respectively. The fibre cable has a maximum

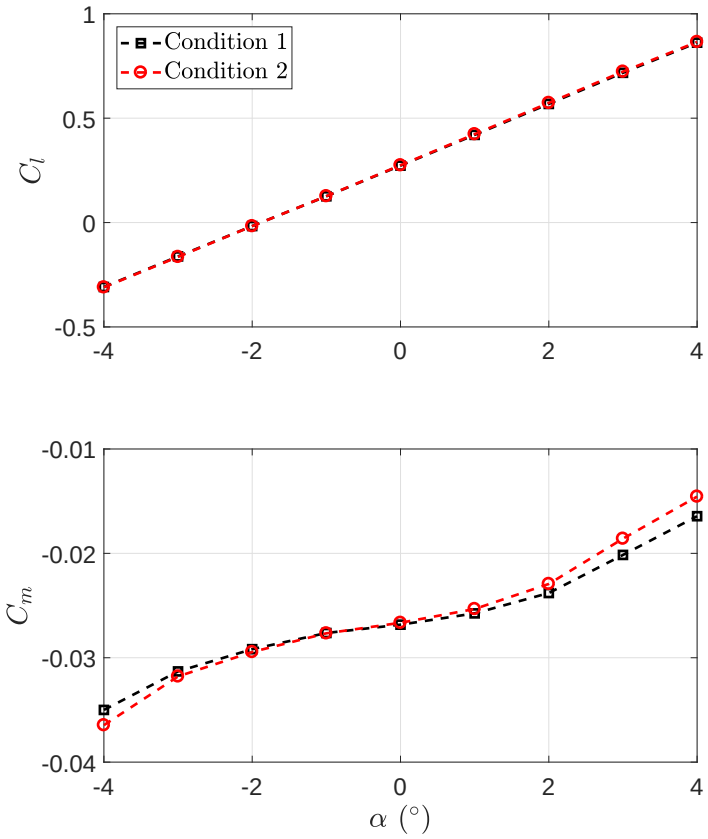

Figure C.3: Coefficient of lift C_l and pitching moment C_m versus angle of attack

thickness of 150μm, and it is assumed that the maximum thickness t_f including adhesive is around 0.001 m. Assuming that the calculated δ^* due to fibre attachment is the same as for the clean blade profile, suitable locations for the fibre cables are where $\delta^* > t_f$, resulting in fibre locations between 50 - 100 % of the chord. However, this has to be confirmed through a detailed study. Otherwise, the lower blade profile is more suitable for fibre optic cable attachment due to lift generation at the top surface. Furthermore, a more detailed analysis has to be done to calculate the displacement thickness for a higher range of angles of attack. Besides it is suggested to use a different CFD programme, such as ANSYS Fluent, as the following limitations have been identified with the use of VGK:

- Maximum Mach number entry is 0.63.
- Meshing grid is not fine enough to include the fibre cable as a parametric study.
- The flow field after a shockwave cannot be obtained.
- VGK does not produce results when the flow is separated.

Additional results were obtained for local skin friction coefficient C_f (Figure C.8), shape factor $\bar{H}$ (Figure C.7), and momentum thickness θ (Figure C.9).

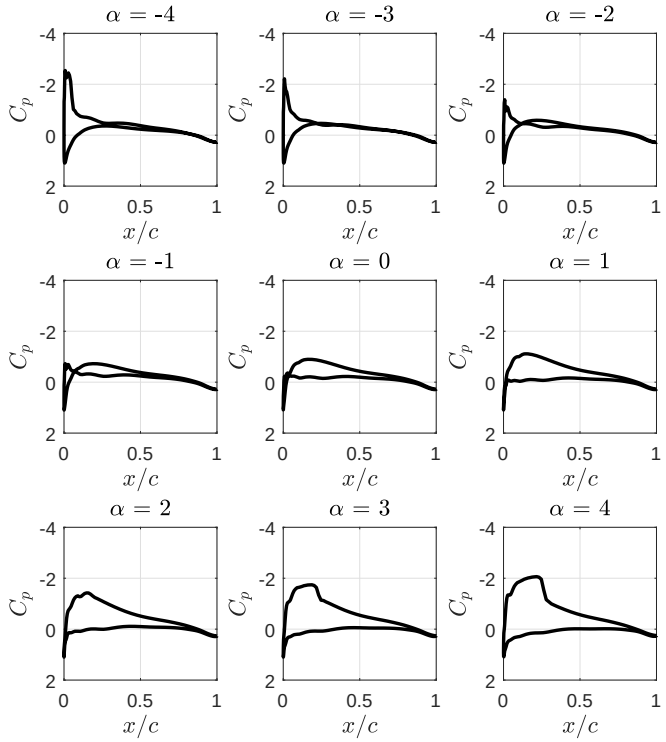

(a) Condition 1

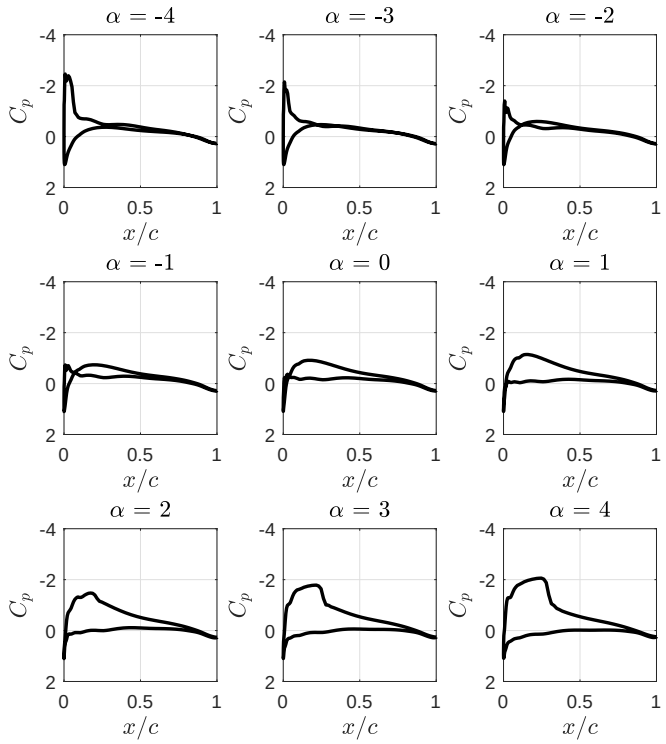

(b) Condition 2

Figure C.4: Pressure distribution C_p

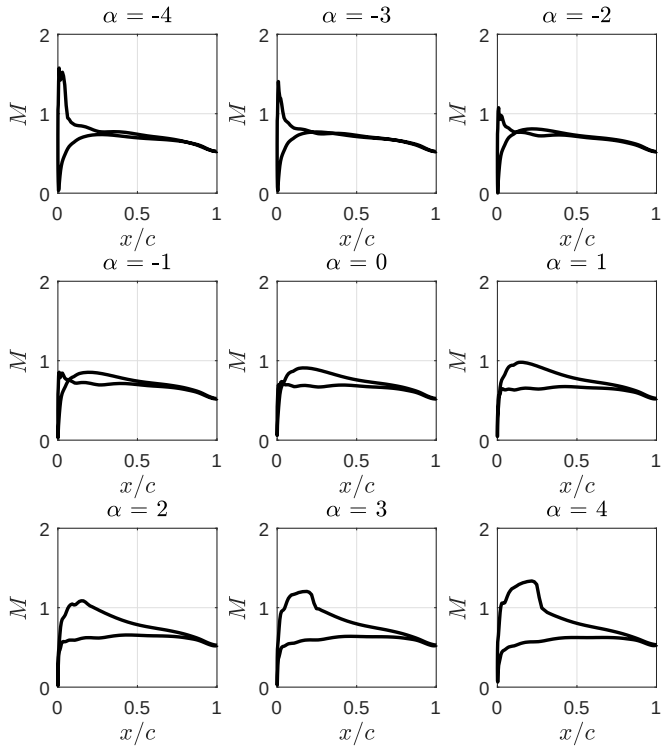

(a) Condition 1

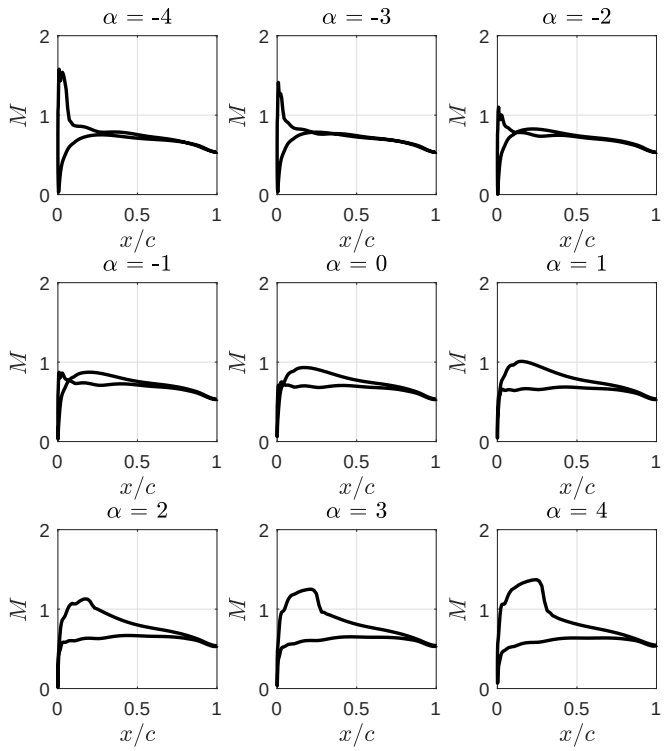

(b) Condition 2

Figure C.5: Local Mach number M

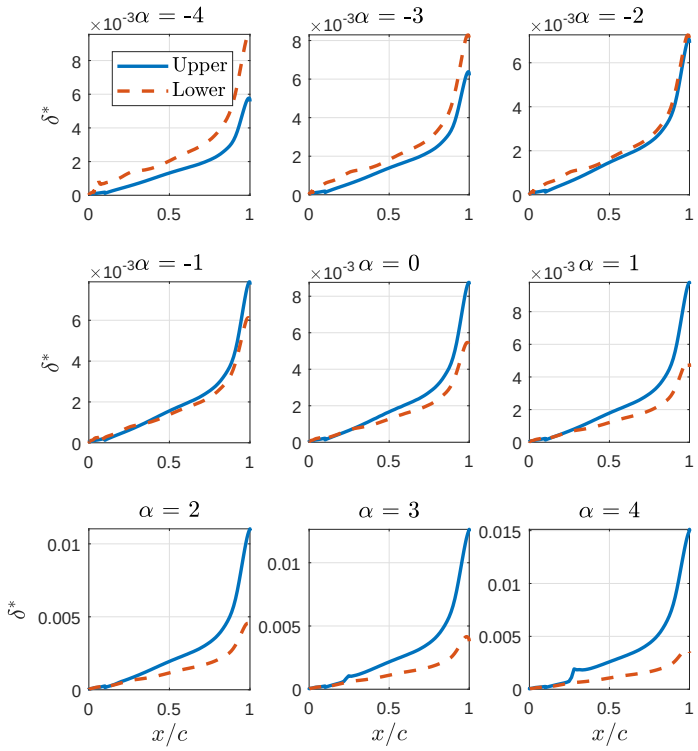

(a) Condition 1

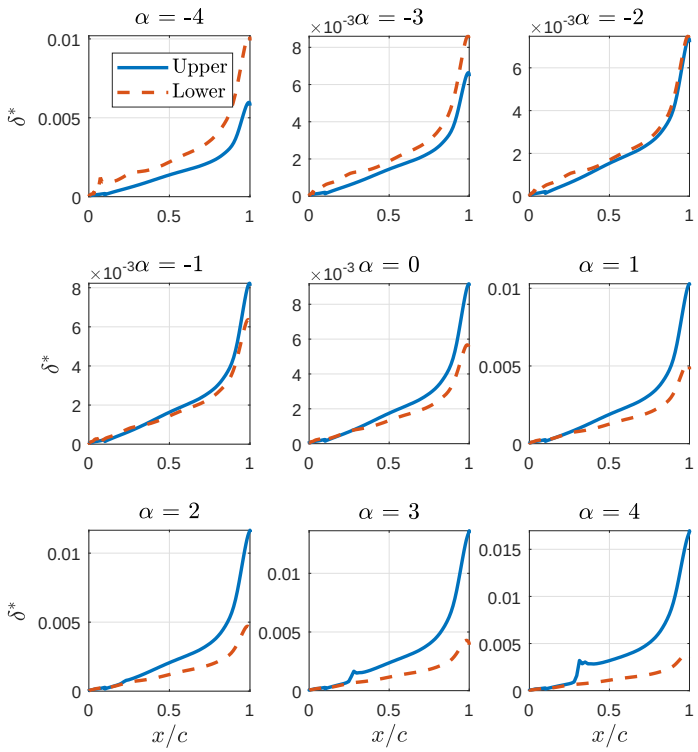

(b) Condition 2

Figure C.6: Local boundary-layer displacement thickness δ^*

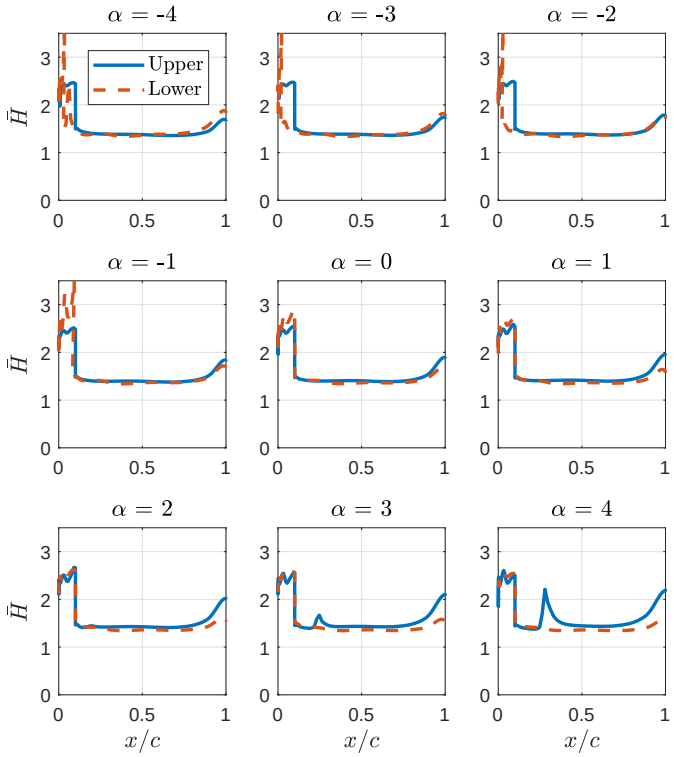

(a) Condition 1

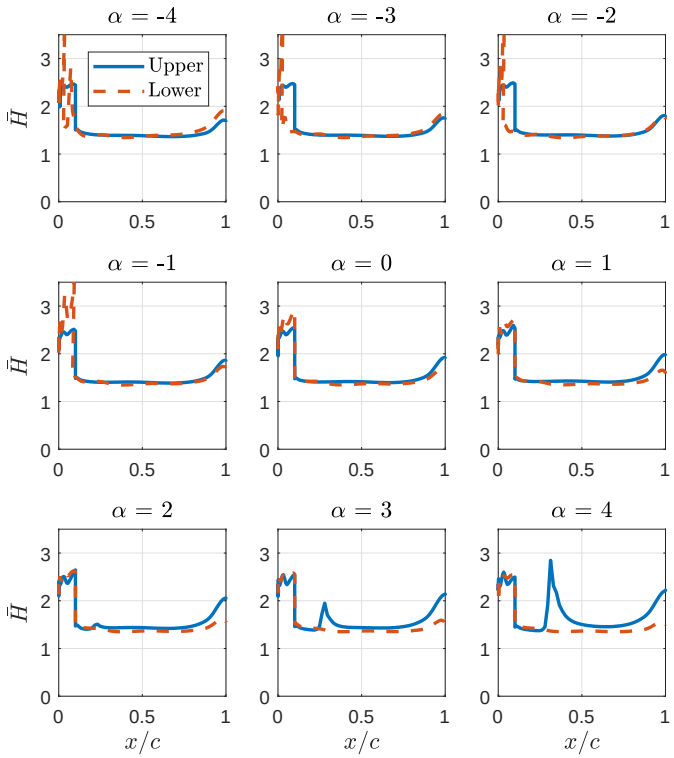

(b) Condition 2

Figure C.7: Transformed boundary-layer velocity-profile shape factor $\bar{H}$

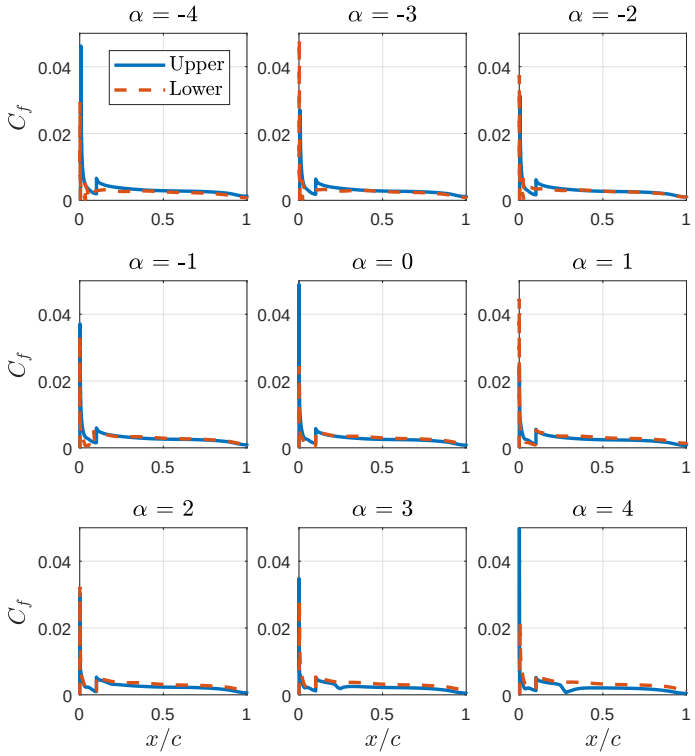

(a) Condition 1

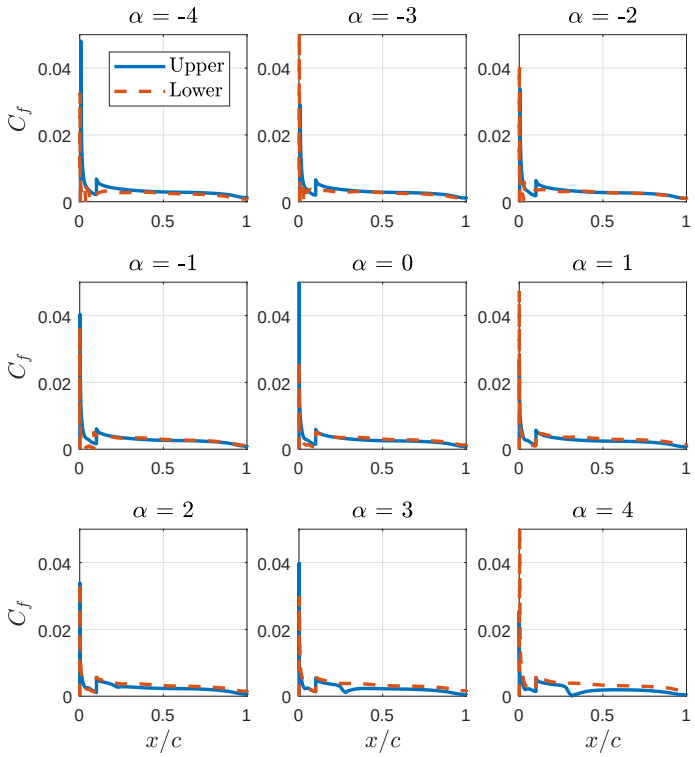

(b) Condition 2

Figure C.8: Local skin friction coefficient C_f

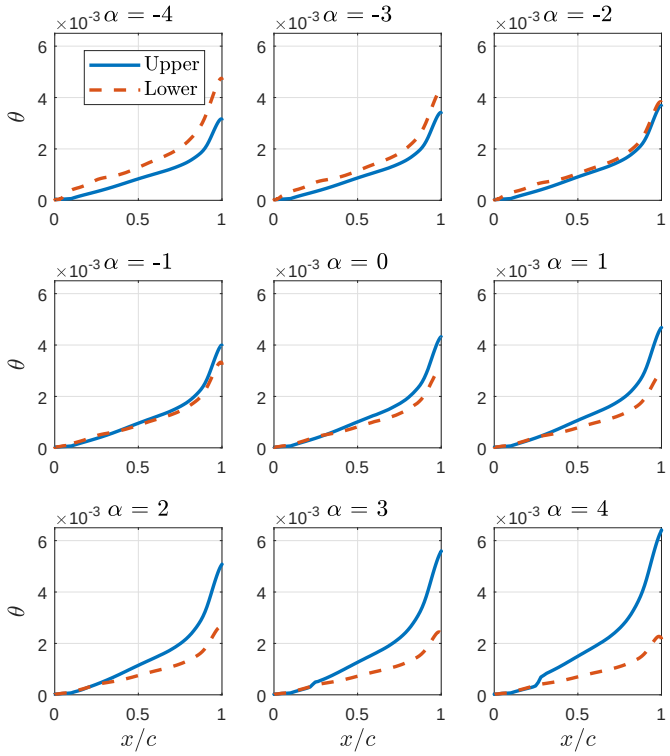

(a) Condition 1

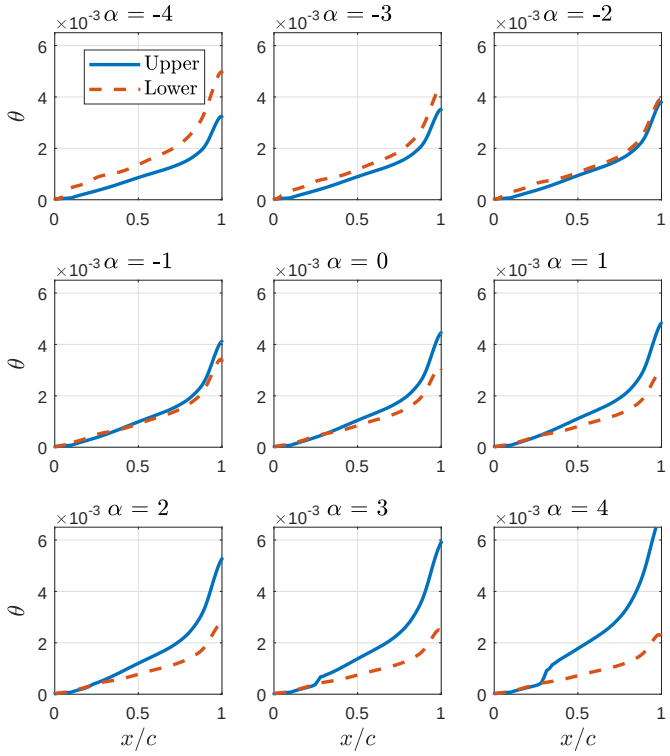

(b) Condition 2

Figure C.9: Local boundary-layer momentum thickness θ

This page is intentionally left blank.

APPENDIX D

Details on structural modelling

D.1 Modal analysis

D.1.1 Unloaded structure

Natural frequency and mode shapes provide important structural information. Each structure has an infinite number of normal mode shapes ϕ. The frequency at which the structure oscillates is called the circular frequency ω or natural frequency f_n. If a force is applied at the structural's natural frequency then the structure resonates and a higher amplitude vibration response is created. In operating conditions, structural resonance should be avoided because it can lead to discomfort due to large vibrations or be a catastrophic failure. The equation of motion for natural frequencies and normal mode shapes for an undamped free vibration is defined as:

$$\mathbf{M}\ddot{\mathbf{q}} + \mathbf{K}\mathbf{q} = 0 \tag{D.1.1}$$

where $\mathbf{M}$ is the mass matrix, $\mathbf{K}$ is the stiffness matrix, $\ddot{\mathbf{q}}$ and $\mathbf{q}$ are the acceleration and displacement state vectors respectively. Assuming harmonic solution of the form $\mathbf{q} = \bar{\mathbf{q}}e^{i\omega t}$, and after differentiation and substituting in Eq. D.1.1 the following is obtained (factoring out the $e^{i\omega t}$ term):

$$-\omega^2\mathbf{M}\bar{\mathbf{q}} + \mathbf{K}\bar{\mathbf{q}} = 0 \tag{D.1.2}$$

which after simplifying becomes:

$$(\mathbf{K} - \omega^2\mathbf{M})\bar{\mathbf{q}} = 0 \tag{D.1.3}$$

These circular frequencies ω and normal mode shapes $\phi = \bar{\mathbf{q}}$ of the structure can be obtained by considering the eigenvalues and eigenvectors of the solution to the characteristic equation:

$$\det(\mathbf{K} - \lambda^2 \mathbf{M}) = 0 \tag{D.1.4}$$

where $\lambda = \omega^2$. The determinant is zero only at a set of discrete eigenvalues λ_j or ω_j^2, which means that there is an eigenvector ϕ_j that satisfies Eq. D.1.3 and corresponds to each eigenvalue:

$$[\mathbf{K} - \omega_j^2 \mathbf{M}]\phi_j = 0 \tag{D.1.5}$$

corresponding to each vibration mode i of the structure. The jth eigenvalue λ_j is related to the jth natural frequency as follows:

$$f_{n_j} = \frac{\omega_j}{2\pi} \tag{D.1.6}$$

D.1.2 Loaded structure

For any given structure, the inertial force $\mathbf{F}(t)_I$ due to mass is defined as [58]:

$$\mathbf{F}(t)_I = -\mathbf{M}\frac{d^2\rho(t)}{dt^2} + \Omega\mathbf{C}^c\frac{d\rho(t)}{dt} + \Omega^2\mathbf{K}^c\rho(t) \tag{D.1.7}$$

where $\rho(t)$ is the position vector in a rotating coordinate system. The mass matrix $\mathbf{M}$ is:

$$\mathbf{M} = \begin{bmatrix} m & 0 & 0 \\ 0 & m & 0 \\ 0 & 0 & m \end{bmatrix} \tag{D.1.8}$$

the centripetal stiffness matrix $\mathbf{K}^c$:

$$\mathbf{K}^c = \begin{bmatrix} m & 0 & 0 \\ 0 & m & 0 \\ 0 & 0 & 0 \end{bmatrix} \tag{D.1.9}$$

and $\mathbf{C}^c$ which generates the velocity dependent Coriolis force:

$$\mathbf{C}^c = \begin{bmatrix} 0 & 2m & 0 \\ -2m & 0 & 0 \\ 0 & 0 & 0 \end{bmatrix} \tag{D.1.10}$$

Inertial forces in Eq. D.1.7 are dependent on the time-varying position of a mass particle [58]. Therefore, the position vector $\rho(t)$ is defined as:

$$\rho(t) = \rho + u(t) \tag{D.1.11}$$

where ρ is the initial component and $u(t)$ is the time varying component. Substituting Eq. D.1.11 into Eq. D.1.7 the inertial force can be rewritten:

$$\mathbf{F}(t)_I = -\mathbf{M}\frac{d^2u(t)}{dt^2} + \Omega\mathbf{C}^c\frac{du(t)}{dt} + \Omega^2\mathbf{K}^c(\rho + u(t)) \tag{D.1.12}$$

In addition, inertial forces due to mass are resisted by the structural stiffness $\mathbf{K}$ and damping $\mathbf{C}$ [58]:

$$\mathbf{C}\frac{du(t)}{dt} + \mathbf{K}u(t) = \mathbf{F}(t)_I \tag{D.1.13}$$

Now substituting Eq. D.1.13 into Eq. D.1.12, the equation of motion for a particle in a rotating elastic structure with no applied force can be expressed as:

$$\mathbf{M}\frac{d^2u(t)}{dt^2} + (\mathbf{C} - \Omega\mathbf{C}^c)\frac{du(t)}{dt} + (\mathbf{K} - \Omega^2\mathbf{K}^c)u(t) = \Omega^2\mathbf{K}^c\rho \tag{D.1.14}$$

The equation above shows that the Coriolis dependent terms $\mathbf{C}^c$ and $\mathbf{K}^c$ reduce the structural damping $\mathbf{C}$ and stiffness $\mathbf{K}$. The right hand term in Eq. D.1.14 is called the centripetal force [58]. An additional stiffness term produced by this centripetal force can be derived by considering the standard equilibrium equation for a single element [58]:

$$Ku = P \tag{D.1.15}$$

where K is the element stiffness, u is the displacement, and P is the load. To balance the applied load P a element reaction force F is produced by the deformation u [58]. As per definition by Nastran's User Guide *"the stiffness, K, can be viewed as the change in the element reaction forces with respect to a change in displacement"* [58]:

$$K = \frac{dF}{du} = \frac{d(TF_e)}{du} = T\frac{dF_e}{du} + F_e\frac{dT}{du} \tag{D.1.16}$$

and thus:

$$K = T\frac{du_e}{du}\frac{dF_e}{du_e} + F_e\frac{dT}{du} \tag{D.1.17}$$

where F is the internal element force in global coordinates, T is a transformation from element to global coordinates, F_e is the internal element force in element coordinates, and u_e is the displacement in element coordinates. The term dF_e/du_e is constant for linear material and a loading which is not dependent on displacement [58]. If only small displacements are considered, T and du_e/du can be assumed constant and calculated from the undeformed geometry [58]. The element stiffness matrices which are computed using the three terms T, du_e/du, and dF_e/du_e complete the linear stiffness matrix for the structure. The effect of the term $F_e(dT/du)$, which is the differential stiffness term, is explained in Figure D.1. The top figure shows a statically loaded bar in the transverse

and axial direction and the bottom figure shows a rotating bar with transverse and axial loading.

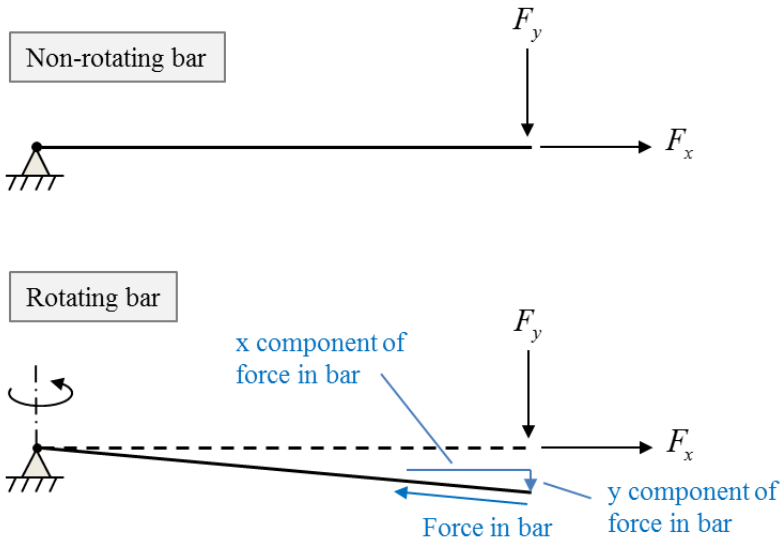

Figure D.1: Non-rotating and rotating bar with axial and transverse loading (Modified from [58])

In the rotating environment, a component of the bar axial force reacts against y-directed load and a component of the bar bending and shear reacts to the x-directed load. This results in a stiffness coupling which is ignored in standard linear analysis [58]. The total stiffness matrix is the sum of the linear $\mathbf{K}$ and differential stiffnesses matrix $\mathbf{K}^d$ that is also called tangent stiffness matrix. Including the additional differential stiffness term in Eq. D.1.14 the complete equation of motion (neglecting the centripetal loading) for a rotating structure is:

$$\mathbf{M}\left(\frac{d^2\rho(t)}{dt^2}\right) + (\mathbf{C} - \Omega\mathbf{C}^c)\left(\frac{d\rho(t)}{dt}\right) + (\mathbf{K} + \Omega^2\mathbf{K}^d - \Omega^2\mathbf{K}^c)\rho(t) = 0 \tag{D.1.18}$$

D.2 Derivation of surface strain

Strain is a mechanics quantity which indicates deformation of an infinitesimal element and is defined as the spatial variation of displacement [270]. Figure D.2 shows an infinitesimal element on the surface of the rotor blade.

Normal strain components are associated with changes in length, whereas shear strain measures the distortion by the change of angle of an infinitesimal element trough forces acting in opposite directions. Figure D.3(a) represents the normal strain and resulting displacement relations and Figure D.3(b) shows the relationship between strain and displacement for shear strain.

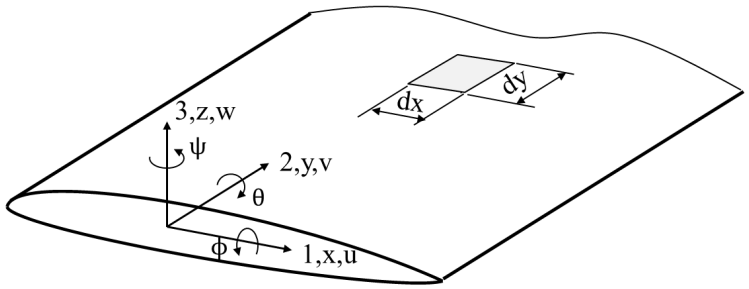

Figure D.2: Infinitesimal element on rotor blade

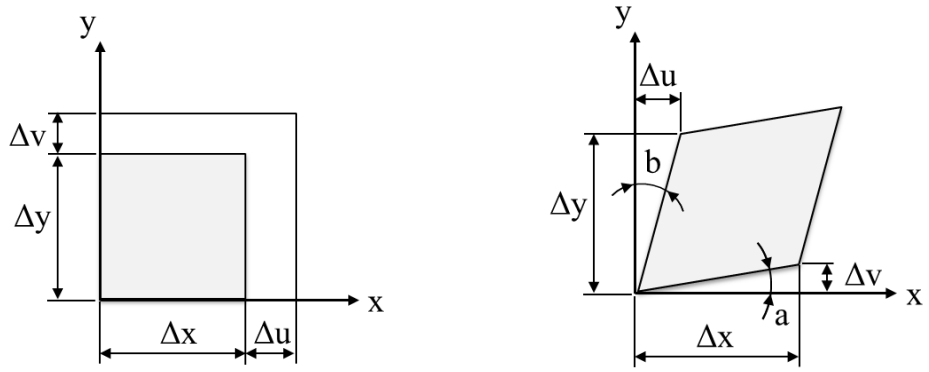

(a) Normal strain-displacement relation

(b) Shear strain-displacement relation

Figure D.3: Strain-displacement relation

Assuming an infinitesimal element the normal strain is given by:

$$\epsilon_x = \lim_{x \to 0} \frac{\Delta u}{\Delta x} = \frac{\partial u}{\partial x} \tag{D.2.1}$$

$$\epsilon_y = \lim_{y \to 0} \frac{\Delta v}{\Delta y} = \frac{\partial v}{\partial y} \tag{D.2.2}$$

From Figure D.3(b) the shear strain is defined:

$$\epsilon_{xy} = \frac{1}{2}(a + b) \tag{D.2.3}$$

with the assumption of small angles, a and b are approximated as follows:

$$a = \tan^{-1} \frac{\partial v}{\partial x} \cong \frac{\partial v}{\partial x} \tag{D.2.4}$$

$$b = \tan^{-1} \frac{\partial u}{\partial y} \cong \frac{\partial u}{\partial y} \tag{D.2.5}$$

Substituting Eq. D.2.4 and D.2.5 into D.2.3 the resulting shear strain-displacement relation is written [270]:

$$\epsilon_{xy} = \frac{1}{2}\left(\frac{\partial v}{\partial x} + \frac{\partial u}{\partial y}\right) \tag{D.2.6}$$

The strain-displacement relation is derived for bending of the structure similar to the in-plane stretching as shown in Figure D.3 and defined in Eq. D.2.1, D.2.2, and D.2.3. It is assumed that the undeformed structure is initially flat and rotates as it deforms. This rotation can be directly related to the first derivative shown by Tsai and Hahn [270].

The total axial surface strain ϵ_T is formulated using a linear superposition of strain due to flapping and lagging movement. Shear strain is neglected as it is assumed that the shape of the cross-sectional profile remains unaltered during deformation. Figure D.4 shows the coupled bending of a rotor blade that is used to establish the sign convention for tension and compression.

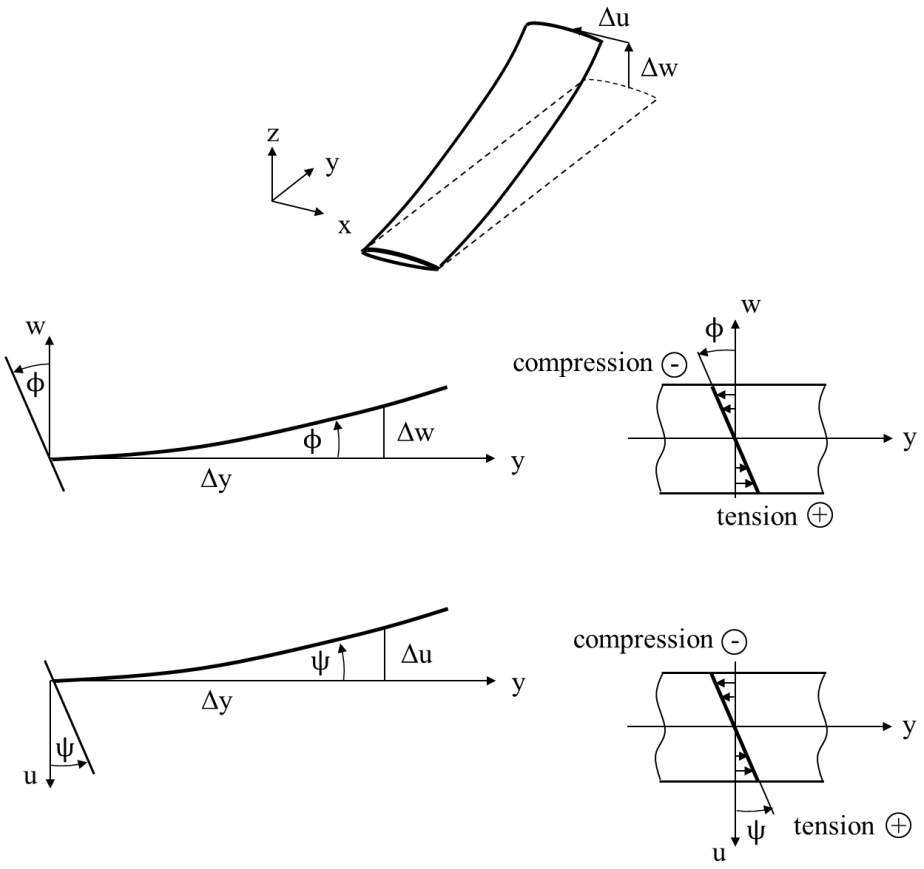

Figure D.4: Definition of the sign convention

With the use of the small angle approximation, the displacement, v, along the y-axis is defined as:

$$v = -z\phi = \frac{\partial w}{\partial y} \tag{D.2.7}$$

Substituting Eq. D.2.7 in Eq. D.2.2 the following strain-displacement formulation can be written:

$$\epsilon_f = -z\frac{\partial^2 w}{\partial y^2} \tag{D.2.8}$$

where ϵ_f is the strain measured in y-direction due to flapping movement. The term $\frac{\partial^2 w}{\partial y^2}$ is also known as curvature. Now, the strain due to lagging bending is derived similarly:

$$v = x\psi = \frac{\partial u}{\partial y} \tag{D.2.9}$$

and substituting into in Eq. D.2.2 the following expression is obtained for the strain measured in the y-direction due to lagging movement:

$$\epsilon_l = x\frac{\partial^2 u}{\partial y^2} \tag{D.2.10}$$

Now the total axial surface strain ϵ_T is defined as::

$$\epsilon_T = \epsilon_f + \epsilon_l$$

Introducing the time variable t and replacing the parameter z (Eq. D.2.7) and x (Eq. D.2.9) by c_z and c_x the total axial surface strain ϵ_T is written:

$$\epsilon_T(x, y, z, t) = -c_z(x, y, z)\frac{\partial^2 w(t)}{\partial y^2} + c_x(x, y, z)\frac{\partial^2 u(t)}{\partial y^2} \tag{D.2.11}$$

where c_z and c_x represent the distance between the location of the measurement and the neutral axis.

D.3 NASTRAN input data deck

D.3.1 Modal analysis for unloaded structure

The NASTRAN input deck for modal analysis SOL 103 is presented below.

```
$$$$$$$$$$$$$$$$$$$$$$$$$$$$$$$$$$$$$$$$$$$$$$$$$$$$$$$$$$$$$$$$$$$$$$$$$$$$
$$                          FILE MANAGEMENT SECTION                          $$
$$$$$$$$$$$$$$$$$$$$$$$$$$$$$$$$$$$$$$$$$$$$$$$$$$$$$$$$$$$$$$$$$$$$$$$$$$$$
$
ASSIGN OUTPUT4='H135_STIFF_MASS_MAT.o4',UNIT=62,
        STATUS=UNKNOWN,FORM=FORMATTED
$
NASTRAN BUFFSIZE = 16897
```

```
INIT MASTER(S)
ID H135
$
$$$$$$$$$$$$$$$$$$$$$$$$$$$$$$$$$$$$$$$$$$$$$$$$$$$$$$$$$$$$$$$$$$$$$$
$$                        EXECUTIVE CONTROL CARD                    $$
$$$$$$$$$$$$$$$$$$$$$$$$$$$$$$$$$$$$$$$$$$$$$$$$$$$$$$$$$$$$$$$$$$$$$$
$
SOL 103
$
$ OBTAIN STIFFNESS AND MASS MATRICES
$
COMPILE DMAP=SEKMR,SOUIN=MSCSOU  NOREF NOLIST $
$
ALTER 'ENDIF.*SEMR'
TYPE PARM,,CHAR8,Y,GETKAA='YES' $
$
IF(GETKAA='YES') THEN $
   PARAM //'STSR'/61/-2                    $  AUF KANAL 61:
   TABPRT   USET,EQEXINS,SILS//'USET'/0/-1//'A' $ ROW SORT U5-SET ONLY
   PARAM //'STSR'/6/-2                     $  AUF KANAL 6:
   OUTPUT4 KAA,MAA,,,//-1/62/2//16/ $ STORE MATRIX ON TAPE 62, ...
      ASCII, FORMAT 3E23.16
ENDIF $
CEND
$
$$$$$$$$$$$$$$$$$$$$$$$$$$$$$$$$$$$$$$$$$$$$$$$$$$$$$$$$$$$$$$$$$$$$$$
$$                          CASE CONTROL CARD                       $$
$$$$$$$$$$$$$$$$$$$$$$$$$$$$$$$$$$$$$$$$$$$$$$$$$$$$$$$$$$$$$$$$$$$$$$
$
TITLE = BEARINGLESS MAIN ROTOR BLADE H135
ECHO = NONE
DISPLACEMENT(PRINT) = ALL
SPCFORCE(PRINT) = ALL
OLOAD(PRINT) = ALL
FORCE(PRINT,CORNER) = ALL
STRESS(PRINT,CORNER) = ALL
$
$$$$$$$$$$$$$$$$$$$$$$$$$$$$$$$$$$$$$$$$$$$$$$$$$$$$$$$$$$$$$$$$$$$$$$
$$                          CASE CONTROL CARD                       $$
$$$$$$$$$$$$$$$$$$$$$$$$$$$$$$$$$$$$$$$$$$$$$$$$$$$$$$$$$$$$$$$$$$$$$$
$
$ Using Nastran default values for RESVEC
SUBCASE 1
   SUBTITLE=Default
   METHOD = 1
   SPC = 2
   VECTOR(PRINT,PUNCH,SORT1,REAL)=ALL
   SPCFORCES(PRINT,PUNCH,SORT1,REAL)=ALL
   STRAIN(PRINT,PUNCH,SORT1,REAL,VONMISES,STRCUR,BILIN)=ALL
$
BEGIN BULK
$
$$$$$$$$$$$$$$$$$$$$$$$$$$$$$$$$$$$$$$$$$$$$$$$$$$$$$$$$$$$$$$$$$$$$$$
$$                        BULK DATA CARDS                           $$
$$$$$$$$$$$$$$$$$$$$$$$$$$$$$$$$$$$$$$$$$$$$$$$$$$$$$$$$$$$$$$$$$$$$$$
$
PARAM    POST    0
PARAM   PRTMAXIM YES
```

```
PARAM,GRDPNT,0
PARAM,COUPMASS,2
$
$$$$$$$$$$$$$$$$$$$$$$$$$$$$$$$$$$$$$$$$$$$$$$$$$$$$$$$$$$$$$$$$$$$$$$
$$           EIGRL CARD FOR EIGENVALUE SPECIFICATION                $$
$$$$$$$$$$$$$$$$$$$$$$$$$$$$$$$$$$$$$$$$$$$$$$$$$$$$$$$$$$$$$$$$$$$$$$
$
EIGRL    1      -.1     200.     14      0                       MAX
$
INCLUDE data_filename.dat
$
ENDDATA
```

D.3.2 Modal analysis for loaded structure

Two options are available to compute the pre-stressed modal analysis. One is to use the normla mode analysis with pre-load, SOL 106. Note that LGDISP = 1 is set to obtain the differential stiffness matrix, while METHOD = 10 activates the eigenvalue module.

```
$$$$$$$$$$$$$$$$$$$$$$$$$$$$$$$$$$$$$$$$$$$$$$$$$$$$$$$$$$$$$$$$$$$$$$
$$                        EXECUTIVE CONTROL CARD                    $$
$$$$$$$$$$$$$$$$$$$$$$$$$$$$$$$$$$$$$$$$$$$$$$$$$$$$$$$$$$$$$$$$$$$$$$
$
SOL 106
TIME 60
CEND
$
$$$$$$$$$$$$$$$$$$$$$$$$$$$$$$$$$$$$$$$$$$$$$$$$$$$$$$$$$$$$$$$$$$$$$$
$$                          CASE CONTROL CARD                       $$
$$$$$$$$$$$$$$$$$$$$$$$$$$$$$$$$$$$$$$$$$$$$$$$$$$$$$$$$$$$$$$$$$$$$$$
$
TITLE = BEARINGLESS MAIN ROTOR BLADE H135
LABEL = CF LOAD 6.53 HZ ROTATION (FULL RPM)
ECHO = NONE
SUBCASE 1
   SUBTITLE = AERODYNAMIC LOADING
   NLPARM = 100
   METHOD = 10
   SPC = 2
   LOAD = 9999
   DISPLACEMENT(SORT1,REAL)=ALL
   SPCFORCES(SORT1,REAL)=ALL
   STRESS(SORT1,REAL,VONMISES,BILIN)=ALL
$
BEGIN BULK
$
$$$$$$$$$$$$$$$$$$$$$$$$$$$$$$$$$$$$$$$$$$$$$$$$$$$$$$$$$$$$$$$$$$$$$$
$$                        BULK DATA CARDS                           $$
$$$$$$$$$$$$$$$$$$$$$$$$$$$$$$$$$$$$$$$$$$$$$$$$$$$$$$$$$$$$$$$$$$$$$$
$
PARAM,COUPMASS,2
PARAM,GRDPNT,0
PARAM    POST    -2
PARAM    AUTOSPC NO
```

```
$
$ PARAMETERS FOR SOL 66
$$$$$$$$$$$$$$$$$$$$$$$
$
PARAM    LGDISP  1
PARAM    NMLOOP  5
PARAM   PRTMAXIM YES
NLPARM   100     1               AUTO    1       40              NO
PARAM   TESTNEG  1
$
$
$$$$$$$$$$$$$$$$$$$$$$$$$$$$$$$$$$$$$$$$$$$$$$$$$$$$$$$$$$$$$$$$$$$$$$$$$$$
$$           EIGRL CARD FOR EIGENVALUE SPECIFICATION                   $$
$$$$$$$$$$$$$$$$$$$$$$$$$$$$$$$$$$$$$$$$$$$$$$$$$$$$$$$$$$$$$$$$$$$$$$$$$$$
$
EIGRL    10     -.1     200.     12      0                       MAX
$
INCLUDE data_filename.dat
$
ENDDATA
```

For the second option the normal mode analysis SOL 103 can be used by defining two subcases. The first subcase applies the load, while the second subcase calculates the eigensolution. Both options provide the same results.

```
$$$$$$$$$$$$$$$$$$$$$$$$$$$$$$$$$$$$$$$$$$$$$$$$$$$$$$$$$$$$$$$$$$$$$$$$$$$
$$                          EXECUTIVE CONTROL CARD                     $$
$$$$$$$$$$$$$$$$$$$$$$$$$$$$$$$$$$$$$$$$$$$$$$$$$$$$$$$$$$$$$$$$$$$$$$$$$$$
$
SOL 103
TIME 60
CEND
$
$$$$$$$$$$$$$$$$$$$$$$$$$$$$$$$$$$$$$$$$$$$$$$$$$$$$$$$$$$$$$$$$$$$$$$$$$$$
$$                           CASE CONTROL CARD                         $$
$$$$$$$$$$$$$$$$$$$$$$$$$$$$$$$$$$$$$$$$$$$$$$$$$$$$$$$$$$$$$$$$$$$$$$$$$$$
$
TITLE = BEARINGLESS MAIN ROTOR BLADE H135
LABEL = CF LOAD 6.53 HZ ROTATION (FULL RPM)
ECHO = NONE
   SUBTITLE = AERODYNAMIC LOADING FROM BHR
   METHOD = 10
   SPC = 2
   LOAD = 9999
   DISPLACEMENT=ALL
SUBCASE 1004
  SPC = 2
  LOAD = 9999
SUBCASE 3004
  METHOD = 10
  STATSUB = 1004
$
BEGIN BULK
$
$$$$$$$$$$$$$$$$$$$$$$$$$$$$$$$$$$$$$$$$$$$$$$$$$$$$$$$$$$$$$$$$$$$$$$$$$$$
$$                           BULK DATA CARDS                           $$
```

```
$$$$$$$$$$$$$$$$$$$$$$$$$$$$$$$$$$$$$$$$$$$$$$$$$$$$$$$$$$$$$$$$$$$$$$$$$$$$
$
PARAM,COUPMASS,2
PARAM,GRDPNT,0
PARAM    POST    -1
PARAM    AUTOSPC NO
$
$$$$$$$$$$$$$$$$$$$$$$$$$$$$$$$$$$$$$$$$$$$$$$$$$$$$$$$$$$$$$$$$$$$$$$$$$$$$
$$           EIGRL CARD FOR EIGENVALUE SPECIFICATION                  $$
$$$$$$$$$$$$$$$$$$$$$$$$$$$$$$$$$$$$$$$$$$$$$$$$$$$$$$$$$$$$$$$$$$$$$$$$$$$$
$
EIGRL    10     -.1     200.     12      0                       MAX
$
INCLUDE data_filename.dat
$
ENDDATA
```

This page is intentionally left blank.

APPENDIX E

Inflow modelling

A derivation of the quasi-steady dynamic inflow model is presented here. Figure E.1 shows the inflow components in the hub reference frame $\mathcal{F}_H$, as well as Peters axis system[1], as defined in Reference [83], and the wind axis reference frame $\mathcal{F}_W$. A wind angle Δ is introduced to transfer between $\mathcal{F}_W$ and $\mathcal{F}_H$ and defined as a function of forward velocity.

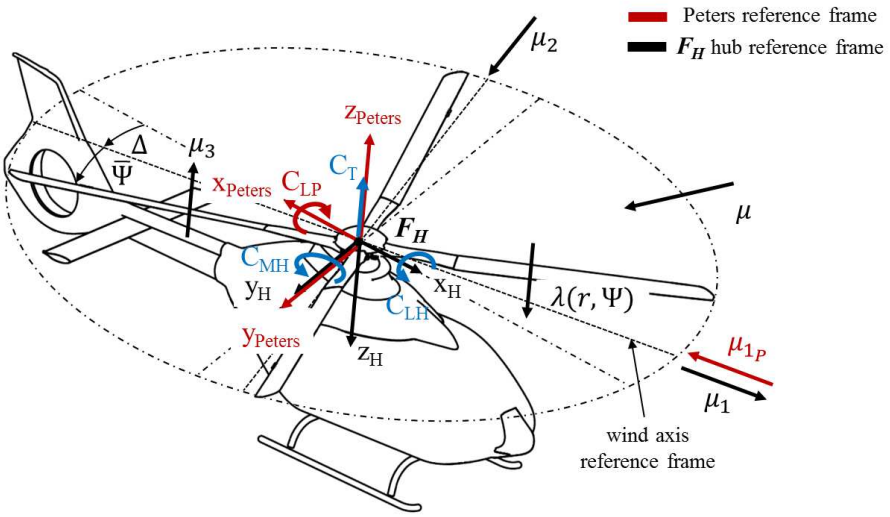

Figure E.1: Inflow components on rotor hub (reproduced from Reference [83])

The non-dimensional velocity components μ_1, μ_2, and μ_3 are obtained by normalising the hub velocity V_H with the tangential velocity as follows:

$$\mu_1 = \frac{V_{H_x}}{\Omega R}, \quad \mu_2 = \frac{V_{H_y}}{\Omega R}, \quad \mu_3 = \frac{V_{H_z}}{\Omega R} \tag{E.0.1}$$

[1]It should be noted that due to the orientation of Peters axis system, the sign convention of the rolling moment is adjusted accordingly: $-C_{L_H} = C_{L_P}$.

where μ_1, μ_2 represent the non-dimensionalised forward and sideward velocities respectively. μ_3 is located perpendicular to the rotor disc, Ω is the rotor idle speed and R is the rotor radius. The resultant forward velocity[2] μ is a velocity component parallel to the rotor disc:

$$\mu = \sqrt{\mu_1^2 + \mu_2^2} \tag{E.0.2}$$

The induced inflow λ_i is dependent on the radial distance r along the rotor blade and on the azimuth angle Ψ and is expressed in the wind axis system as follows:

$$\lambda_i(r, \bar{\Psi}) = \nu_0 + \frac{r}{R}\nu_s \sin(\bar{\Psi}) + \frac{r}{R}\nu_c \cos(\bar{\Psi}) \tag{E.0.3}$$

where $\bar{\Psi}$ is defined as:

$$\bar{\Psi} = \Psi - \Delta \tag{E.0.4}$$

and Δ is the wind angle ν_0, ν_s, and ν_c are the uniform, lateral, and longitudinal variations in rotor inflow, respectively. The resultant flow V_R through the rotor disc is given by:

$$V_R = \sqrt{\lambda^2 + \mu^2} \tag{E.0.5}$$

where λ is the total inflow through the rotor. The mass-flow parameter V_M due to cyclic disturbances is calculated as follows:

$$V_M = \frac{\mu^2 + (2\lambda_m - \mu_3)(\lambda_m - \mu_3)}{V_R} \tag{E.0.6}$$

where λ_m is the normal induced inflow. The mass-flow parameter matrix $\mathbf{V_M}$ can be constructed as:

$$\mathbf{V_M} = \begin{bmatrix} V_R & 0 & 0 \\ 0 & V_M & 0 \\ 0 & 0 & V_M \end{bmatrix} \tag{E.0.7}$$

The non-linear version of the inflow gains matrix $\hat{\mathbf{L}}$ is expressed as:

$$\hat{\mathbf{L}} = \mathbf{V_M}\mathcal{L}^{-1} \tag{E.0.8}$$

with $\mathcal{L}$:

[2]Because of the different axes conventions μ_1 should have a minus sign, however this is negligible due to the squared term in Eq.E.0.2.

$$\mathcal{L} = \begin{bmatrix} \frac{1}{2} & -B\sin\Delta & -B\cos\Delta \\ B\sin\Delta & E\cos^2\Delta + D\sin^2\Delta & (D-E)\sin\Delta\cos\Delta \\ B\cos\Delta & (D-E)\cos\Delta\sin\Delta & E\sin^2\Delta + D\cos^2\Delta \end{bmatrix} \tag{E.0.9}$$

$$E = \frac{4}{1+\sin\chi}$$

$$(E-D) = 4\frac{1-\sin\chi}{1+\sin\chi}$$

$$D = \frac{4\sin\chi}{1+\sin\chi}$$

$$B = \frac{15\pi}{64}\sqrt{\frac{1-\sin\chi}{1+\sin\chi}} \tag{E.0.10}$$

and the wake angle with respect to the rotor disc is given by:

$$\chi = \tan^{-1}\frac{\mid \lambda_m - \mu_3 \mid}{\mu} \tag{E.0.11}$$

The normal induced inflow λ_m due to the effect of rotor thrust C_T is defined as [83]:

$$\lambda_m = \frac{1}{2}\begin{bmatrix} 1 \\ 0 \\ 0 \end{bmatrix}^T \mathcal{L}^{-1}\begin{bmatrix} \lambda_0 \\ \lambda_s \\ \lambda_c \end{bmatrix} \tag{E.0.12}$$

where λ_0, λ_s, and λ_c are the uniform, lateral, and longitudinal variations in rotor inflow respectively. To calculate the non-linear dynamic inflow with respect to the rotor disc plane a first order differential equation is used [83]:

$$\begin{bmatrix} \dot{\lambda}_0 \\ \dot{\lambda}_s \\ \dot{\lambda}_c \end{bmatrix} = -\mathbf{M}^{-1}\hat{\mathbf{L}}^{-1}\begin{bmatrix} \lambda_0 \\ \lambda_s \\ \lambda_c \end{bmatrix} + \mathbf{M}^{-1}\begin{bmatrix} C_T \\ C_{L_H} \\ -C_{M_H} \end{bmatrix} \tag{E.0.13}$$

where C_T, C_{L_H} and C_{M_H} are the instantaneous rotor thrust, roll and pitching moments coefficients, respectively, in $\mathcal{F}_H$. These are defined in Chapter 4.6. As explained by Peters and HaQuang [83], *"$\mathbf{M}$ is the matrix of the apparent mass terms, which is a time delay effect due to the unsteady wake"*. It should be noted that the non-linear version of the inflow gains matrix $\hat{\mathbf{L}}$ is non-linear in C_T and λ_0, but linear in C_{L_H} and C_{M_H} [83]. Only aerodynamic contributions are considered in C_T, C_{L_H} and C_{M_H} [83].

This page is intentionally left blank.

APPENDIX F

Main rotor track and balancing

Helicopter track and balancing procedures during maintenance checks ensure that the tip height of all rotor blades are within an admissible tolerance, and consequently this determines whether the helicopter can return to service. The maximum admissible tip tracking deviation is 5 mm in the ground run and hover in ground effect [254]. Apart from matching the tip height by adjusting the angle of the trim tab or increasing/decreasing the length of the pitch link[1] (see Figure F.1), dynamic balancing can be achieved by adding/removing weights of up to 250 grams (max) to the pitch control cuff "pocket".

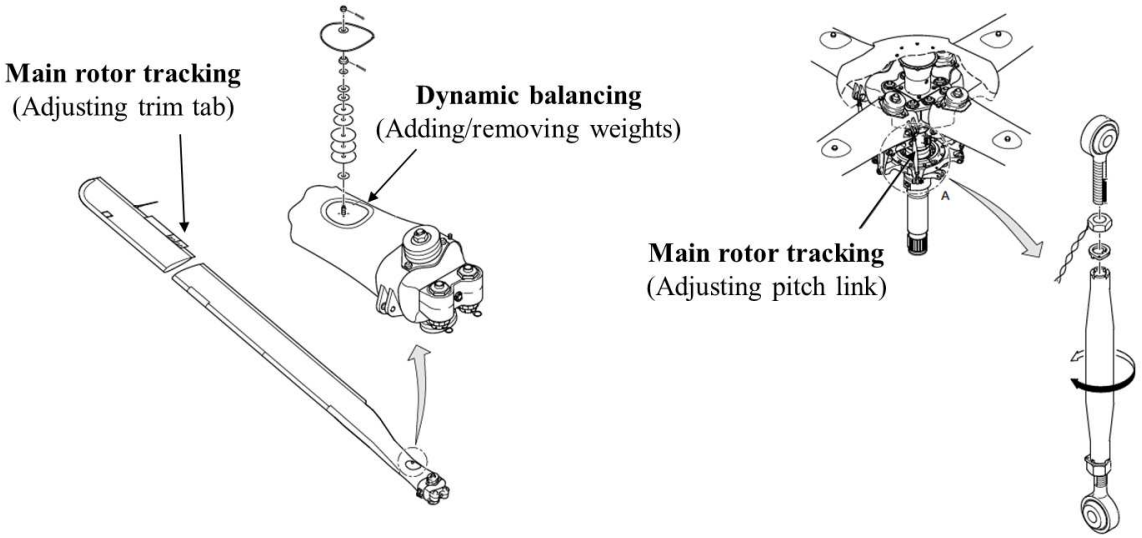

Figure F.1: Rotor track and balancing procedure of H135 (reproduced from References [271])

The main purposes of the track and balancing is to adjust the 1/rev vibrations[2] transmitted to the fuselage, and while its maximum admissible unbalance is 0.06 IPS in theory, it

[1]Only the flapping modes can be impacted by these adjustments, while the lagging modes stay constant, which is the reason why the lead-lag figures of all blades need to match.

[2]For a 4-bladed helicopter the natural vibration is N_b/rev, e.g. 4/rev or 8/rev.

is about 0.1 IPS in practice for hovering in ground effect. The vertical acceleration is measured on the left-hand side of the co-pilot seat, and the lateral vibrations are measured on the gearbox transmission deck. A compromise has to be made between balancing and tracking. However, balance (ensure small vibrations at fuselage) is considered to be more important than an equal track of the blade. In a scenario where a damaged blade is to be exchanged, it is important to match the life hours and lead-lag figure (stated on the blade by the manufacturer) with the existing blades.

APPENDIX G

Experimental testing

G.1 Theory on stochastic subspace identification

The experimental modal analysis was carried out in the time domain by using a stochastic subspace identification (SSI) algorithm that is referred to as "Canonical Variate Analysis" (see Van Overschee and De Moor [272]). The essential quality of all the algorithms within the subspace family is their ability to work out the matrices describing a linear system starting from subspaces containing the projections of data matrices; in particular, these algorithms project the space of the matrix rows of future outputs into the space of the rows of past outputs. Most of SSI algorithms benefit by the use of a stabilisation diagram. In fact, in the case of a stochastic state-space model, assuming the system to be linear and time-invariant, one can write:

$$\mathbf{x}_{k+1} = \mathbf{A}\mathbf{x}_k + \mathbf{w}_k$$

$$\mathbf{y}_k = \mathbf{C}\mathbf{x}_k + \mathbf{v}_k \tag{G.1.1}$$

Where $\mathbf{x}_k$ is the state vector with dimension $n \times 1$ (where n is the system order yet to be determined) and $\mathbf{y}_k$ is the system response and $\mathbf{w}_k$ and $\mathbf{v}_k$ are the process and measurement noise vectors, respectively. $\mathbf{A} \in R^{n \times n}$ and $\mathbf{C} \in R^{m \times n}$ are the state and observation matrices. For a detailed discussion on how to determine $\mathbf{A}$ and $\mathbf{C}$ the reader is referred to Reference [272]. With regards to the input-output identification, a SSI algorithm implementation allowing for input-output was used, still referring to the "Canonical Variate Analysis" implementation [272]. In this case, the state-space representation becomes:

$$\mathbf{x}_{k+1} = \mathbf{A}x_k + \mathbf{B}\mathbf{u}_k + \mathbf{w}_k$$

$$\mathbf{y}_k = \mathbf{C}\mathbf{x}_k + \mathbf{D}\mathbf{u}_k + \mathbf{v}_k \tag{G.1.2}$$

It is noteworthy that Eq. G.1.1 is just a particular case of Eq. G.1.2 where the input and feedthrough matrices **B** and **D** have been merged within the process and measurement noise. Once the system matrices are estimated, one can compute the modal parameters of the structural system. Natural frequencies f_i , damping ratios ζ_i and mode shapes ϕ_i can be determined from:

$$\mathbf{A} = \mathbf{\Psi}\mathbf{\Lambda}\mathbf{\Psi}^{-1}, \mathbf{\Lambda} = diag(\lambda_i) \in \mathbf{C}^{n\times n}, i = 1, ..., n \tag{G.1.3}$$

$$\lambda_i^c = \frac{ln\lambda_i}{\Delta t}, i = 1, ..., n \tag{G.1.4}$$

$$f_i = \frac{|\lambda_i^c|}{2\pi}, i = 1, ..., n \tag{G.1.5}$$

$$\zeta_i = \frac{real(\lambda_i^c)}{|\lambda_i^c|}, i = 1, ..., n \tag{G.1.6}$$

$$\mathbf{\Phi} = \mathbf{C}\mathbf{\Psi}, \mathbf{\Phi} = [\phi_1, ..., \phi_n] \tag{G.1.7}$$

G.2 Test equipment

G.2.1 Test rig

Figure G.1 presents the overall dimensions of the test rig. The blade mount height is used to determine absolute measurements.

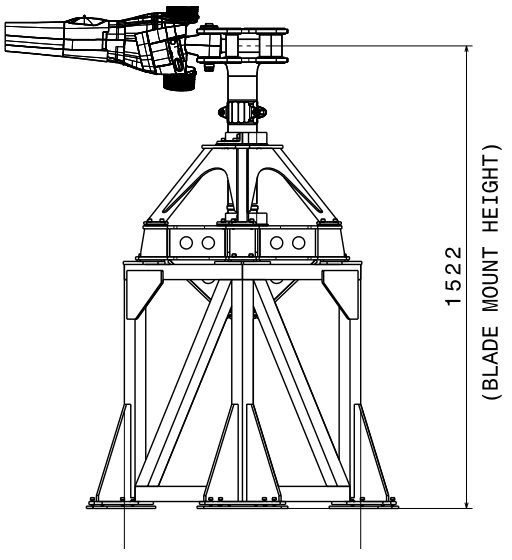

Figure G.1: Test rig

G.2.2 Laser range finder

A digital laser range finder (PLR15[1]) was used to measure the absolute displacement at each measurement point in out-of-plane direction (see Figure G.2 - G.3).

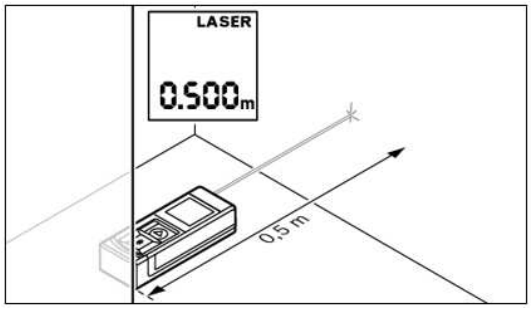

Figure G.2: Laser Range Finder for distance measurement (reproduced from Reference [273])

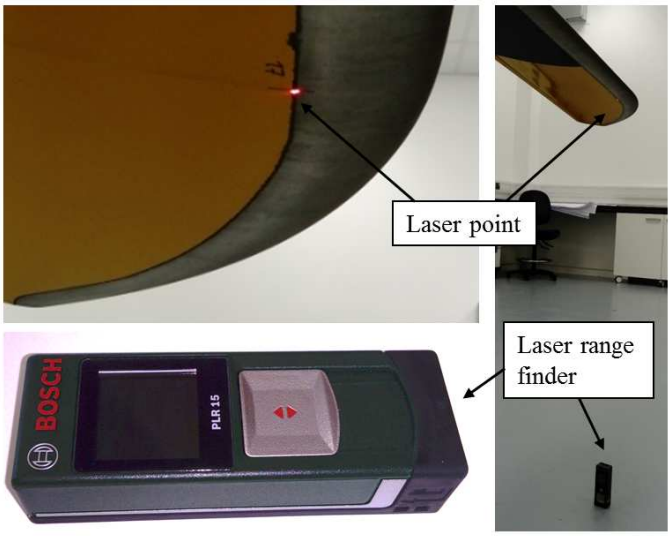

Figure G.3: A digital laser range finder was used to measure the displacement

G.2.3 Ground vibration test equipment

The ground vibration test equipment consists of the following items, and its key specifications are summarised in Table G.1:

- Modal exciter type 4825 (Brüel & Kjær)
- Power amplifier of type 2720 (Brüel & Kjær)
- Spider-81 vibration control system (Crystal Instruments)
- Stinger (Brüel & Kjær)

[1]Type: PLR15 3 603 F72 000.

- 5x uni-axial accelerometers of type 4507 (Brüel & Kjær)
- 1x force transducer of type 8230-001 (Brüel & Kjær)

Table G.1: Specification of ground vibration test equipment

Equipment	Description	Specification
Modal exciter	Useful frequency range	2 - 5000 Hz
	Operating frequency range	DC - 5000 Hz
	Max. rated travel	25.4 mm
	Weight of trunnion	21 kg
Power amplifier	Output voltage capacity	45 V RMS, DC to 15 kHz
	Output current capacity	5 A RMS at or below 5 Hz
		11 A RMS, 40 Hz to 15 kHz
	Full frequency capacity	40 Hz - 15 kHz
	Weight	21 kg
Stinger	Length	500 mm
	Diameter	2.5 mm
Uni-axial accelerometer	Frequency range	0.3 Hz - 6 kHz
	Mounted resonance frequency	18 kHz
	Measuring range	700 ms^2 peak ($\pm$ 71 g peak)
	Inherent noise (RMS)	$< 35\ \mu V$
Force transducer	Mounted resonance (unloaded)	75 kHz
	Measuring range compression	220 N
	Measuring range tensile	220 N

Figure G.4: Typical set-up of vibration control system (top) and power amplifier (bottom)

G.3 Measurement errors

A summary of sources of errors and aspects that added to uncertainties during the structural loading test is listed below:

- Unknown service life history of sample blades.
- Difference in boundary condition between the numerical model and experiment: no pitch link is available during the structural loading test.

- Creep behaviour of the rotor blade.
- Errors during the structural loading test in flapping direction:
  - Air condition in the laboratory caused the blade to oscillate.
  - possible misalignment of the mass pieces underneath location A, B, C may have induced torsional movement.
  - Laser Range Finder was not perpendicular to the floor due to the rough floor surface.
- Errors during the structural loading test in torsional direction:
  - Difference in boundary condition between numerical model and experiment: 1) no pitch link is available during the structural loading test, and 2) with the use of the support pillar no free rotational movement around spanwise direction can be achieved.
  - Alignment of support pillar underneath the quarter chord line. The assumption is that the quarter chord line acts as the structural rotational centre.
  - Additional moments induced by the weight of clamp parts are neglected for data comparison.
  - The height of the pillar was not the same as "centre of flexbeam height", which resulted in a 16 mm difference.
  - Creep behaviour was discovered after suspending weights at the lever end.
  - Laser Range Finder was not perpendicular to the floor due to the rough floor surface.

This page is intentionally left blank.

APPENDIX H

Experimental test results

H.1 Frequency spectra

Figures H.1 - H.6 present the PSD obtained from each FBG array (CH1b - CH6b) during RoR excitation input.

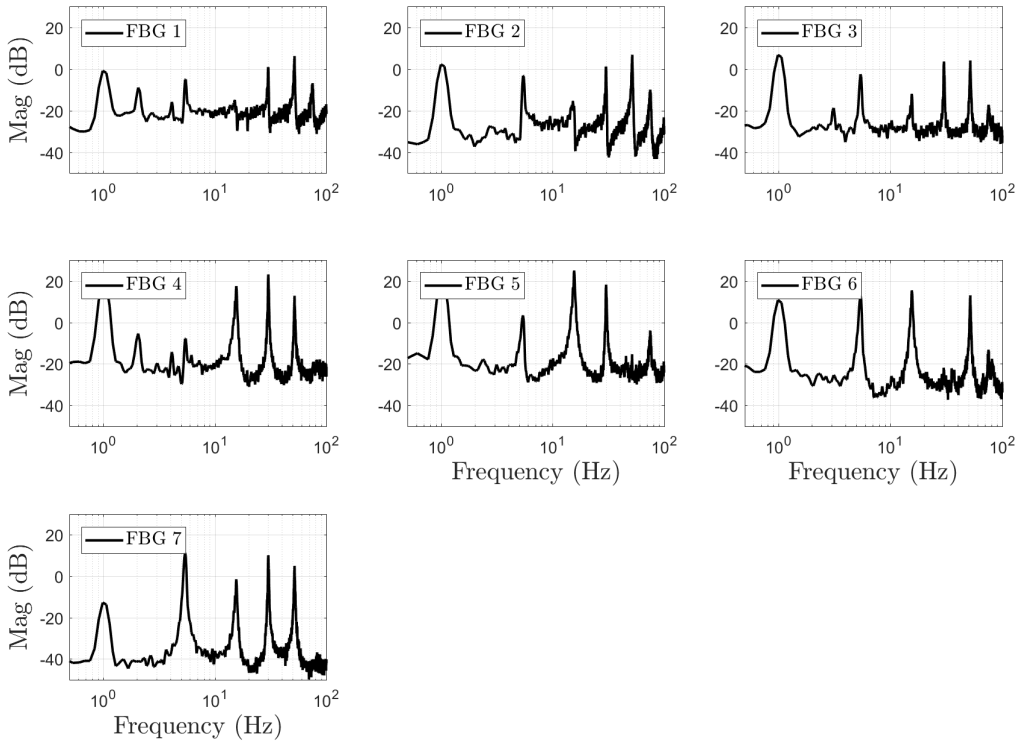

Figure H.1: PSD collected from CH1b

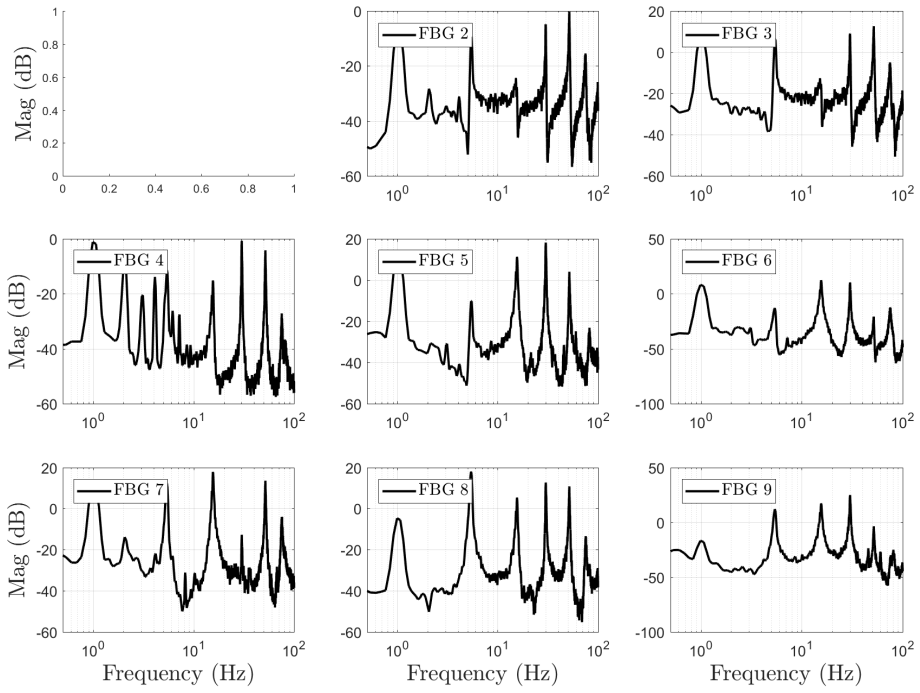

Figure H.2: PSD collected from CH2b

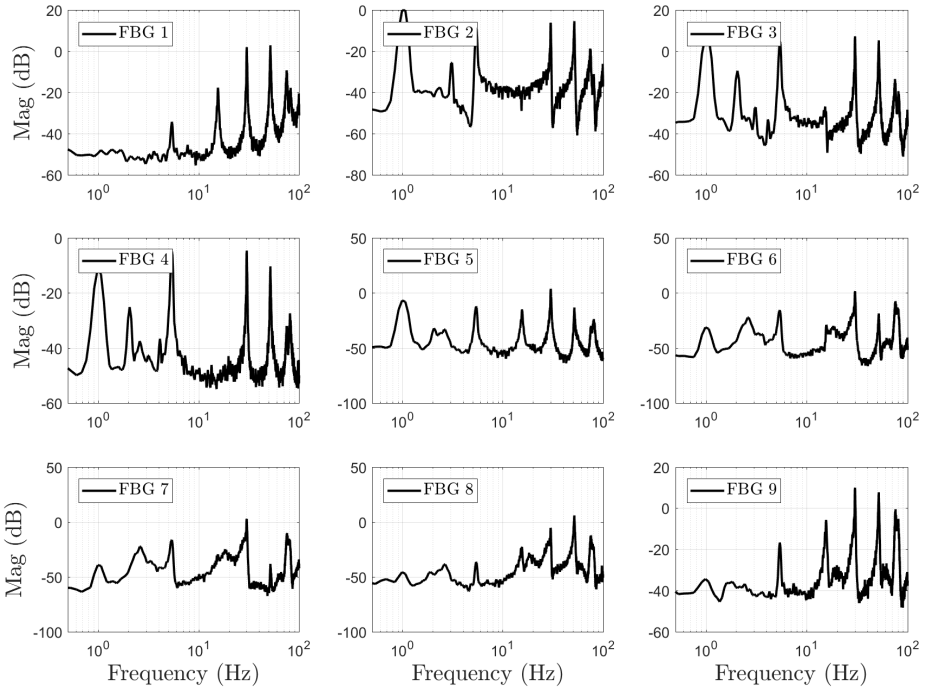

Figure H.3: PSD collected from CH3b

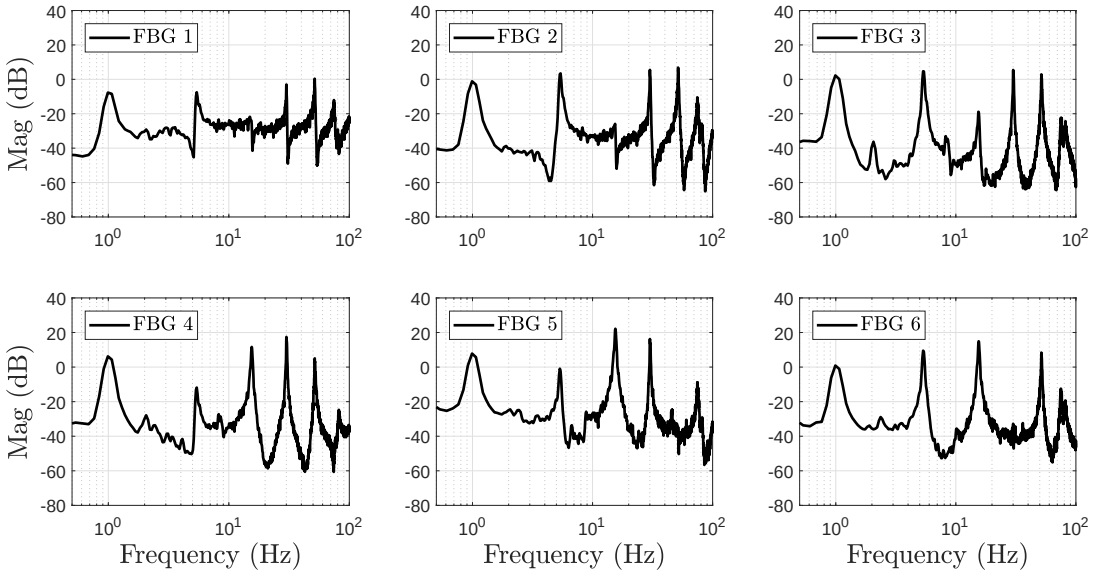

Figure H.4: PSD collected from CH4b

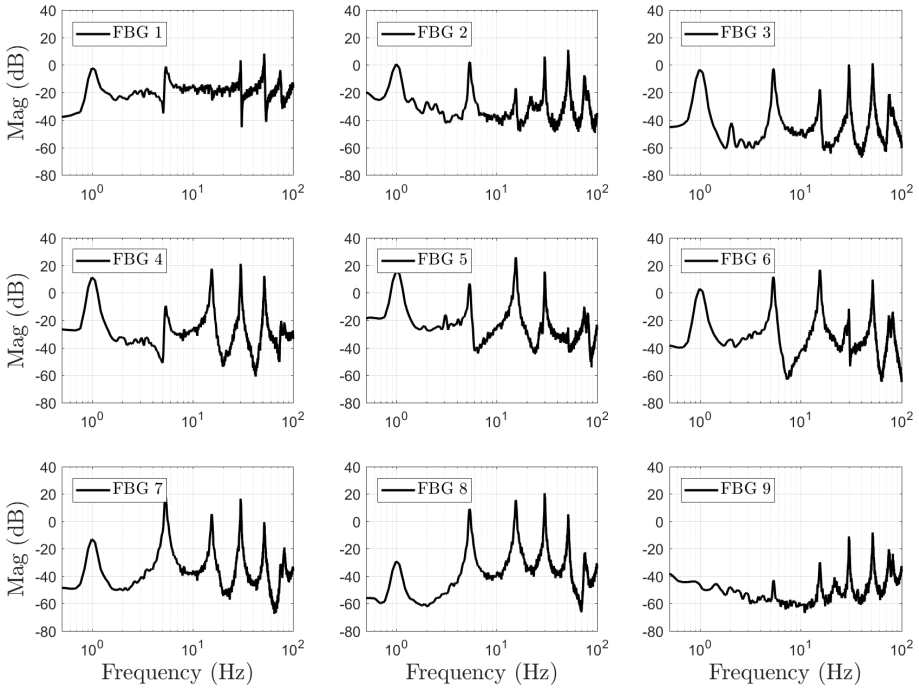

Figure H.5: PSD collected from CH5b

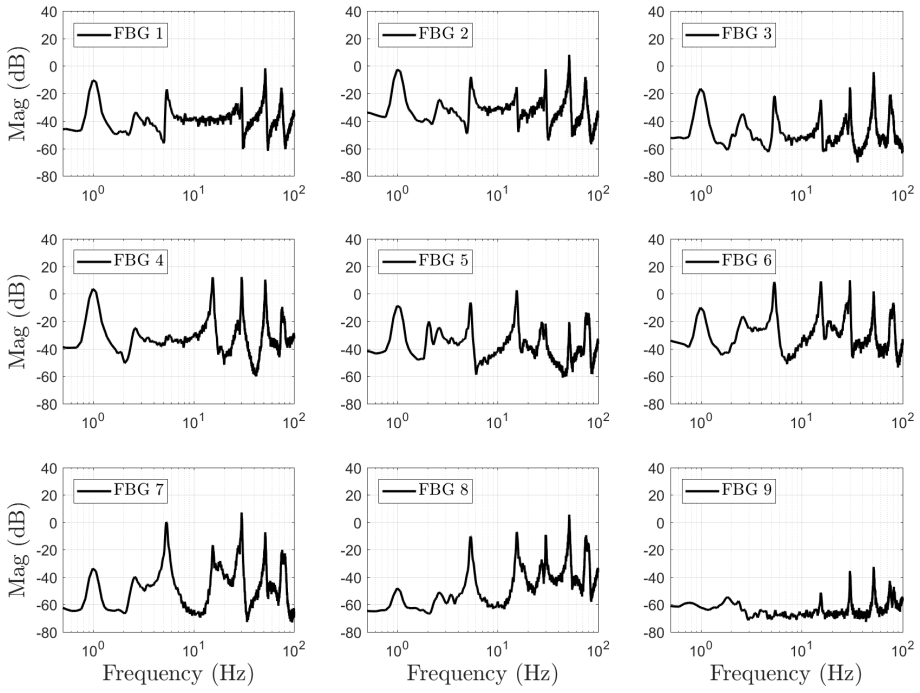

Figure H.6: PSD collected from CH6b

H.2 Strain mode shapes

MAC comparison for each FBG array position is shown in Table H.1, while the extracted mode shapes are presented in Figures H.7 - H.12.

Table H.1: Comparison of all MAC values obtained from FBG measurements

Mode number	Mode type	MAC					
		CH1b	CH2b	CH3b	CH4b	CH5b	CH6b
1	1st flapping	0.87	0.24	0.12	0.95	0.83	0.54
2	1st lagging	0.00	0.03	0.10	0.03	0.29	0.77
3	2nd flapping	0.01	0.03	0.04	0.65	0.80	0.61
4	3rd flapping	0.75	0.00	0.00	0.89	0.94	0.86
5	2nd lagging	0.12	0.24	0.08	0.01	0.03	0.81
6	1st torsion	0.17	0.00	0.41	0.74	0.58	0.01
7	4th flapping	0.64	0.00	0.25	0.97	0.94	0.30
8	5th flapping	0.44	0.00	0.13	0.95	0.79	0.23

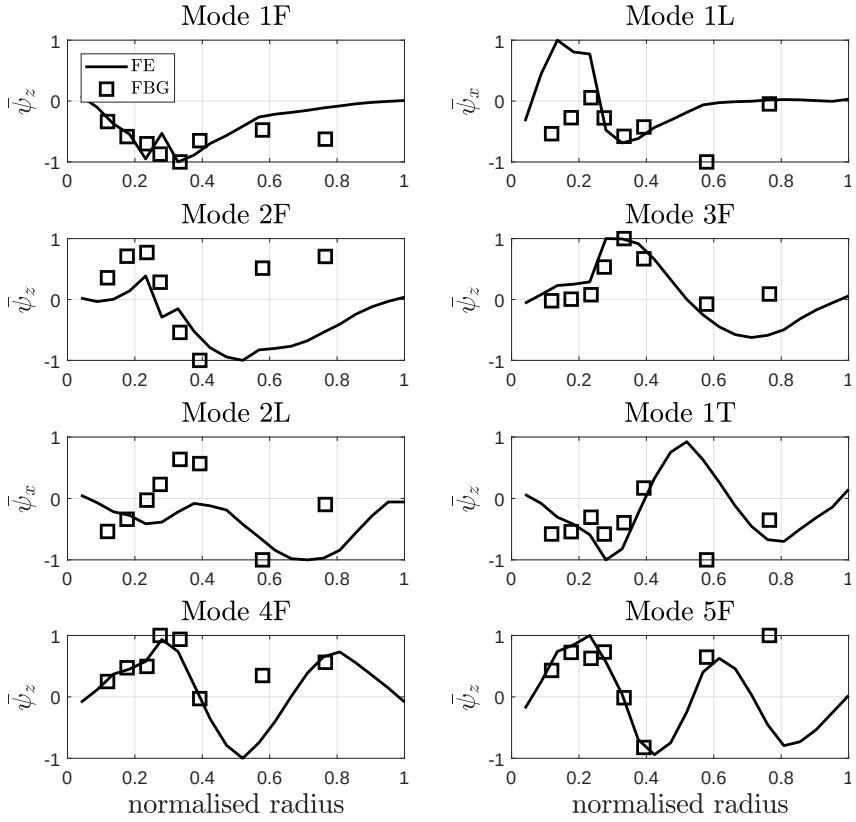

Figure H.7: Local normalised surface strain mode shape $\bar{\psi}_T$ obtained from CH1b

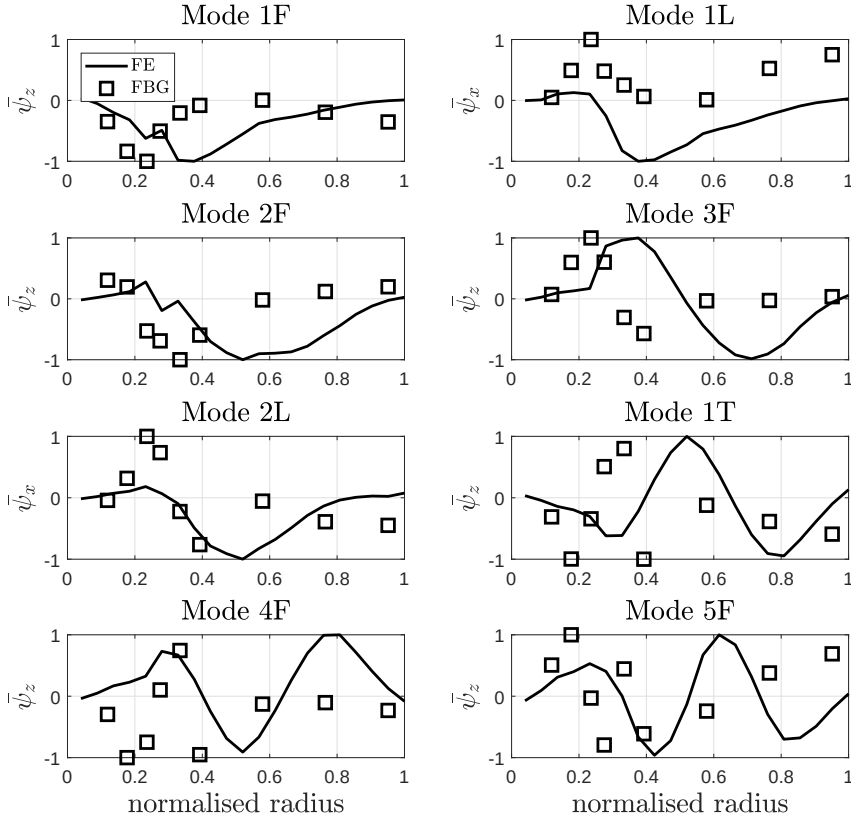

Figure H.8: Local normalised surface strain mode shape $\bar{\psi}_T$ obtained from CH2b

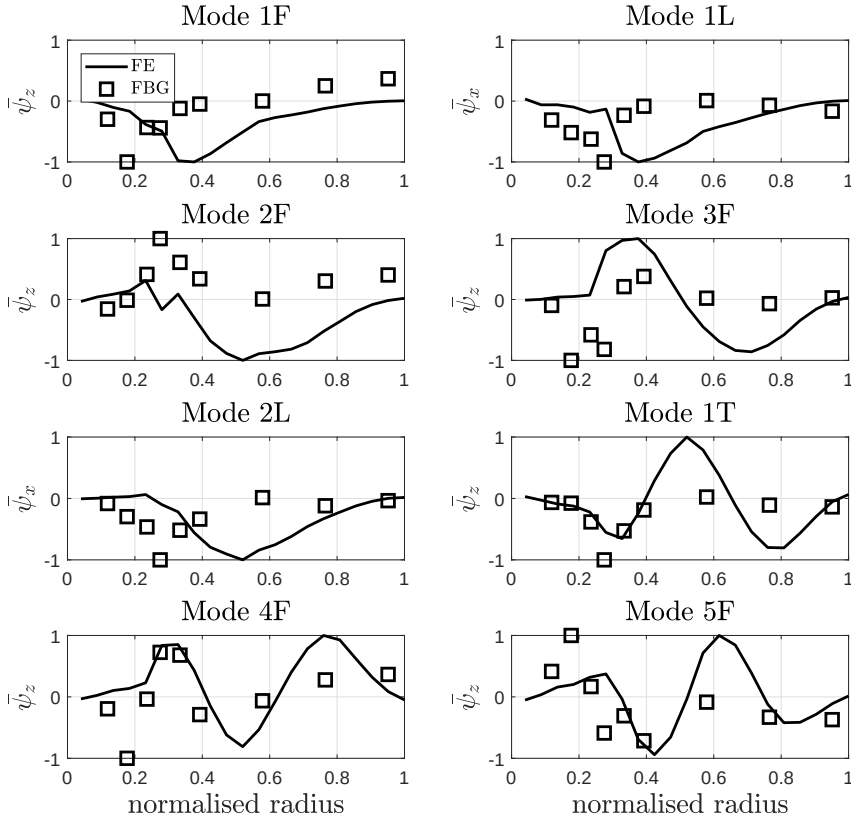

Figure H.9: Local normalised surface strain mode shape $\bar{\psi}_T$ obtained from CH3b

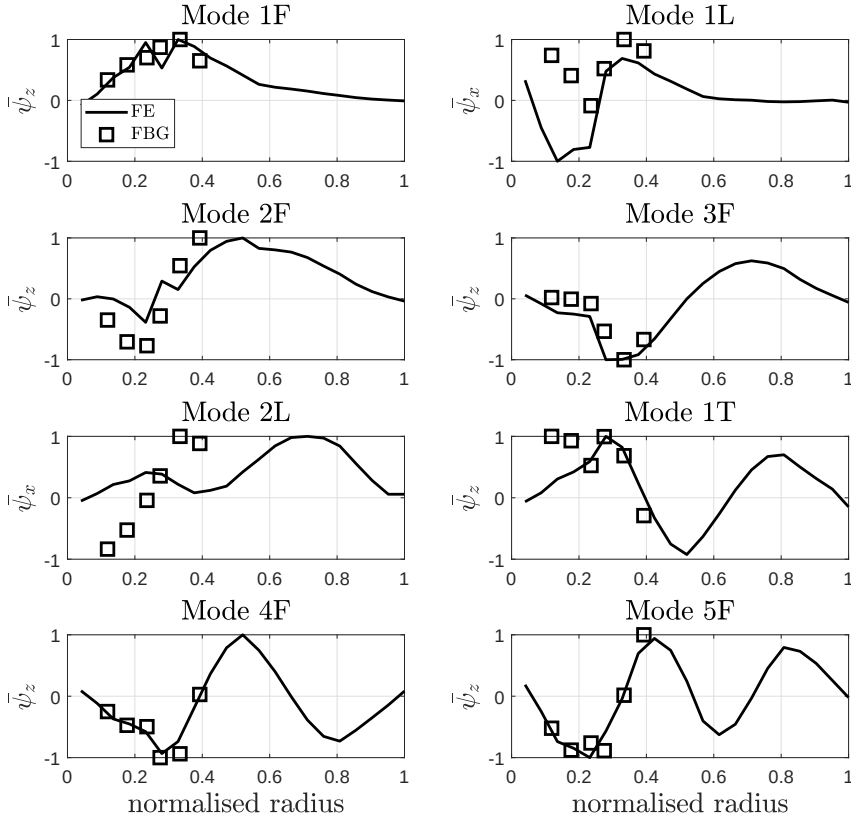

Figure H.10: Local normalised surface strain mode shape $\bar{\psi}_T$ obtained from CH4b

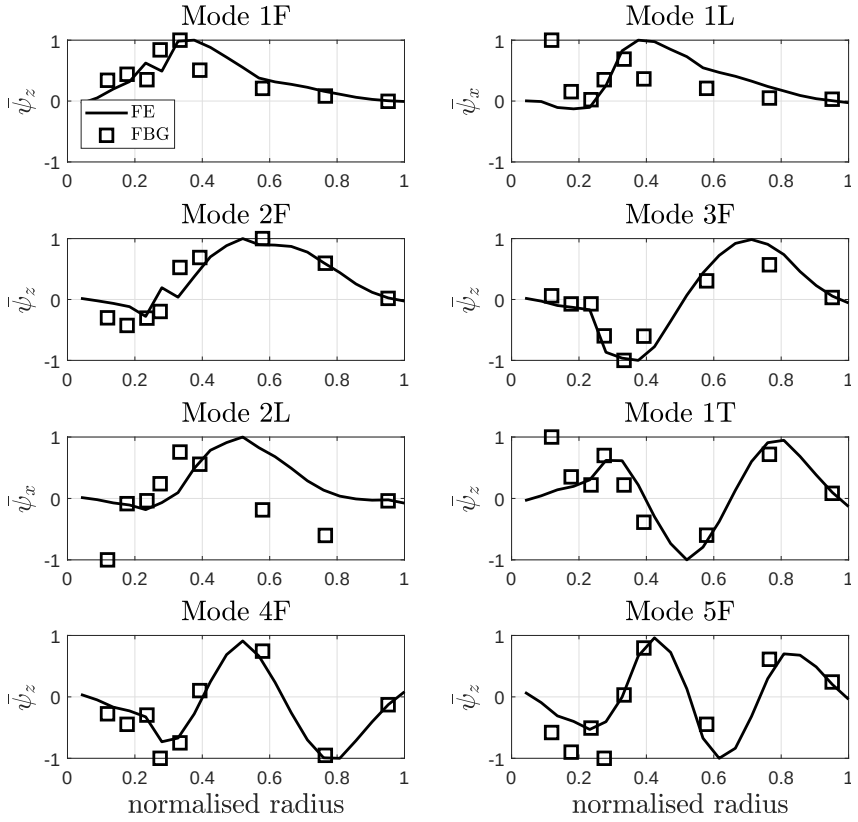

Figure H.11: Local normalised surface strain mode shape $\bar{\psi}_T$ obtained from CH5b

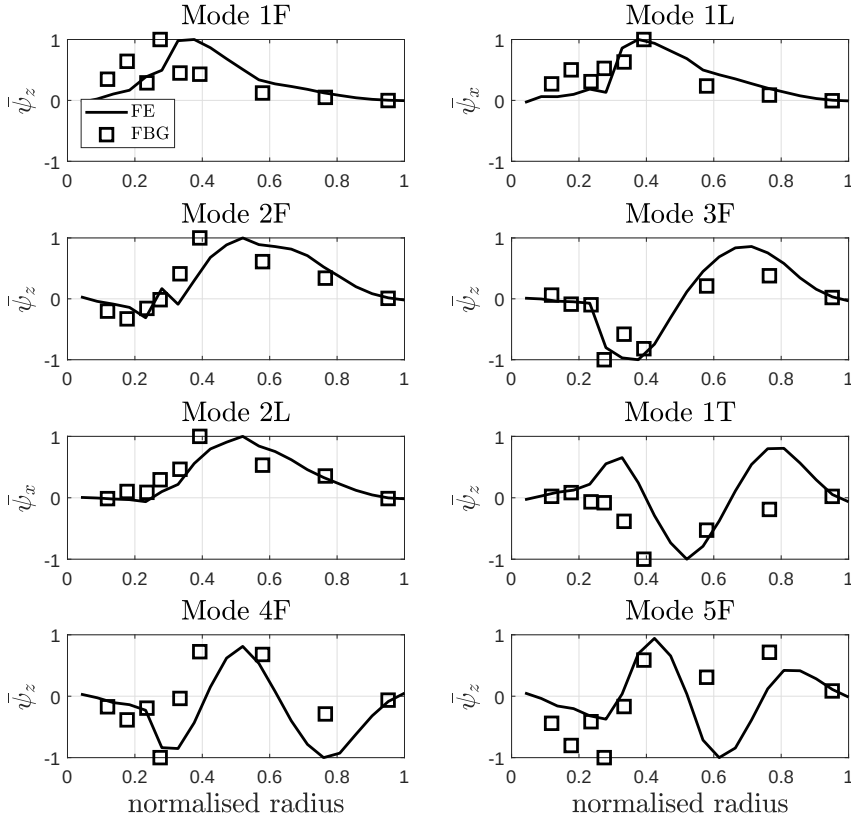

Figure H.12: Local normalised surface strain mode shape $\bar{\psi}_T$ obtained from CH6b